UNIVERSITÉ DE SHERBROOKE
Faculté de génie
Département de génie civil et génie du bâtiment

STRUCTURAL PERFORMANCE OF PRECAST CONCRETE TUNNEL LINING SEGMENTS REINFORCED WITH GFRP BARS UNDER BENDING LOAD

PERFORMANCE STRUCTURELLE DE VOUSSOIRS DE TUNNEL PRÉFABRIQUÉS EN BÉTON ARMÉ D'ARMATURES EN PRFV SOUS CHARGE DE FLEXION

Thèse de doctorat
Spécialité : Génie Civil

Seyed Mohammad HOSSEINI

Sherbrooke (Québec) Canada

May 2023

MEMBRES DU JURY

Prof. Brahim BENMOKRANE

Supervisor/Directeur

Prof. Sébastien LANGLOIS

Examiner/Rapporteur et Évaluateur

Prof. Adel El-SAFTY

External Examiner/Évaluateur externe

Dr. Steve NOLAN

External Examiner/Évaluateur externe

Dr. Hamdy MOHAMED

External Examiner/Évaluateur externe

DEDICATION

To Imam Mahdi who I love him more than everyone
To my wife and my daughter
To my father and my mother
To those who tries to help humanity

ABSTRACT

In underground tunnels made using tunnel boring machine (TBM), the lining is constituted of precast concrete tunnel linings (PCTL) segments. Such PCTL are subjected to corrosive environment especially where they are exposed to wastewater or aggressive soil. Rehabilitation or renovation of corroded reinforced concrete (RC) tunnel segments is accompanied by problems such as very high cost, difficulty and serviceability interruption. An alternative approach to deal with corrosion problem in conventional RC tunnel segments is the use of glass fiber-reinforced polymer (GFRP) bars as a substitution of conventional steel reinforcement. Application of GFRP bars in tunnel segments requires a comprehensive research program for experimental, and analytical investigation of GFRP-reinforced PCTL segments. In this project, novel PCTL segments were tested under three-point bending load. Different parameters of longitudinal reinforcement ratio, size and spacing, configuration of transverse reinforcement (closed stirrups and U-shape stirrups) and type of concrete (normal-strength, high-strength and fiber-reinforced concretes) were considered in the experimental program. In order to achieve the objectives of the experimental phase, a total of 12 full-scale tunnel segments were tested. The segments had parallelogram shape with the arc length of 3100 mm, width of 1500 mm and thickness of 250 mm. The experimental results were evaluated through cracking behavior, failure mechanism, load carrying capacity, serviceability, load-deflection behavior, strain analysis, ductility, and deformability. The experimental program was followed by analytical investigation to evaluate existing models and propose new models to predict flexural strength, shear strength, crack width, deflection and interaction diagrams. In addition, newly developed models were provided to consider the effect of curvilinear shape of a segment on its flexural and shear strength. According to the test results, GFRP-reinforced PCTL segments showed satisfactory failure mechanism, cracking behavior, deflection behavior, and deformability. The structural performance can be further improved by using high strength concrete and fiber-reinforced concrete. Increasing the reinforcement ratio improved the post-cracking stiffness, cracking behavior, flexural strength, and shear strength while changing the mode

in some cases. The overall structural performance of GFRP-reinforced PCTL segments with closed ties and U-shaped ties was similar. Finally, the developed analytical models showed a good agreement with the experimental results.

Keywords: Precast concrete tunnel lining (PCTL) segments; glass fiber-reinforced polymer (GFRP) bars and ties; experimental and analytical investigation; reinforcement ratio; bending load; load-deflection; flexural and shear strength; high strength concrete (HSC); fiber-reinforced concrete (FRC).

RÉSUMÉ

Dans les tunnels souterrains réalisés à l'aide de tunnelier (TBM), le revêtement est constitué de voussoirs de revêtement de tunnels en béton préfabriqué (RTBP). Ces RTBP sont soumis à un environnement corrosif, en particulier lorsqu'ils sont exposés aux eaux usées ou au sol agressif. La réhabilitation ou la réparation des voussoirs de tunnels en béton armé corrodés s'accompagne de problèmes tels que des coûts très élevés, des difficultés et des interruptions de service. Une approche alternative pour traiter le problème de corrosion dans les voussoirs de tunnels en béton armé (BA) conventionnels est l'utilisation de barres d'armature en polymère renforcées de fibres de verre (PRFV) en remplacement de l'armature en acier conventionnelle. L'application de barres PRFV dans des voussoirs de tunnels nécessite un programme de recherche complet pour une étude expérimentale, analytique et théorique sur des voussoirs de revêtement de tunnels en béton armé de PRFV. Dans ce projet, de nouveaux voussoirs de revêtement de tunnels en béton préfabriqué ont été testés sous une charge de flexion en trois points. Différents paramètres tels que le taux d'armature longitudinale, le diamètre et l'espacement des barres, la configuration d'armature transversale (étriers fermés et étriers en U) et le type de béton (béton normal, béton à haute résistance et béton fibré) ont été pris en compte dans le programme expérimental. Un total de 12 voussoirs de revêtement de tunnels en béton préfabriqué (RTBP) grandeur nature ont été testés. Les voussoirs avaient une forme de parallélogramme avec une longueur d'arc de 3100 mm, une largeur de 1500 mm et une épaisseur de 250 mm. Les résultats expérimentaux ont été examinés à travers le comportement de fissuration, le mode de rupture, la charge de rupture, les états limites de service, le comportement charge-déformation, la ductilité et la déformabilité. Des études analytiques ont été menées pour évaluer les modèles existants et proposer de nouveaux modèles pour prédire la résistance à la flexion, la résistance à l'effort tranchant, la largeur des fissures, la déflexion et le diagramme d'interaction charge-moment. De plus, des modèles nouvellement développés ont été mis au point pour considérer l'effet de la forme curviligne du voussoir de tunnel sur sa résistance à la flexion et à l'effort tranchant. Les résultats des essais ont montré que les voussoirs de revêtement de tunnels en béton préfabriqué (RTBP) armés de PRFV présentent de bonnes caractéristiques en termes de mécanisme de rupture,

de comportement à la fissuration, de comportement en déflexion et de déformabilité. Ces performances peuvent être encore améliorées en utilisant du béton à haute résistance ou du béton fibré. L'augmentation du taux d'armature a amélioré la rigidité post-fissuration, le comportement à la fissuration, la résistance à la flexion et la résistance à l'effort tranchant. La performance structurelle globale des voussoirs de revêtement de tunnels en béton préfabriqué (RTBP) armé de PRFV avec des étriers fermés ou des étriers en forme de U était similaire. Enfin, les modèles analytiques développés ont montré une bonne concordance avec les résultats expérimentaux.

Mots-clés: voussoirs de revêtement de tunnels en béton préfabriqué (RTBP); barres et étriers en polymère renforcé de fibres de verre (PRFV); recherche expérimentale et analytique; taux d'armature ; charge de flexion ; charge-courbure ; résistance à la flexion et à l'effort tranchant ; béton à haute résistance (BHR); béton aux fibres (BF).

Acknowledgments

In the name of God, the beneficent the merciful. First of all, thanks to God for enabling me to complete this work. He gave me the ambition, ideas, strength, and endurance to go through all difficulties and achieve this work.

It was a great opportunity for me to carry out this work under the supervision of Prof. Brahim Benmokrane, one of the most knowledgeable professors in the field. He kindly supported me throughout this work, and he helped to gain valuable experiences during my PhD.

I am very thankful to all of those who I have had the pleasure to work with during this research project. I would like to greatly thank Dr. Hamdy Mohamed for his kind help and support during this work. He willingly helped me in every possible way during my PhD. I would also like to greatly acknowledge Dr. Salaheldin Mousa for his valuable assistance with laboratory work, for his help during the preparation of journal papers, and for his willingness to help in every possible way. Furthermore, I really appreciate Dr. Abolfazl Eslami for his valuable help and support before and during my PhD. I am also very grateful to the members of my thesis committee, Prof. Adel Elsafty, Dr. Steven Nolan, Prof. Sébastien Langlois and Dr. Hamdy Mohamed for their valuable comments and suggestions on my PhD thesis. Special thanks to the technicians of our research group, Marc Demers, Jérôme Lacroix and Steven MacEachern, for their help and technical assistance during casting and testing of the specimens.

The author would like to express his special thanks and gratitude to the Natural Science and Engineering Research Council of Canada (NSERC), Canada Research Chair Program, the Fonds de la recherche du Quebec–Nature et Technologie – (FRQ-NT) for their financial support, Pultrall Inc. for the donation of the FRP materials, and Sym-Tech Béton Préfabriqué, Sainte-Hyacinthe, for the contribution in casting of the specimens.

Most importantly, I would like to greatly appreciate my wife, Bahareh Nader Tehrani, for her valuable help and support during my PhD. Her love was the main motivation for me to

continue my work. In addition, owe a dept of gratitude to my parents whose infallible love and continuous encouragement are with me in whatever I pursue.

TABLE OF CONTENTS

LIST OF TABLES

LIST OF FIGURES

CHAPTER 1 INTRODUCTION

1.1. Statement of Problem

Tunnels play a key role in assisting the movement of people, goods, and special services. The functionality of tunnels depends on the structural and durability performance of their lining systems. Tunnel lining systems act as lines of defense against large overburden loads and surrounding complex geotechnical conditions. In underground tunnels made using tunnel boring machine (TBM), the lining is constituted of precast concrete tunnel linings (PCTL) segments. Normally, PCTL segments are designed for 100 years of service life. Such precast concrete tunnel linings (PCTL) segments are subjected to corrosive environment especially where exposed to the wastewater or aggressive soil (ACI 533.5R-20; Caratelli et al., 2016). According to ACI 533.5R-20, the main reasons for corrosion of steel reinforcement in PCTL segments are chloride attack in tunnels adjacent to seawater, carbonation attack in heavily trafficked roadway tunnels, tunnels adjacent to aggressive soils, and stray current corrosion in subway and railway tunnels (ACI 533-5R-20). Mitigation of such corrosion problems in tunnels requires costly and difficult methods that sometimes cannot eliminate the risk of corrosion. Rehabilitation or renovation of the corroded reinforced concrete (RC) tunnel segments is accompanied by such problems as high cost and serviceability interruption. An alternative approach to deal with corrosion problem in conventional reinforced concrete tunnel segments is the use of glass fiber-reinforced polymer (GFRP) bars as a substitution of conventional steel reinforcement (Caratelli et al. 2016; Spagnuolo et al. 2017). GFRP bars offer such distinct advantages over conventional steel rebars as corrosion resistance, chemical resistance, electromagnetic neutrality, high strength-to-weight ratio, high tensile strength, competitive life cycle cost, and fatigue resistance. Further, reduction in concrete cover, suitability for parts of the tunnel that eventually should be demolished and possibility to create dielectric joints are among the merits of using GFRP reinforcement in tunnel segments (ACI 440.1R-15, Caratelli et al., 2016). Due to low modulus of elasticity of GFRP bars, controlling of cracking and deflection in GFRP-reinforced flexural elements is the main concern in their design. In addition, shear

capacity of GFRP-RC members is generally lower than their steel-reinforced counterparts (ACI 440.1R-15). In tunnel segments, arc shape of segments as well as loading and boundary conditions in the ring are beneficial for controlling of deflection. Furthermore, allowable crack width in GFRP-RC structures is more than steel-reinforced ones (CAN/CSA S6-19) and the cracking behavior can be improved by using high-strength concrete (HSC) and fiber-reinforced concrete (FRC) in GFRP-RC flexural elements (Yang et al., 2012 and CAN/CSA S6-19). These issues help adoption of GFRP reinforcement in PCTL segments. Degradation of the concrete induced by sulfate, acid, and frost attacks is another important degradation mechanism in tunnels (ACI 533.5R-20). Using HSC and FRC can effectively improve concrete durability in resisting such attacks (de Almeida 1991; Mostofinejad et al. 2021). Consequently, a hybrid use of GFRP reinforcement and HSC and FRC is a viable solution to improve durability of PCTL segments.

PCTL segments are subjected to different loading conditions during construction and service stages, which induce bending moments, shear force, and axial load in the segments (ACI 544.7R-16). The literature offers no design procedures or recommendations for designing GFRP-reinforced PCTL segments. In addition, the current FRP-related design guidelines and standards—such as ACI 440.11-22, CAN/CSA S806-12 (R2017), and CAN/CSA S6-19—make no recommendations for using FRP bars in tunnel segments. Furthermore, tunneling-related design standards—such as ACI 533.5R-20, ITA-WG2-19, JSCE (2007), and AFTES-WG7-9.—offer no design procedures for GFRP-reinforced tunnel segments. Innovative utilization of GFRP reinforcement in PCTL segments in real tunneling projects necessitates comprehensive research program to evaluate their structural behavior and investigate the effect of different parameters which affect the performance of GFRP-reinforced PCTL segments. Furthermore, analytical and theoretical investigation to propose design guidelines and equations is needed before major application of GFRP reinforcements in PCTL segments.

1.2. Research Motivations

The primary motivations beyond this research can be summarized as

- Construction of thousands of kilometers of tunnels per year with high service life demand and vulnerability of steel-reinforced tunnel segments to corrosion especially in harsh environment.
- Lack of enough experimental and analytical data on the structural behavior of GFRP-reinforced PCTL segments as well as the effect of different parameters such as reinforcement ratio and spacing, type of concrete and tie configuration.
- Scarcity of design guidelines, provisions and equations related to GFRP-reinforced PCTL segments.

1.3. Research Significance

Although using non-corrosive rebars in tunnel segments is essential to ensure their proper long-term performance in harsh environment, current design provisions of CAN/S806-12; CAN/CSA S6-19; and ACI 440.11-22 are not applicable to precast segmental tunnel linings reinforced internally with GFRP bars. In addition, no design provisions were provided by tunneling-related design standards of ACI 533.5R-20, ITA-WG2-19, JSCE (2007), and AFTES-WG7-93 regarding the design of GFRP-reinforced PCTL segments. Moreover, only a very limited number of studies are available in the technical literature related to the application of GFRP bars in tunnel segments. This study pioneers investigation of the parameters reinforcement ratio, tie configurations, and concrete type in GFRP-reinforced PCTL segments. The experimental program was followed by an extensive analytical investigation aiming at validating the existing models and proposing new design equations and procedures for GFRP-reinforced PCTL segments.

1.4. Research Objectives

The main objectives of the proposed research project are:

1. To examine the feasibility and efficiency of using GFRP bars instead of conventional steel reinforcement in precast segmental tunnel linings.

2. To open the door to major applications of non-corrosive GFRP bars in precast segmental tunnel linings.

The specific objectives can be summarized as follows:

- To assess the structural performance of full-scale PCTL segments reinforced with GFRP bars under bending load compared to conventional PCTL segments reinforced with steel reinforcement.
- To investigate the effect of different parameters of reinforcement ratio, tie configurations, and concrete type on the structural performance of GFRP-reinforced PCTL segments.
- To evaluate the validity of the current analytical and design approaches for designing GFRP-reinforced PCTL segments.
- To develop design equations, recommendations, and procedure for designing GFRP reinforcing bars in PCTL segments.

1.5. Research Methodology

To achieve the objectives of the research project, two steps including experimental, and analytical phases are proposed. In the following section, a brief description of each phase is provided.

1.5.1. Experimental Program

The structural performance of full-scale GFRP-reinforced PCTL segments in terms of failure mechanism, cracking behavior, deflection behavior, serviceability, load carrying capacity, strain behavior, ductility, and deformability was investigated through conducting bending full-scale tests. A total of 12 full-scale precast concrete tunnel segments were tested under bending monotonic loading at structural lab of department of Civil Engineering, University of Sherbrooke. The specimens measured 3100 mm in length (arc length), 1500 mm in width, and 250 mm in thickness with a parallelogram shape. The test parameters include reinforcement type (steel and GFRP), reinforcement ratio (0.48, 69, 0.90, and 1.28%), tie

configurations (closed ties with U-shaped ties), concrete strength (NC and HSC), and concrete type (NC and FRC).

1.5.2. Analytical Investigations

The obtained experimental results were used to derive design models and recommendations for designing of GFRP-reinforced tunnel segments. The results obtained through the existing models in ACI 440.11-22, CAN/CSA S806-12 (R2017) and CAN/CSA S6-19 for predicting flexural strength, shear strength, and crack width were compared with the experimental data. In addition, procedures for obtaining design interaction diagrams in GFRP-reinforced PCTL segments were developed. Then, deflection prediction methodologies were proposed to calculate deflection in GFRP-reinforced curvilinear members focusing on PCTL segments. Finally, an analytical procedure was developed to consider the effect of curvilinear shape of the segments on its flexural and shear strength.

1.6. Dissertation Layout

The dissertation consists of eight chapters. The contents of each chapter can be summarized as follows:

Chapter 1 presents the statement of problem, research motivations, research significance, research objectives, and research methodology of this study.

Chapter 2 provides a brief summary about tunneling and applied loads on the tunnel segments in different loading stages. Then, the main properties of the FRP materials used as internal reinforcement were reviewed. Following that, flexural strength, shear strength, ductility and deformability of GFRP-RC beams and one-way slabs were reviewed according to the literature. Thereafter, the literature on the application of FRC in PCTL segments and GFRP-RC elements was reviewed. In the next step, the summary of studies performed on the GFRP-RC PCTL segments was presented. Then, the provisions of design codes and guidelines on the flexural strength, shear strength, cracking and deflection were presented.

Chapter 3 presents the outline of the experimental research program carried out in this study. After presenting the material properties, this chapter describes details of test specimens, construction process, test setup, instrumentations, and loading procedure.

Chapter 4 (1st article) investigates the behavior of GFRP-reinforced PCTL segments under bending load using four full-scale specimens. The investigated parameters were the reinforcement type (GFRP and steel) and reinforcement ratio (0.48%, 0.9, and 1.3%) with different configurations of GFRP bar spacing and size. The structural performance was evaluated in terms of cracking behavior, failure mechanism, load–deflection curve, strain analysis, and deformability. Lastly, an analytical investigation was conducted to evaluate the ACI 440.1R-15 design provisions for predicting the flexural strength, shear capacity, and crack width of GFRP-reinforced PCTL segments [**Reference:** Hosseini, S.M., Mousa, S., Mohamed, H.M. and Benmokrane, B., 2022. Structural Behavior of Precast Reinforced Concrete Tunnel Segments with Glass Fiber-Reinforced Polymer Bars and Ties under Bending Load. *ACI Structural Journal*, 119(1), pp.307-319].

Chapter 5 (2nd article) investigates the structural performance of GFRP-reinforced PCTL segments constructed with HSC by testing four full-scale specimens. The investigated parameters included concrete compressive strength (normal-strength concrete [NSC] and HSC), reinforcement ratio (0.48% and 0.90%), and tie configuration (closed ties with U-shaped ties). The results are presented and discussed in terms of cracking behavior, failure mechanism, deflection behavior, strain in reinforcement and concrete, ductility, and deformability. An analytical investigation was carried out to evaluate and modify the existing design provisions (ACI 440.1R-15, CAN/CSA S806-12 (R2017), CAN/CSA S6-19, and AASHTO 2018) for use in predicting the shear and flexural strength of GFRP-reinforced HSC PCTL segments [**Reference:** Hosseini, S.M., Mousa, S., Mohamed, H.M., Eslami, A. and Benmokrane, B., 2022. Experimental and Analytical Study on Precast High-

Strength Concrete Tunnel Lining Segments Reinforced with GFRP Bars. *Journal of Composites for Construction*, 26(5), p.04022062].

Chapter 6 (3rd article) presents results obtained from both experimental and analytical studies on the behavior of GFRP-reinforced FRC PCTL segments under bending load. Four full-scale tunnel segment specimens were constructed and tested under three-point bending load. The influence of concrete type, reinforcement ratio, and tie configurations on the cracking behavior, deflection behavior, failure mechanism, load-carrying capacity, strain behavior, and deformability of GFRP-reinforced FRC PCTL segments was evaluated. Then, an analytical investigation was carried out in order to propose and evaluate different methods for predicting the flexural and shear capacities of such elements [**Reference:** Hosseini, S. M., Mousa, S., Mohammad, HM., Ferrier, E., Benmokrane, B., 2022. Experimental and Analytical Investigation of Precast Fiber-reinforced Concrete Tunnel Lining Segments Reinforced with GFRP Bars Under Bending Load. *Tunneling and Underground Space Technology*, 139, p.105230].

Chapter 7 (4th article) investigates the effect of reinforcement ratio and tie configuration on the behavior of GFRP-reinforced PCTL segments at the service and ultimate stages. Novel procedures and equations were developed to obtain axial load–bending moment interaction diagrams at the ultimate and service stages. In addition, interaction diagrams were developed to consider the creep-rupture stress limits in GFRP bars. Furthermore, axial load–shear-strength interaction diagrams were developed for GFRP-reinforced PCTL segments, as well as a simplified procedure to control cracking. Afterward, a parametric study was performed to evaluate the effect of concrete compressive strength, reinforcement ratio, and cross-sectional thickness on the axial load–bending moment interaction diagrams of GFRP-reinforced PCTL segments. The analytical results were compared to the experimental results from the current study and the literature [**Reference**: Hosseini, S. M., Mousa, S., Mohammad, HM., Benmokrane, B., Development of Strength Interaction Diagrams for Designing Precast Concrete Tunnel Lining Segments Reinforced with GFRP Bars. *Engineering Structures,* 284, p.115976].

Chapter 8 (5th article) reports the results of a comprehensive analytical study implemented to develop deflection prediction methodologies for curvilinear RC members with GFRP reinforcement, focusing on PCTL segments. The first step involved modifying the procedures for estimating elastic deflection, cracking moment, and cracked moment of inertia. In the next step, three methodologies of effective moment of inertia, integration of curvature, and integration of curvature considering tension–stiffening were developed for curvilinear members. Then, the analytical results were compared to the experimental database, and a novel method was developed for predicting deflection in curvilinear GFRP-RC members. In the final step, a procedure was developed to adapt the presented methodologies for use with a tunnel segment under real load and boundary conditions [**Reference**: Hosseini, S. M., Mousa, S., Mohammad, HM., Benmokrane, B., Deflection Control Methodologies for Curvilinear Concrete Members Reinforced with GFRP Bars. *ACI Structural Journal* ***(accepted)***].

Chapter 9 (6th article) reports the results of an analytical study performed to develop in-depth models to predict flexural and shear strength of GFRP-reinforced curvilinear members with focus on precast concrete tunnel lining segments. The effect of curvilinear shape on the additional stresses due to deviation of the forces was discussed. In the next step, a model was developed to consider the effect of curvilinearity on the flexural strength of GFRP-reinforced curvilinear members. Following that, two shear strength prediction models were developed based on modified compression field theory and critical shear crack theory for estimating shear capacity of curvilinear GFRP-RC members. The experimental results were then employed to validate the proposed models. Finally, a parametric study was conducted to investigate the effect of different parameters on the flexural and shear strength of curvilinear GFRP-RC members [**Reference**: Hosseini, S. M., Mousa, S., Mohammad, HM., Benmokrane, B., Curvilinearity Effect on The Flexural and Shear Strength of Curved GFRP-Reinforced Concrete Members. *Submitted to ACI Structural Journal* ***(under review)***].

Chapter 10 presents the thesis summary, conclusions, and recommendation for future research.

CHAPTER 2 BACKGROUND AND LITERATURE REVIEW

2.1. Introduction

In this chapter, general information about tunneling is presented. Then, applied loads on tunnels during construction and serviceability as well as their design method are discussed. Then, the main characteristics and properties of the FRP materials used as internal reinforcement are reviewed. Following that, flexural strength, shear strength, ductility and deformability of GFRP-RC beams and one-way slabs are reviewed according to the literature. Thereafter, the literature on the application of FRC in PCTL segments and GFRP-RC elements was reviewed. In the next step, the summary of studies performed on the GFRP-RC PCTL segments are presented. Then, the provisions of design codes and guidelines on the flexural strength, shear strength, cracking and deflection are presented.

2.2. Tunneling

2.2.1. Precast concrete tunnel lining segments

Tunnels can be classified either based on their function or their construction method. According to their function, tunnels are classified as metro tunnels, highway tunnels, railway tunnels, wastewater tunnels, pedestrian tunnels and other types. Based on their construction technique, tunnels are classified as mechanized shield tunneling, drill-and-blast push, cut-and-cover, new Austrian tunneling method (NATM), and other types (Tengilimoglu 2019). One of the most popular methods for underground tunneling is mechanized shield tunneling in which temporary support structure is provided for tunnel during the excavation phase. At the same time, lining is installed using the TBM directly (Fig. 2.1). TBM's equipment systems are able to construct tunnels in various geological situations such as soft soils and high groundwater pressure which are known as difficult geological conditions. In

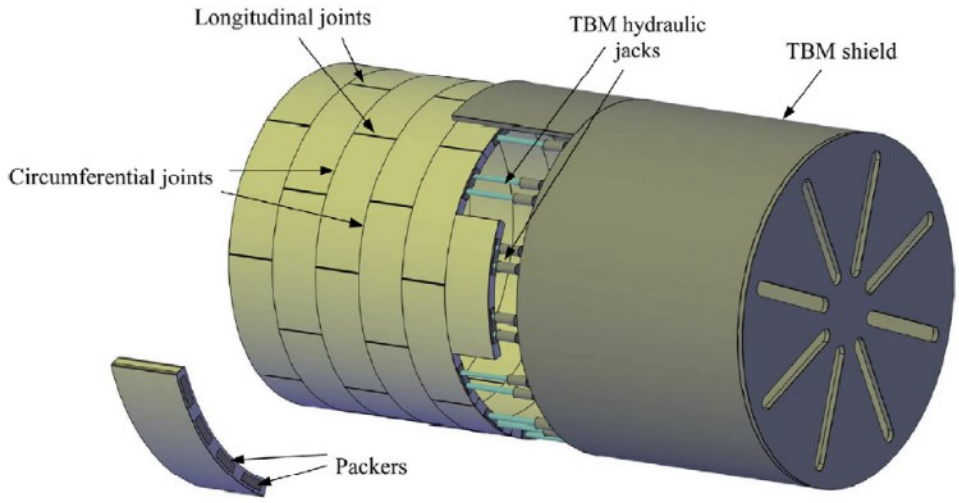

Figure 2.1 Segmental tunnel linings and TBM (Arnau and Molins 2015).

mechanized shield tunneling, the is bolstered by segmental linings which are single segments, with specific dimension and shape, assembled within the TBM tail shield to form a continuous ring. Subsequent rings are assembled together with offset joints using TBM thrust action (Fabozzi 2017). Segments can be rectangular, trapezoidal, rhomboidal, or hexagonal in shape except the key segment that is the last segment placed to close the ring. The most common shape in design practice specially for the rings with large diameters are rectangular, trapezoidal and rhomboidal shapes (Fabozzi 2017). The typical thickness of the segments is between 200 to 700 mm which depends on the function and design loads. The thickness is determined in such a way that the segment can withstand the external forces while providing the area required for bearing the thrust jacking force. In the tunnels with typical diameters, the thickness of the lining segments is about 1/20 of the tunnel diameter (Blom 2004).

The adjacent segments in each ring are connected with each other using longitudinal joints. The Axial force in ring direction, bending moment from eccentric axial forces, and shear forces can be transferred through longitudinal joints. In designing of tunnel segments, longitudinal joints are considered as hinges or partial hinges which have limited ability to transfer bending moments. Three typical forms of longitudinal joints are two-flat-contact-surfaces, two-

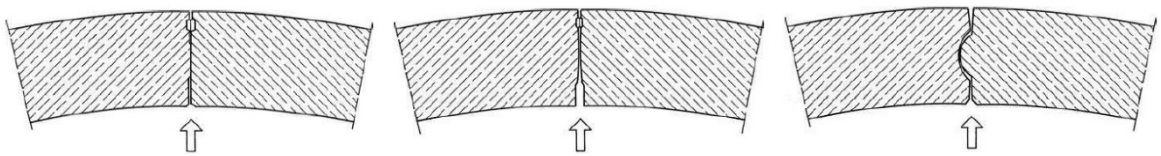

a) Longitudinal joints with flat contact surfaces

b) Longitudinal joint with two-convex-contact- surfaces

c) longitudinal joint with convex/concave-contact-surfaces

Figure 2.2 Longitudinal joints contact surfaces (Maidl B. et al. 2011).

convex-contact- surfaces and convex/concave-contact-surfaces joints as shown in Fig. 2.2 (Maidl B. et al. 2011). In segmental tunnel linings, the adjacent rings are connected via transversal, circumferential or ring joints. The main transferred load between adjacent rings is the thrust load which is applied using hydraulic actuators against the TBM during construction of tunnels. If the adjacent rings vary in pattern, additional coupling forces occur in transversal joints (Maidl B. et al. 2011).

2.2.2. Applied loads, analysis and design

Tunnel segments are subjected to permanent and temporary loads. Permanent loads are from the ground and groundwater pressure. Temporary loads are from production, transportation, and construction. Tunnel segments are designed to provide enough capacity to withstand the loads at serviceability limit state (SLS) and ultimate limit state (ULS) (ACI 544.7R-16). The detailed description of different loads applied on the tunnel segments in different loading stages is presented as follows according to ACI 544.7R-16; ACI 533.5R-20.

2.2.2.1. Segment stripping

Lifting and stripping of the segments from the form at the manufacturing plant is recognized as segment stripping load. During lifting of the segments, they should be considered as cantilever beams from the lifting point which are subjected to their own weight multiplied by the load factor. The factored bending moment in this stage is compared with the design moment strength and the tensile stress in concrete is compared with tensile strength of concrete at the time of stripping (ACI 544.7R-16).

2.2.2.2. Segment storge

After stripping, the segments are stacked together in the storage area. Wood blocks are normally used between the segments and between the first segment and the ground. In practical applications, there is some unintended eccentricities between the stack supports in upper and lower rows. For design approaches, an eccentricity of 100 mm is recommended. The self-weight of the bottom segments, the weight of the above segments as well as the eccentricity cause bending moment, should be multiplied by the load factor and compared with the flexural strength of the segment at the storage time. Furthermore, the tensile stress resulting from the bending moment in the segment should be checked with the tensile strength of concrete at the time of storage (ACI 544.7R-16).

2.2.2.3. Segment transportation

After achievement of specified concrete compressive strength, segments are transported to the job site. During the transportations, segments are subjected to different dynamic shock loadings. Normally, half of the segments in a full ring are stacked together and the wood blocks are used between the segments. Considering the eccentricity of 100 mm, the dead load should be multiplied by the load factor as well as the dynamic factor (typically 2.0) to simulate the transportation loadings. The concrete strength at 28 days may be considered for design check in this load case (ACI 544.7R-16).

2.2.2.4. Segment handling

Vacuum lifters are usually used for handling of segments from the stack yard into rail cars and TBM. The segments in this stage are modeled as cantilever beams similar to stripping stage. In addition to the dead load factor, a dynamic shock factor of 2.0 is recommended for design. The concrete strength at 28 days may be considered for design check in this load case (ACI 544.7R-16).

2.2.2.5. Tunnel boring machine thrust back force

The TBM advancement is achieved by thrusting against the jacking pads positioned along the circumferential joint of the latest completed ring (Fig. 2.3). As a result of the thrust load, considerable bursting tensile stresses are induced in the segment. Also, spalling tensile force

are induced as a result of acting between adjacent jack pads along the circumferential joint. The TBM thrust load depends on the type of geologic materials which are excavated. ACI 544.7R-16 presents different methods for predicting the amount of thrust load and design of tunnel segments accordingly.

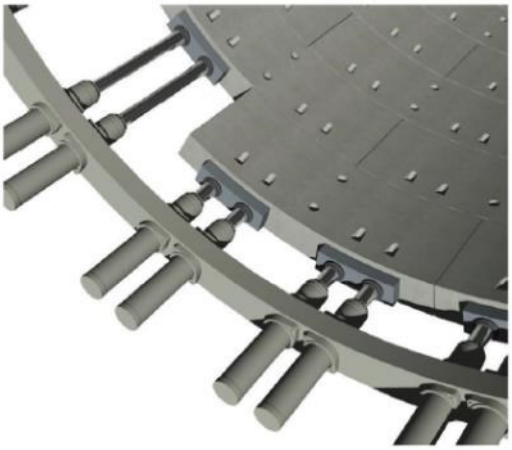

Figure 2.3 Segmental tunnel linings and TBM machine (Arnau and Molins 2015).

2.2.2.6. Tail skin back-grouting pressure

In shield tunneling, the excavated diameter is greater than the assembled tunnel ring diameter. Therefore, a tail void exists between the lining and the ground. In order to fill this annular space, grout is injected with high pressure to ensure the complete contact between the lining and the ground as well as restrict the ground settlement. The grouting pressure can be estimated using equations presented in ACI 544.7R-16 and multiplied by the load factor (1.25 is recommended for self-weight and grout pressure load combination). Then, the resulting axial load and bending moment should be checked using the compressive and tensile strengths of concrete at 28 days.

2.2.2.7. Localized back grouting (secondary) pressure

The secondary or check grouting is performed using holes prefabricated in the segments to ensure that the annular gap has been filled. Secondary grouting produces local pressure on the tunnel segment which also need to be considered in the design procedure.

2.2.2.8. Earth pressure, ground water, and surcharge load

In the serviceability stage, tunnel segments are subjected to horizontal earth pressure, groundwater, self-weight, surcharge and ground reaction loads. Appropriate load factors should be considered for both serviceability limit state (SLS) and ultimate limit state (ULS). In order to analyze the tunnel segments under the mentioned loads, different analyzing methods such as elastic equation method, beam-spring method, finite element method and discrete element method can be used. A brief description of each method is presented as follows:

2.2.2.8.1. Elastic equation method

A simple method for calculation of forces in circular tunnels is presented by ITA WG2-19 and JSCE Tunnel Engineering Committee 2007 which is known as elastic equation method. In this method, the effect of uniform vertical ground and groundwater pressure, linearly varying lateral pressure of earth, lining self-weight, and triangularly distributed horizontal ground reaction is considered in the analyses of tunnel segment. The forces in the members then are calculated according to the elastic equations presented in ITA WG2-19 and JSCE Tunnel Engineering Committee 2007. The segments in this method are modeled using uniform reduced bending rigidity. Therefore, the influence of longitudinal joints between the segments intrinsically considered.

2.2.2.8.2. Beam-spring method

In beam-spring method, the segments are modeled as a series of beams between the longitudinal joints. Also, linear translational springs in the radial direction are used to model the lining-ground interaction (ACI 544.7R-16).

2.2.2.8.3. Finite element method and discrete element method simulations

Finite element method (FEM) and finite difference method (FDM) are appropriate for analyzing the tunnels in soft ground, loose rock, and partially homogenous solid rock. For tunnels in fractured rock, the discrete element method (DEM) is more appropriate for analyzing the loads. Both two-dimensional and three-dimensional approaches can be used for analysis of the tunnel segments according to complexity of geometry and loadings. With

utilizing FEM, the ground deformations, stress redistribution and post-yielding behavior of materials can be modeled. As this method can analyze complex underground and structural conditions, it is a reliable method for analyzing the tunnel segments (ACI 544.7R-16).

2.2.2.9. Longitudinal joint bursting load

The normal forces between adjacent segments are transferred using longitudinal joints. The cross-sectional area where the load is transferred are smaller than the segments width. Therefore, bursting tensile stress may develop along the longitudinal joints. In order to analyze this load case, the maximum obtained normal force should be applied to the longitudinal joints without applying additional load factors. FEM analysis and simplified equations of ACI 318-19 may be used to analyze this load case (ACI 544.7R-16).

2.2.2.10. Loads induced due to additional distortions

Additional distortion in tunnel segments can take place due to misalignment and yielding of joints, excessive grouting pressure, ground movement due to construction of adjacent tunnel. These loads may be considered in design process using different approaches such as FEM, theory of elasticity, or the formula proposed by Morgan (ACI 544.7R-16 ; Morgan 1961)

2.2.2.11. Other loads

Earthquake, fire, explosion, excessive longitudinal bending moments, breakouts at cross passageways, portals and shafts loads are other load effects that need to be considered in the design process of tunnel segments specifically according to the situation where the tunnel is located (ACI 544.7R-16).

2.3. FRP reinforcement

2.3.1. FRP materials

FRP is a composite material consisting of polymeric resins and reinforcing fibers. Fiber quality, orientation, shape, volumetric ratio, adhesion to the matrix, and the manufacturing process determine the mechanical properties of the FRP composite. However, the matrix not

only binds and holds the fibers in position and allows transfer and redistribution of load between fibers, but also is responsible for protecting fibers from environmental attack. In addition to fiber and resin, additives and fillers are added for curing or other reasons. Carbon, glass, and aramid are the most commonly used fibers in FRP composites (ACI 440.1R-15, ISIS Canada 2007). The choice of fibers influences some properties of FRP materials such as density, tensile strength, compressive strength, impact resistance, fatigue properties, modulus of elasticity, resistance to environmental conditions, and cost. Selection of appropriate matrix also affects manufacturing process of FRP composites as well as durability properties. Different types of FRP products are manufactured including bars, fabric, grids, standard structural shapes, tendons, plates, sheets, and pipes. There is a huge potential for use of different types of FRP in construction industry. FRP materials can be used as internal or external reinforcement in structures. In new concrete structures, the main use of FRP materials is in form of FRP bars as a substitute for conventional steel reinforcement (longitudinal and transverse reinforcement). It is recommended to use FRP reinforcements in structures exposed to harsh environments such as highway infrastructures (bridges, retaining walls, concrete pavement), marine structures, and structures in chemical plants, to achieve more durable structures (ISIS Canada 2007). Three common types of FRP bars used in construction industry as internal reinforcement are glass fiber-reinforced polymer (GFRP), carbon fiber-reinforced polymer (CFRP) and aramid fiber-reinforced polymer (AFRP). Basal fiber-reinforced polymer (BFRP) is another emerging technology that has recently been standardized via ASTM D8505-23. In general, the tensile strength and modulus of elasticity of CFRP bars are greater than GFRP, BFRP and AFRP bars while the GFRP bars has the lowest tensile strength and modulus elasticity (CAN/CSA S807-19).

FRP bars could be used as an internal reinforcement in different structural elements such as beam, slab, columns, walls, piles, *etc*. A great number of research projects have been conducted to investigate the performance of FRP-reinforced structural elements. This study deals with the behavior of the GFRP-reinforced PCTL segments under bending load. Such behavior is somewhat similar to the behavior of beams and one-way slabs. Therefore, a brief

review is presented in this section on the behavior of FRP-RC beams and one-way slabs under bending load.

2.3.2. Behavior of FRP-RC beams under bending load

2.3.2.1. Flexural strength

The most important parameters that affect the flexural strength of FRP-RC members are reinforcement ratio (El-Nemr et al., 2013; Kassem et al., 2011; Masmoudi et al., 1998; and Mousa et al., 2019), concrete strength (Theriault and Benmokrane, 1998; and Yost and Gross, 2002), and FRP reinforcement surface (Nanni 1993). By increasing the reinforcement ratio, the flexural strength increases, but the concrete compressive strength at failure limits the increment in the over-reinforced concrete beams (Theriault and Benmokrane, 1998; and Masmoudi et al., 1998). In this regard, Kassem et al. (2011) concluded that increasing in reinforcement ratio did not lead to considerable increment in flexural capacity. They reported that 50% and 100% increase in reinforcement ratio led to only 4 and 16% enhancement in flexural strength. Furthermore, it is reported by El-Nemr et al. (2013) that increasing the reinforcement ratio from 0.36 to 1.47% and from 0.55 to 1.78% enhanced the load-carrying capacity by 143% and 224% in NSC, respectively, while this increment was 28% and 116% in HSC beams.

Generally, flexural strength of FRP-RC beams increases with increment of concrete compressive strength. However, the increment is limited to the concrete compressive strain at failure which normally decreases with increment of the concrete compressive strength (Nanni 1993; Theriault and Benmokrane, 1998; and Yost and Gross, 2002).

Using sand-coated FRP rebars enhances the flexural strength of FRP-RC beams compared to uncoated rebars (Nanni, 1993); however, there is not considerable difference between flexural strength of beams reinforced with sand-coated and ribbed-surface bars (Kassem et al, 2011).

2.3.2.2. Shear strength

Shear strengths is an important factor that should be considered in designing FRP-reinforced structural elements under bending load. In general, lower modulus of elasticity of GFRP bars and their weaker contribution in dowelling action leads to a lower shear capacity of GFRP-RC members compared to the steel-RC ones (ACI 440.1R-15). Many parameters affect the shear strength of FRP-RC members, such as concrete type and strength, reinforcement rigidity, size effect, interaction of shear force and bending moment at the critical section, distance of the critical section from the supports, and strain in longitudinal reinforcement. Increasing reinforcement ratio and concrete compressive strength enhance the shear capacity of GFRP-RC elements (Khavaran 2019).

2.3.2.3. Cracking behavior

One of the important criteria in the design of FRP-RC flexural elements is control of cracking. In some cases, crack control even limits the design of FRP-RC members. On the other hand, as FRP bars are resistant against corrosion, the allowable crack width in FRP-RC structures is wider than that of steel ones. Reinforcement ratio, reinforcement spacing, FRP reinforcement surface, stiffness of FRP bar, and concrete cover are the main parameters affects the cracking behavior of FRP-RC beams (ACI 440.1R-15; CAN/CSA S806-12, R2017; and CAN/CSA S6-19).

According to Masmoudi et al. (1996), increasing the reinforcement ratio leads to narrower cracks with closer spacing. However, Theriault and Benmokrane (1998) concluded that the effect of concrete strength and reinforcement ratio on the crack spacing of FRP-RC beams is negligible. However, increment in reinforcement ratio resulted in smaller crack width. Furthermore, they reported that the crack width is wider in concrete with higher strength at the same applied moment due to higher stress at crack initiation. To predict the crack width, different methods and equations are proposed in the literature mainly by modifying the equations and methods used for prediction of crack width in steel-RC elements (Masmoudi et al., 1996; Ospina and Bakis, 2007; and Toutanji and Saafi, 2000). In addition, the coefficient factor for taking into account the surface condition of FRP bar based on the

experimental results was proposed by different researchers (El-Nemr et al., 2013; Kassem et al, 2011; Masmoudi et al., 1996; Ospina and Bakis, 2007; Toutanji and Saafi, 2000).

2.3.2.4. Deflection behavior

Control of deflection and cracking are one of the important factors in serviceability design of FRP-RC structures. Under identical conditions, FRP-RC members develop larger deformations than that of steel ones due to difference in stiffness, and bond characteristics of FRP bars. Specially, flexural members reinforced with GFRP bars experience a large deflection in service stage due to low modulus of elasticity of GFRP bars. The parameters affected the deflection behavior of FRP-RC flexural members with a specific span, supports, loading and geometry are type of reinforcement, reinforcement ratio, concrete strength, tension stiffening characteristics, and bond quality (ACI 440.1R-15; CAN/CSA S806-12, R2017; and CAN/CSA S6-19). In calculation of deflection, the effective moment of inertia is normally used which depends on the gross moment of inertia (I_g), cracked moment of inertia (I_{cr}), and the ratio of cracking moment (M_{cr}) to applied moment (M_a). Different researchers tried to modify the equations used for calculating the effective moment of inertia of steel-reinforced concrete beams for FRP-RC beams using some modification factors (Alsayed et al., 2000; Benmokrane et al. 1996; Bischoff and Gross, 2011a, b; Razaqpur et al. 2000; Theriault and Benmokrane, 1998; Toutanji and Saafi, 2000; Yost et al., 2003).

2.3.2.5. Ductility and deformability

In steel-RC structures, ductility is defined based on the yielding point. However, as the behavior of FRP reinforcement in linear elastic, the traditional definition cannot be directly applied for FRP-RC structures. To calculate ductility of GFRP-RC members, numerous methods have been proposed which can be divided into three categories of energy-based ductility index, deformability factor and curvature-based deformability index in terms of the considered approach. The ratio of the total absorbed energy to the elastic energy is defined as the energy-based ductility (μ_e) which can be calculated using Eq. 2.1.

$$\mu_e = \frac{1}{2}\left(\frac{E_{tot}}{E_{el}} + 1\right) \tag{2.1}$$

where E_{tot} denotes the total energy computed as the area under the load-deflection curve, and E_{el} is the elastic energy released upon failure computed as the area of the triangle formed at failure load by the line having the weighted average slope of the two initial straight lines of the load deflection curve, as presented in Fig. 2.4 (Naaman and Jeong, 1995).

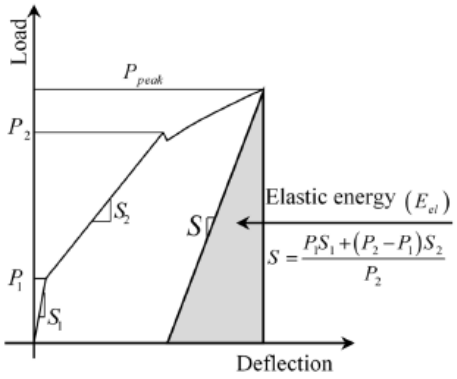

Figure 2.4 Energy-based ductility factor.

According to CAN/CSA S6-19, deformability factor (J) is used to evaluate the capacity of the FRP-RC member to develop suitable deformation using Eq. 2.2. According to this code, J value should exceed 4.0 for rectangular section and 6.0 for T-sections.

$$J = \frac{M_{ultimate}}{M_c} \times \frac{\psi_{ultimate}}{\psi_c} \tag{2.2}$$

Where ψ_c denotes curvature at a concrete strain equal to 0.001 (service condition); $\psi_{ultimate}$ is curvature at ultimate; M_c is moment at concrete strain equal to 0.001; and $M_{ultimate}$ is ultimate moment. Curvature-based deformability factor can be calculated by using Eq. 2.3.

$$J_{VG} = \frac{E_{tot}}{E_{\psi=0.005/d}} \tag{2.3}$$

where E_{tot} denotes energy absorption at ultimate and $E_{\psi=0.005/d}$ is energy absorption at a limiting curvature value of 0.005/d (Vijay and GangaRao, 2001).

2.3.2.6. Behavior of FRP-RC one-way slabs under bending load

The behavior of PCTL segments under the applied load during production and serviceability stages is somewhat similar to the one-way slabs according to the geometry and supports. In the following, some useful studies conducted to investigate the behavior of GFRP-RC one-way slabs under bending load are reviewed.

Michaluk et al. (1998) evaluated the flexural behavior of GFRP-RC one-way slabs by testing eight one-way concrete slabs reinforced with GFRP, CFRP and steel bars. The slabs were 3500 mm in length, 1000 mm in width and 150 or 200 mm in thickness with the clear span of 3000 mm. The investigated parameters were type of reinforcement, slab thickness, and reinforcement ratio. The reinforcement ratio in GFRP bars was designed in such a way that the slabs experience both tension and compression failure mode according to theoretical predictions. They reported that the slabs reinforced with GFRP bars experienced bilinear elastic behavior up to the failure while stiffness of GFRP-reinforced slabs was significantly reduced after initiation of cracks. Also, they concluded that in under-reinforced slabs GFRP bars ruptured prior to reach to their ultimate strain based on the pure tension test due to localized failure of the fibers at the cracked zone. According to their results, heavily GFRP-reinforced slabs could fail in shear by rupture of the GFRP reinforcement at crack location within the maximum shear-flexural zone.

Ombres et al. (2000) tested four one-way slabs, three reinforced with GFRP bars and one reinforced with traditional steel bars, to investigate the flexural behavior of GFRP-RC one-way slabs. The specimens had a total span of 2743.2 mm, width of 457.2 mm and thickness of 101.6 mm. The investigated parameter in GFRP-RC slabs was reinforcement ratio. They concluded that the flexural capacity of GFRP-RC slabs increased with increasing of the reinforcement ratio when the failure mode is crushing of concrete.

El-Sayed et al. (2005) investigated the shear strength of one-way concrete slabs reinforced with different types of FRP bars by testing eight full-scale slabs measured 3100 mm in length 1000 mm in width and 320 mm in thickness. The test parameters were the type and size of FRP reinforcing bars and the reinforcement ratio. Five slabs were reinforced with GFRP and

three were reinforced with CFRP bars. According to the test results, all the slabs experienced a shear failure mode. In addition, they reported that the shear capacity of FRP-reinforced one-way slabs is proportional to the reinforcement ratio and stiffness.

Sivagamasundari and Kumaran (2008) investigated the flexural behavior of GFRP-RC one-way slabs under monotonic and two different schemes of repeated loadings by testing 21 slabs. The specimens were divided in three groups of seven specimens and subjected to monotonic loading (first group), constant amplitude repeated loading (second group), and variable amplitude repeated loading (third group) conditions. In addition to loading type, the experimental parameters were concrete grade, surface condition of GFRP bar, thickness of slab and reinforcement ratio (0.65, 0.82, and 1.15%). Also, the behavior of GFRP-RC slabs was compared with steel-reinforced one in each group. According to their results, the specimens experienced concrete crushing followed by the rupture of GFRP reinforcements. They reported that by increasing the thickness, concrete grade, and reinforcement ratio of slabs, the ultimate load carrying capacity increased and the deflection and crack width reduced. Also, they concluded that fatigue behavior of GFRP-RC slabs using sand-coated bars were better than that of conventional steel-reinforced one.

Chang and Seo (2012) tested 18 one-way slabs with dimensions of 4000x1000x150 mm and 4000x1000x200 mm under four-point monotonic loading to investigate the behavior of GFRP-RC slabs including pre-cracking behavior, crack width and pattern, deflection, failure mode, load carrying capacity and strains. The investigated parameters were the reinforcement ratio and type of GFRP bars. In addition, for each thickness, a steel-reinforced slab was tested to compare the results of GFRP-RC slabs with steel-RC one. According to their results, the failure mode of the GFRP-RC slabs with reinforcement ratio lower or near to the balanced ratio was tension failure of the GFRP bars. However, the specimens with higher reinforcement ratio than the balanced ratio experienced mixed mode failure of concrete crushing and shear failure. Their results indicated that increasing the reinforcement ratio improved the load carrying capacity, cracking behavior and deflection behavior of slabs. Moreover, they reported that the concrete strain at failure was between 4000 to 4500

micro-strain in the specimens. Furthermore, the deformability of specimens varied approximately from 5 to 22 suggesting that the GFRP-RC slabs met the requirements of the standards for deformability.

Ali et al. (2015) conducted an experimental study to investigate the newly developed GFRP bars by testing nine one-way slabs with length, width and depth of 2100, 500, and 140 mm, respectively. The considered parameters were the cross-sectional shape of GFRP bars, reinforcement ratio, concrete strength, and adding polypropylene fibers into the concrete mix. The test results indicated that the stiffness of load-displacement diagram after cracking was dependent on the axial stiffness of the reinforcing bars. They concluded that the mechanical properties and stiffness of GFRP-RC slabs can be improved by increasing the concrete compressive strength and reinforcement ratio. Furthermore, they reported that the deflection of slabs decreased by increasing the amount of polypropylene fibers in the concrete mix.

Abdul-Salam et al. (2016) tested 16 one-way RC slabs reinforced with glass- and carbon-FRP bars in addition to steel-reinforcement under four-point flexural loading. The structural performance was reported in terms of failure mechanisms, crack patterns, main shear cracks, and ultimate capacities. The test results confirmed the effect of the axial stiffness of longitudinal FRP reinforcement on shear strength. They concluded that the use of HSC had a positive impact on the initial shear-cracking load and ultimate-load capacity. According to test results, most of the CFRP-reinforced slabs experienced brittle failure, while most of the GFRP reinforced slabs—with reinforcement axial stiffness equivalent to that of the CFRP reinforced slabs—kept their integrity even after failure, thereby avoiding brittle modes of failure.

Khavaran (2019) performed experimental and numerical investigations on the shear performance of GFRP-reinforced one-way slabs. Twenty full-scale specimens categorized into two groups of small and large slabs with cross-sectional dimensions of 200x1000 mm and 400x1500 mm, and shear-span-to-depth ratios of 6.6 and 3, respectively, were constructed and tested. The specimens were simply supported and tested to failure under

monotonic four-point loading. The test parameters included concrete strength, longitudinal reinforcement ratio, longitudinal bar spacing, bar type and surface characteristics, and amount of shear resisting GFRP headed studs. According to their test results, employing HSC may not always be of advantageous, and in small slabs particularly resulted lower capacity. They concluded that increasing reinforcement ratio and reducing longitudinal bar spacing improved the behavior of slabs. In addition, they reported that application of GFRP headed studs, acting as shear reinforcement, showed promising results in specimens with larger depth and made with NSC.

Hatami and Dehghani (2021) tested eight one-way slabs measured 2400 mm in length, 400 mm in width, and 200 mm in thickness. The specimens were reinforced with steel, GFRP and hybrid reinforcement. In addition, a FEM was developed and compared with the experimental results. The test parameters were the type of longitudinal bars, and bar type in the top and bottom meshes. They concluded that using a combination of steel and GFRP reinforcements, respectively on the lower and upper grid of one-way slabs, slightly decreases the ultimate strength, but the corresponding deflection is not increased significantly. In addition, energy absorption, flexural stiffness, and linear ductility are slightly decreased.

2.3.3. Fiber-reinforced concrete

2.3.3.1. Introduction

Fiber-reinforced concrete (FRC) is defined as a composite materials which its post-cracking residual tensile strength enhances by using the tensile capacity of fibers (di Prisco et al. 2013). After concrete cracking, fibers act like a bridge between cracks which able transferring tensile force between the cracks. The normalized fiber force with respect to the cracked area is defined as residual strength (ACI 544.8R-16). In addition, using fibers in RC structures improves the bond between reinforcing bars and concrete which leads to reduction in crack spacing (Vandewalle 2000). Fibers may be employed in structural elements for plastic cracks prevention before loading and crack control during loadings. The structural performance of FRC is highly dependent on the type and quantity of the utilized fibers.

Numerous advantages of FRC encouraged their use in the structural elements (Löfgren 2005).

2.3.3.2. Fiber-reinforced PCTL segments

The use of FRC in PCTL segments has encountered a great interest in recent years due to its unique advantages such as improving post-cracking behavior, better crack control characteristics, better resistance against the bursting and spalling stresses and increasing the impact and fatigue resistance. However, in some cases, the use of FRC without reinforcing bars cannot satisfy the structural demands. In such cases, the hybrid system of FRC and reinforcing bars is recommended (ACI 544.7R-16).

Field application of FRC in PCTL segments started in the 1980s. Several advantages such as elimination of time and cost needed for assembling the rebars as well as improvement of structural performance were the main reasons which have encouraged engineers to utilize FRC in tunnel segments. Furthermore, as the tunnels are mainly subjected to compression during their service stage (except asymmetric loadings), the reinforcing rebars may be fully eliminated from tunnel segments (Liao et al. 2015).

A great number of studies have been conducted in the literature on the behavior of fiber-reinforced PCTL segments. The flexural behavior under concentration load (Waal 1999; Schnütgen 2003; Poh et al. 2005; Plizzari and Tiberti 2006; Plizzari and Tiberti 2007; Caratelli et al. 2011; Caratelli et al. 2012; Nehdi et al. 2015; Yan et al. 2015; Liao et al. 2016; Conforti et al. 2017; Conforti et al. 2019), structural response under real-work conditions (Molins and Arnau 2011), behavior under thrust load (Poh et al. 2005; Caratelli et al. 2011; Cignitti et al. 2012; Abbas et al. 2014b; Nehdi et al. 2015; Conforti et al. 2017; Conforti et al. 2019), structural behavior in fire (Yan et al. 2013; Yan et al. 2015), behavior under punching shear load (Abbas et al. 2014a), structural performance under settlement load (Abbas et al. 2014a), behavior under flexural cyclic loading (Abbas et al. 2014b), structural behavior of joints in fire (Yan et al. 2016), behavior under biaxial loading test (Meng et al. 2016), capacity of segmental joints (Gong et al. 2017), effect of traditional reinforcement

combination with fiber reinforcement (Plizzari and Tiberti 2007; Meng et al. 2016; Conforti et al. 2017; Conforti et al. 2019), effect of fiber dosage (Poh et al. 2005; Ding et al. 2011; Abbas et al. 2014b; Liao et al. 2015; Nehdi et al. 2015; Meng et al. 2016), and seismic assessment (Avanaki et al. 2018) were among the issues investigated in the literature in fiber-reinforced PCTL segments.

Table 2.1 and Table 2.2, adopted from Gong et al. (2017) and completed, present a summary of the main experimental and theoretical (or analytical) studies in the use of FRC in PCTL segments, respectively. In Tables 2.1 and 2.2, the abbreviations are described as follows. PC is plain concrete, SFRC denotes steel fiber reinforced concrete, PFRC is polypropylene fiber reinforced concrete; CFRC: conventional fiber reinforced concrete; SCFRC is self-compacting fiber reinforced concrete, UHPFRC denotes ultra-high fiber reinforced concrete, HPC is high performance concrete, FRHPC denotes fiber reinforced high performance concrete, HFRC is hybrid fiber reinforced concrete that consist of polypropylene and steel fibers. The general conclusion from all of the mentioned studies is that using fibers in concrete mix of PCTL segments improve the cracking behavior as well as splitting stresses.

2.3.3.3. Behavior of FRC elements reinforced with GFRP reinforcement

Numerous advantages of using GFRP reinforcement and FRC in structures is an extreme motivation to develop FRP-reinforced FRC concrete elements. Moreover, employing FRC in FRP-reinforced elements has some advantages such as improving the bond behavior of FRP reinforcement (Won et al. 2008; Kim et al. 2013; Ding et al. 2014), reduction of crack widths (Yang et al. 2012), increasing the ductility level, enhancing the shear capacity (Dev et al. 2020), and improving the overall flexural performance (Issa et al. 2011; Yang et al. 2012).

Won et al. (2008), investigated the effect of using synthetic and steel fibers on the bond behavior of HSC and FRP bars using direct bond test. Type of FRP bars (GFRP and CFRP), concrete compressive strength, fiber type (steel and synthetic) and fiber percentage were the

Table 2.1 Experimental studies on the behavior of fiber-reinforced PCTL segments [adopted from Gong et al. (2017) and completed]

Reference	Type of test	objective	Materials and reinforcement of specimens	Fiber dosage* (kg/m^3)	Dimensions (mm) Length x width x thickness
Poh et al. (2005)	Flexural and thrust tests	Load bearing capacity	PC and SFRC	0, 30 and 40	2359 x 1400 x 350
Cratelli et al. (2011)	Flexural and thrust test	Structural behavior	RC and SFRC	0, and 40	3640 x 1500 x 200
Molins and Arnau (2011)	In situ real-scale testing	Response under real work conditions	SFRC	60	Unknown x 1800 x 350
Ding et al. (2011)	Bending on symmetric – inclination beam	Mechanical behavior of segments	HPC and FRHPC	0, 25, and 50	1100 x 150 x 150
Caratelli et al. (2012)	Flexural and thrust test	Structural behavior	SFRC	40	1840 x 1200 x 250
Yan et al. (2013)	1/3-scale vertical and horizontal loading	Structural behavior in fire	RC and SFRC	0, and 63	1530 x 300 x 120
Abbas et al. (2014a)	Settlement and punching test	Structural behavior	RC and SFRC	0, and 120	3180 x 1500 x 235
Abbas et al. (2014b)	Monotonic & cyclic flexural and thrust test	Structural behavior	UHPFRC	0, 30, 60, and 90	1000 x 500 x 100
Nehdi et al. (2015)	1/3-scale flexural and thrust test	Ultimate bearing capacity	UHPFRC	0, 30, 60, and 90	1000 x 500 x 100
Yan et al. (2015)	1/3-scale flexural and axial loading test	Structural behavior in fire	RC and HFRC	0, and 80	1530 x 300 x 120
Yan et al. (2016)	1/3-scale flexural and axial loading test	Structural behavior of joints in fire	RC and HFRC	0, and 80	1530 x 300 x 120
Liao et al. (2016)	Flexural test	Ductile behavior of the segment	CFRC and SCFRC	0, and 50	5500 x 1200 x 350
Meng et al. (2016)	Real-scale biaxial loading test	Mechanical behavior	RC+SFRC**	25 and 30	3167 x 1200 x 300
Conforti et al. (2017)	Flexural and thrust test	Structural behavior	RC, PFRC RC+PFRC	0, and 10	1810 x 1200 x 250
Gong et al. (2017)	Monotonic vertical and horizontal loading	Ultimate bearing capacity of joints	RC and SFRC	0 and 80	1200 x 1000 x 600
Conforti et al. (2019)	Flexural and thrust test	Structural behavior	RC, and RC+PFRC	0, and 10	3020 x 1420 x 300

* This value corresponds to each material and reinforcement used.
** Initial SFRC tunnel segment proposed for the project investigated in Meng et al. (2016).

Table 2.2 Analytical and theoretical studies on the behavior of fiber-reinforced PCTL segments [adopted from Gong et al. (2017) and completed].

Reference	Approach	Numerical simulation	Objective	Materials and reinforcement of specimens	Fiber dosage* (kg/m^3)	Dimensions (mm) Length x width x thickness
Plizzari and Tiberti (2006)	Numerical	2D &3D (DIANA)	Structural behavior	PC and SFRC	0, and 40	Unkn. x Unkn. x Unkn.
Plizzari and Tiberti (2007)	Numerical	3D (DIANA)	Structural behavior	PC, SFRC, and RC+SFRC	0, 30, and 30	2700 x 1700 x 300
Kasper et al. (2008)	Numerical	2D (FLAC)	Design check	SFRC	35	Unkn. x 1500 x 300
Arnua and Molins (2011)	Numerical	2D &3D (DIANA)	Comparison with experimental results	SFRC	60	Unkn. x 1800 x 350
Cignitti et al. (2012)	Numerical	3D (DIANA)	Comparison with experimental results	Unkn.	Unkn.	3000 x 1400 x 300
De la Fuente et al. (2012)	Numerical	3D (FLAC)	Optimization of the fiber amount	SFRC	25 25	Unkn. x 1400 x 250 Unkn. x 1500 x 300
Liao et al. (2015)	Analytical	None	Analysis of the design of FRC segment	SFRC	20, 30, 40, 50, and 60	Unkn. x Unkn. x Unkn.
Di Carlo et al. (2016)	Analytical	None	Design procedure of segments	SFRC	Unkn.	3500 x 2500 x 300
Yao et al, (2018)	Analytical	None	Interaction diagram for hybrid FRC segments	All types of FRC	Unkn.	Unkn. x Unkn. x Unkn.
Avanaki et al. (2018)	Numerical	2D (ABAQUS)	Seismic assessment of SFR tunnel segments (obtaining response modification factor)	SFRC	(0.5 Macro,0 Micro) (0 Macro, 0.5 Micro) (0.5 Macro, 0.5 Micro) (0.5 Macro, 0.3 Micro) (0.3 Macro, 0.5 Micro)	Unkn. x Unkn. x Unkn.

investigated parameters in this study. They concluded that the bond strength is affected by the type and percentage of fibers.

Issa et al. (2011) evaluated the influence of employing steel fibers on the flexural behavior and ductility of GFRP-reinforced concrete beams. Seven beams measured 1850 mm in length and 150x150 mm^2 in cross-section were tested under four-point loading test setup. They studied the effect of using internal polypropylene (PP), glass and steel fibers in the concrete mix. The specimens observed three types of failure of tension failure, tension failure combined by a major shear crack, and tension failure combined with the concrete crushing at the top. They concluded that the ductility of GFRP-reinforced concrete beams improved by using all types of fibers. Also, they reported that the ACI 440.1R-15 yielded a good estimation for the experimental results.

Yang et al. (2012) investigated the influence of employing steel and synthetic fibers on the flexural behavior of HSC beams in terms of cracking behavior, ductility and ultimate load bearing capacity by testing six GFRP-reinforced concrete beams under four-point load. The specimens were 2300 mm in length, 230 mm in width and 250 mm in height. The investigated parameters were the type of FRP reinforcement (GFRP and CFRP), fiber type (steel and synthetic). According to their results, the influence of fibers on the post-cracking stiffness was negligible. The GFRP-RC specimens experienced concrete crushing failure mode. However, in the CFRP-FRC beams, tension failure of the bars was observed while the specimens were designed to experience concrete crushing failure mode. It was attributed to the greater compressive strain of FRC compared to that of normal concrete. They concluded that the first cracking load, ductility and ultimate flexural strength improved with using fibers in the concrete mix. Furthermore, their results indicated that fibers could prevent formation of wide cracks in FRP-reinforced concrete beams. Finally, they presented some equations and methods to predict flexural strength of FRP-FRC beams and compared them with the experimental results.

Kim et al. (2013), performed 63 pullout tests on sand-coated and helically-wrapped GFRP bars as well as steel bars anchored in concrete cubic specimens reinforced with steel, PP, and polyvinyl alcohol (PVA) fibers to investigate the influence of using the mentioned fibers on the interfacial bond behavior between bars and FRC. Surface treatment of the bars, fiber type and fiber volume fraction were the investigated parameters. The results indicated that using fibers changed the interfacial bond behavior before and after the maximum stress which led to considerable increase in the relative bond strength. In addition, they concluded that PVA and hook-end steel fibers were able to improve cracking behavior as a result of induced closing pressure.

Wang and Belarbi (2013) investigated long-term performance of FRP bars embedded in FRC using accelerated aging test. The specimens were 2032 mm in length, 178 mm in width and 229 mm in height which were subjected to four-point load testing and the ratio of fibers in mix design was 0.5%. They reported that combined environmental condition including freeze-thaw cycles, high temperature and de-icing salt solution did not cause noticeable effect on the ultimate flexural strength and ductility. Their results indicated that compared to the reference specimen, ductility level increased by more than 30% by using of fiber with a volume fraction of 0.5%.

Ding et al. (2014) studied the effect of steel and macro PP fibers on the bond capacity of GFRP bars by pullout testing of 21 cubic samples 150 mm in dimension. Fiber type and percentage were the main investigated parameters on the bong behavior of GFRP bars and concrete. They concluded that bond strength and toughness can be improved by using macro mono or hybrid fibers in plain concrete especially when steel and PP fibers used as a hybrid system. They also reported that the bond capacity of GFRP bars in concrete reinforced with hybrid fibers can be equivalent or even more than that of steel rebars in plain concrete.

Yoo et al. (2015a) investigated the bond behavior of steel and GFRP bars in UHPFRC using pullout test. The investigated parameters were the rebar diameter as well as the embedment length. Their results indicated that steel rebars have 2.8-3.6 times greater bond strength than

that of GFRP bars. In addition, they suggested some equations for normalized bond strength and development length if the GFRP bars embedded in UHPFRC.

Attia et al. (2019) investigated the behavior of one-way slabs reinforced with either basalt FRP or GFRP longitudinal bars embedded in FRC incorporating basalt macro-fibers (BMF). Twelve one-way concrete slabs were tested until failure under four-point loading test. The investigated parameters included the type of bars (BFRP and GFRP), the longitudinal reinforcement ratio (1.4 and 2.8 times of balanced reinforcement ratio), and the volume fraction of the fibers added (0, 0.5, 1, and 2% per volume). The test results demonstrated the promise of BMF to enhance the flexural performance of the tested slab in terms of ductility and load-carrying capacities. The formulations of different available codes and design guidelines were used to predict the test results. Comparison between the experimental and predicted results showed the adequacy of the models to predict the flexural performance of the tested slab strips.

Dev et al. (2020) investigated the effect of structural fibers on the shear behavior of RC beams with GFRP bars as longitudinal reinforcement to understand the efficiency of macrosynthetic polyolefin (PO) polymer and a hybrid combination of steel and PO fibers in improving the shear behavior of GFRP-reinforced beams. Thirteen full-scale RC beams were cast with GFRP bars as internal reinforcement and varying PO and hybrid fiber dosages. Three different fiber dosages by volume of concrete, namely 0.35%, 0.70%, and 1.0% are considered. According to the experimental results, addition of fibers enhanced the post-cracking stiffness, peak load, and ductility when compared with control beams with no fibers. The addition of PO and hybrid fibers reduced the load drop after cracking considerably and enhanced the post-cracking performance by improving the aggregate interlock and through reduction of residual tensile stresses at the crack tip.

Patil et al. (2020) investigated the effectiveness of structural macro-synthetic polyolefin (PO) and a hybrid combination of steel and synthetic fibers on the flexural performance of GFRP-reinforced concrete beams. In total, 14 full-scale RC beams were tested under four-

point bending configuration. The test series includes: 1) control specimen with GFRP reinforcement; 2) GFRP-reinforced members with 0.35, 0.70, and 1.0% volume of PO fibers; and 3) GFRP-reinforced members with 0.35, 0.70, and 1.0% volume of hybrid steel and PO fibers in equal ratio. According to the experimental results, addition of synthetic and hybrid fibers significantly improved the post-cracking stiffness, peak strength, and energy dissipation capacity of GFRP-reinforced members. In addition, deflection at service loads reduced with increase in fiber dosage.

Sun et al. (2021) tested seven Polyvinyl Alcohol-FRC (PVA-FRC) GFRP-reinforced concrete beams to investigate the effect of PVA fiber content and GFRP reinforcement diameter. The experimental findings revealed that presence of PVA fibers effectively restricts crack width in PVA-FRC GFRP reinforced concrete beams. The experimental results were compared to theoretical predictions based on ACI 318-19, and ACI 440.1R-15 and a maximum crack correction formula specifically designed for PVA-FRC GFRP reinforced concrete beams was proposed.

Lu et al. (2022) investigated the flexural characteristics of SFRC beams that utilize a combination of GFRP and steel bars. The experimental outcomes from the present SFRC beams were compared with those of plain concrete (PC) beams. Taking into consideration the disparities in nominal reinforcement ratios and reinforcement configuration among seven investigated SFRC beams, aspects such as cracking load, ultimate load, failure patterns, crack spacing and width, and mid-span deflection were initially assessed. Consequently, a detailed comparison of flexural tendencies between SFRC and PC beams with equivalent reinforcements was presented. Importantly, the profound influence of concrete type and strength on the flexural ability and failure patterns of test beams was analyzed. Their study concluded with a recommendation for the optimization of two equivalent nominal reinforcement ratios for concrete beams fortified with a hybrid combination of GFRP and steel bars, thereby ensuring a suitable flexural failure mode without the rupture of GFRP bars.

2.3.4. GFRP-reinforced precast concrete tunnel lining segments

An effective approach to deal with corrosion problem in conventional RC tunnel segments is the use of GFRP bars as a substitution of conventional steel reinforcement (Caratelli et al. 2016; Spagnuolo et al. 2017). GFRP bars offer such distinct advantages over conventional steel rebars as corrosion resistance, chemical resistance, electromagnetic neutrality, high strength-to-weight ratio, high tensile strength, competitive life cycle cost, and fatigue resistance (440.1R-15 2015). Further, reduction in concrete cover, suitability for parts of the tunnel that eventually should be demolished and possibility to create dielectric joints are among the merits of using GFRP reinforcement in tunnel segments (Caratelli et al. 2016).

There are few studies which investigated the performance of GFRP-reinforced PCTL segment. The main issues investigated in the literature were: 1- Structural performance of GFRP-reinforced PCTL segments subjected to flexural and thrust loadings terms of load carrying capacity, cracking, stiffness, ductility, and failure mode (Caratelli et al. 2016), 2- influence of GFRP reinforcement configuration on the behavior of segments subjected to flexural and thrust loads (Caratelli et al. 2017), 3- efficiency of theoretical analysis based on the ACI 440.1R-15 in prediction of load carrying capacity of GFRP-reinforced PCTL segments (Spagnuolo et al. 2017), 4- capability of GFRP-reinforced segments to withstand the loads from different loading stages (Spagnuolo et al. 2017), 5- Hybrid use of GFRP reinforcement and FRC in tunnel segments (Meda et al. 2019), and 6- The physical, mechanical and durability characteristic of curvilinear GFRP bars used in tunnel segments (Spagnuolo et al. 2018). The summary of the studies in the literature on the GFRP-reinforced PCTL segments as well as characterization of curvilinear GFRP bars are presented in the following:

Caratelli et al. (2016) compared the performance of GFRP-reinforced and steel-reinforced tunnel segments in terms of load carrying capacity, crack pattern, stiffness, ductility and failure mode using flexural and thrust tests. They tested two specimens in flexure using three-point-loading test (Fig. 2.5a) with dimensions of 4150 mm in length, 1483 mm in width and 400 mm in thickness. Also, one segment with the thickness of 250 mm was tested under

TBM thrust load. The reinforcement details were designed in such a way that ultimate load carrying capacity of steel-reinforced and GFRP-reinforced specimens was the same (with considering the design reduction factors). The flexural failure mode was rupture of rebars in both GFRP reinforced and steel reinforced specimens. They concluded that flexural behavior (load carrying capacity and ductility) of the steel-reinforced and GFRP-reinforced segments did not have significant difference as shown in Fig. 2.5(b). They also reported that segments reinforced with GFRP bars and tested under TBM thrust loads exhibited a suitable behavior. Moreover, design approach suggested by the codes appears in accordance with the tests evidence. Nevertheless, the adoption of safety coefficients for the GFRP can lead to a structural over-strength, which could be penalizing mainly for temporary structures.

Spagnuolo et al. (2017) performed a theoretical analyses on the specimens tested by Caratelli et al. (2016). They obtained the theoretical design axial load-bending moment interaction diagrams using ACI 318-14 and ACI 440.1R-15 and compared them with the experimental data. They evaluated the applied loads according to ACI 544.7R-16 such as stripping, storage, transportation and handling. In addition, soil pressure was evaluated using software FLAC 7.0. They concluded that the simplified check procedure for the tunnel segment based on interaction diagrams built on the constitutive relationship of the materials, appears suitable for predicting the capacity of a tunnel segment; and to obtain successful results on GFRP application in tunnel segments. The also reported that an adequate conceptual design has to be performed with the aim of highlighting the advantages of GFRP use and, at the same time, maintaining a sustainable cost level.

Caratelli et al. (2017) investigated the effect of different configuration of GFRP reinforcement on their behavior under four-point flexural and TBM thrust loadings. The

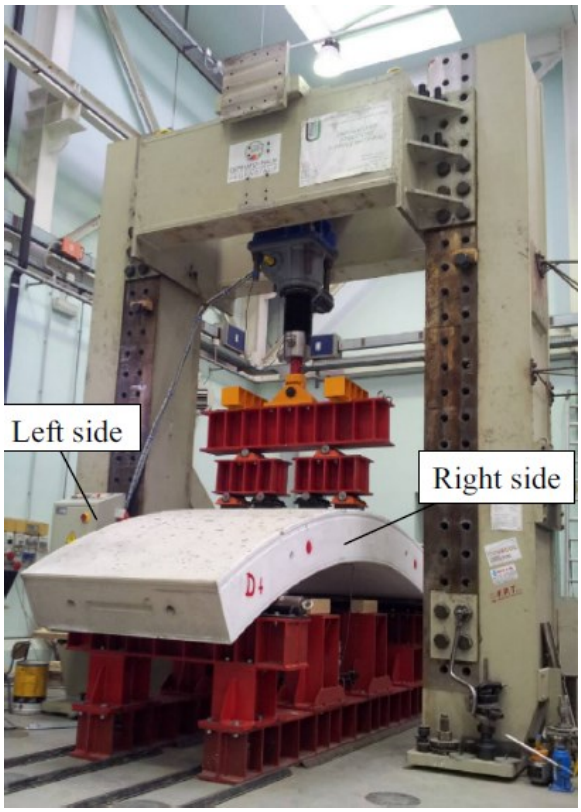

(a) Bending test of the segments

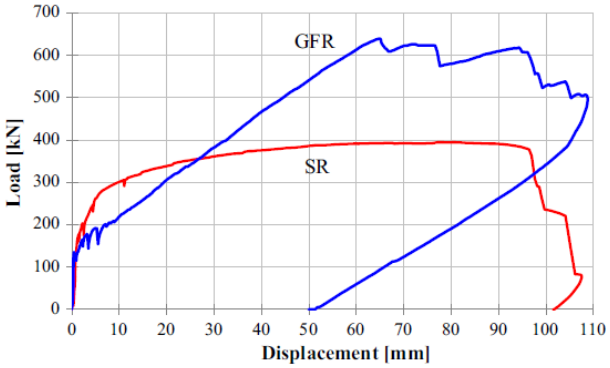

(b) Comparison between the load-displacement behavior of GFRP-reinforced and steel-reinforced segments

Figure 2.5 Flexural test of segments and results (Caratelli et al. 2016).

specimens were 3200 mm in length (approximately on average), 1420 mm in width and 300 mm in thickness. Different types of ties and configuration were introduced for curvilinear GFRP rebars. Closed-ring prototype was employed and compared with Lattice

reinforcement and Wirenet reinforcement. In addition, the performance of tunnel segment reinforced with sand coated GFRP reinforcement compared with specimen reinforced with ordinary one. In total, they tested ten specimens, five of which under flexural load and the rest under thrust load. Taking into account technical feasibility, commercial feasibility and technological feasibility as well as experimental results, the specimen with closed ring reinforcement represented the best solution among the tested prototypes. They concluded that the coating treatment, besides increasing the load at first crack, led to a reduction of about 70% the crack width and better dispersion of the cracks.

Meda et al. (2019) investigated the possibility of adopting a hybrid solution of FRC tunnel segments with GFRP reinforcement. Four full-scale specimens were cast and two of which were subjected to four-point bending test and the rest were subjected to point load tests. The specimens had internal diameter of 6400 mm which is equal to typical metro tunnel lining. Also, the width and thickness of the segments were 1420 and 300 mm, respectively. Two types of specimens were used, one SFRC without any rebar and one with GFRP rebars (with very low reinforcement ratio as shown in Fig. 2.6). The glass fiber reinforcement was suitably designed according to the CNR-DT203-06 guidelines for GFRP bars and *fib* Model Code Code-2010 (for the FRC in order to provide an increase of the ultimate bending moment of about 50%, with respect to the SFRC) section. They concluded that the hybrid segment exhibited a peak load about 63% higher than the FRC solution. Similar spread of cracks was observed during the tests, with a reduction of the crack width of about 60% in the hybrid segment.

Figure 2.6 Hybrid SFRC-GFRP tunnel segments (Meda et al. 2019).

Tengilimoglu and Akyuz (2020) evaluated the structural applicability of using polypropylene (PP) macro-synthetic fibres (MSFs) in precast tunnel segments by testing full-scale specimens. Fourteen full-scale precast tunnel segments were investigated which can be categorized as follows: a) specimens reinforced with typical conventional steel reinforcement; ii) specimens reinforced with the combination of MSFs and conventional reinforcement; iii) the specimens reinforced with the combination of MSFs and GFRP bars; and iv) the specimens reinforced with MSFs only. Flexural tests were carried out to compare the flexural behavior of specimens at the allowable crack opening width, while point load tests were conducted to observe the structural performance of precast tunnel segments under the effect of design thrust forces. The experimental results showed that the combination of MSFs and GFRP could be an innovative solution for precast tunnel segments in case of using a suitable quantity that satisfied the project requirements. Although PP fibres exhibited adequate spalling and splitting stress control, it is observed that they could not overcome high flexure forces without using reinforcement bars at a low volume of fractions.

Spagnuolo et al. (2018) investigated the physical, mechanical and durability characteristics of rebars with four different curve radios (one straight and other curvilinear) and diameters. The following properties were investigated: Actual cross-sectional area, fiber content, glass transition temperature (Tg) by dynamic mechanical analysis (DMA), tensile strength, modulus of elasticity and ultimate strain, transverse shear strength, moisture absorption and alkaline environment resistance. They concluded that the characteristics of curvilinear GFRP bars in majority of tests meet the acceptance criteria.

2.3.5. Review on GFRP design standards and guidelines

2.3.5.1. Introduction

In order to design tunnel segments under bending load, it is necessary to predict their flexural strength at ultimate and serviceability phases, shear capacity, cracking behavior, and deflection at service load. There is not any specific standard or guideline for designing tunnel segments reinforced with GFRP reinforcements. However, there are provisions for designing GFRP-RC flexural elements in different standards and guidelines. The summary of the

related provisions of different standards and guidelines which are applicable for designing GFRP-reinforced flexural elements were reviewed in the following.

2.3.5.2. Flexural strength

ACI 440.1R-15

This guideline allows using both compression and tension failure mode for GFRP-reinforced flexural elements. However, it is declared that compression control failure mode is more desirable since it exhibits more inelastic behavior prior to failure. To specify the failure mode, the balanced reinforcement ratio can be determined using Eq. 2.4.

$$\rho_{fb} = 0.85\beta_1 \frac{f_c^{'}}{f_{fu}} \left(\frac{E_f \varepsilon_{cu}}{E_f \varepsilon_{cu} + f_{fu}}\right) \tag{2.4}$$

where β_1 is the factor which should be taken 0.85 for concrete strength up to 28 MPa. For the strength more than 28 MPa, this value reduces by 0.05 per each 7 MPa of strength excess of 28 MPa; however, this value should not be considered less than 0.65. $f_c^{'}$ and f_{fu} are concrete strength and design strength of FRP (guaranteed tensile strength multiplied by environmental resistance factor, C_E), respectively. E_f is designed guaranteed modulus of elasticity of FRP and ε_{cu} is ultimate strain of concrete which is assumed to be 0.003.

When the failure mode is concrete crushing, the nominal flexural strength (M_n) can be calculated using Eq. 2.5. It should be noted that in design calculations, the effect of FRP in compression should be ignored.

$$M_n = A_f f_f \left(d - \frac{a}{2}\right) \tag{2.5}$$

where

$$a = \frac{A_f f_f}{0.85 f_c^{'} b} \tag{2.6}$$

and

$$f_f = (\sqrt{\frac{(E_f \varepsilon_{cu})^2}{4} + \frac{0.85\beta_1 f_c^{'}}{\rho_f} E_f \varepsilon_{cu}} - 0.5 E_f \varepsilon_{cu}) \le f_{fu} \quad (2.7)$$

in the above-mentioned equations, A_f denotes the area of tension FRP reinforcement, f_f denotes the stress in FRP bars, d effective depth of the section, and b is the section width. The nominal flexural strength of the member can be calculated using the Eqns. 2.5 to 2.7 or directly from the Eq. 2.8.

$$M_n = \rho_f f_f (1 - 0.59 \frac{\rho_f f_f}{f_c^{'}}) b d^2 \quad (2.8)$$

where ρ_f is calculated using Eq. 2.9.

$$\rho_f = \frac{A_f}{bd} \quad (2.9)$$

In the cases when the failure mode is tensile rupture of FRP bars before concrete crushing, the nominal flexural resistance can be calculated using the following equation.

$$M_n = A_f f_{fu} (d - \frac{\beta_1 c}{2}) \quad (2.10)$$

in tension failure mode, the strain in reinforcement is known; however, the depth of natural axis and the strain in concrete is unknown. Also, as the strain in concrete is unknown, the equivalent stress block in concrete is different from the compression failure mode. In this case, iteration must be employed by assuming the amount of c and determining the values of α_1 and β_1 (equivalent rectangular stress block parameters) according to the obtained concrete strain. In the next step, the assumption can be controlled by equilibrium relationship between tension and compression forces. The strength reduction factor can be determined using Eq. 2.11.

$$\phi = \begin{cases} 0.55 & \rho_f \le \rho_{fb} \\ 0.3 + 0.25\dfrac{\rho_f}{\rho_{fb}} & \rho_{fb} < \rho_f < 1.4\rho_{fb} \\ 0.65 & \rho_f > \rho_{fb} \end{cases} \quad (2.11)$$

As specified in ACI 440.1R-15 the minimum reinforcement should be provided in the cases of tension control failure mode. The reinforcement should be provided in such a way that the flexural resistance multiplied by resistance factor exceed the cracking moment of the section. Furthermore, the minimum area of reinforcement should be provided according to Eq. 2.12.

$$A_{f,\min} = \frac{0.41 f_c^{'}}{f_{fu}} b_w d \quad (2.12)$$

CAN/CSA S806-12, R2017

In order to determine the failure mode in this code, balanced ratio can be obtained using the Eq. 2.13.

$$\rho_{frp,b} = \alpha_1 \beta_1 \frac{\phi_c}{\phi_f} \frac{f_c^{'}}{f_{frp,u}} \left(\frac{\varepsilon_{cu}}{\varepsilon_{cu} + \varepsilon_{frp,u}}\right) \quad (2.13)$$

Where ϕ_c and ϕ_f are the resistance factor of concrete and FRP which should be considered as 0.65 and 0.75, respectively. The resistance factors in CAN/CSA S806-12, R2017 are not dependent on the failure mode. Also, the ultimate strain in concrete (ε_{cu}) should be considered as 0.0035. The ratio of average stress in rectangular compression block to the specified concrete strength (α_1), and ratio of depth of rectangular compression block to the depth of natural axis (β_1) are calculated based on the Eq. 2.14(a) and 2.14(b), respectively.

$$\alpha_1 = 0.85 - 0.0015 f_c^{'} \ge 0.67 \quad (2.14(a))$$

$$\beta_1 = 0.97 - 0.0025 f_c^{'} \ge 0.67 \quad (2.14(b))$$

In the case of compression control failure mode, the tensile stress in FRP bar can be calculate using Eq. 2.15.

$$f_{frp} = (0.5E_{frp}\varepsilon_{cu}\left[(1+\frac{4\alpha_1\beta_1\phi_c f_c^{'}}{\rho_{frp}\phi_{frp}E_{frp}\varepsilon_{cu}})^{0.5}-1\right]) \quad (2.15)$$

with specifying the stress in the FRP tension bar, and solving the force equilibrium, the natural axis depth (c) can be obtained. Then, the moment resistance (M_r) of the member can be calculated using Eq. 2.16.

$$M_r = A_{frp}\phi_{frp}f_{frp}(d-\frac{\beta_1 c}{2}) \quad (2.16)$$

for tension failure mode, the force equilibrium should be checked by assuming the neutral axis depth.

According to CAN/CSA S806-12, R2017, the minimum reinforcement should be provided in such a way that the requirement of Eq. 2.17 is met. Also, in the case of tension failure mode, in addition to Eq. 2.17, the Eq. 2.18 should be also met where M_{cr} is the cracking moment and M_f is the factored moment.

$$M_r \geq 1.5M_{cr} \quad (2.17)$$

$$M_r \geq 1.5M_f \quad (2.18)$$

CAN/CSA S6-19

CAN/CSA S6-19 does not provide specific provisions for calculation of moment resistance of GFRP-RC elements. In addition, the minimum reinforcement provisions are the same with CAN/CSA S806-12, R2017. According to this code, for calculation of cracking moment, the cracking stress in concrete should be taken as $0.4\sqrt{f_c^{'}}$ for normal density concrete.

AASHTO LRFD bridge design guide specifications for GFRP-reinforced concrete (AASHTO 2018)

The equations presented in AASHTO-18 for calculating moment resistance of GFRP-RC elements is the same with ACI 440.1R-15. However, AASHTO-18 uses f_{fd} and ε_{fd} instead of f_{fu} and ε_{fu} for design stress and strain of FRP bar, respectively. For calculation of f_{fd}, Eq. 2.19(a) and 2.19(b) should be used.

$$f_{fd} = C_e f_{fu} \tag{2.19(a))}$$

$$\varepsilon_{fd} = C_e \varepsilon_{fu} \tag{2.19(b))}$$

where C_e is the environmental reduction factor which is 0.8 for concrete not exposed to earth or weather and 0.7 for concrete exposed to earth or weather. The resistance factor in this code is calculated using Eq. 2.20.

$$\phi = \begin{cases} 0.55 & \varepsilon_f = \varepsilon_{fd} \\ 1.55 - \dfrac{\varepsilon_{ft}}{\varepsilon_{fd}} & 0.8\varepsilon_{fd} < \varepsilon_{ft} < \varepsilon_{fd} \\ 0.75 & \varepsilon_{ft} \le 0.8\varepsilon_{fd} \end{cases} \tag{2.20}$$

According to AASHTO-18, in the case of non-compression-controlled flexural components, the factored flexural resistance (M_r), should be provided according to Eq. 2.21.

$$M_r \ge \min \begin{cases} 1.33\, \textit{times the factored moment required by} \\ \textit{the applicable strength load combination} \\ 1.6 f_r S_c - M_{dnc}\left(\dfrac{S_c}{S_{nc}} - 1\right) \end{cases} \tag{2.21}$$

Where f_r is modulus of rupture of concrete; S_c is section modulus for the extreme fiber of the composite section where tensile stress is caused by externally applied loads; M_{dnc} is total

un-factored dead load moment acting on the monolithic or non-composite section; S_{nc} is section modulus for the extreme fiber of the monolithic or non-composite section where tensile stress is caused by externally applied loads. Suitable values for M_{dnc} and S_{nc} shall be used for any intermediate composite sections. Where the beams are designed for the monolithic or non-composite section to resist all loads, S_{nc} shall be substituted for S_c. In this case, M_r should be at least 60 percent greater than the M_{cr}.

2.3.5.3. Shear strength

ACI 440.1R-15

ACI 440.1R-15 considers the contribution of the uncracked compression block as the only shear transferring mechanism of concrete. The equation in this standard is the modified equation presented in ACI 318-14 considering the effect of the axial stiffness of the FRP bars on the compression-block depth. The shear capacity of concrete (V_c) according to ACI 440.1R-15 can be calculated with Eq. 2.22

$$V_c = \frac{2}{5}\sqrt{f_c'}\,b_w(kd) \tag{2.22}$$

where b_w is the section width and k can be calculated with the following equation

$$k = \sqrt{2\rho_f n_f + (\rho_f n_f)^2} - \rho_f n_f \tag{2.23}$$

where ρ_f and n_f are the longitudinal reinforcement ratio and the ratio of the modulus of elasticity of longitudinal FRP bars to concrete modulus of elasticity, respectively. ACI 440.1R-15 does not provide any provisions regarding the shear strength of GFRP-reinforced members under axial load.

CAN/CSA S806-12, R2017

In CAN/CSA S806-12, R2017, the contribution from the uncracked concrete and aggregate interlock are both considered as the shear-transferring mechanisms of the concrete. The effect of important parameters such as reinforcement rigidity, size effect, interaction of shear force and bending moment at the critical section, and arc action is considered in the shear strength of concrete by some coefficients obtained empirically (Khavaran 2019). Equations 2.24 and 2.25 can be used for calculating the concrete shear strength of members

subjected to axial tension and axial compression, respectively, according to CAN/CSA S806-12, R2017.

$$V_c = \left[0.05\lambda\phi_c k_m k_r (f_c')^{\frac{1}{3}} b_w d_v \right] k_s k_a (1 - \frac{0.3N_f}{A_g}) \geq 0 \quad 2.24$$

$$V_c = \left[0.05\lambda\phi_c k_m k_r (f_c')^{\frac{1}{3}} b_w d_v \right] k_s k_a (1 - \frac{N_f}{14A_g}) \quad 2.25$$

where λ and ϕ_c are the concrete density factor and reduction factor, respectively; N_f is the amount of axial load, which should be positive for tension and negative for compression; d_v is the effective shear depth which should be considered to be the greater of $0.9d$ or $0.72h$; and k_m, k_r, k_s, and k_a can be calculated with Eqns. 2.26 to 2.29, respectively.

$$k_m = \sqrt{\frac{V_f d}{M_f}} \leq 1.0 \quad (2.26)$$

$$k_r = 1 + (E_f \rho_{Fw})^{\frac{1}{3}} \quad (2.27)$$

$$1.0 \leq k_a = \frac{2.5}{\frac{M_f}{V_f d}} \leq 2.5 \quad (2.28)$$

$$k_s = \frac{750}{450 + d} \leq 1.0 \quad (2.29)$$

where M_f is the factored bending moment; V_f is the factored shear force; ρ_{Fw} is the longitudinal reinforcement ratio; and k_a is related to the sections within 2.5 d of the face of a support and should be considered as 1.0 in other sections. In addition, k_s should be considered to be 1.0 in members with an effective depth less than 300 mm and in members with an effective depth greater than 300 mm with the minimum shear reinforcement. It should be noted that the value in the bracket of the Eqns. 2.24 and 2.25 should not be taken less than $0.1\lambda\varphi_c\sqrt{f_c'}b_w d$ or $0.11\sqrt{f_c'}b_w d_v$, respectively. In addition, the product of $k_a(1 - \frac{N_f}{14A_g})$ in Eq. 2.25 should be considered to be less than 3.0. Moreover, the value of V_c

should not be taken greater than $0.22\varphi_c\sqrt{f_c'}b_w d_v$ and f_c' should not be taken greater than 60 MPa.

CAN/CSA S6-19

The shear capacity in this standard is presented based on the simplified modified compression field theory model (SMCFT). Equation 2.30 presents the shear capacity of concrete according to CAN/CSA S6-19.

$$V_c = 2.5\beta\phi_c f_{cr} b_v d_{long} \tag{2.30}$$

where f_{cr} is concrete tensile strength, which should be considered as $0.4\sqrt{f_c'} \le 3.2MPa$ for normal-density concrete; and b_v and d_{long} are essentially the same as b_w and d_v in CAN/CSA S806-12, R2017. Equation 2.31 is calculating β, which is a coefficient to consider size effect, reinforcement rigidity, and the ratio of bending moment to shear force at the critical section.

$$\beta = \left[\frac{0.4}{1+1500\varepsilon_x}\right]\left[\frac{1300}{1000+S_{ze}}\right] \tag{2.31}$$

where ε_x is the strain in the longitudinal reinforcement, and S_{ze} is a coefficient for considering the effect of aggregate size and crack control characteristics of the longitudinal reinforcement. Equations 2.32 and 2.33 are used to calculate ε_x and S_{ze}, respectively.

$$\varepsilon_x = \frac{\frac{M_f}{d_{long}} + V_f + 0.5N_f}{2E_{FRP}A_{FRP}} \le 0.003 \tag{2.32}$$

$$s_{ze} = \frac{35s_z}{15+a_g} \ge 0.85s_z \tag{2.33}$$

where E_{FRP} and A_{FRP} are the modulus of elasticity and area of the longitudinal FRP bars; a_g is the nominal size of the coarse aggregate; and s_z is the crack spacing parameter, which should be taken as d_v in a member without transverse reinforcement.

AASHTO LRFD bridge design guide specifications for GFRP-reinforced concrete (AASHTO 2018)

This standard presents almost the same approach as CAN/CSA S6-19 for determining the shear capacity of GFRP-reinforced elements with some differences in the coefficients. However, while CAN/CSA S6-19 limits the maximum compressive strength of concrete to 64 MPa in calculations, the AASHTO 2018 define 69 MPa as the upper limit of concrete compressive strength.

2.3.5.4. Cracking

ACI 440.1R-15

For controlling the crack width, ACI 440.1R-15 recommends an indirect procedure to control the flexural crack widths using maximum spacing of reinforcing bars ($S_{\max}$) as presented in Eq. 2.34.

$$S_{\max} = 1.15\frac{E_f w}{f_{fs} k_b} - 2.5c_c \le 0.92\frac{E_f w}{f_{fs} k_b} \tag{2.34}$$

where w denotes maximum allowable crack width (mm), f_{fs} is the stress level induced in FRP at service loads (MPa), c_c is the clear cover (mm); and k_b is the bond-dependent coefficient. In the cases that k_b is not known from experimental data, a value of 1.4 should be assumed. It should be noted that smooth bars and grids are excluded from this recommendation. According to ACI 440.1R-15, the maximum allowable crack width can be varied based on the environmental conditions and the situation of the member. However, where the crack width is limited by aesthetic reason, this guideline accepts limiting the crack width in the rage of 0.4 to 0.7 mm. This guideline also states that the Eq. 2.34 is valid when the value of concrete cover (d_c) complies with the Eq. 2.35.

$$d_c \le \frac{E_f w}{2 f_{fs} \beta k_b} \tag{2.35}$$

CAN/CSA S806-12, R2017

According to CAN/CSA S806-12, R2017, if the maximum strain of FRP bars in the tension zone under service loads exceeds 0.0015, the quantity of z should be calculated according to Eq. 2.36 and checked.

$$z = k_b \frac{E_s}{E_f} f_f \sqrt[3]{d_c a} \tag{2.36}$$

where A denotes the effective tension area of concrete surrounding the flexural tension reinforcement and extending from the extreme tension fiber to the centroid of the flexural tension reinforcement and an equal distance past the centroid, divided by the number of bars. The quantity z should not exceed 45,000 N/mm for interior exposure and 38,000 N/mm for exterior exposure. The stresses in the reinforcement at the specified load, f_f, is calculated as the internal moment divided by the product of the reinforcement area and the internal moment arm. In the absence of experimental data, CAN/CSA S806-12, R2017 recommends using the value of 1.2 for k_b in the deformed rods. Also, this code specifies that effective clear cover should not be greater than 50 mm in the calculation d_c and A.

CAN/CSA S6-19

According to CAN/CSA S6-19, in the cases that the maximum tensile strain in FRP reinforcement under service load exceeds 0.0015, cross-sections of the component in maximum positive and negative moment regions should be proportioned in such a way that the crack width does not exceed 0.5 mm for members subject to aggressive environments and 0.7 mm for other members. The crack width is calculated using Eq. 2.37.

$$w_{cr} = \frac{2 f_{FRP}}{E_{FRP}} \frac{h_2}{h_1} k_b \sqrt{d_c^2 + (s/2)^2} \tag{2.37}$$

where d_c is distance from the centroid of the tension reinforcement to the extreme tension surface of concrete. In calculation of d_c, the clear cover shall not be greater than 50 mm. h_2 is distance from the extreme flexural tension surface to the neutral axis, h_1 denotes the distance from the centroid of tension reinforcement to the neutral axis, and s is spacing of

flexural reinforcements. The value of k_b shall be determined by using the experimental test, but in the absence of test data may be taken as 0.8 for sand-coated and 1.0 for deformed FRP bars.

AASHTO LRFD bridge design guide specifications for GFRP-reinforced concrete (AASHTO 2018)

AASHTO-18 use the same procedure and equations for controlling the crack width as ACI 440.1R-15. According to this code, the maximum crack width in a concrete component shall be limited to 0.028 in (0.71 mm). Furthermore, the clear cover should not be greater than 2 in. plus half the bar diameter and the bond reduction factor shall be considered equal to 0.83 unless otherwise established through independent experimental tests.

2.3.5.5. Deflection

ACI 440.1R-15

According to ACI 440.1R-15, deflection can be calculated using effective moment of inertia (I_e) based on the Eq. 2.38.

$$I_e = \frac{I_{cr}}{1-\gamma(M_{cr}/M_a)^2(1-I_{cr}/I_g)} \le I_g \quad where\ M_a \ge M_{cr} \tag{2.38}$$

Where M_{cr} and M_a denotes the cracking moment and maximum bending load moment, respectively and I_g is gross moment of inertia of the section. I_{cr} denotes the moment of inertia of the cracked section. The value of γ depends on the load and boundary condition which can be taken as $1.72-0.72(M_{cr}/M_a)$ for simply supported beam with uniform distributed load. M_{cr} and I_{cr} can be obtained using Eqns. 2.39 and 2.40, respectively.

$$M_{cr} = \frac{0.62\lambda\sqrt{f_c'}I_g}{y_t} \tag{2.39}$$

$$I_{cr} = \frac{bd^3}{3}k^3 + n_f A_f (d-kd)^2 \tag{2.40}$$

where λ is lightweight concrete coefficient, y_t is distance from centroid axis of gross section to tension face (mm), k is ratio of natural axis depth to reinforcement depth which

is calculated using Eq. 2.41, and n_f is the ratio of FRP bar modulus of elasticity to the concrete modulus of elasticity.

$$k = \sqrt{2\rho_f n_f + (\rho_f n_f)^2} - \rho_f n_f \tag{2.41}$$

CAN/CSA S806-12, R2017

CAN/CSA S806-12, R2017 recommends using integration of curvature along the span to calculate the deflection of the beam. In this method, tension stiffening effect is ignored. Different equations were presented in CAN/CSA S806-12, R2017 for different load and boundary conditions. Eq. 2.42 presents the formula for calculating the deflection of a simply supported beam with the length of L which is subjected to a point load of P at the midspan.

$$\delta_{\max} = \frac{PL^3}{48E_c I_{cr}}\left[1 - 8\eta(L_g / L)^3\right] \tag{2.42}$$

where I_{cr} is the transformed moment of inertia of cracked section, L_g is distance from the support to the point where $M_a = M_{cr}$, and η is calculated using Eq. 2.43.

$$\eta = 1 - \frac{I_{cr}}{I_g} \tag{2.43}$$

CAN/CSA S6-19

CAN/CSA S6-19 does not provide specific recommendations for calculating of deflection in GFRP-reinforced concrete elements.

AASHTO LRFD bridge design guide specifications for GFRP-reinforced concrete (AASHTO 2018)

This code recommends almost the same method as ACI 440.1R-15 for calculating of deflection.

CHAPTER 3 EXPERIMENTAL PROGRAM

3.1. Introduction

In order to pave the way for major application of GFRP reinforcement in precast concrete tunnel lining segments, extensive research project is ongoing at the University of Sherbrooke including several experimental and analytical phases to improve current practices and develop more efficient design and construction approaches. As a part of the mentioned research project, this study aims to investigate the performance of GFRP-reinforced PCTL segments under monotonic bending load. This chapter presents the outline of the experimental research program carried out in this study. After presenting the material properties, this chapter describes details of test specimens, construction process, test setup, instrumentations, and loading procedure.

3.2. Material Properties

3.2.1. Concrete

Three types of concrete were used in this study classified as normal concrete (NC), high-strength concrete (HSC), and fiber-reinforced concrete (FRC). Table 3.1 lists the mix design of the concrete types used to cast the specimens. The actual compressive strength of the specimens was obtained through testing three 100×200 mm cylinders according to ASTM C39/C39M-21. Polypropylene fibers 12 mm in length were used to fabricate FRC. Flexural characteristics of FRC were obtained through testing three concrete prism samples 100×100×500 mm in size for each specimen fabricated with FRC according to ASTM C1609-19. The peak strength, residual strength at the deflection of $L/600$, and the residual strength at deflection of $L/150$ were obtained based on the recommendations of ASTM C1609-19.

Table 3.1 Mix design for NC, HSC and FRC

Type of concrete	Cement (kg/m^3)	Sand (kg/m^3)	Limestone 5/10 (kg/m^3)	Superplasticizer* (ml/ m^3)	Air entrainment agent (ml/ m^3)	Water* (L/ m^3)	Fiber (kg/m^3)
NSC	450	615	1015	4500	140	170	-
HSC	475	778	800	7000	170	145	-
FRC	450	615	1015	V*	140	170	5.85

* The values marginally varied for each batch to achieve the target slump.

3.2.2. Reinforcement

The specimens comprised from longitudinal reinforcement, transverse reinforcement and end-anchorage U-shaped bars for longitudinal reinforcement. Two types of reinforcement were used including steel and GFRP. Curvilinear No. 5 (15 mm) and No. 6 (20 mm) sand-coated bars with radii of 3,305 mm and 3,445 mm were used in GFRP-reinforced specimens as longitudinal reinforcement for the bottom and top meshes, respectively. Since thermoset GFRP bars cannot be bent after production, curvilinear bars were fabricated with the specified radii using an innovative manufacturing process. U-shaped sand-coated bars the same size as the longitudinal bars were used to provide end anchorage for the longitudinal bars. Transverse reinforcement was provided as No. 4 (13 mm) with two types of closed and U-shaped sand-coated GFRP ties. Table 3.2 presents the tensile strength, modulus of elasticity, and ultimate strain of the curvilinear GFRP bars determined by performing tensile tests according to ASTM D7205-21. Deformed 15M and 10M steel bars were used as the longitudinal and transverse reinforcement, respectively, in the steel-reinforced specimen. The properties of steel reinforcement are provided in Table 3.2

3.3. Details of Test Specimens

In order to investigate the performance of GFRP-reinforced PCTL segments, a total of 12 full-scale specimens were constructed and tested under three-point bending load. The test specimens include one steel-reinforced NC tunnel segment, five GFRP-reinforced NC tunnel segments, three GFRP-reinforced HSC tunnel segments, and three GFRP-reinforced FRC tunnel segments. The tunnel dimension considered in this study was a subway/vehicle tunnel lining with internal diameter of 6500 mm and thickness of 250 mm. A full ring of the

Table 3.2 Mechanical properties of GFRP and steel reinforcement

Reinforcement Type	Bar Size	Bar Diameter, mm	Nominal Cross-sectional Area, mm^2	Modulus of Elasticity, GPa	Tensile Strength, MPa	Tensile Strain, %
GFRP curvilinear bars	#5	15.0	199	55.1 ± 1.25	1115 ± 60	2.0 ± 0.1
	#6	20.0	284	52.9 ± 0.6	1068 ± 49	2.0 ± 0.1
GFRP U-shaped bars*	#5	15.0	199	53.5 ± 1.1	1,283 ± 42	2.4 ± 0.1
	#6	20.0	284	53.2 ± 2.2	1,131 ± 35	2.1 ± 0.0
GFRP closed ties*	#4	13.0	129	55.6 ± 1.6	1,248 ± 74	2.2 ± 0.1
GFRP U-shaped ties	#4	13.0	129	55.6 ± 1.6	1,248 ± 74	2.2 ± 0.1
Steel	10 M	11.3	100	200.0	f_y §=480 ± 10	ε_y §=0.24
	15 M	16.0	200	200.0	f_y =480 ± 15	ε_y =0.24

* The reported properties obtained by testing of the straight bars manufactured with the same process as the bent bars.

§ f_y and ε_y represent the yield strength and strain of the steel bars, respectively.

considered tunnel comprises seven segments with different shapes and geometries. In this study, a segment rhomboidal in shape was selected, complying with the original geometry and shape of the considered subway/vehicle tunnel lining. The specimens measured 3100 mm in length (arc length), 1500 mm in width, and 250 mm in thickness with internal and external radii of 3250 mm and 3500 mm, respectively (Fig. 3.1). The concrete cover was kept constant at 40 mm. Each specimen had longitudinal reinforcement, transverse ties, and U-shaped end-anchorage bars. Table 3.3 and Fig. 3.2 present the test matrix and reinforcement details of the tested specimens, respectively. The test matrix was designed to investigate the effect of different test parameters, including the reinforcement type (GFRP and steel), reinforcement ratio (0.48%, 0.68%, 0.88%, and 1.26%), concrete strength (NSC and HSC), concrete type (NC and FRC), and tie configurations (closed ties and U-shaped ties). The segments were characterized with numbers designating the number of longitudinal bars (7 or 13), followed by letters designating the reinforcement type (G for GFRP and S for steel). The term after "G" or "S" denotes the size of longitudinal bars (#5 and #6 for GFRP and 15M for steel bars). Finally, the letters "H" and "F" refers to the specimens made with HSC and FRC, respectively.

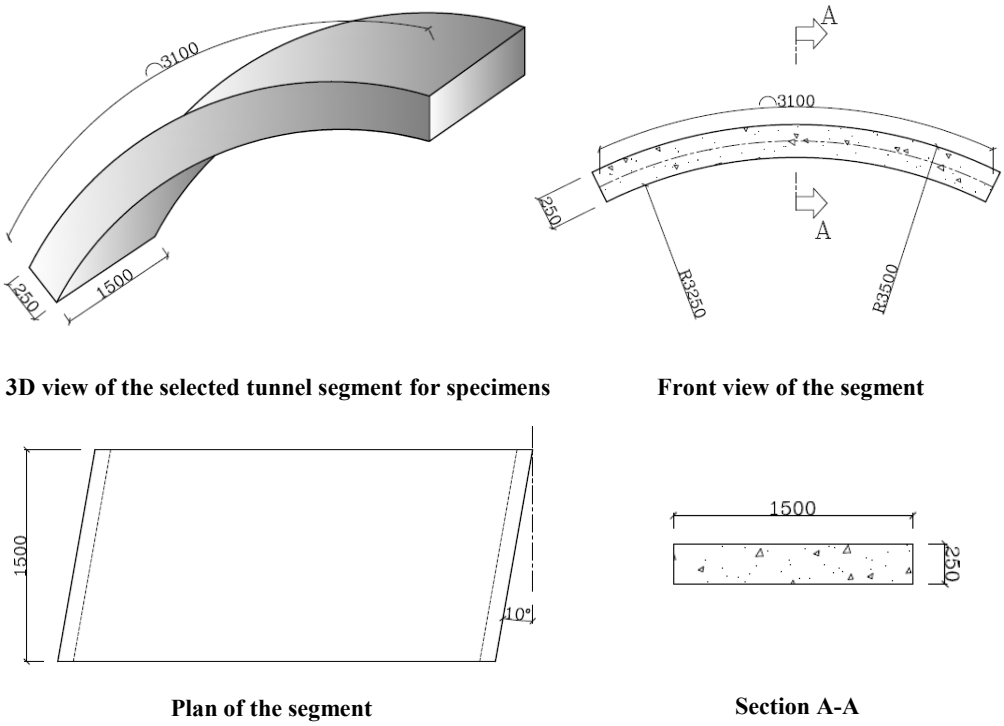

3D view of the selected tunnel segment for specimens

Front view of the segment

Plan of the segment

Section A-A

Figure. 3.1 Geometry of the test specimens

Table 3.3 Test matrix of test specimens.

Segment ID	Type of reinforcement	Reinforcement Design	Longitudinal reinforcement (ρ_L)	Transverse reinforcement	Type of transverse reinforcement	Type of Concrete
7S15M	Steel	I	7 bar #15M (0.50)	#10M @ 200	Closed ties	Normal
7G#5	Glass FRP bars	I	7 bar #5 (0.48)	#4 @ 200	Closed ties	Normal
13G#5	Glass FRP bars	II	13 bar #5 (0.88)	#4 @ 200	Closed ties	Normal
7G#6	Glass FRP bars	III	7 bar #6 (0.68)	#4 @ 200	Closed ties	Normal
13G#6	Glass FRP bars	IV	13 bar #6 (1.26)	#4 @ 200	Closed ties	Normal
7G#5U	Glass FRP bars	I	7 bar #5 (0.48)	#4 @ 200	U-shaped ties	Normal
7G#5H	Glass FRP bars	I	7 bar #5 (0.48)	#4 @ 200	Closed ties	HSC
13G#5H	Glass FRP bars	II	13 bar #5 (0.88)	#4 @ 200	Closed ties	HSC
7G#5HU	Glass FRP bars	I	7 bar #5 (0.48)	#4 @ 200	U-shaped ties	HSC
7G#5F	Glass FRP bars	I	7 bar #5 (0.48)	#4 @ 200	Closed ties	FRC
13G#5F	Glass FRP bars	II	13 bar #5 (0.88)	#4 @ 200	Closed ties	FRC
7G#5FU	Glass FRP bars	I	7 bar #5 (0.48)	#4 @ 200	U-shaped ties	FRC

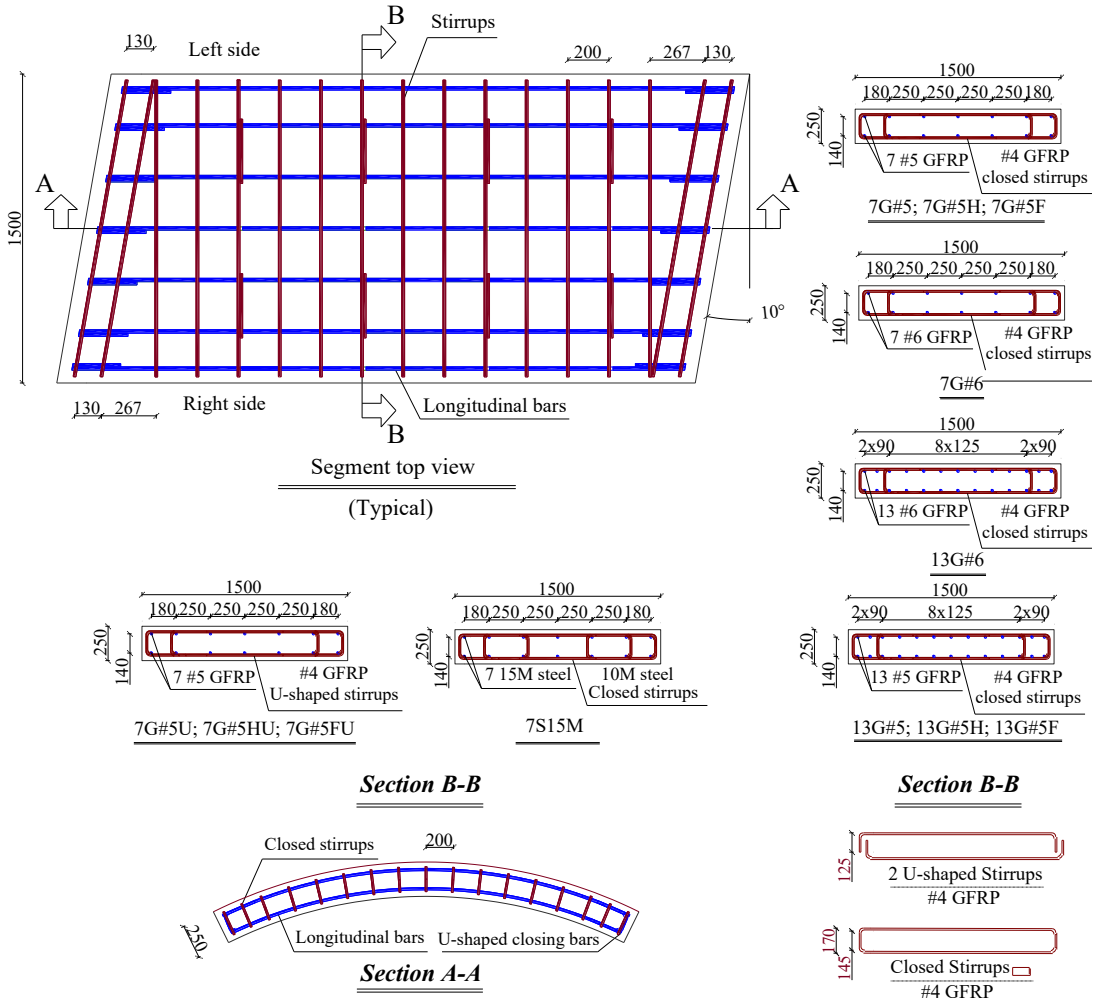

Figure. 3.2 Details of the test specimens.

3.4. Specimen Fabrication

The tunnel segment cages were fabricated at University of Sherbrooke CME laboratory. The specimens were then shipped and cast at SYM-TECH precast company. A wooden formwork was designed and fabricated at the precast company according to the specimens geometry. After casting, the specimens were demoulded and cured for seven days. The tunnel segment specimens were then shipped to University of Sherbrooke CFI laboratory for testing. Figure 3.3 shows the specimen fabrications.

(a) (b)

(c) (d)

(e) (f)

Figure 3.3 Casting and curing of specimens: (a) Cage assembling; (b) Installation of strain gauges; (c) Specimen before casting; (d) Specimen during casting; (e) Specimen after demoulding; (f) Specimen during curing.

3.5. Test Setup and Instrumentations

Three-point load flexural test setup is selected for testing of tunnel segments in this study as shown in Figure 3.4. The supports were cylindrical allowing the specimens to easily rotate and move on the supports. In order to minimize friction, Teflon sheets were placed between the supports and specimens. The test setup was designed and constructed at the Canada Foundation of Innovation (CFI) laboratory located at the University of Sherbrooke. An 11,400 kN MTS testing machine was used to apply a load through a spreader beam at a displacement-controlled rate of 0.8 mm/min. Mid-span deflection was measured with three linear potentiometers (LPOTs) distributed along the width of the specimen center. In addition, two LPOTs measured the deflection at the quarter-span of the specimens. Ten strain gauges 10 mm in length and 5 strain gauges 60 mm in length were installed to measure the strain in the reinforcement and concrete, respectively. Figure 3.5 shows the identification and location of the strain gauges. The gauges installed on the bottom longitudinal bars, top longitudinal bars, and concrete surface are identified by the letters B, T, and C, respectively. If present, a second letter (Q and S) stands for strain gauges installed at the quarter-span and on the side of the specimens, respectively. S_1 identifies the strain gauge installed at the mid-length of the tie leg at the quarter-span.

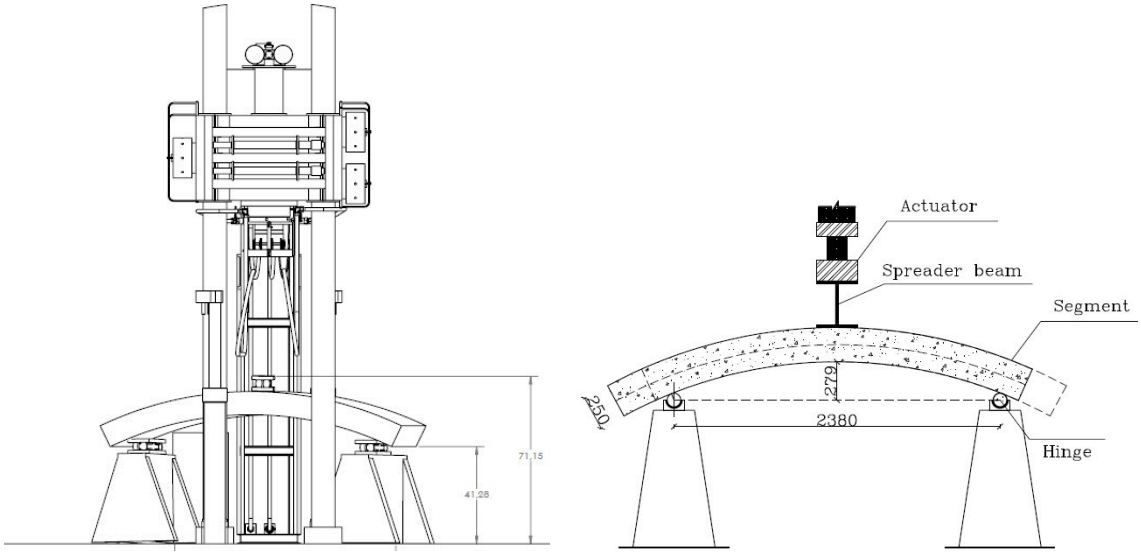

3D view of the Test setup **Front view of test setup**

Figure. 3.4 Test setup.

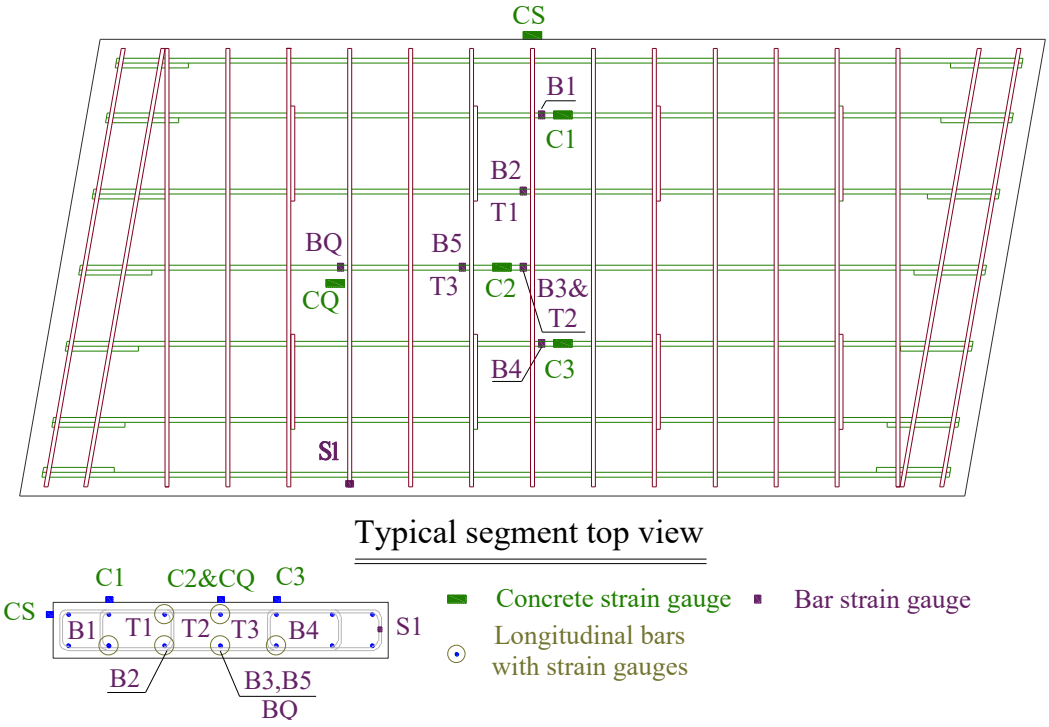

Figure. 3.5 Location of strain gauges.

CHAPTER 4. STRUCTURAL BEHAVIOR OF PRECAST RC TUNNEL SEGMENTS WITH GFRP BARS AND TIES UNDER BENDING LOAD

Foreword

Authors and Affiliation:

Seyed Mohammad Hosseini: Ph. D. Candidate, Department of Civil Engineering, University of Sherbrooke, Sherbrooke, Quebec, Canada, J1K 2R1

Salaheldin Mousa: Postdoctoral fellow, Department of Civil Engineering, University of Sherbrooke, Sherbrooke, Quebec, Canada, J1K 2R1

Hamdy M. Mohamed: Research associate and lecturer, Department of Civil Engineering, University of Sherbrooke, Sherbrooke, Quebec, Canada, J1K 2R1.

Brahim Benmokrane: Professor, Department of Civil Engineering, University of Sherbrooke, Sherbrooke, Quebec, Canada, J1K 2R1.

Journal title: ACI Structural Journal

Paper status: Final version, published online in January 2022.

Contribution in thesis:

In this chapter, the effect of different parameters of reinforcement type (GFRP and steel) and reinforcement ratio (0.48, 0.9, and 1.3%) was evaluated on the structural performance of GFRP-reinforced PCTL segments. The performance of the specimens was evaluated in terms of cracking behavior, failure mechanism, load-deflection curve and strain analysis. Lastly, an analytical investigation was conducted to evaluate the ACI 440.1R-15 design provisions for predicting flexural strength, shear capacity and crack width of GFRP-reinforced PCTL segments.

4.1. Abstract

Using glass fiber-reinforced polymer (GFRP) reinforcement in precast concrete tunnel lining (PCTL) segments is a practical approach to overcome corrosion problems in underground tunnels. This study involved fabricating full-scale PCTL segments 3,100 mm (122 in) in length, 1,500 mm (59 in) in width, and 250 mm (10 in) in thickness reinforced with curvilinear sand-coated GFRP bars and testing them under three-point bending load. The investigated parameters were the reinforcement type (GFRP and steel) and reinforcement ratio (0.48%, 0.9, and 1.3%) with different configurations of GFRP bar spacing and size. The structural performance of the tested PCTL segments was evaluated in terms of cracking behavior, failure mechanism, load–deflection curve, strain analysis, and deformability. The test results indicate that the structural performance of GFRP-reinforced specimens under bending load was satisfactory in terms of cracking and deflection behavior at service load, ultimate load-carrying capacity, ultimate deflection, and deformability. In addition, increasing the reinforcement ratio changed the failure mode while enhancing the load-carrying capacity, stiffness, and cracking behavior. Lastly, an analytical investigation was conducted to evaluate the ACI 440.1R-15 design provisions for predicting the flexural strength, shear capacity, and crack width of GFRP-reinforced PCTL segments. The experimental and analytical results are presented and discussed herein. The test results and outcomes of this study can serve in assessing and exploring the feasibility of using curvilinear GFRP bars in precast concrete tunnel segments in underground tunnel applications.

Keywords: Precast concrete tunnel segments (PCTL); glass fiber-reinforced polymer (GFRP) bars and ties; experimental and analytical investigation; reinforcement ratio; bending load; load-deflection; cracking patterns and strains; flexural and shear strength; design codes

4.2. Introduction

Tunnels play a key role in assisting the movement of people, goods, and special services. The functionality of tunnels depends on the structural and durability performance of their lining systems. Tunnel lining systems act as lines of defense against large overburden loads and surrounding complex geotechnical conditions. In tunnels mechanically excavated in soft ground, weak rock, or fractured hard rock, precast concrete tunnel lining (PCTL) segments are placed to support tunnel boring machines (TBM) during advancement. The use of PCTL segments has been increasing because they can be installed more efficiently and economically than normal cast in situ linings. PCTL segments are subjected to different loading conditions during construction and service stages, which induce bending moments, shear force, and axial load in the segments (ACI 544.7R-16). Normally, PCTL segments are designed for 100 years of service life. The corrosion of steel reinforcement, however, is one of the major causes of degradation in steel-reinforced PCTL segments, jeopardizing the integrity and efficiency of tunnel segments (Abbas 2014a; ACI 533.5R-20). Corrosion induces distress in PCTLs, leading to micro- and macro-cracking. This causes the concrete cover to spall, which accelerates corrosion and further damage. According to ACI 533.5R-20, the main reasons for corrosion of steel reinforcement in PCTL segments are chloride attack in tunnels adjacent to seawater, carbonation attack in heavily trafficked roadway tunnels, tunnels adjacent to aggressive soils, and stray current corrosion in subway and railway tunnels (ACI 533.5R-20). Mitigation of such corrosion problems in tunnels requires costly and difficult methods that sometimes cannot eliminate the risk of corrosion (Caratelli et al. 2016). A practical approach to the corrosion problems in conventional steel-reinforced PCTL segments is to replace the steel reinforcement with noncorroding materials such as glass fiber-reinforced polymer (GFRP) bars. GFRP bars offer distinct advantages over conventional steel rebars such as corrosion resistance, chemical resistance, electromagnetic neutrality, high strength-to-weight ratio, high tensile strength, competitive life-cycle cost, and fatigue resistance. Further, reduction in concrete cover, suitability for parts of the tunnel that eventually should be demolished, and the possibility of creating dielectric joints are among the merits of using GFRP reinforcement in tunnel segments (ACI 440.1R-15; Caratelli et al. 2016).

Caratelli et al. (2016) investigated the possibility of using GFRP reinforcement in PCTL segments by comparing the behavior of a steel-reinforced segment with a GFRP-reinforced segment under bending and thrust loads. They concluded that the flexural behavior of steel- and GFRP-reinforced segments did not significantly differ. Bar rupture was the failure mode observed in their segments, which is unfavorable according to FRP design standards (CAN/CSA S806-12, R2017; ACI 440.1R-15) and is penalized in design with lower strength reduction factors. In addition, at a service load equal to 30% of the ultimate load attained, the maximum reported crack width was 1.3 mm (0.05 in). This exceeds the allowable crack width in CAN/CSA S6-19 as a result of using smooth GFRP bars with a low modulus of elasticity and bond strength. Spagnuolo et al. (2017) performed a theoretical analysis on the specimens tested by Caratelli et al. (2016) according to ACI 440.1R-15 to obtain a bending moment–axial load interaction diagram. Comparing the simplified procedure in Spagnuolo et al. (2017) to the experimental results reported by Caratelli et al. (2016) indicate that the simplified procedure was suitable for predicting the capacity of GFRP-reinforced tunnel segments. Caratelli et al. (2017) compared the flexural and thrust behavior of PCTL segments reinforced with pultruded GFRP bars with those produced by three different prototypes. The prototypes were closed ring reinforcement, lattice reinforcement, and wirenet reinforcement. In addition, the performance of sand-coated GFRP bars was compared to that of smooth bars. Caratelli et al. (2017) observed bar rupture failure mode in their bending tests. Based on their results and technical/commercial feasibility, the closed ring reinforcement seems to be the best solution among the prototypes tested. In addition, they reported that the maximum crack width in the specimen reinforced with sand-coated GFRP bars was about 70% narrower than that reinforced with smooth bars.

GFRP-reinforced beams and one-way slabs are among the well-investigated structural elements that can be considered to behave somewhat similarly to PCTL segments. Flexural strength, deformability, cracking behavior, deflection, creep rupture, fatigue behavior, and shear strength are important factors that affect the flexural behavior of concrete members reinforced with FRP bars (ACI 440.1R-15). Reinforcement ratio and axial stiffness are the most influential parameters that control the flexural strength and serviceability of FRP-RC

members (Masmoudi et al. 1998; Sivagamasundari and Kumaran 2008; Kassem et al. 2011; El-Nemr et al. 2013; Mousa et al. 2019a,b). Increasing the reinforcement ratio increases the flexural strength. The concrete compressive strain at failure, however, limits the enhancement of flexural strength in over-reinforced concrete beams (Masmoudi et al. 1998; Theriault and Benmokrane 1998). Increasing the reinforcement ratio and axial stiffness enhances the deflection and cracking behavior of FRP-reinforced flexural elements (Chang and Seo 2012; El-Nemr et al. 2018; Mousa et al. 2020). Additionally, adopting closer spacing between longitudinal reinforcement elements leads to closer crack spacing (Ospina and Bakis 2007). Shear strength—in addition to flexural strength, cracking, and deflection—is an important factor that should be considered in designing FRP-reinforced structural elements under bending load (ACI 440.1R-15). Many parameters affect the shear strength of FRP-RC members, such as concrete type and strength, reinforcement rigidity, size effect, interaction of shear force and bending moment at the critical section, distance of the critical section from the supports, and strain in longitudinal reinforcement (Khavaran 2019).

Due to their curvilinear shape, PCTL segments behave somewhat differently than one-way slabs. In fact, GFRP-reinforced PCTL segments require curvilinear GFRP bars, which have different mechanical behavior than straight bars (Spagnuolo et al. 2018). The arched shape of the segments causes differences in the applied tensile and compressive forces on each section along the span. This leads to PCTL segments having different flexural and shear behaviors than straight one-way slabs and beams (Fernández Ruiz et al. 2010; Campana et al. 2014). Furthermore, PCTL segments are generally under a combination of axial load and flexural moment, unlike one-way slabs. Our study investigated the structural performance of GFRP-reinforced PCTL segments and assessed the effect of different parameters on their flexural and shear behavior. This paper presents the structural behavior of full-scale GFRP-reinforced PCTL segments under flexure. The effect of reinforcement type and ratio on the behavior of GFRP-reinforced precast concrete tunnel lining segments under flexure was investigated.

Research is ongoing at the University of Sherbrooke to improve current practices and develop more efficient design and construction approaches for using curvilinear GFRP bars and stirrups in precast concrete tunnel lining segments. This research was initiated in 2019 in collaboration with Quebec's Ministry of Economy and Innovation, Pultrall Inc. (a manufacturer of GFRP reinforcement), and Sym-Tech Béton Préfabriqué (a precaster of concrete structural units). The objectives of the research project are to (1) determine the optimal design parameters to allow the use of GFRP reinforcement in concrete segments; (2) develop and compare the performance of GFRP-reinforced concrete segments with that of steel-reinforced concrete segments subjected to different loading conditions during construction and service stages, which induce bending moments, shear forces, and axial loads in the segments (ACI 544 7R-16); (3) develop new construction and design methods for FRP-reinforced concrete tunnel segments; and (4) establish recommendations for ACI and CSA design codes and guidelines for the use of GFRP bars in precast reinforced concrete tunnel segments. This paper presents the structural behavior of full-scale GFRP-reinforced PCTL segments under flexural load. The effect of reinforcement type and ratio on the behavior of GFRP-reinforced precast concrete tunnel lining segments under flexural load was investigated.

4.3. Research Significance

Incorporating GFRP bars and stirrups into precast concrete tunnel lining segments can potentially increase the overall service life of these structures, while significantly cutting maintenance and saving on major repair costs. The literature contains only a few studies on the structural behavior of GFRP-reinforced PCTL segments under flexural load. The tension-controlled failure mode was reported in the literature for the tested GFRP-reinforced PCTL segments, which is undesirable for design purposes. In addition, the cracking behavior in most of the tested specimens reported on in the literature did not satisfy the requirements of CAN/CSA S6-19. Furthermore, smooth square GFRP bars were used in the majority of tested specimens reported on in the literature and that is not one of the bar surfaces recommended in ACI 440.1R-15. Moreover, there are no investigations in the literature dealing with the impact of various test parameters on the flexural and shear behavior of

GFRP-reinforced PCTL segments. Furthermore, the results of GFRP-reinforced one-way slabs cannot be directly applied to GFRP-reinforced PCTL segments due to their curvilinear shape. In this study, full-scale PCTL segments reinforced with sand-coated GFRP bars with different reinforcement ratios, bar sizes, and spacing were compared. In addition, their behavior was compared to a steel-reinforced PCTL segment serving as a reference. An analytical investigation was also conducted to evaluate the ability of ACI 440.1R-15 to predict the flexural and shear capacities of GFRP-reinforced PCTL segments. The findings of this study represent a vital step towards the design and field applications of GFRP-reinforced PCTL segments in major tunneling projects.

4.4. Experimental Program

4.4.1. Material properties

All of the tunnel segment specimens in this study were fabricated with normal-strength concrete with a 28-day target compressive strength of 40 MPa (5.8 ksi). This strength is within the range of 34 to 60 MPa (4.9 to 8.7 ksi) for segmental tunnel lining systems in ACI 533.5R-20. The actual compressive strength at the time of testing was 50 ± 3 MPa (7.3 ± 0.4 ksi), obtained as the average test results of three 100×200 mm (4×8 in) concrete cylinders for each specimen.

Curvilinear No. 5 (15 mm) and No. 6 (20 mm) sand-coated bars with radii of 3,305 mm (130 in) and 3,445 mm (136 in) were used in GFRP-reinforced specimens as longitudinal reinforcement for the bottom and top meshes, respectively. It should be noted that GFRP bars have been selected to replace steel reinforcement to present a more economical choice for field applications compared to other types of FRP bars (such as CFRP). Since thermoset GFRP bars cannot be bent after production, curvilinear bars were fabricated with the specified radii using an innovative manufacturing process. The curvilinear No. 5 and No. 6 GFRP bars were manufactured with boron-free E-CR glass fibers impregnated in thermoset vinyl-ester resin with a fiber content of 78% by weight according to ASTM D3171-15 and CAN/CSA S807-19. U-shaped sand-coated bars the same size as the longitudinal bars were

used to provide end anchorage for the longitudinal bars. Although closed-ring reinforcement has been reported to yield more satisfactory results than the traditional assembly process of curvilinear bars with end anchorage (Caratelli et al. 2017), the closed-ring prototype was not used in this study due to the different manufacturing procedures needed for FRP composite bars. Transverse reinforcement was provided as No. 4 (13 mm) closed sand-coated GFRP ties. Figure 4.1 shows the No. 5 curvilinear bars, U-shaped end-anchorage bars, and closed ties. The tensile strength, modulus of elasticity, and ultimate strain of the curvilinear GFRP bars were determined by performing tensile tests according to ASTM D7205-21 on the curvilinear bars with a radius of 3305 mm (130 in) used for the bottom longitudinal reinforcement (Fig. 4.1). It is worth mentioning that before applying the tensile force to the specimen, the curvilinear bars were straightened using the test fixture with a novel method. Therefore, the provisions of ASTM D7205-21 could be used in the tensile testing of the bars. Deformed 15M and 10M steel bars were used as the longitudinal and transverse reinforcement, respectively, in the steel-reinforced specimen. Table 4.1 reports the mechanical properties of the GFRP and steel reinforcement. Figure 4.2 shows a typical assembled GFRP cage before casting.

Table 4.1 Mechanical properties of GFRP and steel reinforcement

Reinforcement Type	Bar Size	Bar Diameter, mm	Nominal Cross-sectional Area, mm^2	Modulus of Elasticity, GPa	Tensile Strength, MPa	Tensile Strain, %
GFRP curvilinear bars	#5	15.0	199	55.1 ± 1.25	1115 ± 60	2.0 ± 0.1
	#6	20.0	284	52.9 ± 0.6	1068 ± 49	2.0 ± 0.1
GFRP U-shaped bars*	#5	15.0	199	53.5 ± 1.1	1,283 ± 42	2.4 ± 0.1
	#6	20.0	284	53.2 ± 2.2	1,131 ± 35	2.1 ± 0.0
GFRP closed ties*	#4	13.0	129	55.6 ± 1.6	1,248 ± 74	2.2 ± 0.1
Steel	10 M	11.3	100	200.0	f_y §=480 ± 10	ε_y §=0.24
	15 M	16.0	200	200.0	f_y =480 ± 15	ε_y =0.24

* The reported properties obtained by testing of the straight bars manufactured with the same process as the bent bars.

§ f_y and ε_y represent the yield strength and strain of the steel bars, respectively.

Notes: 1 mm = 0.0394 in.; 1 mm^2 = 0.00155 in.2; 1 MPa = 0.145 ksi.

4.4.2. Specimen Details and Test Matrix

Four full-scale PCTL segments, including three specimens reinforced with GFRP reinforcement and one reinforced with steel as a reference, were constructed (Fig. 4.2) and tested under three-point bending load. The tunnel dimension considered in this study was a subway/vehicle tunnel lining with internal diameter of 6500 mm and thickness of 250 mm.

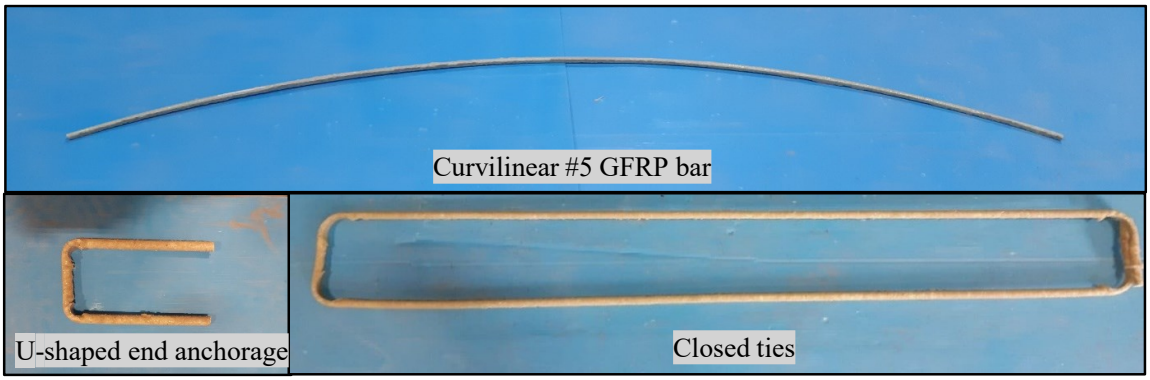

(a)

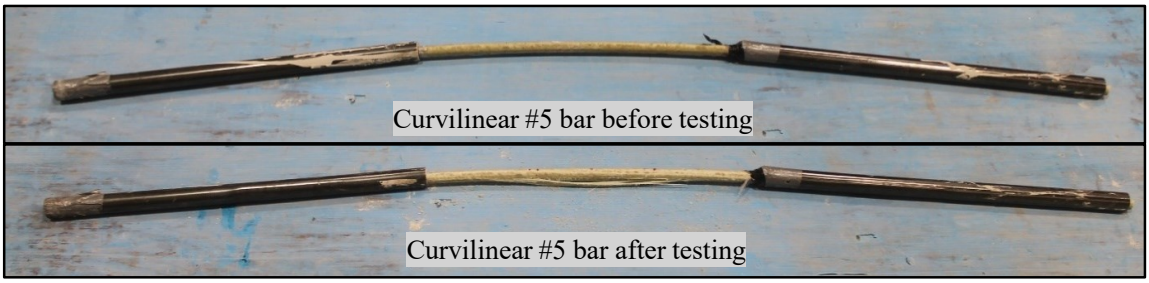

(b)

Figure 4.1 (a) GFRP curvilinear bars, U-shaped end anchorage, and closed ties; (b) curvilinear #5 GFRP bar before and after testing.

Figure 4.2 GFRP-reinforced tunnel segment cage and specimen fabrication.

A full ring of the considered tunnel comprises seven segments with different shapes and geometries. In this study, a segment parallelogram was selected, complying with the original geometry and shape of the considered subway/vehicle tunnel lining. The specimens measured 3100 mm (122 in) in length (arc length), 1500 mm (59 in) in width, and 250 mm (10 in) in thickness with internal and external radii of 3250 mm (128 in) and 3500 mm (138 in), respectively. The concrete cover was kept constant at 40 mm (1.6 in), which meets the minimum specified in ACI 533.5R-20. Figure 4.3 presents the dimensions and reinforcement details of the specimens. Each specimen had longitudinal reinforcement, transverse ties, and U-shaped end-anchorage bars. The test matrix was designed to investigate the effect of different test parameters, including the reinforcement type (GFRP and steel) and reinforcement ratio (0.48%, 0.88%, and 1.26%) by considering two configurations of longitudinal bar spacing (125 and 250 mm [4.9 and 9.8 in]) and two bar sizes (#5 and #6). The experimental testing program comprised four full-scale PCTL segments (7G#5, 13G#5, 13G#6, and 7S15M) fabricated, instrumented, and tested up to failure. The segments were characterized with numbers designating the number of longitudinal bars (7 or 13), followed by letters designating the reinforcement type (G for GFRP and S for steel) and finally by the size of longitudinal bars (#5 and #6 for GFRP and

M15 for steel bars). Table 4.2 gives the test matrix and reinforcement details of the tested specimens. Although existing FRP design guidelines and codes (ACI 440.1R-15; AASHTO-18; CAN/CSA S806-12, R2017; CAN/CSA S6-19) accept both types of flexural failure (concrete crushing or FRP reinforcement rupture), concrete crushing failure is more desirable because it is more gradual and has a greater degree of deformability (ACI 440.1R-15, CAN/CSA S6-19). When the longitudinal reinforcement ratio (ρ_l) was greater than the balanced reinforcement ratio (ρ_b), the section was considered as over-reinforced and flexural failure was induced by concrete crushing (compression failure). Table 4.2 presents the ratio of longitudinal reinforcement ratio to the balanced reinforcement ratio for different specimens according to ACI 440.1R-15. As can be seen, all the specimens had a reinforcement ratio higher than the balanced reinforcement ratio.

4.4.3. Specimen Fabrication

The PCTL segments were precast at Sym-Tech Béton Préfabriqué in Saint-Hyacinthe, Quebec. The GFRP cages were assembled and instrumented at the University of Sherbrooke and then shipped to the precast concrete company. The cages were then placed in wooden

Table 4.2 Test matrix and specimen details

Specimen ID	Longitudinal Reinforcement	ρ_l (%)	ρ_l / ρ_b	Transverse Reinforcement
7G#5	7 #5 GFRP bars	0.48	1.4	#4 @ 200 mm
13G#5	13 #5 GFRP bars	0.90	2.7	#4 @ 200 mm
13G#6	13 #6 GFRP bars	1.30	3.7	#4 @ 200 mm
7S15M	7 15M steel bars	0.5	-	10M @ 200 mm

Notes: 1 mm = 0.0394 in.

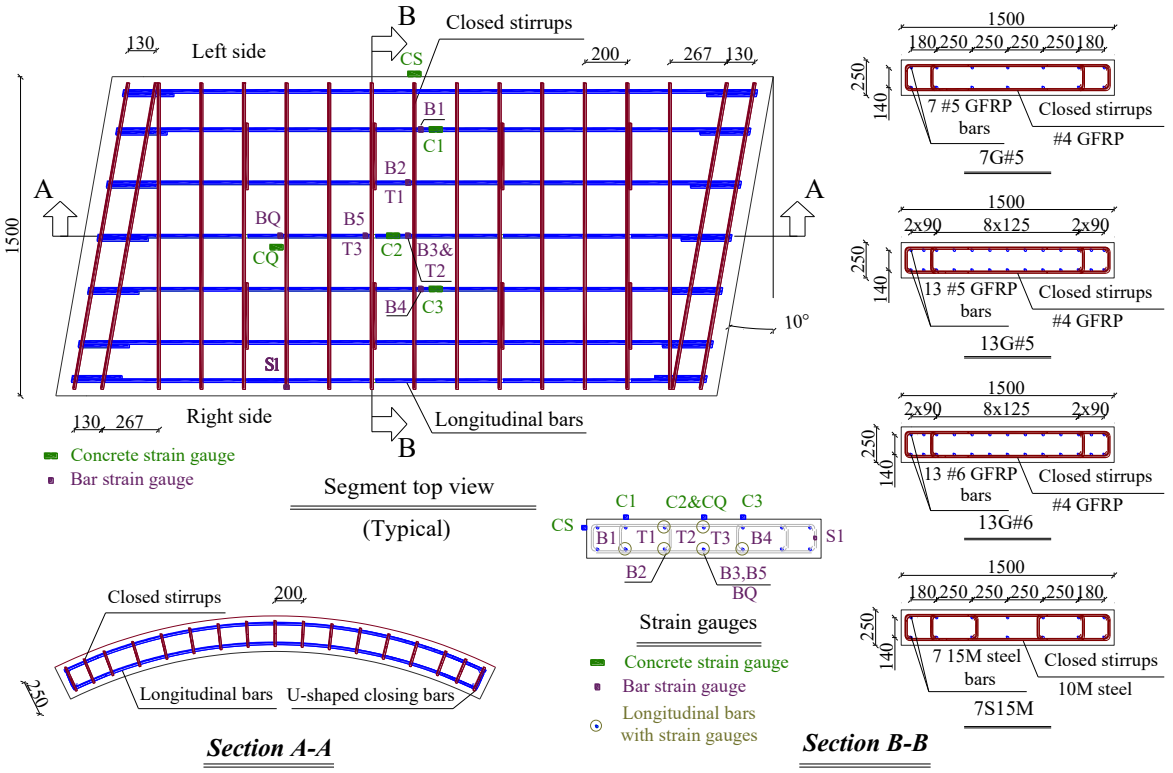

Figure. 4.3 Details of reinforcement, geometry, and strain gauges. (Note: All dimensions in mm; 1 mm = 0.0394 in.)

formwork designed and fabricated to cast one specimen each time, as shown in Fig. 4.2. As mentioned previously, the PCTL segments were constructed using normal-strength concrete with a 28-day target compressive strength of 40 MPa (5.8 ksi). An electric vibrator was used to consolidate the concrete and to prevent concrete segregation. Once the casting and finishing were complete, the formwork was covered with plastic to ensure a uniform curing temperature during the first day. Lastly, the PCTL segments were then demolded, cured for seven days, and transferred to the University of Sherbrooke for testing.

4.4.4. Instrumentation and Test setup

Ten strain gauges 10 mm (0.4 in) in length and 5 strain gauges 60 mm (2.4 in) were installed to measure the strain in the reinforcement and concrete, respectively. Figure 4.3 shows the identification and location of the strain gauges. The gauges installed on the bottom longitudinal bars, top longitudinal bars, and concrete surface are identified by the letters B, T, and C, respectively. If present, a second letter (Q and S) stands for strain gauges installed

at the quarter-span and on the side of the specimens, respectively. S_1 identifies the strain gauge installed at the mid-length of the tie leg at the quarter-span. The bending tests were performed using three-point loading setup with a clear span of 2400 mm (94.5 in), as shown in Fig. 4.4. The supports were cylindrical allowing the specimens to easily rotate and move on the supports. In order to minimize friction, Teflon sheets were placed between the supports and specimens. The test setup was designed and constructed at the Canada Foundation of Innovation (CFI) laboratory located at the University of Sherbrooke. An 11,400 kN (2563 kip) MTS testing machine was used to apply a load through a spreader beam at a displacement-controlled rate of 0.8 mm/min (0.03 in/min). Mid-span deflection was measured with three linear potentiometers (LPOTs) distributed along the width of the specimen center. In addition, two LPOTs measured the deflection at the quarter-span of the specimens.

4.5. Test Results and Observations

4.5.1. Failure Modes and Cracking Patterns

Crack propagation in the specimens followed a typical pattern of flexural cracks in a simply supported member subjected to three-point bending load. The first flexural crack initiated at the zone beneath the loading plate where the bending moment was maximum. By increasing the load, the number and width of flexural cracks increased; the direction of the cracks was

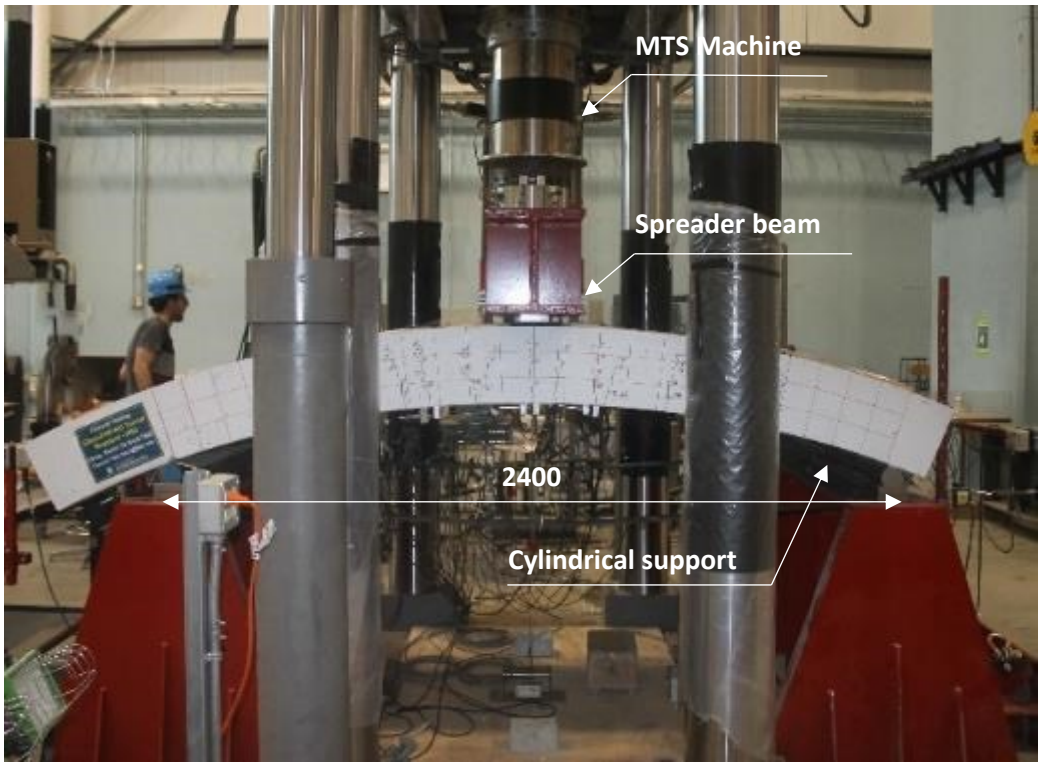

Figure 4.4 Test setup. (Note: All dimensions in mm; 1 mm = 0.0394 in.)

almost perpendicular to the segment bottom surface. Uniform trends in flexural crack distribution and crack width increment were observed in the GFRP-reinforced specimens at the post-cracking stage. With three-point loading, the maximum bending moment and shear force act in the same zone of the structural element. Increasing the load produced a combination of flexural and shear stresses causing the flexural cracks to incline towards the loading plate in the specimens. Further increments in load led to initiation of shear cracks as an extension of the inclined part of flexural cracks. Shear cracks initiated at loads of 232, 350, and 326 kN (52, 79, and 73 kip) in specimens 7G#5, 13G#5, 13G#6, respectively. Figures 4.5 and 4.6, respectively, provide the cracking patterns at different loading stages and failure modes of the specimens. Specimen 7G#5 failed due to concrete crushing at mid-span. After a load reduction due to concrete spalling in this specimen, the load was gradually

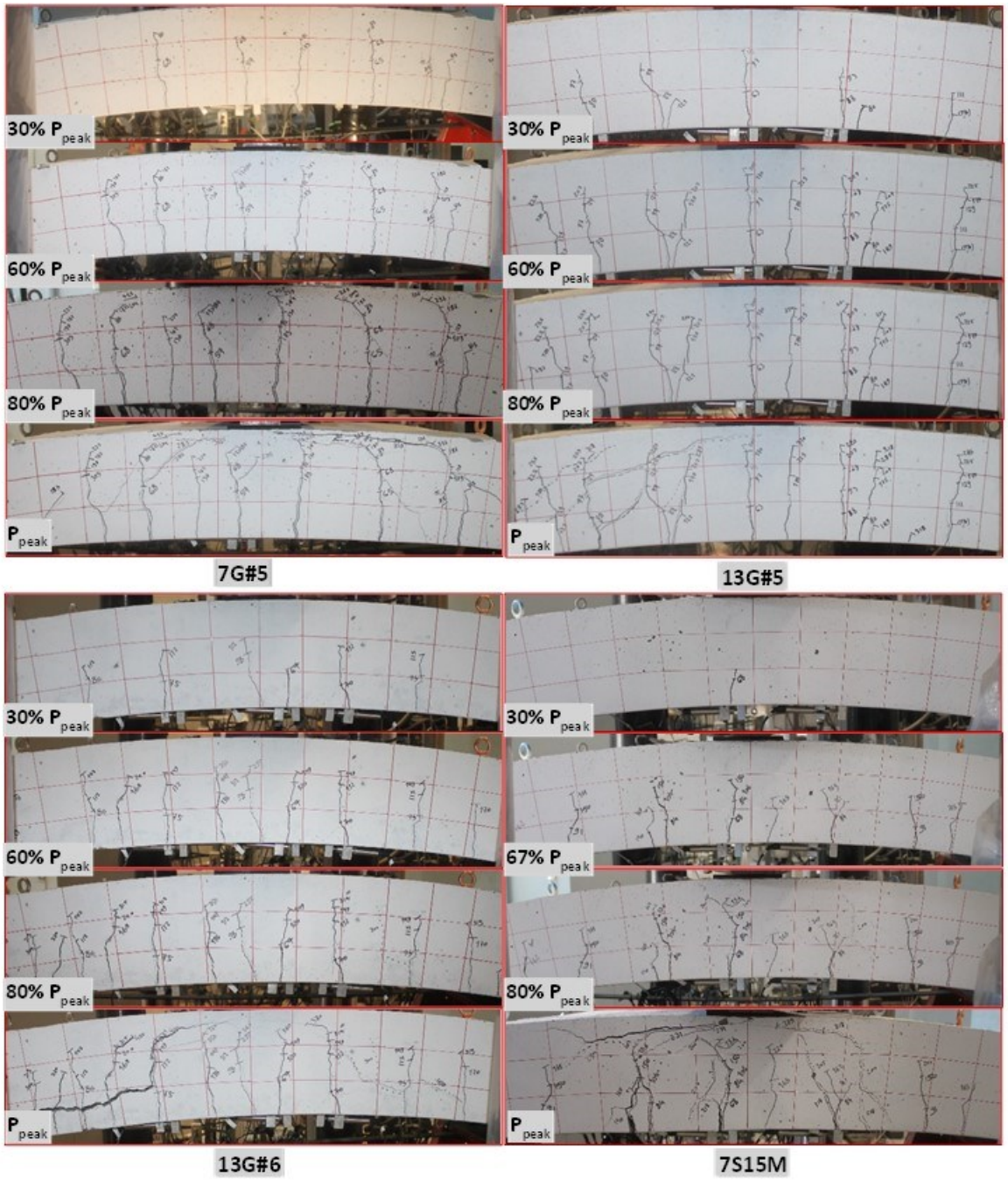

Figure 4.5 Cracking pattern of the tested specimens at different loading stages.

increased until the concrete in compression zone was fully crushed. In specimen 13G#5, a shear crack appeared (at 95% of the peak load) and then widened as the specimen lost the possibility of redistributing stress to other shear-resistance mechanisms. The widening of the shear crack caused a temporary load reduction. After a short period, the specimen

experienced diagonal tension failure, while it had flexure-dominant behavior until 95% of the peak load. The shear crack in this specimen had an inclination angle of approximately 45°. Up to the peak load in the specimen 13G#6, the width of flexural and shear cracks increased gradually with a flexure-dominant behavior. With further load increases widened a diagonal shear crack, causing the specimen to experience diagonal tension failure followed by splitting of longitudinal bars. Inclination of the shear cracks was almost 55° on the left side and 80° on the right side of the segment. As for the steel-reinforced specimen, its crack distribution and opening followed a uniform trend until the yielding point. After the steel yielded, however, the crack opening concentrated at the region of maximum bending moment. Specimen 7S15M failed by concrete crushing after yielding of the steel reinforcement, which denotes tension-controlled flexural failure. Concrete crushing in this specimen occurred in three steps starting from concrete spalling to full crushing of the compression block, which led to a considerable drop in load.

Table 4.3 presents the actual compressive strength of the specimens at the time of testing, cracking load, peak load, mode of failure, and measured crack width at the service load. In this study, the service load of the GFRP-reinforced specimens was defined based on two reference points. The first point defines the service load as the load corresponds to 2000 microstrains (με) in the tensile reinforcement (ISIS Canada Research Network 2007), while the second point defines the service load as the load corresponds to 30% of the specimen nominal capacity, $0.3M_n$ (Bischoff et al. 2009). In the case of the steel-reinforced specimen, the two reference points were considered as 1200 με and $0.67M_n$. The measured crack

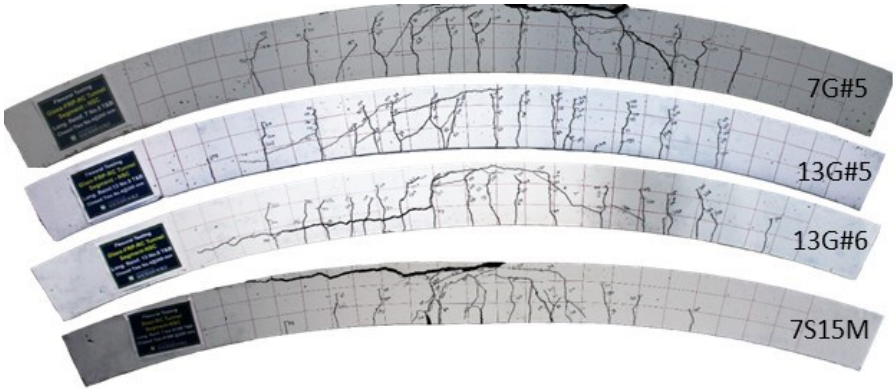

Figure 4.6 Failure modes of the tested specimens.

Table 4.3 Experimental results

Specimen ID	$f_c'^{*}$, MPa	P_{cr}, kN	P_{peak}, kN	Failure Mode[ǂ]	Maximum Crack Width at Service Load (mm)[§]		Deformability, J
					2000 $\mu\varepsilon$	0.3 M_n	
7G#5	48	57	315	CC	0.35	0.7	9.39
13G#5	51	63	365	DT	0.35	0.4	4.76
13G#6	47	63	412	DT	0.25	0.25	3.99
7S15M	53	68	236	TC	0.2	0.4	-

[*] Compressive strength of specimens at the test date obtained by testing three cylinders.

[ǂ] TC is tension-controlled, CC is compression-controlled, and DT is diagonal tension.

[§] The values in 7S15M specimen are calculated in 1200 μs and 0.67 M_n.

Notes: 1 mm = 0.0394 in; 1 MPa = 145 psi; 1 kN = 0.225 kip.

widths in the GFRP-reinforced specimens at service load ranged between 0.25 and 0.35 mm (0.010 and 0.014 in) and between 0.25 and 0.7 mm (0.010 and 0.028 in) at 2000 με and $0.3M_n$, respectively. According to CAN/CSA S6-19 and AASHTO-18, the maximum allowable crack width in GFRP-reinforced members is 0.5 and 0.7 mm (0.020 and 0.028 in) for members subjected to aggressive environments and for other members, respectively. It can be concluded that the crack width in specimens 13G#5 and 13G#6 was consistent with the requirements in CSA S6-19 for maximum crack width even in harsh environments. In addition, the crack width in specimen 7G#5 at service load corresponding to 2000 $\mu\varepsilon$ was 0.35 mm (0.014 in), which is less than the allowable maximum crack width in harsh environments. The average crack spacing at the middle third of the specimens was 210, 160, and 140 mm (8.3, 6.3 and 5.5 in) in specimens 7G#5, 13G#5, and 13G#6, respectively, at a service load equal to $0.3M_n$. By increasing the load and due to the initiation of more cracks, the average crack spacing at the mid-center of specimens 7G#5, 13G#5, and 13G#6 was 160, 120, and 110 mm (6.3, 4.7, and 4.3 in), respectively, at a load corresponding to 80% of the peak load (Fig. 4.5).

4.5.2. Load-Defection Relationships

Figure 4.7a depicts the load versus mid-span deflection of the tested specimens. In the pre-cracking stage, all specimens behaved linearly with almost the same stiffness. After the first crack formed, the specimens experienced a reduction in load. This reduction was more noticeable in specimen 7G#5, which can be ascribed to its lower reinforcement ratio compared to the other specimens. In the post-cracking stage, the flexural stiffness of the specimens decreased compared to the uncracked section due to the transition from gross section to effective section. The effective section moment of inertia is the main parameter that affects flexural stiffness, which is highly dependent on reinforcement axial stiffness (Mousa et al. 2019b). The GFRP-reinforced specimens behaved almost linearly up to failure due to the linear elastic behavior of GFRP reinforcement. On the other hand, specimen 7S15M had a nearly linear load-deflection relationship until the yielding point. After that, it followed a typical steel stress–strain plateau up to failure with significantly reduced stiffness. The peak load was 58% higher than the yield load, which can be attributed to strain hardening of the steel rebars and increasing the bending moment arm in the section (Hassoun and Al-Manaseer 2020). According to Fig. 4.7a, failure in specimens 7G#5 and 7S15M occurred in three steps, which can be explained by local concrete spalling in the first step to major crushing of the concrete at the final drop. After unloading occurred, the GFRP-reinforced specimens recovered most of their deflection. Due to yielding of steel reinforcement, however, permanent deflections were observed in the steel-reinforced specimen. It should be noted that recovering deflection can be a great advantage for PCTL segments subjected to non-seismic loadings. The load–deflection relationship at the quarter-span exhibited almost the same behavior as at mid-span (Fig. 4.7b). The quarter-span deflections in specimens 7G#5, 13G#5, 13G#6 and 7S15M at peak load was 32%, 29%, 27%, and 38% lower than their mid-span deflections, respectively. It shows a concentration of deformation at mid-span in the steel-reinforced specimen and more uniform deformation distribution in the GFRP-reinforced specimens, especially those with higher reinforcement ratios.

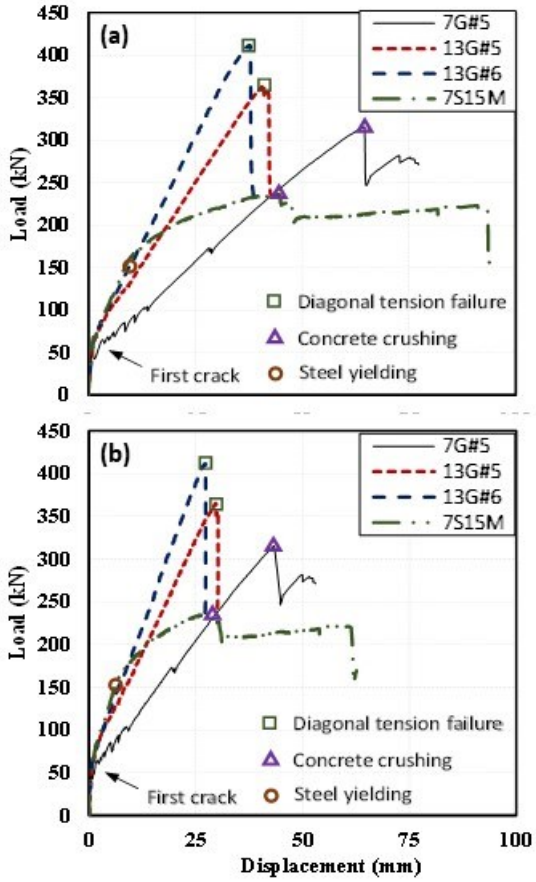

Figure 4.7 Load–deflection diagram of the tested specimens: (a) Mid-span; (b) Quarter-span. (Note: 1 mm = 0.0394 in.; 1 kN = 0.2248 kip.)

4.5.3. Strain in the Reinforcement

Figures 4.8a to 4.8d present the load versus strain in the longitudinal reinforcement up to the peak load at different locations. Before the first crack appeared, the strain in all the reinforcement was negligible. After cracking, all the specimens experienced gradual increases in the measured strain values. The load versus strain at mid-span in the GFRP-reinforced specimens followed a trend similar to their load–deflection behavior, as shown in Fig. 4.8a. At a service load equal to $0.3M_n$, the longitudinal bar strain was 4800, 1630, and 1900 $\mu\varepsilon$ in specimens 7G#5, 13G#5, and 13G#6, respectively. The longitudinal bar strain increased almost linearly as the load increased. At peak load, the maximum strain in the bottom longitudinal reinforcement was 16,300 (82% of the ultimate tensile strain of #5 GFRP bars), 9,400, and 8,300 $\mu\varepsilon$ in 7G#5, 13G#5, and 13G#6, respectively. Until the load levels of 68, 74, and 70 kN (15, 17, and 16 kip) were reached, the strain in the longitudinal

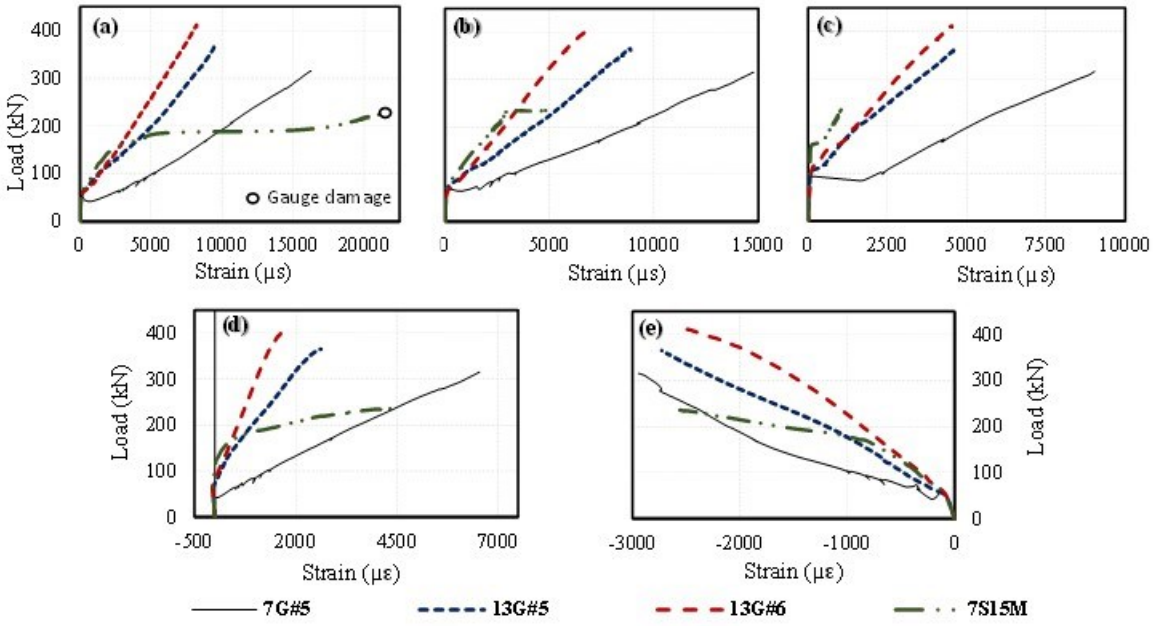

Figure 4.8 Load–strain relationship in the reinforcement and concrete: (a) Bottom bar, mid-span; (b) Bottom bar, B5; (c) Bottom bar, quarter-span; (d) Top bar, mid-span; (e) Concrete, mid-span. (Note: 1 kN = 0.2248 kip.)

reinforcement at a distance of 200 mm (7.9 in) from the mid-span (strain gauge B5) was marginal in specimens 7G#5, 13G#5, and 13G#6, respectively. After initiation of the second crack in the specimens at those loads, the bar strain started to increase with a higher rate (Fig. 4.8b) The maximum strains recorded by strain gauge B5 were 14,800, 8,900, and 6,900 $\mu\varepsilon$ in 7G#5, 13G#5, and 13G#6, respectively, which were less than the maximum recorded mid-span strains average by 10%. The maximum strains at the quarter-span specimens 7G#5, 13G#5, and 13G#6 were 9040, 4660, and 4530 με, respectively, which is 45%, 50%, and, 45% lower than the measured mid-span strains (Fig. 4.8c). This indicates an almost uniform distribution of strain with respect to the flexural moment along the span in the GFRP-reinforced specimens.

Prior to the reinforcement yielding, the stress–strain relationship of the longitudinal bars at mid-span was similar to the load–deflection curve. After that point, bar strain increased rapidly from 5000 to 15,000 $\mu\varepsilon$ without any considerable increase in load (Fig. 4.8a). This is consistent with the test observations during the same strain period as the crack width of the flexural crack at mid-span was rapidly increasing. The maximum mid-span strain

recorded in the bottom bar was greater than 21,000 με. According to Fig. 4.8b, strain gauge B5 revealed a trend in strain increment in specimen 7S15M that was much slower than at the mid-span strain, indicating a concentration of strain distribution at mid-span. Figure 4.8d shows the load versus the measured strain in the top longitudinal reinforcement at mid-span. Before cracking, there was marginal compressive strain in the top longitudinal bars. After the first crack appeared, the compression strain reduced rapidly, and the top reinforcement performed in tension after a load ranged from 60 to 100 kN (13.5 to 22.5 kip) depending on the axial stiffness of the longitudinal bars. The maximum value of recorded strains in the top reinforcement was 6540, 2620, and 1800, and 4030 $\mu\varepsilon$ in 7G#5, 13G#5, and 13G#6, and 7S15M, respectively. The recorded values were 36%, 15%, and 10% of the ultimate strain of the longitudinal GFRP bars in specimens 7G#5, 13G#5, and 13G#6, respectively, while the recorded strain in 7S15M was 1.8 times higher than the yield strain of the steel bars.

4.5.4. Concrete Strain

Figure 4.8e represents the relationship between the load and concrete strain in the specimens' top surface at mid-span. Before the first crack appeared, the recorded concrete compressive strain in the specimens was around -150 με. After cracking occurred, the slope of the load–strain curve at mid-span reduced significantly up to the failure. In contrast, nearly linear behavior was observed in GFRP-reinforced specimen, while the load–strain relationship in specimen 7S15M followed a typical steel stress–strain curve plateau. The maximum recorded concrete compressive strain in the specimens was -2950, -2730, -2500, -2530 $\mu\varepsilon$ in specimens 7G#5, 13G#5, 13G#6, and 7S15M, respectively. The compressive strain values were lower than the suggested ultimate compressive strain by American (ACI 440.1R-15; ACI 318-19; AASHTO-18) and Canadian (CAN/CSA S806-12, R2017; CAN/CSA S6-19) standards, namely 3000 and 3500 με, respectively. Although specimens 7G#5 and 7S15M experienced concrete crushing, their ultimate concrete compressive strain was 2% and 16% lower than 3000 με. This agrees with the findings from past studies on steel- and GFRP-reinforced one-way slabs, as their ultimate compressive strain before concrete crushing was lower than 3000 $\mu\varepsilon$ (Zhang et al. 2004; Chang and Seo 2012; Nigro et al. 2012; Al-Rubaye et al. 2020).

4.5.5. Strain Distribution over the Cross Section

Figure 4.9 shows the distribution of strain over the cross-section depth of the specimens at different load levels up to peak load using concrete and reinforcement strain gauges at mid-span. The figure shows that the strain in the reinforcement increased gradually as the load increased in the GFRP-reinforced specimens. In contrast, after the steel reinforcement yielded, the strain values in the reinforcement increased rapidly in the steel-reinforced specimen. In the GFRP-reinforced specimens, the strain profile was almost linear until 50% of the ultimate tensile strain of the GFRP bars. Figure 4.10 represents the relationship between the applied load and neutral-axis depth at mid-span of the tested specimens. Before initiation of the first crack, the neutral-axis depth position remained unchanged at the geometrical centroid of the cross section. The neutral-axis depth dropped after cracking, which was more pronounced in specimen 7G#5. By increasing the applied load, the neutral-axis depth in the GFRP-reinforced specimens began to stabilize up to the peak load. In contrast, the neutral-axis depth experienced a rapid decrease after yielding of the steel reinforcement in specimen 7S15M. The neutral-axis depth at the peak load was 31, 45, 47, and 19 mm (1.2, 1.8, 1.9, 0.7 in) in specimens 7G#5, 13G#5, 13G#6, and 7S15M, respectively. The neutral-axis depth in specimen 7G#5 was 60% greater than that of 7S15M. In addition, increasing the reinforcement ratio in the GFRP-reinforced specimens increased the neutral-axis depth.

4.6. Discussion of Test Results

4.6.1. Influence of Reinforcement Type

Specimens 7G#5 and 7S15M were designed with similar reinforcement ratios and configurations to investigate the effect of reinforcement type on the structural performance of PCTL segments. The calculated cracking moment of specimens 7S15M and 7G#5 using the transformed moment of inertia was 72 and 66 kN.m (53 and 49 kip-ft), respectively. While the calculated cracking moment of specimen 7S15M was 9% greater than that of specimen 7G#5, its experimental cracking load was 19% greater than that of 7G#5. This is

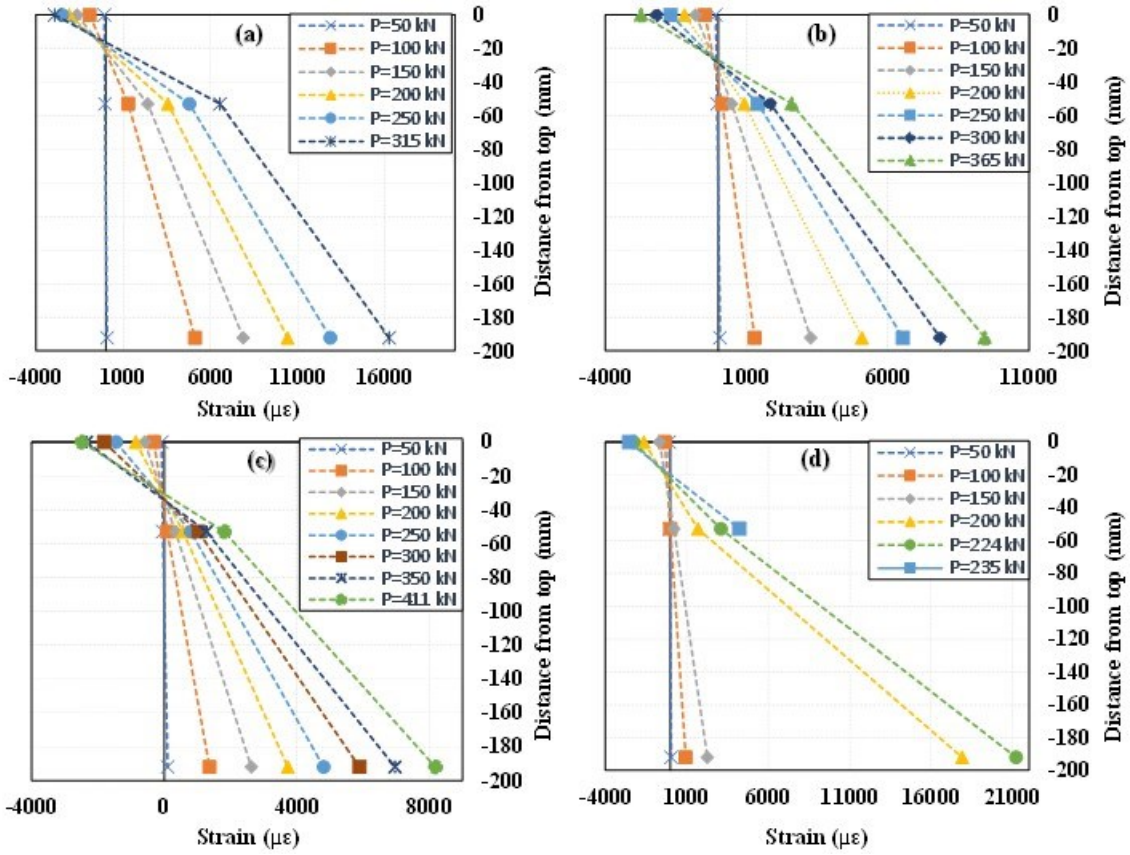

Figure 4.9 Distribution of strain over the cross section: (a) 7G#5; (b) 13G#5; (c) 13G#6; and (d) 7S15M. (Note: 1 mm = 0.0394 in.; 1 kN = 0.2248 kip.)

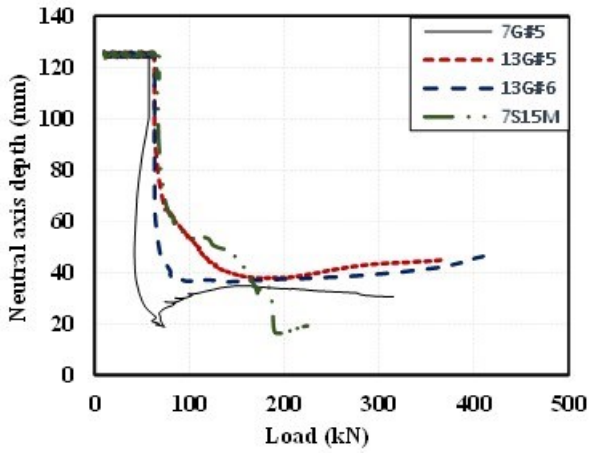

Figure 4.10 Relationship between load and neutral-axis depth. (Note: 1 mm = 0.0394 in.; 1 kN = 0.2248 kip.)

consistent with the results of Mousa et al. (2019a) and Barris et al. (2017) as they recorded 24% and 30%, respectively, higher cracking moment in steel-reinforced specimens compared to GFRP-reinforced ones with the same reinforcement details. After cracking

occurred, the stiffness of the load–deflection curve of specimen 7S15M (until yielding point) was 2.7 times greater than that of specimen 7G#5. This ratio is close to 3.1, which is the ratio of specimen 7S15M's analytical cracked section moment of inertia (I_{cr}) to that of specimen 7G#5 specimen obtained according to ACI 440.1R-15, while the ratio of axial stiffness of the steel bars to that of the GFRP bars is 3.8. Both specimens 7S15M and 7G#5 were lower the allowable crack width at service load. Specimen 7G#5 had 33% lower service load deflection compared to 7S15M, so that the deflection at service load calculated at a strain of 2000 $\mu\varepsilon$ and 1200 $\mu\varepsilon$ in specimens 7G#5 and 7S15M was 2.47 and 3.67 mm (0.097 and 0.144 in), respectively. In addition, the recorded peak load in specimen 7G#5 was 33% greater than that of specimen 7S15M, although they had the same reinforcement ratio.

4.6.2. Influence of Reinforcement Ratio, Size, and Spacing

In this study, increments in reinforcement ratio were governed by changing the bar spacing and size. Therefore, bar size and spacing are not independent parameters. Since bar size and spacing affect bond and cracking behavior regardless of the reinforcement ratio, investigating their effect is beneficial for design purposes (Ospina and Bakis 2007). The analytical cracking moment of specimens 13G#5 and 13G#6 was 69 and 66 kN·m (51 and 49 kip-ft), respectively. Although the analytical cracking moment of the GFRP-reinforced specimens ranged between 66 to 69 kN·m (49 to 51 kip-ft), specimens 13G#5 and 13G#6 had 11% greater experimental cracking load than specimen 7G#5, which can be attributed to their lower reinforcement spacing and higher axial stiffness. The post-cracking stiffness of specimens 13G#5 and 13G#6 was higher than specimens 7G#5 by 90% and 140%, respectively. The I_{cr} obtained in specimens 13G#5 and 13G#6 according to ACI 440.1R-15 were 75% and 140% higher than that of specimen 7G#5, respectively. In addition, the post-cracking stiffness of specimen 13G#6 was 26% higher than that of specimen 13G#5, while its axial stiffness and I_{cr} were 42% and 37% higher, respectively. This means that the analytical cracked moment of inertia obtained according to ACI 440.1R-15 yields good estimations for post-cracking stiffness as it accounts for both axial stiffness and compression-block depth. At a specific load of 100 kN ([22.5 kip] for example), specimens

7G#5, 13G#5, 13G#6, and 7S15M had mid-span deflections of 12.5, 5.0, 4.4, and 4.1 mm (0.49, 0.20, 0.17 and 0.16 in), respectively. At the same load level, their measured crack widths were 0.7, 0.31, 0.25, and 0.28 mm (0.028, 0.012, 0.010, and 0.011 in), respectively. This shows that deflection and crack width in GFRP-reinforced tunnel segments could be close to steel-reinforced ones by providing around 50% of the axial stiffness of steel reinforcement. The crack spacing was mainly affected by the spacing of longitudinal reinforcement, so that it was 158 mm and 115 mm ([6.2 and 4.5 in] at 75% of ultimate load), on average, in the specimens with longitudinal reinforcement spacing of 125 mm ([4.9 in] specimens 13G#5 and 13G#6) and 250 mm ([9.8 in] specimens 7G#5 and 7S15M), respectively. In the GFRP-reinforced segments, increasing the reinforcement ratio relative to specimen 7G#5 enhanced the peak load by 16% and 31% in specimens 13G#5 and 13G#6, respectively. Although all the specimens had flexural-dominant behavior, increasing the reinforcement ratio in the GFRP-reinforced specimens changed the failure mode from flexural to shear. This was mainly due to the fact that the maximum bending moment and shear force acted at the same location in the specimens. This, however, is not usually the case in real tunnel segments since the regions of the maximum bending moment and maximum shear force are different (ACI 533.5R-20).

Deformability is an important feature of FRP-RC structural elements subjected to bending loads. CAN/CSA S6-19 adopted a *J*-factor that depends on both strength and curvature at service load and ultimate condition. The following equation can be used to calculate the *J*-factor

$$J = \frac{M_{ultimate}}{M_c} \times \frac{\Psi_{ultimate}}{\Psi_c} \tag{4.1}$$

where M_c and Ψ_c are the moment and curvature at the concrete strain of 0.001, respectively, denoting the service condition. $M_{ultimate}$ and $\Psi_{ultimate}$ are the moment and curvature at ultimate load. It should be noted that the moment and curvature at ultimate load were obtained from the experimental data provided by the strain gauges by dividing the concrete compressive strain at the peak load to the obtained neutral-axis depth. Table 4.3 shows that the deformability factor for all the GFRP-reinforced specimens was equal to or

higher than 4.0, which is the minimum requirement in CAN/CSA S6-19 for rectangular sections.

4.7. Analytical Investigation

4.7.1. Flexural Strength of Segments

The specimens were subjected to bending moment and an induced axial load due to the arch geometry. It should be noted that, in a tunnel segmental ring under different loading conditions, both axial compression and tensile forces can occur. This section presents the analytical procedure to calculate the flexural strength according to ACI 440.1R-15. The flexural failure governed by concrete crushing is the preferable failure mode in FRP-RC members based on these design standards. The reinforcement ratios in all the specimens were higher than the balanced reinforcement ratio. Therefore, the analytical procedure is presented by assuming compression failure mode in a GFRP-reinforced PCTL segment. To calculate the flexural capacity of a segment with a specified axial load, the following steps are considered:

1. Assuming the neutral-axis depth of c.
2. Calculation of the longitudinal bar strain in the top and bottom mesh by assuming 0.003 as the ultimate compressive strain of concrete and a linear strain distribution over the cross section.
3. Calculation of compression and tension forces in the concrete and reinforcement. An equivalent rectangular stress block is assumed for distribution of concrete compressive strength with the parameters α_1 and β_1 as the coefficients of concrete stress ($f_c^{'}$) and neutral-axis depth, respectively. Equations 4.2 and 4.3 represent the values of α_1 and β_1.

$$\alpha_1 = 0.85 \tag{4.2}$$

$$\beta_1 = 0.85 - \left[0.05(f_c^{'} - 28)/7\right] \geq 0.65 \tag{4.3}$$

4. Check the force equilibrium and adjust the neutral-axis depth with trial and adjustment.
5. Calculate the nominal flexural capacity (M_n) with the following equation:

$$M_n = A_f' f_f' \times (d' - \frac{\beta_1 c}{2}) + A_f f_f \times (d - \frac{\beta_1 c}{2}) - P(\frac{h - \beta_1 c}{2}) \quad (4.4)$$

where h denotes the section depth and P is the induced axial load (positive for tension and negative for compression) due to arch geometry. In addition, d, A_f, and f_f are the effective depth, area, and stress of the bottom longitudinal bars, respectively; d', A_f', and f_f' denote those values for the top longitudinal bars.

4.7.2. Shear Strength of Segments

Tunnel segments are subjected to a combination of axial load, bending moment, and shear force. Therefore, predicting the shear capacity of segments is necessary for design purposes. In this section, the provisions of ACI 440.1R-15—which can be used in determining the shear capacity of PCTL segments—are presented.

ACI 440.1R-15 considers the contribution of uncracked compression block as the only shear transferring mechanism for concrete. The shear capacity of concrete (V_c) according to ACI 440.1R-15 can be calculated with Eq. 4.5

$$V_c = \frac{2}{5}\sqrt{f_c'} b_w (kd) \quad (4.5)$$

where b_w is the section width and k can be calculated with the following equation

$$k = \sqrt{2\rho_f n_f + (\rho_f n_f)^2} - \rho_f n_f \quad (4.6)$$

where ρ_f and n_f are the longitudinal reinforcement ratio and the ratio of modulus of elasticity of the longitudinal FRP bars to the concrete modulus of elasticity, respectively.

4.7.3. Crack-Width Prediction

It is necessary to control the crack width when performing the serviceability design of PCTL segments [ITAWG2-19; ACI 533.5R-20]. ACI 440.1R-15 recommends an indirect method

for controlling crack width that limits the maximum spacing of longitudinal bars using the following equation

$$S_{\max} = 1.15\frac{E_f w}{f_{fs} k_b} - 2.5c_c \le 0.92\frac{E_f w}{f_{fs} k_b} \tag{4.7}$$

where $S_{\max}$ is the maximum allowable longitudinal bar spacing (mm), w is the maximum permissible crack width (mm), f_{fs} is the service stress in the FRP bars, c_c is the clear cover, and k_b is the bond-dependent coefficient, which should conservatively be taken as 1.4 when experimental data is not available.

4.7.4. Comparison between Analytical and Experimental Results

Table 4.4 compares the experimental results with the values calculated based on the analytical procedure in ACI 440.1R-15 for flexural strength, shear strength, and crack width. In all calculations, the reduction factors were considered to be equal to 1.0. Note that the crack width was calculated indirectly with Eq. (4.7) by assuming the spacing of longitudinal bars to be 250 mm (9.8 in) in specimens 7G#5 and 125 mm (4.9 in) in specimens 13G#5 and

Table 4.4 Comparison between analytical and experimental results

Specimen ID	Flexural Strength							Shear Strength			Cracking	
	$M_{\exp.}$, kN.m§	$\varepsilon_{cu,\exp.}$	$\varepsilon_{fu,\exp.}$	$N_{\exp.}$ ¥	$M_{Theo.}/M_{\exp.}$	$\varepsilon_{fu,Theo.}$	$N_{theo.}$	$V_{\exp.}$, kN§	$V_{dem.}$, kN↓	$V_{Theo.}/V_{\exp.}$	$w_{Theo.}/w_{\exp.}$	
											2000 $\mu\varepsilon$	0.3 M_n
7G#5	215	0.00295	0.0162	67	1.04	0.0161	67	158	163	0.63	2.43	2.92
13G#5	249	0.00273	0.0094	77	1.19	0.0119	91	183	219	0.72	1.37	1.35
13G#6	281	0.00251	0.0081	87	1.19	0.0097	102	206	244	0.73	2.19	2.12
7S15M*	161	0.00252	0.0212	50	1.04	0.0162	50	-	-	-	-	-

* The flexural strength analytical values reported for specimen 7S15M were obtained as in ACI 318 (2019) considering the ultimate strength of the steel bars.
§ Obtained according to the experimental peak load.
↓ Calculated based on $M_{Theo.}$.
¥ Axial load induced in the specimens at mid-span.
Notes: 1 kN·m = 0.7376 kip-ft; 1 kN = 0.225 kip.

13G#6. The predicted theoretical flexural strength of specimen 7G#5 was 4% greater than the experimental values. This might be due to the slightly lower ultimate compressive strain in this specimen compared to what is ACI 440.1R-15 recommends. As specimens 13G#5 and 13G#6 failed prior to their ultimate compressive strength, the theoretical predicted value was on average 19% higher than the experimental ones. This can be attributed to the fact that the nominal load capacity of the tested specimens was controlled by a combination of flexural and shear loads. ACI 440.1R-15 provided conservative predictions of the shear strengths; on average, the experimental to the predicted value was equal to 1.3. This is rational as this standard only considers the contribution of the uncracked compression block as the shear-transferring mechanism. Comparing the theoretical shear demand ($V_{dem.}$) with the calculated shear capacity indicates that the design of the GFRP-reinforced specimens in this study was governed by shear capacity based on ACI 440.1R-15. According to Table 4.4, ACI 440.1R-15 overestimated the crack width by 165%, 35%, and 115% in specimens 7G#5, 13G#5, and 13G#6, respectively, by using k_b equal to 1.4. Using the suggested value of 0.8 for k_b according to CAN/CSA S6-19 yielded more accurate predictions of crack width.

CONCLUSIONS

This paper reported on an experimental and analytical study to investigate the effect of reinforcement type and ratio on the behavior of GFRP-reinforced precast concrete tunnel lining segments under bending load. The following conclusions may be drawn:

1. Concrete-crushing failure mode was observed in the GFRP-reinforced specimen with the reinforcement ratio 40% higher than the balanced ratio. Increasing the reinforcement ratio in the GFRP-reinforced specimens changed the failure mode to diagonal-tension failure. Nevertheless, flexural-dominant behavior was observed in all the GFRP-reinforced specimens up to peak load. The steel-reinforced specimen experienced concrete crushing after yielding of the steel reinforcement.
2. The GFRP-reinforced specimen 7G#5 had 33% higher load-carrying capacity than its steel-reinforced counterpart (7SM15). On the other hand, the GFRP-reinforced specimen had 33% lower deflection at its specified service load compared to the steel-reinforced specimen. Increasing the reinforcement ratio by 85% and 165% in the GFRP-reinforced

specimen enhanced the load-carrying capacity by 16% and 30%, respectively, and improved the post-cracking stiffness by 90% and 140%, respectively.

3. The GFRP-reinforced specimens satisfied the crack-width requirement in CAN/CSA S6-19 at service load. In addition, the deflection and crack width in GFRP-reinforced tunnel segments could be close to that of steel-reinforced ones by providing around 50% of the axial stiffness of the steel reinforcement.
4. ACI 440.1R-15 provided conservative predictions of the nominal capacity of the tested specimens as controlled by the shear design provisions and overestimated the crack width by 106% on average.
5. The structural performance of the GFRP-reinforced PCTL segments was satisfactory in terms of crack width and propagation, deflection, and load-carrying capacity. Replacement steel reinforcement with GFRP reinforcement in PCTL segments can effectively eliminate the risk of corrosion while satisfying the structural requirements.
6. The experimental evidence and outcomes of this investigation demonstrate the effectiveness of the curvilinear GFRP bars as reinforcement for PCTL segments. The promising results presented herein open the way for the use of PCTL segments reinforced with the developed curvilinear GFRP bars in major tunneling applications.

CHAPTER 5 EXPERIMENTAL AND ANALYTICAL STUDY ON PRECAST HIGH-STRENGTH CONCRETE TUNNEL LINING SEGMENTS REINFORCED WITH GFRP BARS

Foreword

Authors and Affiliation:

Seyed Mohammad Hosseini: Ph. D. Candidate, Department of Civil Engineering, University of Sherbrooke, Sherbrooke, Quebec, Canada, J1K 2R1

Salaheldin Mousa: Postdoctoral fellow, Department of Civil Engineering, University of Sherbrooke, Sherbrooke, Quebec, Canada, J1K 2R1

Hamdy M. Mohamed: Research associate and lecturer, Department of Civil Engineering, University of Sherbrooke, Sherbrooke, Quebec, Canada, J1K 2R1.

Abolfazl Eslami: Former postdoctoral fellow, Department of Civil Engineering, University of Sherbrooke, Sherbrooke, Quebec, Canada, J1K 2R1

Brahim Benmokrane: Professor, Department of Civil Engineering, University of Sherbrooke, Sherbrooke, Quebec, Canada, J1K 2R1.

Journal title: Journal of Composites for Construction (ASCE)

Paper status: Final version, published online in August 2022.

Contribution in thesis:

In this chapter, the effect of employing HSC on the performance of GFRP-reinforced PCTL segments was investigated using experimental and analytical investigations.

5.1. Abstract

Replacing steel reinforcement with glass fiber-reinforced polymer (GFRP) reinforcement is an effective solution to avoid the corrosion problem in precast-concrete tunnel-lining (PCTL) segments. In addition, using high-strength concrete (HSC) can improve the durability of concrete in the harsh environment of tunnels. This study pioneers in investigating the structural performance of GFRP-reinforced PCTL segments constructed with HSC by testing four full-scale specimens measuring 3100 mm in length, 1500 mm in width, and 250 mm in thickness under three-point bending load. The investigated parameters included concrete compressive strength (normal-strength concrete [NSC] and HSC), reinforcement ratio (0.48% and 0.90%), and tie configuration (closed ties with U-shaped ties). The results are presented and discussed in terms of cracking behavior, failure mechanism, deflection behavior, strain in reinforcement and concrete, ductility, and deformability. An analytical investigation was carried out to evaluate and modify the existing design provisions (ACI 440.1R-15, CAN/CSA S806-12, R2017, CAN/CSA S6-19, and AASHTO-18) for use in predicting the shear and flexural strength of GFRP-reinforced HSC PCTL segments. The results indicate that using HSC improves the flexural and shear strength of GFRP-reinforced PCTL segments, while it had a minimal effect on the post-cracking stiffness and cracking behavior of the specimens. According to the analytical investigation, the procedure presented to modify ACI 440.1R-15 can be used to predict the flexural capacity of GFRP-reinforced HSC PCTL segments with high accuracy. In addition, CAN/CSA S806-12, R2017 predicted the shear capacity of HSC-GFRP-reinforced PCTL segments with an error of less than 7.0%.

Keywords: High-strength concrete (HSC); glass fiber-reinforced polymer (GFRP) bars; precast concrete tunnel-lining (PCTL) segments; structural performance; flexural and shear strength; design codes & standards.

5.2. Introduction

When a tunnel is mechanically excavated with a tunnel boring machine (TBM), precast concrete tunnel-lining (PCTL) segments are installed to support the TBM and resist the temporary and permanent loads. Tunnels are designed for a service life of more than 100 years due to the key role of underground tunnels in today's world (ACI 544.7R-16). The durability of a TBM-excavated tunnel is directly related to the durability of its PCTL segments. Corrosion of conventional steel reinforcement induced by chloride attack, carbonation and stray current in railway and subway tunnels is the main degradation mechanism in reinforced concrete (RC) tunnel segments (ACI 533.5R-20). An effective approach to dealing with the corrosion problem in PCTL segments is to replace steel reinforcement with noncorroding glass fiber-reinforced polymer (GFRP) reinforcement (Caratelli et al. 2016; Caratelli et al. 2017; Spagnuolo et al. 2017). Degradation of the concrete induced by sulfate, acid, and frost attacks is another important degradation mechanism in tunnels (ACI 533.5R-20). Using high-strength concrete (HSC) can effectively improve concrete durability in resisting such attacks (de Almeida 1991; ACI 544.7R-16; ACI 533.5R-20; Mostofinejad et al. 2021). Consequently, a hybrid use of GFRP reinforcement and HSC seems a viable solution to improve durability of PCTL segments. Repairing or strengthening degraded tunnel segments is extremely costly and associated with interruptions in service. Although using GFRP-reinforced HSC PCTL segments might cost more initially than steel-reinforced segments made with NSC, their use can secure the serviceability of tunnels for a long period of time.

PCTL segments are subjected to bending moments, axial loads, and shear forces (ITA 2019) as a result of permanent loads induced by soil and groundwater as well as temporary loads induced during the fabrication, transportation, and construction stages. The cracking behavior, deflection behavior, failure mechanism, flexural strength, and shear strength of PCTL segments must be assessed before field application. To the best of the authors' knowledge, there is nothing in the literature about the behavior of GFRP-reinforced HSC PCTL segments. The literature does, however, contain some studies on the behavior of GFRP-reinforced HSC beams and slabs subjected to bending load (Theriault and

Benmokrane 1998; Ashour 2000; Gross et al. 2003; El-Sayed et al. 2006; El-Nemr et al. 2013; Goldston et al. 2017; Abdelkarim et al. 2019). The general consensus is that increasing the concrete compressive strength enhances the flexural and shear strength of GFRP-reinforced members. The literature contains conflicting points of view on the effect of using HSC on the crack width and spacing in GFRP-reinforced concrete beams. Theriault and Benmokrane (1998) reported negligible effects of concrete strength on crack spacing, but also reported wider cracks for the same applied moment for higher strength concrete citing higher releasing stress at crack initiation, leading to the formation of wider cracks. In contrast, El-Nemr et al. (2013) and Abdelkarim et al. (2019) reported narrower cracks with closer spacing from increasing the concrete compressive strength. These contradictions in the literature can be accounted for by the spacing between longitudinal bars, reinforcement ratio, and bond strength (Ospina and Bakis 2007; Mousa et al. 2019a), which are the primary factors affecting crack width and spacing. According to design codes and guidelines in ACI 440.1R-15, CAN/CSA S806-12, R2017, and CAN/CSA S6-19, increasing concrete compressive strength enhances the bond strength between GFRP bars and concrete. Some studies in the literature, however, reported minimal effect of concrete compressive strength on the bond performance of GFRP bars (Esfahani et al. 2013; Basaran and Kalkan 2020). It can be inferred that the effect of concrete compressive strength on crack width and spacing in GFRP-RC flexural members is unclear and depends on how concrete compressive strength affects the bond strength of GFRP bars to concrete, which has not yet been definitely described in the literature. Another point of view states that cracks were not narrower when HSC was used due to higher initial releasing stress. In contrast, in the cases in which the bond strength of GFRP reinforcement improved with the use of HSC, the cracks were narrower but greater in number. Theoretically, using concrete with a higher strength can improve the post-cracking stiffness of the flexural elements reinforced with GFRP bars. Nevertheless, there are contradictions in the literature regarding how higher-strength concrete might improve the post-cracking stiffness of GFRP-RC beams. The results of Theriault and Benmokrane (1998), Ashour (2000), Goldston et al. (2017), and Goldston et al. (2019) indicated that the effect of compressive strength on the post-cracking stiffness is marginal, especially at smaller reinforcement ratios. In contrast, El-Nemr et al. (2013) and

Abdelkarim et al. (2019) reported a higher post-cracking stiffness in HSC beams compared to NSC beams, particularly in those with larger reinforcement ratios. Factors other than concrete compressive strength that affect the behavior of GFRP-reinforced HSC PCTL segments must be assessed. Reinforcement ratio and axial stiffness are known to be the key factors in the serviceability, flexural strength, and shear capacity of GFRP-reinforced elements subjected to bending load. Increasing the reinforcement ratio enhances the post-cracking stiffness and decreases the crack width in GFRP-reinforced flexural elements (Chang and Seo 2012; El-Nemr et al. 2013; Mousa et al. 2019a,b). In addition, the flexural and shear strength of GFRP-RC elements effectively improve by increasing the reinforcement ratio (El-Nemr et al. 2013; Alguhi and Tomlinson 2021). Reinforcement configuration is known to be a parameter affecting the behavior of GFRP-reinforced PCTL segments (Caratelli et al. 2017). As PCTL segments are normally assembled with automated systems, reinforcement configuration can also be determinative in production feasibility and cost (Heilegger and Beil 2020).

Replacing conventional steel reinforcement with GFRP bars is a viable solution to avoid the corrosion problem in PCTL segments and to take advantage of the unique features of GFRP bars in tunneling. In addition, using HSC is recommended to improve the durability performance of PCTL segments. Moreover, to the best of the authors' knowledge, the structural behavior of GFRP-reinforced HSC PCTL segments has not been reported on in the literature. This investigation is a part of an extensive research program on the behavior of GFRP-reinforced PCTL segments under various loading conditions, which was carried out at the University of Sherbrooke. This study investigated the performance of GFRP-reinforced PCTL segments made with HSC under bending load by evaluating the parameters of reinforcement ratio, tie configuration, and concrete strength. In addition, the paper examines the validity of the available design provisions in codes and guidelines in predicting the nominal flexural and shear capacity of GFRP-reinforced PCTL segments and to propose some modifications for HSC segments.

5.3. Experimental Program

5.3.1. Test Specimens

Four full-scale tunnel segment specimens were designed, fabricated, and tested under three-point loading. The original tunnel considered in this study was a metro tunnel with an internal diameter of 6500 mm and external diameter of 7000 mm, as shown in Fig. 4.1a. A full tunnel ring consists of seven segments. This study focused on segment number two—parallelogram in shape—measuring 1500 mm in width and 250 mm in thickness with an arc length of 3100 mm (Fig. 5.1a). Wooden formwork was designed for casting the specimens (Fig. 5.1b). The specimens were demolded (Fig. 5.1c) and cured for seven days after casting. Longitudinal reinforcement in each specimen was provided as curvilinear GFRP bars in the top and bottom meshes anchored with U-shaped end-anchorage bars (Fig. 5.2a). Two different configurations of closed ties and U-shaped ties were used as transverse reinforcement (Fig. 5.2b). The test parameters were concrete strength (NSC and HSC), longitudinal reinforcement ratio (0.48% and 0.9%), and tie configuration (closed ties and U-shaped ties). It should be noted that the reinforcement ratios were provided by using two different longitudinal bar spacings (125 and 250 mm). Table 5.1 and Fig. 5.3 represent the test matrix and reinforcement detail of the specimens, respectively. The first term in the specimen designation denotes the number of longitudinal bars. The second term—G#5—indicates the type and size of longitudinal bars (#5 GFRP). The letter H indicates specimens cast with HSC. The letter U indicates that U-shaped ties were used in the specimen. Table 5.1 compares the reinforcement ratio for each specimen with balanced reinforcement ratio calculated according to ACI 440.1R-15 and CAN/CSA S806-12, R2017, considering both top and bottom meshes. Theoretically, the specimens were designed to undergo failure in the compression control (CC) mode.

5.3.2. Material Properties

5.3.2.1. Concrete

Table 5.1 Test matrix and specimen details

Specimen ID	Type of Concrete	Longitudinal Reinforcement	ρ_l (%)	ρ_l / ρ_b		Tie Configuration	Transverse Reinforcement
				ACI 440.1R-15	CSA S806-12		
7G#5	NSC	7 #5 bars	0.48	1.7	1.4	Closed ties	#4 @ 200 mm
7G#5H	HSC	7 #5 bars	0.48	1.1	1.0	Closed ties	#4 @ 200 mm
13G#5H	HSC	13 #5 bars	0.90	1.9	1.7	Closed ties	#4 @ 200 mm
7G#5HU	HSC	7 #5 bars	0.48	1.1	1.0	U-shaped ties	#4 @ 200 mm

Table 5.2 Concrete mix design for NSC and HSC

Type of Concrete	Cement (kg/m^3)	Sand (kg/m^3)	Limestone 5/10 (kg/m^3)	Superplasticizer (mL/ m^3)	Air-Entrainment Agent (mL/ m^3)	Water* (L/m^3)
NSC	450	615	1015	4400-4500 (V*)	140	170-190 (V)
HSC	475	778	800	7000	170	135-150 (V)

*The values varied for each batch between the mentioned values to achieve the target slump.

Two self-compacting concrete (SCC) mixes were designed to achieve 28-day concrete compressive strength of 40 MPa for NSC and 75 MPa for HSC with the target slump (Table 5.2). Concrete compressive strength at the test date was obtained as the average compression test results of three 100x200 mm cylindrical concrete specimens. Actual concrete compressive strengths at the test date were 48 MPa and 88 ± 2 MPa in the specimens cast with NSC and HSC, respectively.

5.3.2.2. Reinforcement

The GFRP reinforcing bars in this study were of two different sizes of Grade II sand-coated bars: #5 (15 mm) as the longitudinal and U-shaped end-anchorage bars and #4 (13 mm) as transverse ties. The bottom and top longitudinal reinforcement bars were fabricated with a radius of 3,305 and 3,445 mm, respectively. Pultrall Inc. (Thetford Mines, Quebec, Canada) has developed a novel manufacturing method to produce the curvilinear bars with a desired curvature. Tensile testing according to ASTM D7205-21 was conducted (see Table 5.3) to determine the mechanical properties of the bars, including tensile strength, modulus of elasticity, and ultimate tensile strain (reported values are based on nominal cross-sectional

area). The reported properties of the U-shaped end-anchorage bars and transverse ties were obtained by testing straight bars manufactured with the same process as the bent bars. Curvilinear bars with a radius of 3,305 mm (the same as the bottom longitudinal bars) were straightened through the test fixture and then directly subjected to tensile load in accordance with ASTM D7205-21 to obtain the values reported in Table 5.3.

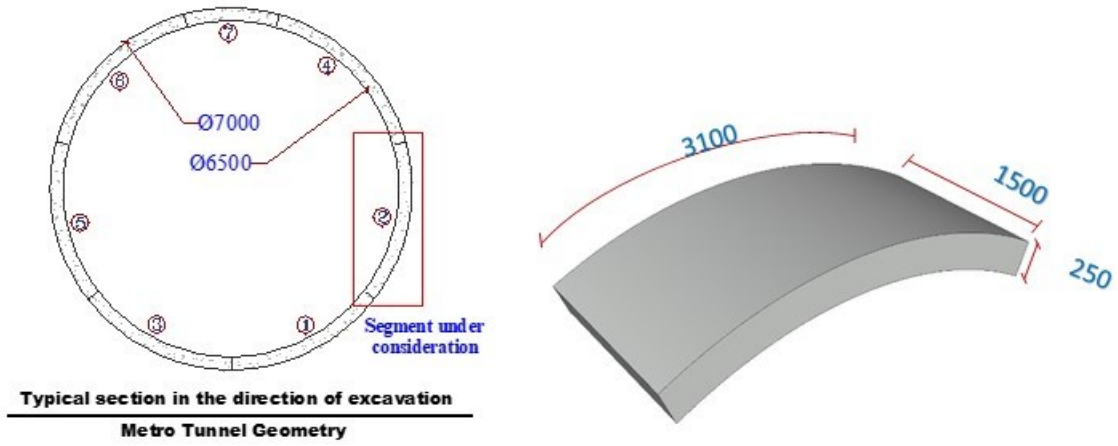

(a)

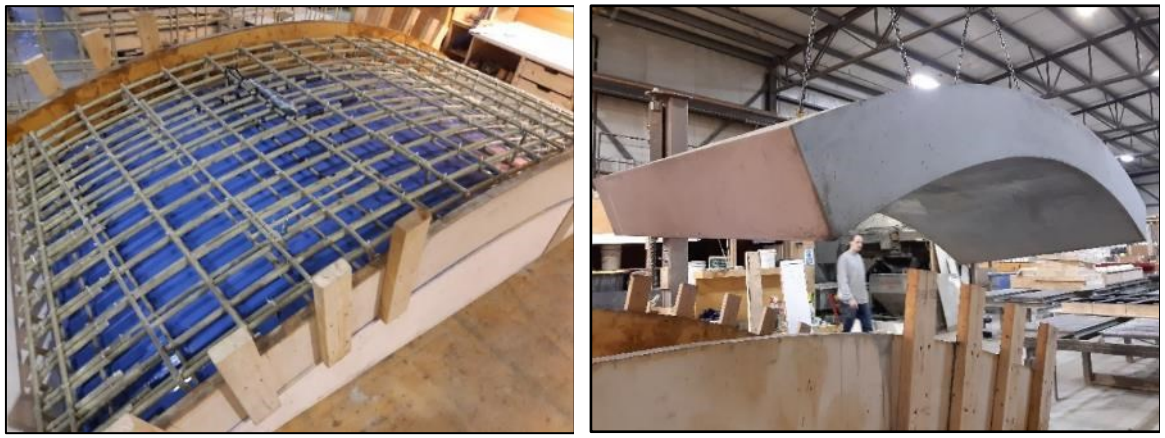

(b) (c)

Figure 5.1 (a) Geometry of tunnel segment specimens (dimensions in mm); (b) fabricated cage inside formwork (13G#5H); (c) specimen demolding.

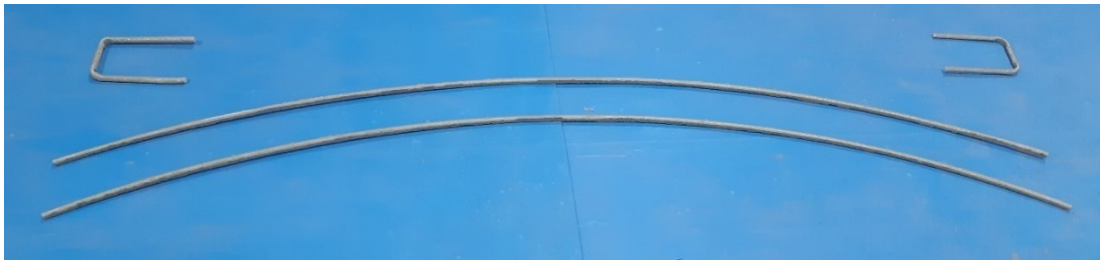

(a)

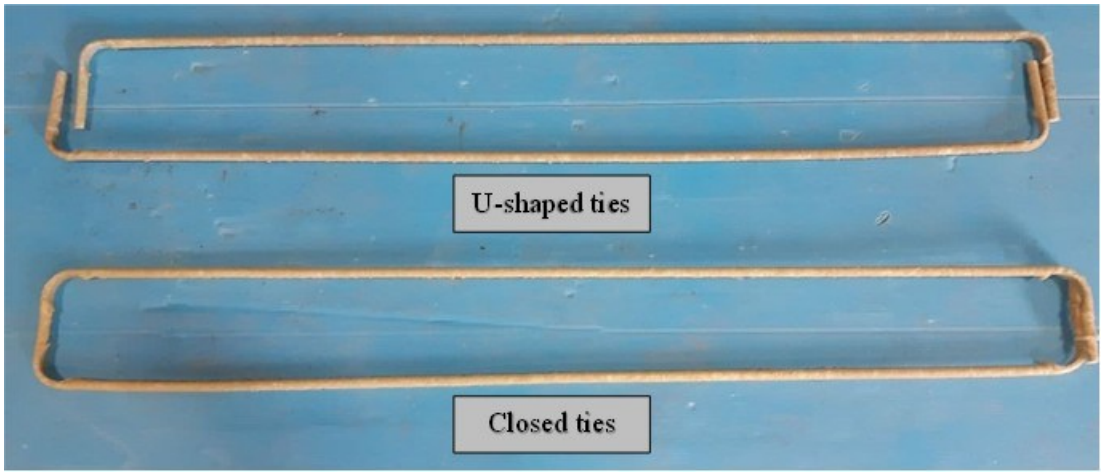

(b)

Figure 5.2 (a) Curvilinear GFRP bars and U-shaped end-anchorage bars; and (b) U-shaped and closed ties.

Table 5.3 Mechanical properties of the reinforcement

Reinforcement Type	Bar Size	Bar Diameter, mm	Nominal Cross-Sectional Area, mm^2	Cross-Sectional Area, mm^2 (Immersion tests)	Modulus of Elasticity, GPa	Tensile Strength, MPa	Tensile Strain, %
Curvilinear GFRP bars	#5	15.0	199	214	55.1 ± 1.25	1115 ± 60	2.0 ± 0.1
U-shaped GFRP bars*	#5	15.0	199	240	53.5 ± 1.1	1,283 ± 42	2.4 ± 0.1
U-shaped and closed GFRP ties*	#4	13.0	129	146	55.6 ± 1.6	1,248 ± 74	2.2 ± 0.1

* The reported properties are those obtained from the straight bars manufactured according to the same process as the bent bars.

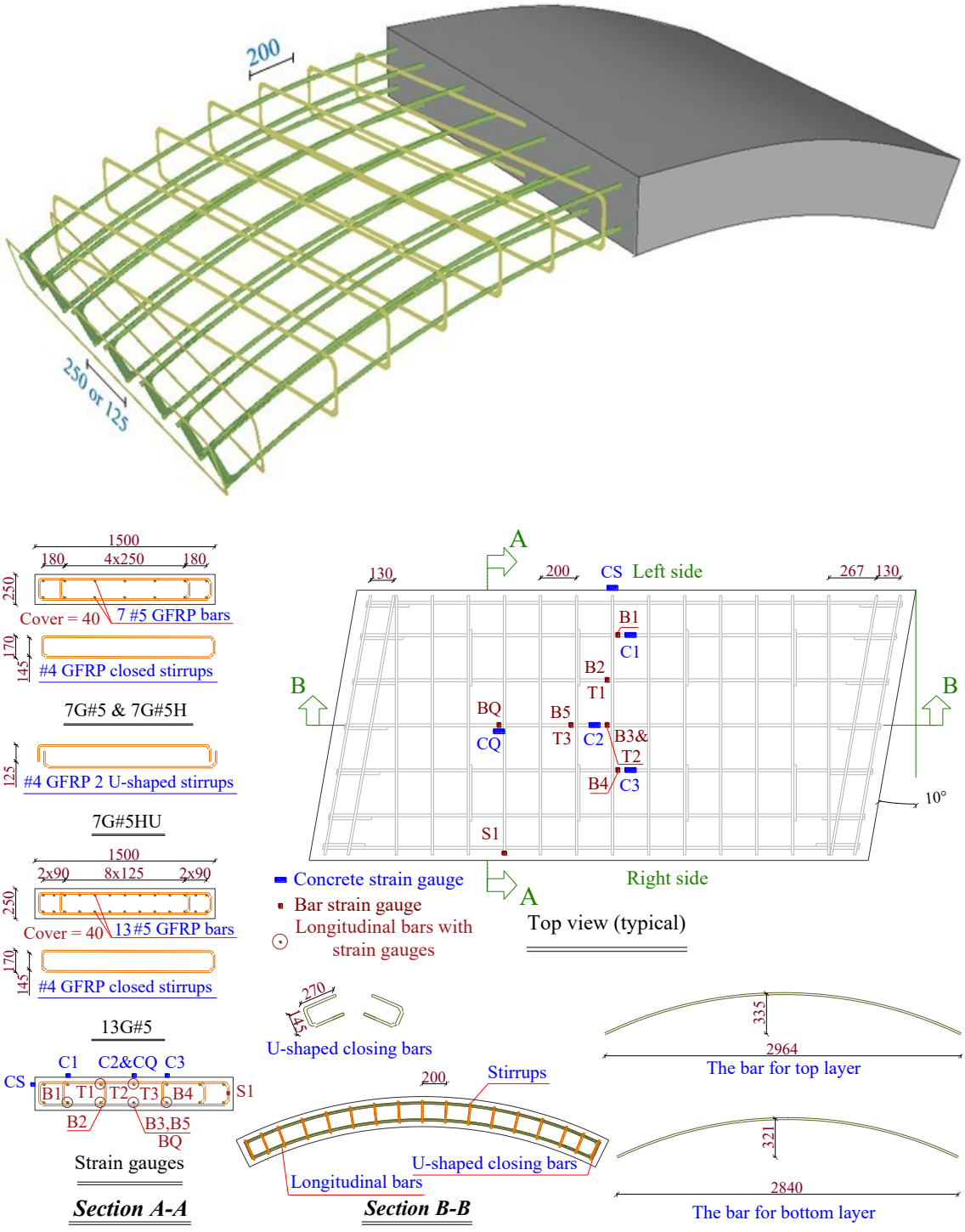

Figure 5.3 Reinforcement details of the specimens and strain-gauge locations (dimensions are in mm).

5.3.3. Instrumentation

Ten and six strain gauges with a gauge length of 10 and 60 mm were used to record the strains in the reinforcement and concrete, respectively. Figure 5.3 identifies and provides the location of the strain gauges. To obtain the strain profile, strain gauges were distributed at mid-span, 200 mm apart from mid-span, and quarter-span. The alphanumeric labels used for identifying the strain gauges are B, T, C, and S, denoting the strain gauges installed on the bottom and top longitudinal bars, concrete surface, and transverse ties, respectively. The letter Q denotes the quarter span, while CS indicates the concrete strain gauge installed on the side of the specimen 60 mm below the top of the specimen. Three linear potentiometers (LPOTs) were distributed along the width of the specimen to uniformly record the deflection at mid-span during the test.

5.3.4. Test Setup

The tunnel segment specimens were monotonically loaded under three-point bending load (Fig. 5.4). Supports were cylindrical in shape and covered with Teflon sheets, to allow free rotation and movement of the segment during the test. By minimizing friction between the segment and the supports, the test setup became a determined system capable of elucidating the relationship between applied load and internal forces. The load was applied to the specimen with a 11,400 kN MTS testing machine with a displacement-control rate of 0.8 mm/min. The tests were performed at the Canada Foundation of Innovation (CFI) laboratory located at the University of Sherbrooke.

5.4. Test Results and Observations

5.4.1. General behavior, cracking, and failure mode

During the early stage of loading, the first flexural crack formed beneath the spreader beam at an average load of 57 and 67 kN in the NSC and HSC specimens, respectively. As the load increased, new flexural cracks initiated, and existing cracks increased in depth and width. After the flexural cracks had stabilized, the combination of flexural and shear stresses

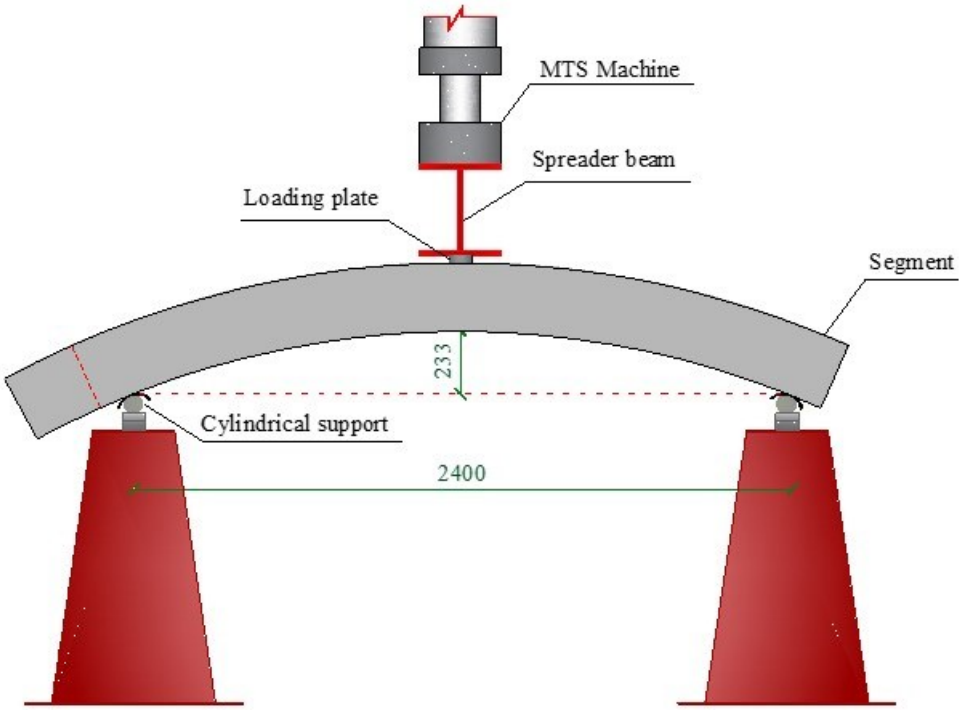

Figure 5.4 Test setup.

led to inclination of flexural cracks towards the applied load location. Shear cracks then appeared as an extension of the inclined part of the flexural cracks at a load of 255, 289, 377, and 297 kN, corresponding to 80%, 80%, 98%, 88% of the peak load in 7G#5, 7G#5H, 13G#5H, and 7G#5HU, respectively. As the load increased, horizontal cracks developed around the spreader beam, and the specimens experienced concrete spalling, leading to a load reduction. The load reduction in specimens 7G#5H and 7G#5HU after concrete spalling was almost 50% greater than that of 7G#5, which can be attributed to the brittle behavior of HSC compared to NSC. After the cover of 7G#5, 7G#5H, and 7G#5HU spalled, load gradually increased until complete concrete crushing occurred. In contrast, after the cover of 13G#5H spalled, the compression block lost its ability to provide shear capacity, and the specimen failed due to widening of a diagonal shear crack, indicating diagonal tension failure. The inclination angle of the shear cracks in this specimen was almost 45° and 65° on the left and right sides, respectively. Figures 5.5 and 5.6 show the cracking pattern of the specimens at different loading stages as well as their failure modes. After unloading, the

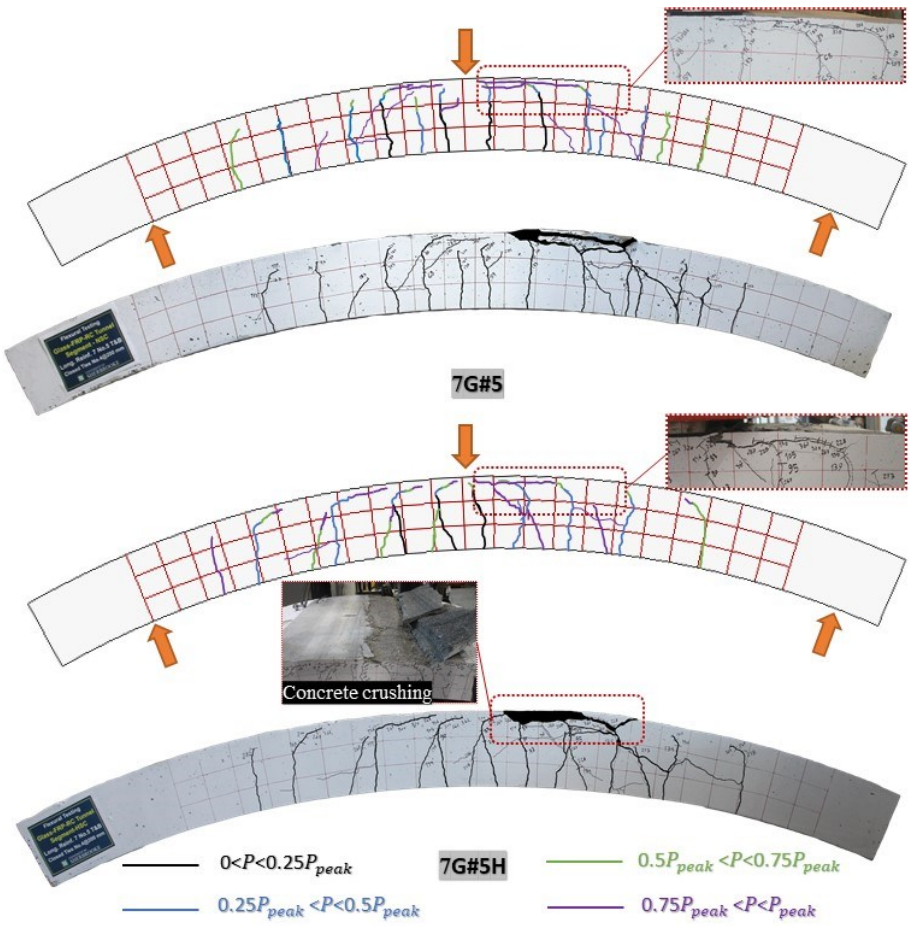

Figure 5.5 Failure modes and crack patterns of specimens 7G#5 and 7G#5H.

specimens recovered most of their deflection, which could be beneficial for a PCTL segment subjected to static loading.

Table 5.4 reports the concrete compressive strength at the test date, cracking load, peak load, mid-span deflection at peak load, and failure mode. In the literature, the service load of GFRP-RC flexural elements were defined using two reference points: (1) load corresponding to strain of 2000 $\mu\varepsilon$ in the tensile reinforcement (ISIS 2001) and (2) load corresponding to 30% of peak load (Bischoff et al. 2009). As the former yields more reasonable results for the experimental service moment (El-Nemr et al. 2018; Mousa et al. 2019b), it was selected as the service load in this study. Table 5.4 lists the crack width of the specimens at this defined service load, which was around 60 kN for 7G#5, 7G#5H, and 7G#5HU and 90 kN for 13G#5H. As shown in Table 5.4, service load crack width was 0.35 mm for 7G#5, 0.3

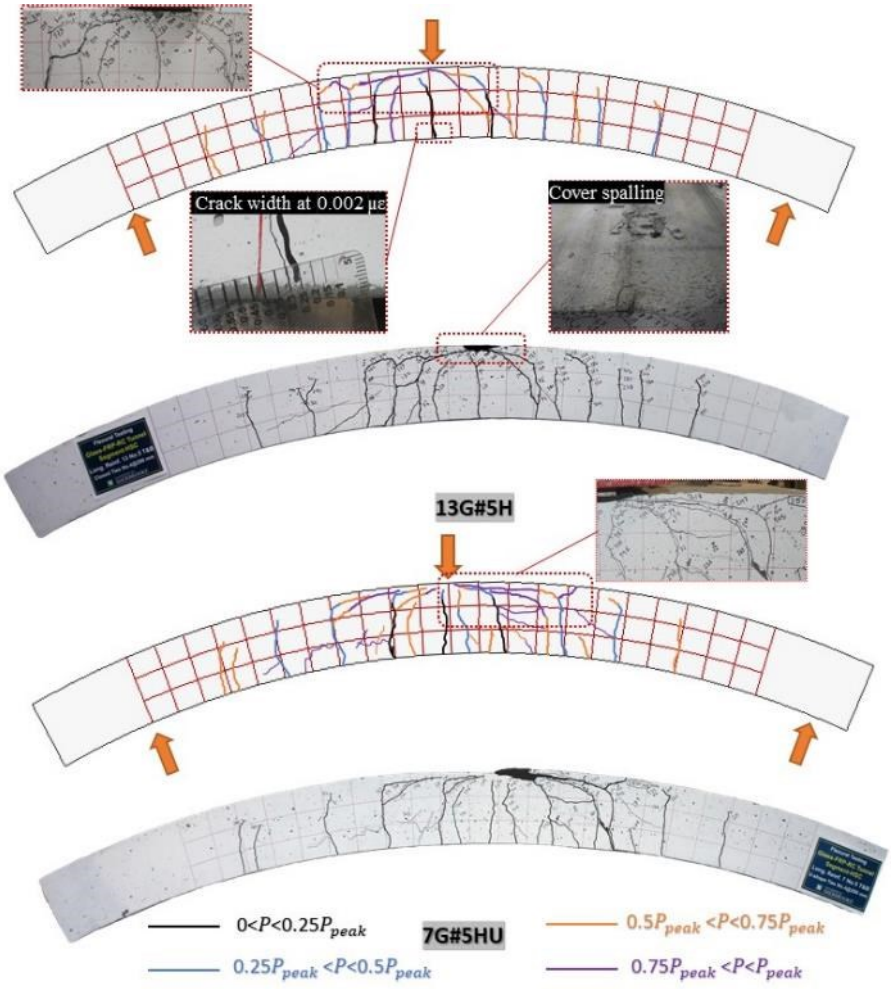

Figure 5.6 Failure modes and crack patterns of specimens 13G#5 and 7G#5HU.

Table 5.4 Experimental results, ductility, and deformability

ID	f_c', MPa	P_{cr}, kN	P_{peak}, kN	δ_{peak}, mm	Failure Mode*	Maximum Crack Width at Service Load (mm)	Deflection at Service Load (mm)	Curvature ψ, $1/d$ at P_{peak}	Ductility, μ_e	Deformability	
										J	J_{VG}
7G#5	48	57	315	64.6	CC	0.35	2.47	0.020	2.2	9.4	15.1
7G#5H	86	73	370	69.4	CC	0.4	2.23	0.025	2.4	6.6	17.6
13G#5H	90	66	385	57.4	CC+DT	0.3	3.84	0.016	1.5	5.4	8.5
7G#5HU	87	61	336	67.4	CC	0.4	2.33	0.023	2.5	5.5	13.3

* CC is concrete crushing and DT is diagonal tension.

mm for 13G#5H, and 0.4 mm for 7G#5H and 7G#5HU, which, on average, is 30% lower than the 0.5 mm limit in CAN/CSA S6-19 for members subjected to harsh environments. Average crack spacing at the middle third of the specimens at 25% of peak load was 180 mm for 7G#5 and 200 mm for 7G#5H, 13G#5H, and 7G#5HU. The spacing reduced to 145, 180, 150, and 170 mm, respectively, at 75% of the peak load.

5.4.2. Load-deflection relationships

Figure 5.7 presents the relationship between applied load and mid-span deflection. The behavior of the specimens can be described by the three stages of pre-cracking, post-cracking and post-peak as follows. In the pre-cracking stage, linear behavior was observed. The pre-cracking stiffness of the specimens was 57, 67, 64, and 72 kN/mm for 7G#5, 7G#5H, 13G#5H, and 7G#5HU, respectively, which denotes 19% greater average pre-cracking stiffness in the specimens from HSC than from NSC. As the span length and sectional geometry of the specimens were the same, the pre-cracking stiffness can be related to concrete modulus of elasticity. Considering $4700\sqrt{f_c'}$ as the modulus elasticity of the NSC and HSC concretes according to ACI 318-19 yields 34% higher analytical pre-cracking stiffness in HSC specimens. In contrast, considering $3320\sqrt{f_c'}+6900$ as the modulus of elasticity of HSC according to ACI 363R-10 yields 17% greater analytical pre-cracking stiffness which is close to the experimental value.

After crack formation, the temporary load drop was more pronounced in 7G#5H and 7G#5HU by 23% than in 7G#5 which can be attributed to the greater released energy upon cracking in HSC (Theriault and Benmokrane 1998). Increasing the reinforcement ratio resulted in 13G#5H having a 90% lower load reduction after crack formation than 7G#5H. Note that load reduction after crack formation is mainly attributed to the displacement-controlled loading, although field loading conditions for tunnel segments is more similar to a load-controlled approach. Test results of GFRP-reinforced flexural elements confirm that the load-controlled approach does not produce load reductions after crack formation (Theriault and Benmokrane 1998; Habeeb and Ashour 2008; Lau and Pam 2010). The

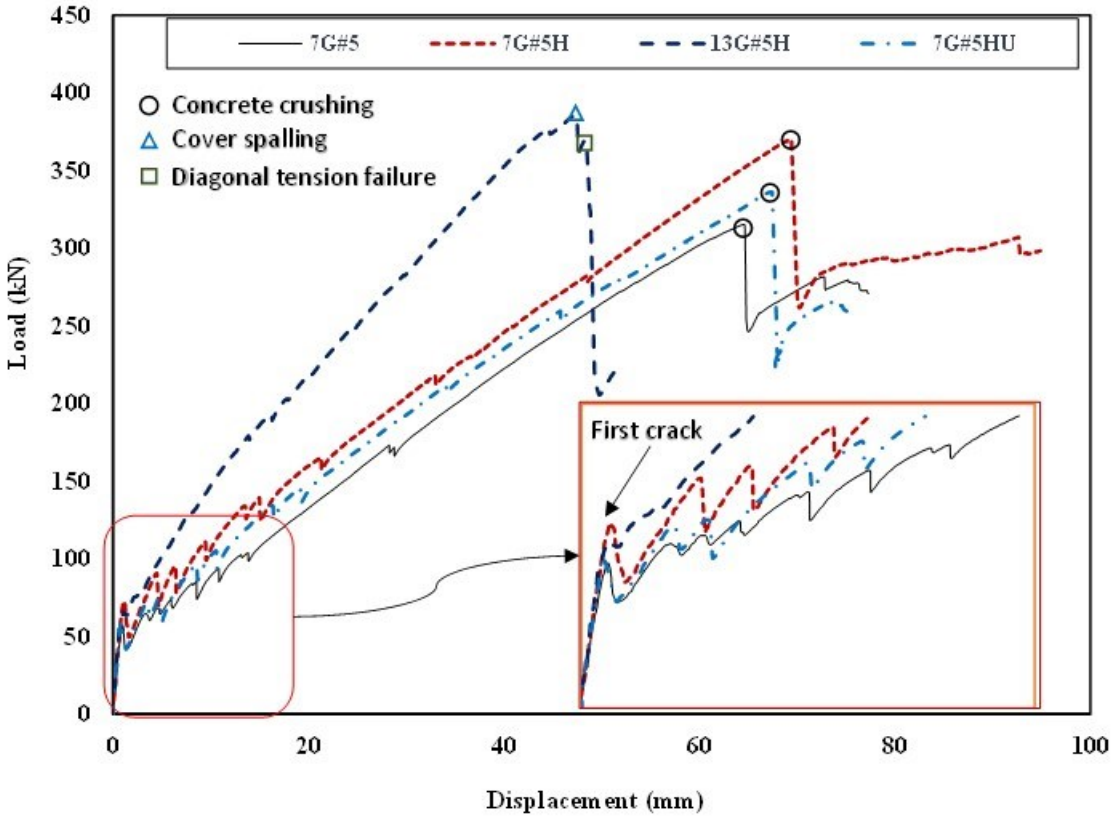

Figure 5.7 Load–deflection diagram of the tested specimens.

overall post-cracking load–deflection relationship was almost linear. Load reduction after each crack, however, caused some deviation in the load–deflection curve of specimens, especially up to approximately 50% of peak load in 7G#5, 7G#5H, and 7G#5HU. The average post-cracking stiffness of 7G#5, 7G#5H, 13G#5, and 7G#5HU was 4.06, 4.35, 7.32, and 4.15 kN/mm, respectively. Table 5.4 reports the service-load deflection. According to ACI 533.5R-20, the recommendations of any relevant design standards, guidelines, and project specifications can be used for allowable deflection of a segmental ring at the service stage. CAN/CSA S806-12, R2017 limits the deflection to $l/480$ (l is the span length) for members attached to nonstructural elements likely to be damaged by large deformations, while the *Austrian Society for Concrete and Construction* (2011) limits deformations to 15 mm for tunnels with diameter of 8 m or greater. Reported deflection at service stage was an average of 2.35±0.12 mm in 7G#5, 7G#5H, and 7G#5HU, and 3.84 mm in 13G#5H which had an approximately 50% larger service load that the other specimens with smaller reinforcement ratios. The recorded deflection at 60 kN (the service-load level in 7G#5,

7G#5H, and 7G#5HU) was, on average, 66% lower in 13G#5H than in the other specimens. According to ACI 440.1R-15, long-term deflection of an FRP-reinforced member can be obtained by multiplying the immediate deflection from sustained load by 0.6ξ, where ξ is the time-dependent factor that should be considered equal to 2 for the duration of 60 months or greater. Considering the sustained load to be the applied load during testing, long-term deflection of specimens 7G#5, 7G#5H, and 7G#5HU was 55% and 84% smaller on average than the specified allowable deflection in CAN/CSA S806-12, R2017 and *Austrian Society for Concrete and Construction* (2011), respectively. The calculated long-term service deflection of 13G#5H was 30% and 74% smaller than the allowable deflection in CAN/CSA S806-12, R2017 and *Austrian Society for Concrete and Construction* (2011). The expected deflection in GFRP-reinforced PCTL segments under actual loading and boundary conditions can be much smaller than the deflection determined from the test setup in this study because: (1) specimen ends in this study were free to move and rotate, but a segment in a segmental ring is supported by adjacent segments; and (2) a segment under actual conditions is subjected to distributed load in different directions, which results in a lower mid-span deflection (ACI 533.5R-20). The load and boundary conditions in this study appear to be the worst case scenario for controlling deflection. GFRP-reinforced PCTL segments should be capable of meeting deflection limits in field applications if the longitudinal strain in the tensile bars does not exceed 2000 $\mu\varepsilon$ under service load. As a tunnel ring is a multiple-joint structure and the geometry might differ in different applications, there is still need for an analytical procedure to estimate the deflection of GFRP-reinforced PCTL segments under field load and boundary conditions, which exceeds the scope of this study.

Specimens 7G#5, 7G#5H, and 7G#5HU experienced load reduction after concrete crushing. These specimens began to retrieve their load-carrying capacity with reduced stiffness. The second load reduction occurred when concrete crushing became more severe. Widening of shear cracks after peak load had a negative effect on load-carrying capacity. Specimen 7G#5H showed a longer post-peak ascending branch before the second load reduction because its shear cracks did not widen considerably. After a minor load reduction due to

concrete spalling in 13G#5H, a second load reduction occurred due to diagonal tension failure.

5.4.3. Strain in the reinforcement and concrete

Figures 5.8a to 5.8f represent the applied load versus the data obtained from reinforcement strain gauges. According to Fig. 5.8a, the strain values in the bottom longitudinal reinforcement was marginal before the first flexural crack developed. After cracking, a sudden increase in strain was observed for a short period until the specimens recovered the dropped load. Thereafter, a nearly linear load–strain curve was observed until peak load. The slope of the load–strain graph was marginally steeper in 7G#5H and 7G#5HU than in 7G#5. The peak load tensile strain was 16300 and 13100 με in specimens 7G#5 and 13G#5H, respectively. Strain gauges in specimens 7G#5H and 7G#5HU were damaged prior to failure; extrapolated strain was 18200 and 16300 με, respectively, considering a linear load–strain curve, as shown in Fig. 5.8a. Similar behavior at mid-span strain was observed in the load–strain relationship of strain gauge B5 with the recorded or extrapolated peak load strain of 14800, 16000, 11600, and 16600 με in specimens 7G#5, 7G#5H, and 13G#5H, and 7G#5HU, respectively (Fig. 5.8b). Before cracking, the specimens experienced minor compressive strain in the top longitudinal reinforcement (Fig. 5.8d). After cracking, the top reinforcement was in tension with maximum recorded mid-span strains of 6500, 6900, 3200, and 4800 με in specimens 7G#5, 7G#5H, 13G#5H, and 7G#5HU, respectively.

Figures 5.9a and 5.9b, respectively, present the load–strain relationship of concrete at mid-span and quarter-span. The pre-cracking slope of the load–strain curve of the HSC specimens at mid-span and quarter-span were almost 42% and 88% greater than that of the NSC specimen, respectively. In the post-cracking stage, the load–strain slope decreased and, after a stabilization period, almost linear behavior was observed in the load–mid-strain diagram of specimens. The recorded ultimate compressive strain of the concrete at peak load was 2950, 2910, 2700, and 2860 με in 7G#5, 7G#5H, 13G#5H, and 7G#5HU, respectively.

5.4.4. Strain distribution along span

Figure 5.10 represents the strain profiles along the span using the recorded strain in the bottom longitudinal bars and concrete. Before the formation of the crack at the quarter-span, the strain distribution in the longitudinal bars was mainly a linear distribution concentrated near mid-span. After the quarter-span crack occurred, a nearly linear strain distribution along the span was observed. As the load increased, the recorded strain at the location 200 mm from the mid-span tended to be closer to the mid-span strain, which shows a slight redistribution of strain near the applied load location. The strain in the concrete had an almost

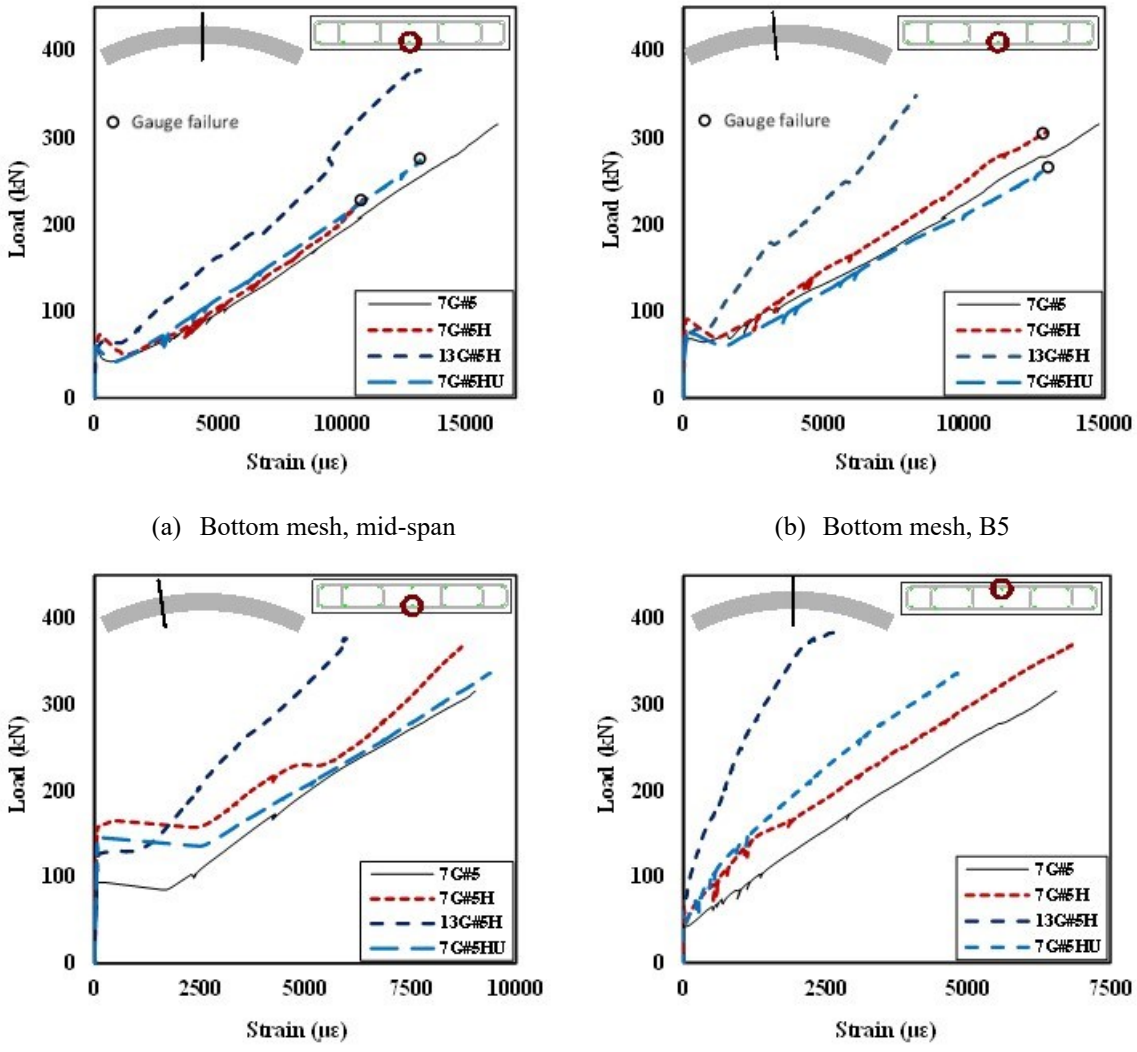

(a) Bottom mesh, mid-span

(b) Bottom mesh, B5

(c) Bottom mesh, quarter-span

(d) Top mesh, mid-span

Figure 5.8 Load–strain relationship in the reinforcement.

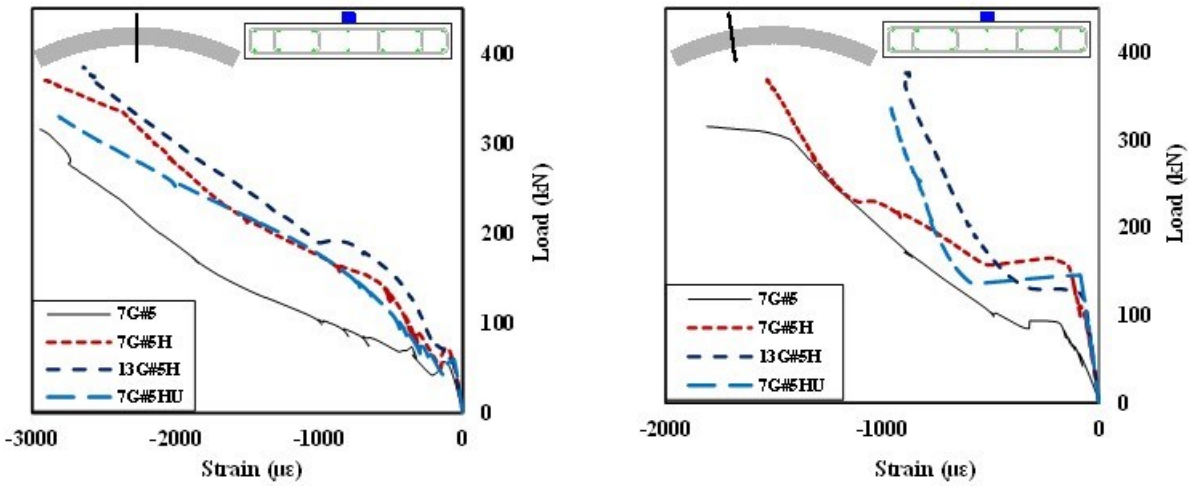

(a) Concrete strain, mid-span (b) Concrete strain, quarter-span

Figure 5.9 Load–strain relationship of concrete.

linear distribution along the span at different load levels in the HSC specimens. Specimen 7G#5 experienced a marginal redistribution of concrete strain in the middle half of the specimen.

5.4.5. Variation of the neutral-axis depth and strain distribution over the cross section

Figure 5.11a illustrates the relationship between the applied load and experimental mid-span neutral-axis depth, calculated using the strains in the longitudinal bottom reinforcement and in the concrete. Prior to the first crack, specimens had an almost constant neutral-axis depth at approximately the geometric centroid of the specimens. After cracking, the neutral-axis depth significantly dropped in all specimens. As load increased, the neutral-axis depth in 7G#5 increased and then remained almost constant until failure, while the neutral-axis depth in the HSC specimens increased gradually up to the peak load. This can be attributed to the stress–strain relationship, which had a nearly linear variation in the HSC as compared to the second-order parabola of the stress–strain curve in the NSC (Ozbakkaloglu and Saatcioglu 2004). At peak load, the neutral-axis depth was 30.4, 27.2, 32.7, and 29.6 mm in 7G#5, 7G#5H, 13G#5H, 7G#5HU, respectively, which was 60%, 86%, 92%, and 97% larger than

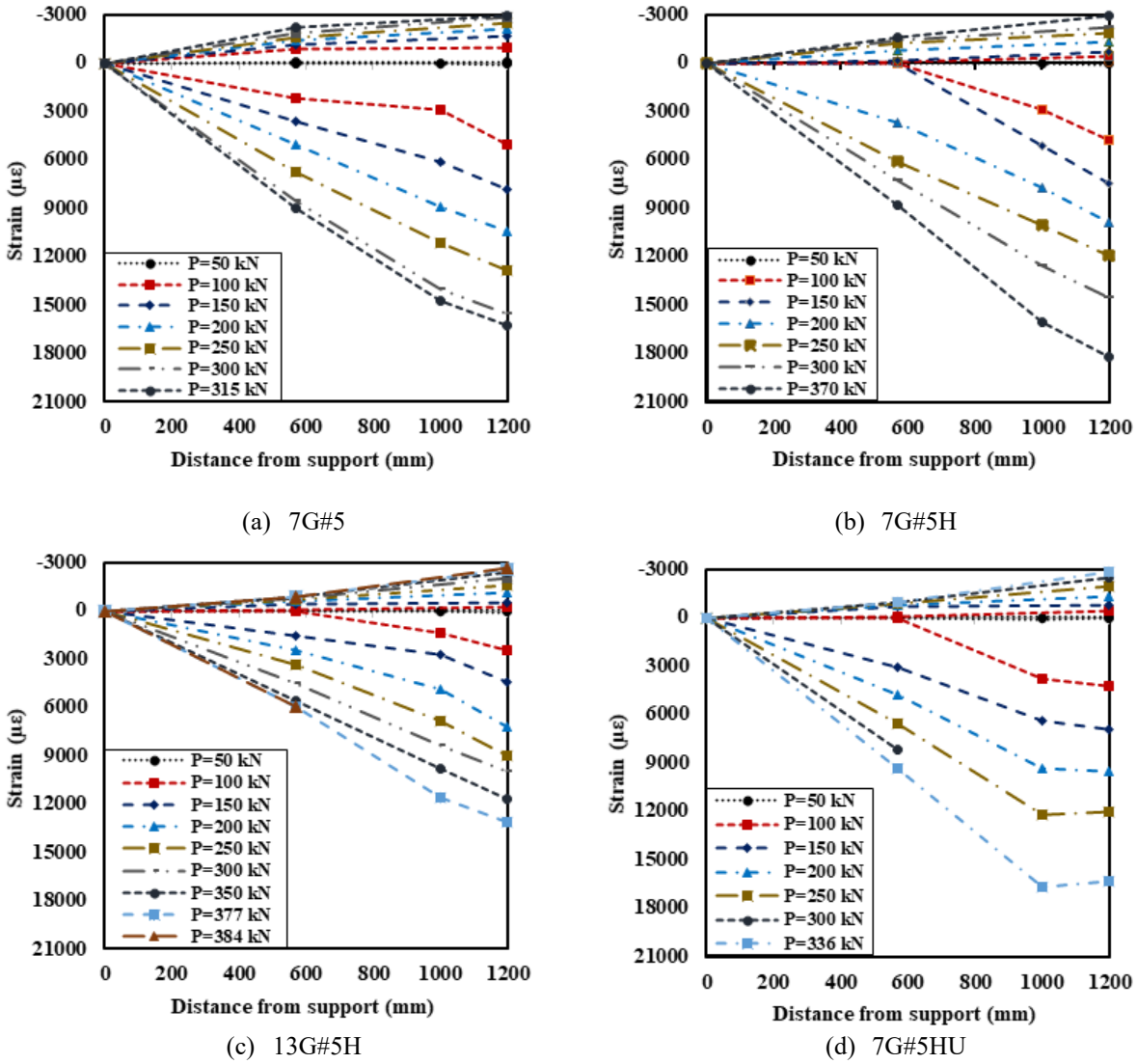

(a) 7G#5

(b) 7G#5H

(c) 13G#5H

(d) 7G#5HU

Figure 5.10 Distribution of strain along the section.

the neutral-axis depth at the onset of cracking. Figure 5.11b presents the strain distribution over the cross section at peak load. A linear distribution can be assumed for the strain, confirming the assumption that the plane sections remained plane after the bending load was applied.

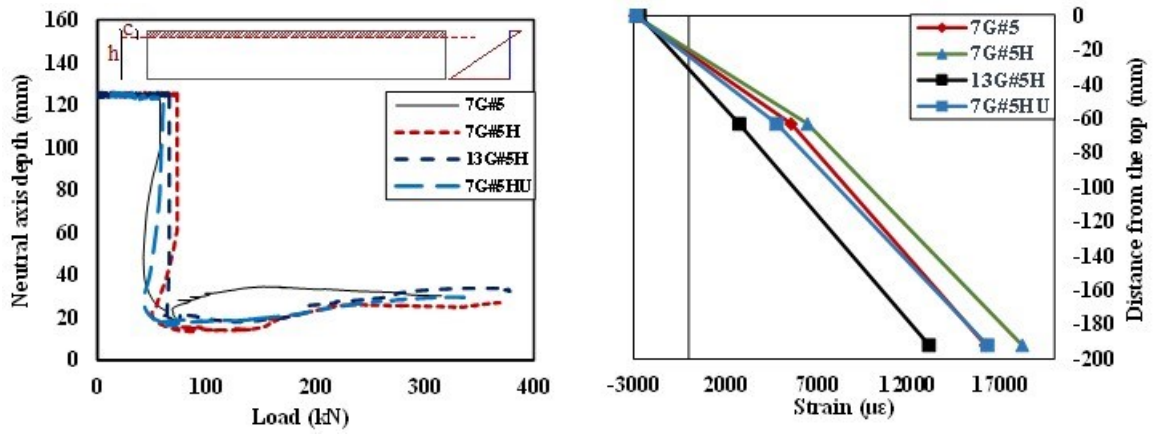

(a) (b)

Figure 5.11 (a) Relationship between load and neutral-axis depth; (b) strain distribution over the cross-section at peak load.

5.5. Discussion of Test Results

5.5.1. Influence of concrete strength

According to Table 5.4, employing HSC enhanced the cracking load by 18% on average compared to the NSC specimen, although 35% higher analytical cracking load obtained for HSC specimens based on ACI 440.1R-15. This is consistent with the results of Theriault and Benmokrane (1998) and Abed et al. (2021). The initial crack width of 7G#5H was almost 100% wider than that in 7G#5. However, using HSC did not have noticeable effect on the crack width and spacing at service load. Shear cracks in 7G#5H appeared at a load 13% higher than in 7G#5 due to the greater tensile strength in the HSC specimen as the main parameter in the formation of web shear cracks (ACI 318-19). The ultimate load-carrying capacity of tunnel segment specimens enhanced by 17% by using HSC. The post-cracking flexural stiffness of 7G#5H was slightly greater than that of 7G#5 (by 7%). This is inconsistent with the results of Theriault and Benmokrane (1998), Goldston et al. (2017), and Abed et al. (2021). The analytical post-cracking flexural stiffness of 7G#5H according to ACI 440.1R-15 was 3% greater than that of 7G#5, confirming the experimental results. Despite the almost equal post-cracking stiffness of 7G#5 and 7G#5H, the experimental and theoretical mid-span deflection of 7G#5H at each applied load was 20% and 30% smaller

on average than in 7G#5, respectively. This can be explained by higher cracking load in 7G#5H as the onset of the post-cracking branch in the load–deflection curve (Fig. 5.7). According to ACI 363R-10, the ultimate compressive strain gradually decreased with increasing concrete strength in plain concrete under uniaxial compression. The ultimate compressive strain of 7G#5H, however, was almost the same as that of 7G#5. This is in agreement with Mansur et al. (1997) and Alca et al. (1997) as they reported almost the same ultimate compressive strain for RC beams tested in flexure with a concrete compressive strength ranging between 50 and 90 MPa. Given almost the same ultimate concrete compressive strain, 7G#5H had 12% higher mid-span tensile strain in the longitudinal bars than 7G#5. This is confirmed by 7G#5H having 11% lower neutral-axis depth at peak load than 7G#5.

5.5.2. Influence of the reinforcement ratio

Increasing the reinforcement ratio by 86% from 7G#5H to 13G#5H significantly tempered the load reduction after crack initiation. In addition, the initial crack width in 13G#5H was 100% narrower than that in 7G#5H. Specimen 13G#5H exhibited a 25% narrower crack width at service load than 7G#5H, despite having a 50% greater service load. The post-cracking flexural stiffness enhanced by 68% in 13G#5H compared to 7G#5H. The analytical post-cracking stiffness of 13G#5H calculated according to ACI 440.1R-15 is 77% greater than that of 7G#5H, which is close to the experimental results. Increasing the reinforcement ratio changed the failure mode from flexural to shear-flexural. Specimen 13G#5H, however, exhibited flexural dominant behavior up to peak load.

5.5.3. Influence of tie configuration

The overall behavior of the tunnel segment specimen with U-shaped ties (7G#5HU) was similar to that of the specimen with closed ties (7G#5H) to some extent. Tie configuration did not noticeably affect the cracking behavior of the tunnel segment specimens. The post-cracking stiffness of 7G#5HU was 5% lower than that of 7G#5H. Using U-shaped ties in 7G#5HU decreased its peak load by 9% compared to 7G#5H but the failure mechanism remained the same. The post-peak ascending branch of 7G#5HU was shorter than that of

7G#5H, which can be attributed to the closed ties providing better confinement than the U-shaped ties. Before the concrete spalled, the neutral axis was above the location of the top mesh, denoting that the tie configuration could not have a noticeable effect on confining the concrete. After the concrete spalled, however, the neutral-axis depth dropped according to test observations. At that stage, the transverse ties could probably have provided some concrete confinement.

5.5.4. Ductility and deformability

The ability of FRP-RC members to undergo large deformation prior to failure could be assessed by the energy-based ductility index (Naaman and Jeong 1995), deformability factor CAN/CSA S6-19 and curvature-based deformability index (Vijay and GangaRao 2001).

5.5.4.1. Energy-based ductility index

This approach relies on the ratio of total absorbed energy (E_{tot}) to elastic energy (E_{el}) and can be used for both steel-reinforced and GFRP-reinforced elements (Naaman and Jeong 1995). Equation 5.1 can be used to calculate the energy-based ductility index (μ_e)

$$\mu_e = \frac{1}{2}\left(\frac{E_{tot}}{E_{el}} + 1\right) \tag{5.1}$$

where E_{tot} is the area under the load–deflection curve until failure and E_{el} is the elastic energy released upon failure (the area of the triangle formed at failure load by the line with the weighted average slope of the two initial straight lines of the load–deflection curve). Table 5.4 represents the value of μ_e for the tested specimens. The ductility index improved by 10% by employing HSC in the tunnel segment specimens. Increasing the reinforcement ratio, however, decreased the ductility by 38%. In addition, according to Table 5.4, the tie configuration did not have a noticeable effect on the ductility index.

5.5.4.2. Deformability factor

In FRP-RC members, a deformability approach is employed to evaluate the ability of a structural element to undergo the required deformation from service condition to failure. The

J-factor was introduced in CAN/CSA S6-19 to consider strength and curvature at service and ultimate condition in calculating deformability. Therefore, both strength and deformability are considered in the J-factor which can be described by a ratio of energy quantity at ultimate load condition to that of service load condition defined as when the concrete strain in the extreme compression fiber reaches a certain limit. The J-factor can be determined with the following equation:

$$J = \frac{M_{ultimate}}{M_c} \times \frac{\Psi_{ultimate}}{\Psi_c} \tag{5.2}$$

where M_c and Ψ_c are the moment and curvature at a concrete strain of 0.001, respectively. $M_{ultimate}$ and $\Psi_{ultimate}$ are the ultimate moment and curvature obtained using the experimental data in this paper. According to Table 5.4, all the tunnel segment specimens had adequate deformability compared to the CAN/CSA S6-19 standard limit of 4.0. While 7G#5H had greater ultimate moment and curvature, it had 30% less deformability than 7G#5. This can be attributed to the greater M_c and Ψ_c in 7G#5H due to its higher concrete strength. Using a higher reinforcement ratio and U-shaped ties in 13G#5H and 7G#5HU decreased deformability by 17% and 18%, respectively.

5.5.4.3. Curvature-based deformability index

Vijay and GangaRao (2001) introduced a curvature-based deformability index as the ratio of absorbed energy (the calculated area under moment–curvature or load–deflection curve) at ultimate load to the absorbed energy at a curvature value of $0.005/d$. The curvature limit of $0.005/d$ was selected since it generally satisfies the cracking and deflection limit for FRP-reinforced flexural elements. The curvature-based deformability index can be calculated with the following equation:

$$J_{VG} = \frac{E_{tot}}{E_{\psi=0.005/d}} \tag{5.3}$$

where E_{tot} is the total absorbed energy at ultimate and $E_{\psi=0.005/d}$ is the absorbed energy until the curvature of $0.005/d$. Table 5.4 gives the curvature-based deformability index for different specimens. The J_{VG} of specimen 7G#5H was 17% higher than that of 7G#5 due to

its greater curvature at each applied load and higher load-carrying capacity. Increasing the reinforcement ratio by 86% decreased the J_{VG} by 52%. Besides, using U-shaped ties in 7G#5HU yielded curvature-based deformability index that was 24% lower than that of 7G#5H.

5.6. Analytical Investigation

5.6.1. Relationship between the Forces Acting on the Segment

Figure 5.12a shows the applied forces acting on the specimens in the test setup. Figures 5.12b and 5.12c present the forces acting on the centerline of the specimens and free body diagram at the section of maximum bending moment, respectively. By using the force and moment equilibrium, Eqns. 5.4, 5.5, and 5.6 can be used to calculate the bending moment, shear force, and tensile axial load at the mid-span, respectively.

$$M = R\cos(\theta) \times \frac{L}{2} + R\Delta\sin(\theta) \tag{5.4}$$

$$V = R\cos(\theta) \tag{5.5}$$

$$N = R\sin(\theta) \tag{5.6}$$

where R is the reaction force of the support, L is the span between reaction forces acting on centerline, and Δ is vertical distance from the center of the specimen to the point at which the reaction forces are applied, as shown in Fig. 5.12b. As mentioned above, the load and boundary conditions in the experimental program differs from field applications. Flexural and shear strength relate mainly to the section. Once the tunnel ring has been analyzed according to the provisions in ACI 533.5R-20, the flexural and shear strength of the GFRP-reinforced HSC PCTL segments presented in this study can be compared with those results. According to some case studies presented in Blom (2002), Arnau Delgado (2012), Bilotta (2017), Spagnuolo et al. (2017), and ACI 533.5R-20, the bending moment and

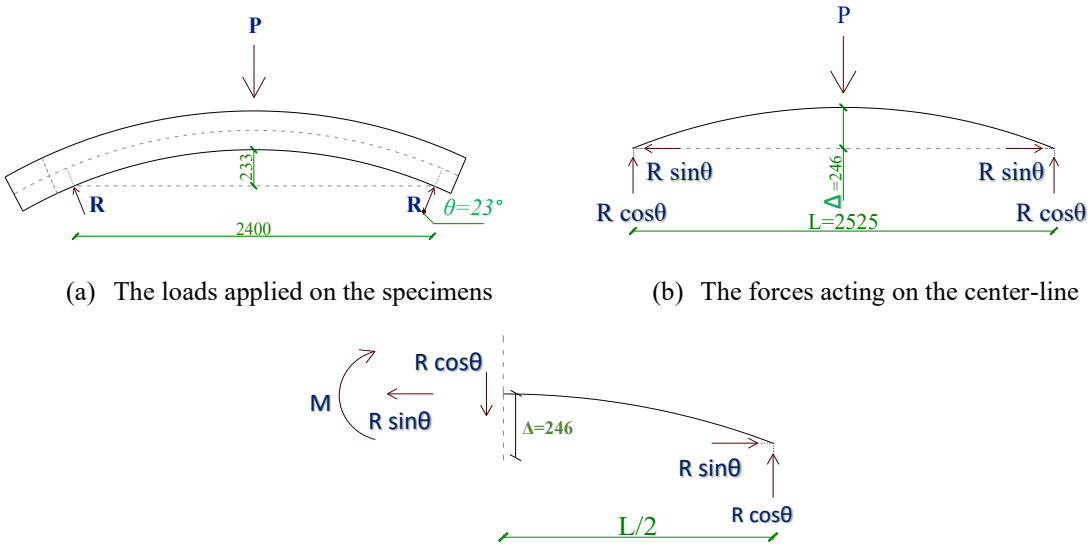

(a) The loads applied on the specimens

(b) The forces acting on the center-line

(c) Free-body diagram of the specimen at the section of maximum bending moment

Figure 5.12 The applied forces and free-body diagram of the specimens (dimensions in mm).

shear forces induced in tunnel segments in field projects can range from 30 to 600 kN.m and from 10 to 200 kN, respectively. As reported in Tables 5.5 and 4.6, the experimental shear and flexural capacities in this study are within the range and near the average. Note that induced forces vary in field projects depending on the geometry and loading conditions; the range referred is only an estimation for some typical applications.

5.6.2. Flexural Strength of Segments

The specimens were subjected to combined axial load and bending moment at different sections. In the field applications, the segments are mostly subjected to axial compression forces. However, in some loading conditions, the segments may be subjected to axial tensile forces (ACI 533.5R-20). Therefore, the analytical procedure in this study is presented so as to cover both compression and tensile axial loads. This section presents the theoretical analysis for GFRP-reinforced NSC PCTL segments according to ACI 440.1R-15, AASHTO (2018), and CAN/CSA S806-12, R2017. Thereafter, some modifications are proposed for applicability to HSC.

Table 5.5 Comparison between the experimental results and values obtained from design standards for flexural strength

ID	$M_{\exp.}$ kN.m	$\varepsilon_{cu,\exp.}$	$\varepsilon_{fu,\exp.}$	$N_{\exp.}$ kN	Theoretical Values, ACI 440.1R and AASHTO 2018		Theoretical Values, CAN/CSA S806-12		Theoretical Values, Modified ACI		Theoretical Values, Modified CSA	
					$\frac{M_{Theo}}{M_{\exp.}}$	$\varepsilon_{fu,Theo.}$	$\frac{M_{Theo}}{M_{\exp.}}$	$\varepsilon_{fu,Theo.}$	$\frac{M_{Theo}}{M_{\exp.}}$	$\varepsilon_{fu,Theo.}$	$\frac{M_{Theo}}{M_{\exp.}}$	$\varepsilon_{fu,Theo.}$
7G#5	215	0.00295	0.016	67	1.00	0.016	1.11	0.018	1.01	0.016	1.05	0.0171
7G#5H	253	0.00291	0.018	78	1.13	0.020	1.17	0.022	1.00	0.019	1.01	0.0187
13G#5H	263	0.00270	0.013	82	1.48	0.015	1.54	0.016	1.28	0.0014	1.31	0.0138
7G#5HU	230	0.00286	0.016	71	1.25	0.021	1.31	0.022	1.10	0.019	1.12	0.0188

Table 5.6 Comparison of the experimental shear demand and analytical shear capacity

Specimen ID	$V_{\exp.}$ kN	$V_{Theo.}/V_{\exp.}$						
		ACI 440.1R	CSA S806	CSA S6	AASHTO 2018	Modified ACI	CSA S806*	CSA S6*
7G#5	158	0.51	1.06	0.84	0.79	0.54	1.06	0.84
7G#5H	185	0.52	1.00	0.83	0.82	0.56	1.21	0.97
13G#5H	193	0.70	0.93	0.80	0.79	0.76	1.15	0.95
7G#5HU	168	0.57	1.10	0.92	0.90	0.61	1.33	1.08

*These values were calculated without considering the upper limits of 60 MPa for concrete compressive strength and 3.2 MPa for f_{cr} according to CAN/CSA S806-12 and CAN/CSA S6-19, respectively.

5.6.2.1. Analytical model for GFRP-reinforced NSC PCTL segments

The following assumptions were made for the theoretical analysis.

1. The plain sections remain plain up to ultimate load.
2. The maximum compressive strain in concrete is assumed to be 0.003 per ACI 440.1R-15 and AASHTO (2018), and 0.0035 per CAN/CSA S806-12, R2017. The GFRP bars have a linear elastic stress–strain curve until failure.
3. The tensile strength of concrete is ignored.

4. A perfect bond exists between the reinforcement and concrete, so that there is no slip between them.
5. An equivalent rectangular stress block is assumed for the distribution of concrete compressive strength where the parameters of α_1 and β_1 are the coefficients of the concrete stress ($f_c^{'}$) and the neutral-axis depth, respectively, which can be obtained according to the provisions of ACI 440.1R-15, AASHTO (2018), and CAN/CSA S806-12, R2017.

The presented analytical procedure is by assuming compression failure mode in a GFRP-reinforced PCTL segment. In addition, it was assumed that both bottom and top reinforcement meshes are under tension. This is what was observed in the specimens in this study and would be probable in segments with almost similar geometry. It should be noted that the presented analytical calculation is also applicable when the top mesh is under compression by assuming the contribution of the top reinforcement mesh is equal to zero, as recommended in ACI 440.1R-15, AASHTO (2018), and CAN/CSA S806-12, R2017. Assuming the neutral-axis depth of c and using the force equilibrium for a linear strain distribution, a closed-form solution was derived to obtain the neutral-axis depth, as presented in Eq. 5.7:

$$c = \frac{\sqrt{4\varepsilon_{cu}E_f\alpha_1\beta_1 f_c^{'}b(dA_f + d^{'}A_f^{'}) + (P + \varepsilon_{cu}E_f(A_f + A_f^{'}))^2} - \varepsilon_{cu}E_f(A_f + A_f^{'}) - P}{2\alpha_1\beta_1 f_c^{'}b} \tag{5.7}$$

where ε_{cu} is the ultimate compressive strain of concrete, E_f is the modulus of elasticity of the FRP reinforcement, b is the width of the section, d is the effective depth, P is the amount of axial load (positive for tension and negative for compression); A_f and $A_f^{'}$ are the area of reinforcement in the bottom and top meshes, respectively. When the reinforcement area in the top and bottom meshes are the same, Eq. 5.7 can be simplified as:

$$c = \frac{\sqrt{4\varepsilon_{cu}E_f\alpha_1\beta_1 f_c^{'}bA_f(d + d^{'}) + (P + 2\varepsilon_{cu}E_fA_f)^2} - 2\varepsilon_{cu}E_fA_f - P}{2\alpha_1\beta_1 f_c^{'}b} \tag{5.8}$$

In the real application for design purposes, the axial-load value normally obtained from analyzing the external loads act on the segment. Since the axial load and bending moment are dependent upon each other in the tests, the axial-load value should be initially assumed

in order to obtain the neutral-axis depth with Eqns. 5.7 and 5.8. After calculating the nominal bending moment, the axial-load value can be modified by trial and adjustment. Equation 5.9 is used to predict the nominal bending moment considering both the top and bottom meshes as well as the axial load.

$$M_n = A_f^{'} f_f^{'} \times (d^{'} - \frac{\beta_1 c}{2}) + A_f f_f \times (d - \frac{\beta_1 c}{2}) - P(\frac{h - \beta_1 c}{2}) \quad (5.9)$$

where h denotes the section depth.

5.6.2.2. Analytical model for GFRP-reinforced HSC PCTL segments

Different stress–strain models for HSC and NSC constitute the main difference between the analytical models for flexural resistance of GFRP-reinforced PCTL segments made with these types of concrete. In particular, the HSC might have a different equivalent rectangular stress block and ultimate concrete compressive strain. According to ACI 318-19 and CAN/CSA A23.3-19, and CAN/CSA S6-19 the coefficients of α_1 and β_1 proposed for NSC can also be used for HSC. Hadhood et al. (2018), however, proposed some modifications to ACI 440.1R-15 Eqns. 5.10 and 5.11, and CAN/CSA S6-19 Eqns. 5.12 and 5.13 to obtain more accurate values for α_1 and β_1 in FRP-reinforced HSC members as follows:

$$\alpha_1 = 0.85 - 0.02(f_c^{'} - 28)/7, \ 0.65 \le \alpha_1 \le 0.85 \quad (5.10)$$

$$\beta_1 = 0.85 - 0.05(f_c^{'} - 28)/7, \ 0.65 \le \beta_1 \le 0.85 \quad (5.11)$$

$$\alpha_1 = 0.85 - 0.002 f_c^{'}, \ 0.67 \le \alpha_1 \le 0.8 \quad (5.12)$$

$$\beta_1 = 0.97 - 0.0035 f_c^{'}, \ 0.67 \le \beta_1 \le 0.9 \quad (5.13)$$

In addition, Ozbakkaloglu and Saatcioglu (2004) proposed the following equation to obtain the ultimate compressive strain of HSC (ε_{cu}):

$$\varepsilon_{cu} = 0.0036 - (f_c^{'} - 30) \times 10^{-5} \ge 0.0027 \quad (5.14)$$

By employing the obtained values of α_1, β_1, and ε_{cu} in the related equations, the flexural strength of GFRP-reinforced HSC PCTL segments can be calculated. This is referred to as the modified ACI and modified CSA methods in the analytical calculations.

5.6.3. Shear Strength of Segments

Shear capacity of segments must be predicted for design purposes. Although transverse reinforcement is normally used in PCTL segments, it is unlikely to provide shear capacity due to the short tie leg as well as the considerable gap between the two tie legs. According to ACI 533.5R-20 and ITA WG2-19, transverse reinforcement is often designed as the minimum temperature and shrinkage reinforcement. Therefore, neglecting the contribution of the transverse reinforcement in PCTL segments when providing their shear capacity might be a conservative and rational design assumption. This is what was considered in the analytical procedure presented for shear strength in this study. This section presents the main assumptions in North American standards that can be used to predict shear capacity of PCTL segments and modified in some cases. Thereafter, modifications and discussion are presented for using the models for GFRP-reinforced HSC PCTL segments.

5.6.3.1. ACI 440.1R-15

ACI 440.1R-15 considers the contribution of the uncracked compression block as the only shear transferring mechanism of concrete. The equation in this standard is the modified equation presented in ACI 318-14 considering the effect of the axial stiffness of the FRP bars on the compression-block depth. The shear capacity of concrete (V_c) according to ACI 440.1R-15 can be calculated with Eq. 5.15

$$V_c = \frac{2}{5}\sqrt{f_c'}\,b_w(kd) \tag{5.15}$$

where b_w is the section width and k is the ratio of neutral axis depth to the effective depth. ACI 440.1R-15 does not provide any provisions regarding the shear strength of GFRP-reinforced members under axial load. Since it only considers the contribution of the compression block, the effect of axial load could be considered to some extent by incorporating the axial load in the determination of the k value. Equation 5.16 was developed to consider the axial load (P) in calculating the value of k_n by considering one row in the bottom longitudinal reinforcement

$$k_n = \frac{\sqrt{P^2 + 2P\rho_f n_f l_n + l_n{}^2 n_f \rho_f (n_f \rho_f + 2)} - n_f \rho_f l_n - P}{l_n} \tag{5.16}$$

where l_n can be calculated with Eq. 5.17

$$l_n = E_c \varepsilon_c b_w d \tag{5.17}$$

where E_c is the concrete modulus of elasticity, which can be considered $4700\sqrt{f_c'}$; and ε_c is the concrete compressive strain. According to ACI 318-99, the assumption of stress linear distribution is almost true until 45% of the ultimate concrete compressive strength. Therefore, ε_c could be considered as equal to or less than 0.001. By replacing k_n with k in Eq. 5.15, the effect of the axial load on concrete shear resistance can be considered. Axial forces, however, induce some axial stresses in the elements of the compression block, which changes the angle and amount of principal stresses. Considering them calls for in-depth analysis that goes beyond the scope of this paper.

5.6.3.2. CAN/CSA S806-12, R2017

In CAN/CSA S806-12, R2017, the contribution from the uncracked concrete and aggregate interlock are both considered as the shear-transferring mechanisms of the concrete. The effect of important parameters such as reinforcement rigidity, size effect, interaction of shear force and bending moment at the critical section, and arc action is considered in the shear strength of concrete by some coefficients obtained empirically (Khavaran 2019). CAN/CSA S806-12, R2017 provides two different equations for shear capacity of GFRP-RC elements subjected to compression and tensile axial loads (the equations were not presented due to limit in the space). According to CAN/CSA S806-12, R2017, f_c' should not be taken greater than 60 MPa in the calculations.

5.6.3.3. CAN/CSA S6-19

The shear capacity in this standard is presented based on the simplified modified compression field theory model (SMCFT). The influence of size effect, reinforcement rigidity, and the ratio of bending moment to shear force at the critical section was considered

in the related equations to calculate shear capacity of GFRP-RC elements. CAN/CSA S6-19 limits the concrete tensile strength to 3.2 MPa in the related equations.

5.6.3.4. AASHTO LRFD bridge design guide specifications for GFRP-reinforced concrete (AASHTO 2018)

This standard presents almost the same approach as CAN/CSA S6-19 for determining the shear capacity of GFRP-reinforced elements with some differences in the coefficients. However, while CAN/CSA S6-19 limits the maximum compressive strength of concrete to 64 MPa in calculations, the *AASHTO LRFD bridge design guide specifications for GFRP-reinforced concrete* (AASHTO 2018) define 69 MPa as the upper limit of concrete compressive strength.

5.6.3.5. Modification of presented models for HSC

As mentioned above, ACI 440.1R-15 considers the contribution of uncracked compression block to be the shear-transferring mechanism. In such cases, the compression-block depth and concrete modulus of rupture play the most important role in the shear capacity of a flexural member. According to ACI 363R-10, assuming a proportional relationship between the modulus of rupture and $\sqrt{f_c'}$ yields good estimation for both HSC and NSC. The concrete modulus of elasticity is a determinative factor in calculating the compression-block depth. Using $4700\sqrt{f_c'}$ overestimates the HSC modulus of elasticity ($E_{c,HSC}$); the following equation yields a better estimation (ACI 363R-10):

$$E_{c,HSC} = 3320\sqrt{f_c'} + 6900 \tag{5.18}$$

When substituting the resultant value in Eqns. 5.16 and 5.17 to calculate the value of k_n, Eq. 5.15 can be used to predict the concrete contribution to the shear strength of GFRP-reinforced HSC PCTL segments according to ACI 440.1R-15. This method is referred to as the modified ACI method in the theoretical calculations in this study.

The aggregate and concrete in HSC have similar strengths, causing cracks to pass though the aggregate pieces. This produces a smoother diagonal shear-crack surface, thereby reducing the effect of aggregate interlock in carrying the shear force in the element (El-Sayed et al. 2006; ACI 363R-10). When the concrete compressive strength is greater than 70 MPa, Angelakos et al. (2001) recommended neglecting the contribution of aggregate interlock in calculating the shear capacity of concrete. CAN/CSA S806-12, R2017 takes this into account by limiting the concrete compressive strength to 60 MPa in calculating concrete shear strength. CAN/CSA S6-19 limits f_{cr} to 3.2 MPa, which means that it does allow for taking into account concrete compressive strengths higher than 64 MPa in calculating the shear capacity of concrete. However, this limit is 69 MPa in *AASHTO LRFD bridge design guide specifications for GFRP-reinforced concrete* (AASHTO 2018).

5.6.4. Comparison Between the Analytical and Experimental Results

Table 5.5 presents a comparison of the experimental results and the values obtained according to ACI 440.1R-15, AASHTO (2018), and CAN/CSA S806-12 (R2017), the modified ACI and modified CSA models for flexural strength, considering the self-weight of the specimens. The reduction factor is considered equal to 1.0 in all calculations. Although ACI 440.1R-15 and AASHTO (2018) accurately predicted the flexural strength of 7G#5, they overestimated the flexural strength of 7G#5H and 7G#5HU by 13% and 25%, respectively, showing that the standard needs some modifications for GFRP-reinforced HSC PCTL segments. The overestimation rate of CAN/CSA S806-12, R2017 was greater than that of ACI 440.1R-15 due to a higher assumed ultimate concrete compressive strain in the former. Modifying the concrete compression block and ultimate compressive strain of concrete according to Hadhood et al. (2018) and Ozbakkaloglu and Saatcioglu (2004) greatly improved the accuracy of ACI 440.1R-15 and CAN/CSA S806-12, R2017 in predicting the flexural strength of GFRP-reinforced PCTL segments made with either HSC or NSC. The best model in this study, the modified ACI model could exactly predict the flexural strength of specimens 7G#5 and 7G#5H, but it gave a 10% overestimation for 7G#5HU. It should be noted that the flexural strength of 13G#5H predicted by all the models was much higher than

the experimental results since the specimen could not reach its ultimate capacity during the test.

Table 5.6 compares the experimental shear demand and analytical shear capacity of the tested specimens according to ACI 440.1R-15, CAN/CSA S806-12 (R2017), CAN/CSA S6-19, AASHTO (2018), and the modified ACI model. The shear strength of 13G#5H was underestimated by 30%, 7%, 20%, 21%, and 24% according to ACI 440.1R-15, CAN/CSA S806-12 (R2017), CAN/CSA S6-19, AASHTO (2018), and the modified ACI model, respectively. Therefore, CAN/CSA S806-12, R2017 yielded the most accurate results of all the models. The upper limit of 60 MPa for concrete compressive strength in this standard seems to be a rational assumption as ignoring the upper limit leads to a 15% overestimation according to CAN/CSA S806-12, R2017. Ignoring the upper limit of 3.2 MPa as the modulus of rupture of concrete according to CAN/CSA S6-19 changed the underestimation from 20% to 5%. Regardless of the reinforcement axial stiffness, CAN/CSA S806-12, R2017 yielded almost the same shear capacity for the HSC specimens since the minimum value specified in this standard governed the shear strength prediction. Besides, the obtained results from CAN/CSA S6-19 for shear strength was equal in HSC specimens since the maximum specified values of 0.003 and 3.2 MPa specified in CAN/CSA S6-19 were used for the strain in the longitudinal reinforcement and concrete tensile strength, respectively. The same issue led to similar results in AASHTO (2018) for HSC specimens. Modifying the ACI 440.1R-15 model for HSC predicted the shear strength of the HSC tunnel segment specimens with 5% more accuracy on average.

5.7. Conclusions

Four full-scale tunnel segment specimens were constructed and tested under bending load to investigate the behavior of GFRP-reinforced HSC PCTL segments. Thereafter, an analytical investigation was conducted to evaluate the efficiency of North American standards and guidelines in predicting the flexural and shear capacity of GFRP-reinforced PCTL segments and to propose some modifications for HSC segments. The following conclusions were drawn.

1- The specimens reinforced with seven longitudinal bars (reinforcement ratio of 0.5) failed in flexure by concrete crushing. Increasing the reinforcement ratio by 86% changed the failure mode from flexure to shear-flexure characterized by concrete spalling followed by diagonal-tension failure.
2- Using HSC enhanced the post-cracking stiffness and load-carrying capacity by 7% and 17%, respectively. Increasing the reinforcement ratio by 86% improved the post-cracking stiffness by 68%. Moreover, the specimen with U-shaped ties had 9% lower load-carrying capacity with almost the same post-cracking stiffness as the specimen with closed ties.
3- Employing HSC enhanced the cracking load by 18% while did not have noticeable effect on the crack width and spacing. The service-load crack width effectively decreased by 50% through increasing the reinforcement ratio. According to the test observations, tie configuration did not affect the cracking behavior of the specimens. In general, all the GFRP-reinforced PCTL segments in this study satisfied the requirements of CAN/CSA S6-19 for the allowable service-load crack width.
4- The mid-span deflection decreased by 20% on average by increasing the concrete strength by 81%. Increasing the reinforcement ratio could decrease the mid-span deflection by 60%. The mid-span service deflection of the tested specimens was 74% to 84% lower than the specified criterion for allowable deflection in *Austrian Society for Concrete and Construction* (2011) and 30% to 55% lower than the maximum allowable deflection in CAN/CSA S6-19.
5- While ACI 440.1R-15 and AASHTO 2018 accurately predicted the flexural strength of the tunnel segment cast with NSC, they overestimated the flexural strength of the segments cast with HSC by 13% and 25% for the specimens fabricated with closed ties and U-shaped ties, respectively. The procedure presented to modify the ACI 440.1R-15 model in terms of the compression-block coefficients and ultimate compressive strain according to Hadhood et al. (2018) and Ozbakkaloglu and Saatcioglu (2004) predicted the flexural strength of both NSC and HSC specimens fabricated with closed ties with an error of less than 1.0% while overestimating that of the HSC specimen fabricated with U-shaped ties by 10%. In addition, the

overestimation rate of the CAN/CSA S806-12, R2017 model was higher than that of the ACI 440.1R-15 model for all specimens.

6- Among the North American standards evaluated, CAN/CSA S806-12, R2017 yielded the most accurate results in predicting the shear capacity of GFRP-reinforced PCTL segments with an underestimation of 7%. ACI 440.1R-15 gave the most conservative results. Modifying the ACI 440.1R-15 model based on the method presented in this study improved the prediction accuracy by 5%. Given that the specimens were full scale, the number of specimens in this study was low. Consequently, the results herein might not be sufficient alone to justify modifying design standards; more research is needed to verify the repeatability of the test results.

CHAPTER 6 EXPERIMENTAL AND ANALYTICAL INVESTIGATION OF PRECAST FIBER-REINFORCED CONCRETE (FRC) TUNNEL LINING SEGMENTS REINFORCED WITH GLASS-FRP BARS

Foreword

Authors and Affiliation:

Seyed Mohammad Hosseini: Ph. D. Candidate, Department of Civil Engineering, University of Sherbrooke, Sherbrooke, Quebec, Canada, J1K 2R1

Salaheldin Mousa: Postdoctoral fellow, Department of Civil Engineering, University of Sherbrooke, Sherbrooke, Quebec, Canada, J1K 2R1

Hamdy M. Mohamed: Research associate and lecturer, Department of Civil Engineering, University of Sherbrooke, Sherbrooke, Quebec, Canada, J1K 2R1.

Emmanuel Ferrier: Professor, Department of Civil Engineering University Lyon 1, IUT LYON 1, Villeurbanne Cedex, France

Brahim Benmokrane: Professor, Department of Civil Engineering, University of Sherbrooke, Sherbrooke, Quebec, Canada, J1K 2R1.

Journal title: Tunneling and Underground Space Technology

Paper status: Final version, published online in September 2023.

Contribution in thesis:

In this chapter, the effect of employing FRC on the performance of GFRP-reinforced PCTL segments was investigated using experimental and analytical investigations.

6.1. Abstract

A hybrid use of glass fiber-reinforced polymer (GFRP) reinforcement and fiber-reinforced concrete (FRC) could be a viable option for producing durable precast concrete tunnel lining (PCTL) segments. There is, however, a gap in the literature regarding the behavior of GFRP-reinforced FRC PCTL segments with typical amounts of reinforcement. This paper presents results obtained from both experimental and analytical studies on the behavior of GFRP-reinforced FRC PCTL segments under bending load (flexure). Four full-scale tunnel segment specimens measuring 3100 mm in length, 1500 mm in width, and 250 mm in thickness were constructed and tested monotonically under three-point bending load. The influence of concrete type, reinforcement ratio, and tie configurations on the cracking behavior, deflection behavior, failure mechanism, load-carrying capacity, strain behavior, and deformability of GFRP-reinforced FRC PCTL segments was evaluated. There is no analytical procedure available to predict the shear and flexural capacities of GFRP-reinforced FRC PCTL segments. Therefore, an analytical investigation was carried out in order to propose and evaluate different methods for predicting the flexural and shear capacities of such elements. The results indicate that the use of FRC significantly improved the cracking behavior and failure mechanism while also increasing the load-carrying capacity and deformability by 12% and 71%, respectively. Increasing the reinforcement ratio by 86% enhanced the post-cracking stiffness and peak load by 92% and 31%, respectively, while reducing the service-load crack width by 57%. According to the analytical investigation, the introduced direct method based on the stress–strain behavior of the FRC and the proposed simplified method based on ACI 440.1R-15 could predict the flexural capacity of GFRP-reinforced FRC PCTL segments with high accuracy. Furthermore, the method proposed to modify CAN/CSA S806-12, R2017 to consider the contribution of fibers in shear transferring mechanism yielded rational conservative values for the shear capacity of GFRP-reinforced FRC PCTL segments. The experimental and analytical results of this study would be useful in improving the current design standards and in facilitating the field application of GFRP-reinforced FRC PCTL segments.

Keywords: Fiber-reinforced concrete (FRC); precast concrete tunnel lining (PCTL) segments; glass fiber-reinforced polymer (GFRP) bars; flexure; structural behavior; analytical investigation; design standards.

6.2. Introduction

In mechanized tunneling with tunnel boring machines (TBMs), precast concrete tunnel lining (PCTL) segments are the key elements carrying the load during construction and service stages. As tunnels are designed to have a service life in excess of 100 years, durability is an important feature to consider in their design. Several deteriorating mechanisms jeopardize the durability of tunnels due to degradation of the conventional steel reinforcement and concrete. The most important degradation mechanisms are chloride attack in tunnels adjacent to salt water, carbonation attack in roadway tunnels, sulfate attack in tunnels adjacent to aggressive soils, acid attack in wastewater tunnels, stray current corrosion in subway tunnels, and frost attack in tunnels subjected to freeze–thaw cycles (Ghafari 2013; Zhiqiang and Mansoor 2013; ACI 533.5R-20; Li et al. 2020). Replacing steel reinforcement with noncorroding glass fiber-reinforced polymer (GFRP) reinforcement is a viable solution to mitigate the corrosion problem in concrete structures reinforced with conventional steel reinforcement (ACI 440.1R-15). In addition to their well-known general advantages in reinforced concrete (RC) structures, GFRP bars offer unique advantages when used in tunnel segments. GFRP bars are suitable for tunnel parts that should be eventually demolished. In addition, they have electromagnetic neutrality which is advantageous in tunnels with stray current (Caratelli et al. 2016; Caratelli et al. 2017; Spagnuolo et al. 2017). There are, however, some challenges associated with the use of GFRP bars in PCTL segments due to their low modulus of elasticity. GFRP-reinforced elements have larger crack width and deflection than steel-reinforced flexural elements. Their shear capacity is also lower (ACI 440.1R-15; CAN/CSA S6-19). Using fiber-reinforced concrete (FRC) in elements reinforced with GFRP bars is an effective solution to improve element structural behavior. When cracks form in GFRP-reinforced FRC flexural elements, fiber bridging tempers the temporary load reduction after crack formation. In addition, fiber bridging controls crack width and improves post-cracking stiffness (Yang et al. 2012; Yoo et al. 2016; Attia et al.

2019; Patil et al. 2020). As FRC has higher ultimate compressive strain than normal concrete (NC) and its compression failure is more gradual, it improves ductility, deformability, load-carrying capacity, and failure mechanism (Issa et al. 2011; Attia et al. 2019; Patil et al. 2020). Fibers contribute to controlling the width of shear and flexural cracks, leading to the improved shear capacity of FRC elements (Dev et al. 2020; Hosseini et al. 2021). Lastly, fibers enhance the bond strength and durability of FRP bars in concrete (Kim et al. 2013; Wang and Belarbi 2013; Yan and Lin 2017; Kim and Lee 2019).

The use of FRC in PCTL segments has generated a great interest in recent years due to its unique advantages such as improving post-cracking behavior, better crack-control characteristics, better resistance against the bursting and spalling stresses, and increasing impact and fatigue resistance. In some cases, however, using FRC without reinforcing bars fails to meet structural demands. In such cases, a hybrid system of FRC and reinforcing bars is preferable. In particular, hybrid reinforcement is recommended for tunnels with a slenderness ratio greater than 12 (ACI 544.7R-16). The literature contains a great number of studies on the behavior of FRC PCTL segments. The issues investigated in the literature on FRC PCTL segments includes the flexural behavior under concentrated load (Waal 1999; Schnütgen 2003; Poh et al. 2005; Plizzari and Tiberti 2006; Plizzari and Tiberti 2007; Caratelli et al. 2011; Caratelli et al. 2012; Nehdi et al. 2015; Yan et al. 2015; Liao et al. 2016; Conforti et al. 2017; Conforti et al. 2019), structural response under field conditions (Molins and Arnau 2011), behavior under thrust load (Poh et al. 2005; Caratelli et al. 2011; Cignitti et al. 2012; Abbas et al. 2014b; Nehdi et al. 2015; Conforti et al. 2017; Conforti et al. 2019), structural behavior in response to fire (Yan et al. 2013; Yan et al. 2015), behavior under punching-shear load (Abbas et al. 2014a), structural performance under settlement load (Abbas et al. 2014a), behavior under flexural cyclic loading (Abbas et al. 2014b), structural behavior of joints exposed to fire (Yan et al. 2016), behavior under biaxial loading testing (Meng et al. 2016), capacity of segmental joints (Gong et al. 2017), effect of traditional reinforcement combined with fiber reinforcement (Plizzari and Tiberti 2007; Meng et al. 2016; Conforti et al. 2017; Conforti et al. 2019), effect of fiber dosage (Poh et al. 2005; Ding et al. 2011; Abbas et al. 2014b; Liao et al. 2015; Nehdi et al. 2015; Meng et al. 2016), and

seismic assessment (Avanaki et al. 2018). All of these studies agree that FRC outperforms NC in PCTL segments. Employing FRC improved the overall structural performance, including cracking behavior, post-cracking behavior (toughness), durability characteristics, shear behavior, and resistance against impact loads. In addition, according to the cited studies, employing FRC improved the resistance against bursting and spalling stresses induced by TBM thrust force or fire. According to the literature, employing steel rebars in FRC PCTL segments improved flexural strength, stiffness, and post-peak behavior. Furthermore, a hybrid configuration of steel rebars and FRC reduced crack widths and deflection at service load in PCTL segments (Liu et al. 2022; Tengilimoglu and Akyuz 2020).

Given the benefits of using GFRP reinforcement and FRC in PCTL segments, as well as the positive influence of FRC on the structural behavior of GFRP-reinforced flexural components, the hybrid use of FRC and GFRP bars is a feasible option for constructing durable PCTL segments with excellent structural performance. The literature contains few studies on investigations on the hybrid use of GFRP reinforcement and FRC in PCTL segments. Meda et al. (2019) and Tengilimoglu and Akyuz (2020) each tested one GFRP-reinforced FRC tunnel segment specimen under bending load to investigate the feasibility of using such hybrid reinforcement in PCTL segments. The former used steel fibers and the latter employed propylene fibers. They used very light reinforcement in their specimens with a ratio of less than 0.1%. They reported that using GFRP reinforcement significantly improved the flexural strength, stiffness, and cracking behavior compared to the FRC specimen without reinforcement. The observed unfavorable tension failure mode in their specimens as a result of the very light reinforcement ratio. Such low amounts of reinforcement—which leads to tension failure mode—is unacceptable according to the North American design guidelines and standards governing FRP reinforcement, such as CAN/CSA S806-12, R2017 and CAN/CSA S6-19.

There are several essential issues related to GFRP-reinforced FRC PCTL segments that have not been reported on in the literature such as the effect of reinforcement ratio and spacing

on the structural performance, the effect of tie configuration, shear behavior, failure mechanism, and strain behavior. In addition, there is no analytical procedure in the literature for calculating the flexural and shear capacities of GFRP-reinforced FRC PCTL segments. Furthermore, there are no provisions in the current design standards regarding GFRP-reinforced FRC elements. Past studies related to GFRP-reinforced FRC PCTL segments (Meda et al. 2019) aimed at improving the behavior of FRC PCTL segments by employing very light GFRP reinforcement. The current study fills the research gaps by employing FRC to improve the structural behavior of GFRP-reinforced PCTL segments with reinforcement ratios greater than the balanced reinforcement ratio, which meets the requirements of design standards. This study pioneers in investigating the influence of the reinforcement ratio and tie configuration on the structural behavior of GFRP-reinforced FRC PCTL segments. Four full-scale specimens were constructed and tested under three-point bending load to investigate the cracking behavior, failure mechanism, flexural strength, shear strength, and deflection behavior of GFRP-reinforced PCTL segments under bending load. In addition, analytical investigation was conducted to evaluate and propose newly developed methods for estimating the flexural and shear capacities of GFRP-reinforced FRC PCTL segments. The experimental and analytical results of this study will be useful for field applications and improve current design standards.

6.3. Experimental program

6.3.1. Details of specimens and test matrix

The experimental program includes testing of four full-scale GFRP-reinforced PCTL segments under bending load. A subway tunnel with an internal diameter of 6500 mm and external diameter of 7000 mm was considered in this study as the original tunnel. The supposed full tunnel ring consisted of seven segments with different shapes. The tunnel segment specimens in this study comply with a typical segment in the mentioned tunnel ring measuring 3100 mm in length, 1500 mm in width, and 250 mm in thickness with a parallelogram shape (Fig. 6.1a). The specimens were curvilinear in shape with internal and external curvature radii of 3250 and 3500 mm, respectively. The specimens were cast in a

Figure 6.1 (a) Geometry of tunnel segment specimens (dimensions in mm); (b) fabricated cage inside formwork (7G#5F); (c) casting of the specimens; (d) demolding; and (e) curing.

wooden formwork on four separate days (Figs. 6.1b and 6.1c) at Sym-Tech Béton 'Préfabriqué in Saint-Hyacinthe, Quebec. The specimens were then demolded and cured for seven days (Figs. 6.1d and 6.1e). Each segment had longitudinal curvilinear bars in the top and bottom layers fastened with transverse ties (Fig. 6.2). The specimens were designed to have typical reinforcement configurations generally used in field applications as based on consultations with local engineers. In addition, the requirements of ACI 440.1R-15 and CAN/CSA S806-12, R2017 for flexural FRP-RC members were considered in designing the specimens. The longitudinal bars were manufactured through an innovative process developed by Pultrall Inc. (a manufacturer of GFRP reinforcement). To provide sufficient anchorage, end-anchorage U-shaped bars were used at the end of the longitudinal bars. The test parameters included concrete type (NC and FRC), longitudinal reinforcement ratio (0.48 and 0.9), and tie configuration (closed ties and U-shaped ties). Table 6.1 presents the test matrix, including specimen ID, concrete type, longitudinal reinforcement configuration and ratio, and tie configuration. Figure 6.3 shows the reinforcement detail of the specimens. As shown, two different longitudinal bars spaced at 125 mm or 250 mm were used to provide two different reinforcement ratios. The bar sizes and spacing in the longitudinal and transverse directions are typically used for steel-reinforced PCTL segments in field applications (ACI 440.1R-15). The specimen label begins with the number of

Table 6.1 Test matrix and specimen details

Tunnel Segment Specimen ID	Concrete Type	Number and Size of Longitudinal Bars	Longitudinal Reinforcement Ratio (%)	Reinforcement Ratio to the Balanced Ratio*		Tie Configuration
				ACI 440.1R	CSA S806-12	
13G#5	NC	13 #5 bars	0.90	2.6	2.4	Closed ties
13G#5F	FRC	13 #5 bars	0.90	3.0	2.5	Closed ties
7G#5F	FRC	7 #5 bars	0.48	1.7	1.3	Closed ties
7G#5FU	FRC	7 #5 bars	0.48	1.9	1.3	U-shaped ties

* Calculated considering both top and bottom meshes using the actual concrete compressive strength at the date of testing.
Contribution of fibers was not considered.

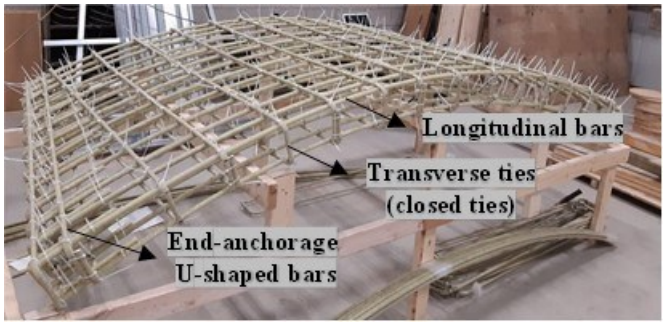

Figure 6.2 A typical assembled cage (13G#5)

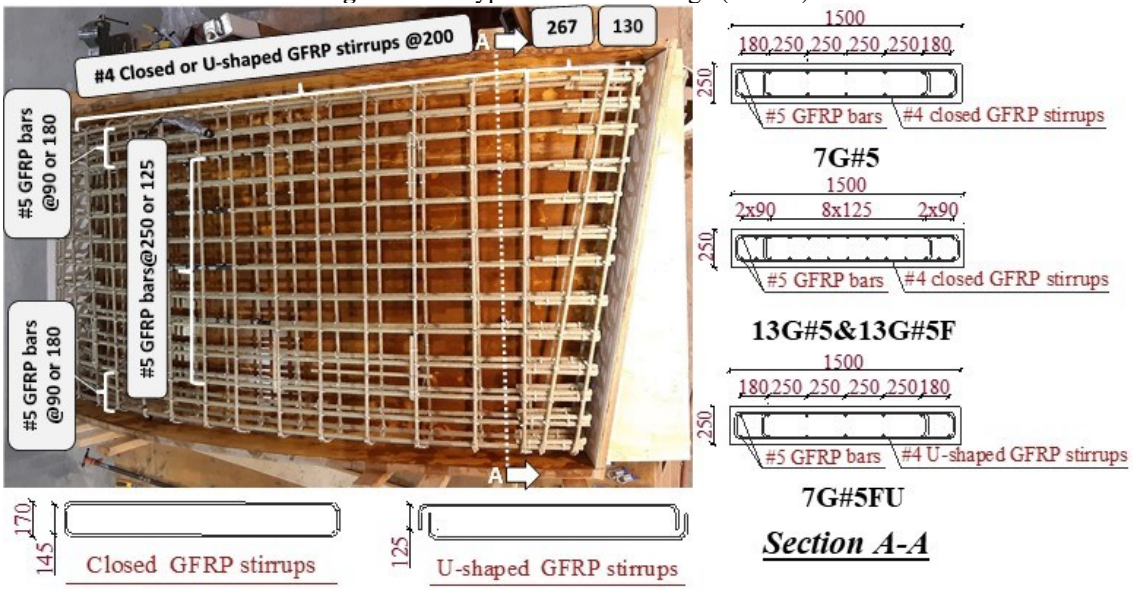

Figure 6.3 Reinforcement details of the specimens (dimensions in mm).

longitudinal bars. The second term (G#5) indicates the type and size of the longitudinal bars (#5 GFRP bars for all the specimens). The letter "F" represents specimens made with FRC and the letter "U" indicates the specimen made with U-shaped transverse ties. Table 6.1 lists the ratio of the provided reinforcement ratio to the balanced reinforcement ratio calculated according to the provisions in ACI 440.1R-15 and CAN/CSA S806-12, R2017. Based on this Table, all the segments were designed to undergo the preferred failure mode of concrete crushing.

6.3.2. Material properties

6.3.2.1. Concrete

Two different concrete mixes for the NC and FRC specimens were designed (Table 6.2). The actual compressive strength at the time of testing was 51 MPa and 47±3 MPa, respectively, for the NC and FRC obtained by testing three cylinder specimens measuring 100 × 200 mm as according to ASTM C39/C39M-21. The FRC concrete mix was designed by the precast company so that the specimens would have appropriate mechanical properties. Polypropylene fibers were added to the concrete mix before the water. The manufacturer's datasheet (Sika Group 2019) recommends the use of such fibers in PCTL segments. To determine the flexural behavior of the FRC, three concrete prisms measuring 100 × 100 × 500 mm were taken for each specimen cast with the FRC. The samples were tested in flexure according to ASTM C1609-19 on the test date. Figure 6.4 shows the test setup used to apply four-point bending load to the FRC prisms. As provided for in ASTM C1609-19, the mid-span deflection was recorded with two linear variable differential transformers (LVDTs) installed on each side of the samples. The peak load (P_p), the residual load at the net deflection of $L/600$ (P_{600}^D), and the residual load at the net deflection of $L/150$ (P_{150}^D) were specified according to ASTM C1609-19. The following equation was used to calculate the peak strength (f_p), the residual strength at the net deflection of $L/600$ (f_{600}^D), and the residual strength at the net deflection of $L/150$ (f_{150}^D):

$$f = PL/b_b h_b^2 \tag{6.1}$$

Table 6.2 Concrete mix design for the NC and FRC

Concrete Type	Cement (kg/m^3)	Sand (kg/m^3)	Limestone 5/10 (kg/m^3)	Superplasticizer (ml/ m^3)	Air-Entrainment Agent (ml/ m$^{3)}$	Water* (L/m^3)	Fiber (kg/m^3)
NC	450	615	1015	4500	140	170	-
FRC	450	615	1015	V*	140	170	5.85

*The values varied for each batch to achieve the target slump.

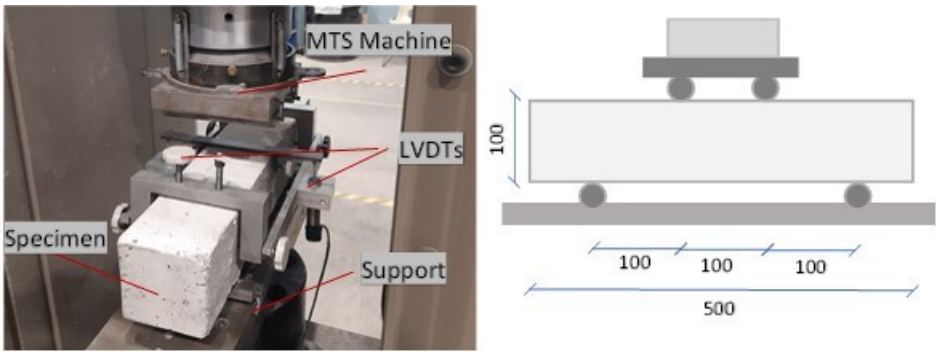

Figure 6.4 Test setup for testing the FRC samples (beam test).

Table 6.4 reports f_p, f_{600}^D, and f_{150}^D for the specimens made with FRC. As can be seen, the higher the compressive strength, the higher the peak strength and the lower the residual strength. This observation is consistent with some studies in the literature according to fiber type and ratio (Yoo et al. 2015b; Lee et al. 2016; Lee 2017; Lee et al. 2017; Shi et al. 2020). Before a FRC sample cracks, the concrete mix plays the main role in its flexural strength, while the effect of the fibers is marginal. As a result, the concrete with higher strength reaches higher peak strength. Once cracking occurs, however, fibers provide residual strength by bridging between the cracks (Shi et al. 2020). In such situations, the greater energy released upon the cracking in concrete with higher strength can lead to lower residual strength, particularly in cases with low fiber ratios (Lee et al. 2017).

6.3.2.2. Reinforcement

Curvilinear sand-coated #5 GFRP bars with curve radii of 3,305 and 3,445 mm were used as longitudinal bars in the bottom and top meshes, respectively. Longitudinal bars were anchored with sand-coated U-shaped #5 GFRP bars. Sand-coated #4 GFRP bars were also

provided as transverse closed ties and U-shaped ties. The mechanical properties of the reinforcement were determined by tensile testing according to ASTM D7205-21 (ASTM D7205-21) (Table 6.3). The mechanical properties of the closed and U-shaped ties, however, were obtained by testing the straight bars manufactured with the same process as the bent bars.

6.3.3. Test setup and instrumentation

PCTL segments are subject to bending load during production, transition, and service stage with different loading and boundary conditions (ACI 533.5R-20). Therefore, three-point loading was selected to investigate their behavior under bending load (Fig. 6.5). As shown in Fig. 6.5, cylindrical supports covered with a Teflon sheet with a center-to-center distance of 2400 mm were used to minimize the friction, so that the specimens could easily move and rotate. The test setup is one of those commonly used in the literature to investigate the behavior of PCTL segments (ITA WG2-19). It should be noted that the actual load and boundary conditions for a tunnel segment are different from that provided through the test setup used in this study and some studies in the literature. Simulating actual loading and boundary conditions for a tunnel segment in a test setup is quite difficult due to interaction between the soil and structure in the field as well as the complex connection between segments and variations in the applied loads. Our test setup provides a determined system and facilitates finding the relationship between the internal forces and the external loads required for the analytical procedure. As the flexural strength, shear strength, and crack width are mostly related to the section, the obtained experimental and theoretical results can be used to design tunnel segments in real applications. Once the full ring has been analyzed using the methods in the related standards, the internal forces under real load and boundary conditions can be estimated and compared to those presented in this study. The load was applied through a spreader beam in a displacement-controlled manner with an MTS machine with a capacity of 11000 kN located in the CFI laboratory at the University of Sherbrooke. Mid-span deflections during the test were recorded with three linear potentiometers (LPOTs) distributed along specimen width while two LPOTs installed at the quarter-span recorded

Table 6.3 Mechanical properties of the GFRP reinforcement

Reinforcement Type	Bar Size	d_b (mm)	A_{fb} (mm^2)	E_f (GPa)	f_{fu} (MPa)	ε_{fu} (%)
Longitudinal GFRP bars	#5	15.0	199	55.1 ± 1.25	1,115 ± 60	2.0 ± 0.1
U-shaped GFRP bars	#5	15.0	199	53.5 ± 1.1	1,283 ± 42	2.4 ± 0.1
U-shaped and closed GFRP ties	#4	13.0	129	55.6 ± 1.6	1,248 ± 74	2.2 ± 0.1

Note: d_b is bar diameter; A_{fb} is nominal cross-sectional area; E_f is tensile modulus of elasticity; f_{fu} is the ultimate tensile strength; and ε_{fu} is the ultimate tensile strain.

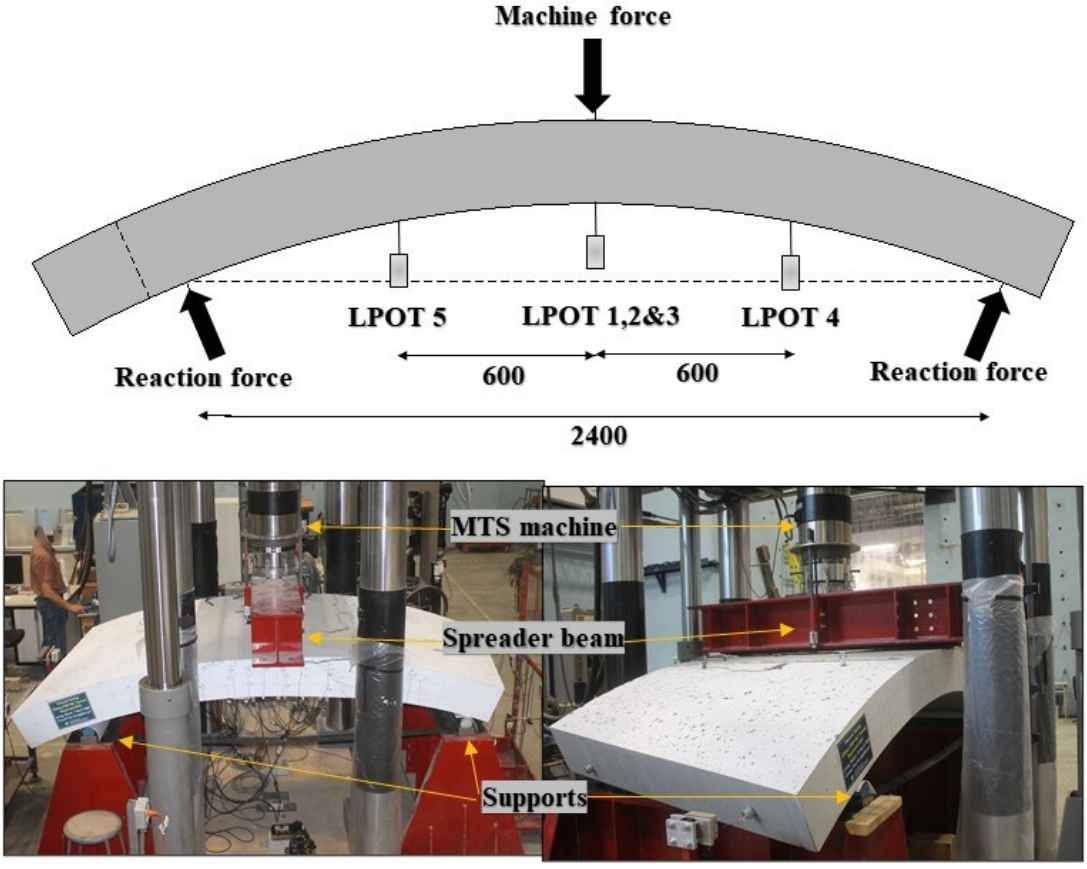

Figure 6.5 Test setup.

the quarter-span deflections (Fig. 6.5). Figure 6.6 shows the strain gauge installed on the reinforcement (designated by the letter "B") and concrete (designated by the letter "C") in the specimens. As can be seen in the figure, mid-span strain in the top and bottom reinforcement, concrete compressive strain at mid-span and quarter span, strain of the

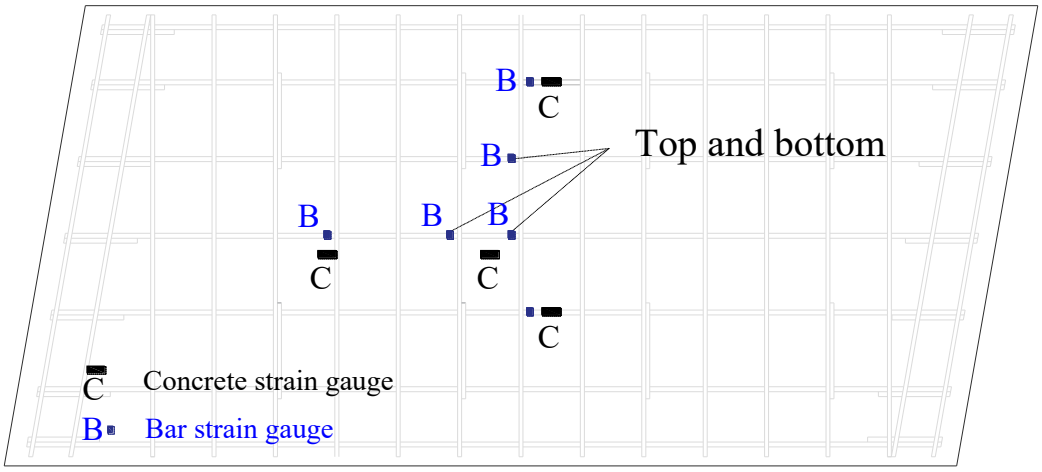

Figure 6.6 Strain-gauge locations.

longitudinal top and bottom reinforcement at the distance of 200 mm apart from the mid-span, and strain of reinforcement at the quarter-span were recorded with the strain gauges.

6.4. Test results and observation

6.4.1. Failure mechanism and cracking pattern

The first flexural crack initiated at loads ranging from 46 to 63 kN. The cracks in the FRC specimens initiated gradually with a width of less than 0.05 mm in 13G#5F and 0.1 mm in 7G#5F and 7G#5FU. In contrast, the cracks initiated abruptly in 13G#5 with an initial width of 0.15 mm. The number and width of flexural cracks increased as the load increased. The cracks initiated from the bottom surface of the specimens perpendicular to the segment axis and tended to have some inclination towards the loading plate as the load increased. With further loading, shear cracks appeared in the zone subjected to a combination of shear and flexural stresses at a load of 350, 384, 255, and 266 kN in specimens 13G#5, 13G#5F, 7G#5F, and 7G#5FU, respectively. The shear cracks formed gradually in the FRC specimens at an initial width of less than 0.05 mm; the widths were less than 0.25 mm at 95% of the peak load. In contrast, the shear cracks in 13G#5 formed with a large initial width and widened up to the peak load, so that this specimen failed due to diagonal tension failure. Due to the bridging role of fibers in shear cracks, specimen 13G#5F experienced minor concrete

Table 6.4 Experimental results, ductility, and deformability

Specimen ID	$f_c^{'}$ MPa	f_p MPa	f_{600}^{D} MPa	f_{150}^{D} MPa	P_{cr} kN	P_{peak} kN	Peak Load Deflection (mm)	Failure Mode	Crack Width at Service Load (mm)	Deflection at Service Load (mm)	Curvature $1/d$ at P_{peak}	J
13G#5	51	-	-	-	63	365	41	D.T	0.35	3.76	0.012	4.1
13G#5F	44	4.0	1.5	1.3	62	412	51	C.C+ D.T	0.15	3.74	0.016	7.0
7G#5F	50	4.5	1.0	0.8	49	312	73	C.C	0.35	2.51	0.021	5.5
7G#5FU	46	4.3	1.3	1.0	46	308	74	C.C	0.35	3.10	0.019	5.4

Note: D.T refers to diagonal tension failure and C.C refers to compression-controlled flexural failure; J refers to deformability factor.

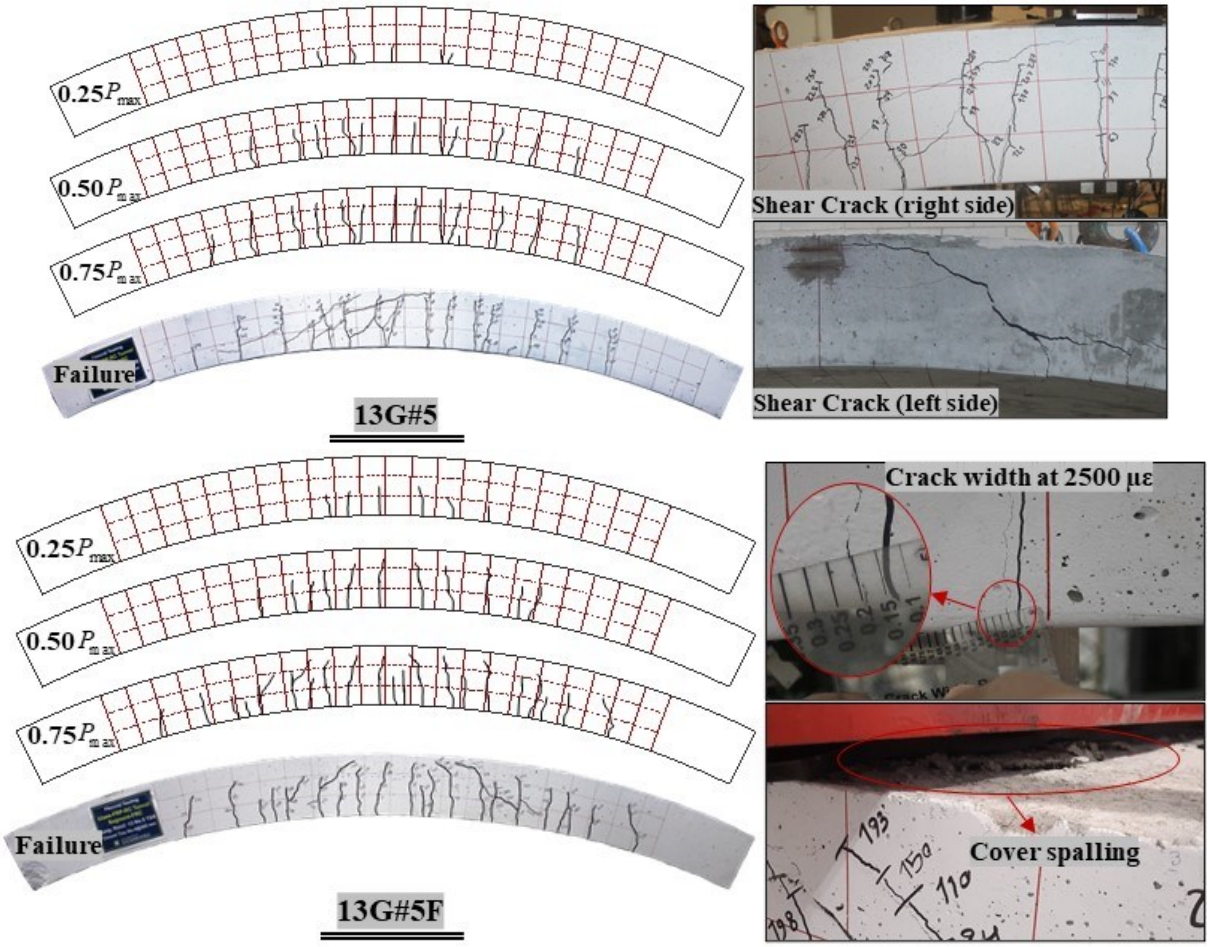

Figure 6.7 Failure modes and crack patterns of specimens 13G#5 and 13G#5F.

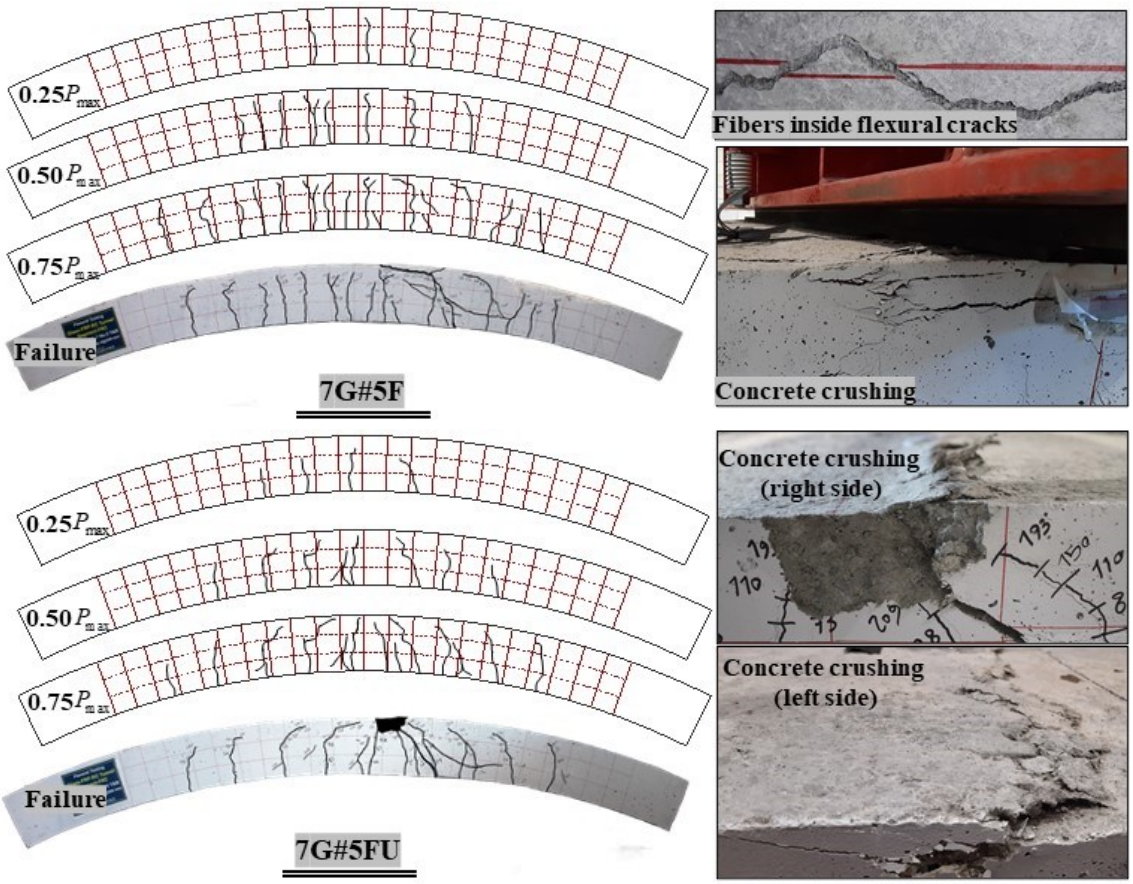

Figure 6.8 Failure modes and crack patterns of specimens 7G#5F and 7G#5FU.

spalling beneath the loading plate. Following that, the width of the shear cracks increased. As a result, this specimen failed by diagonal tension failure followed by concrete spalling. Specimens 7G#5F and 7G#5FU experienced gradual concrete crushing starting with concrete spalling in the zones near the loading plate and ending will full crushing of concrete and a reduction in the applied load denoting the concrete-crushing failure mode. A hybrid configuration of GFRP bars and FRC provided a more gradual failure mechanism compared to some FRC PCTL segments without reinforcement tested by Abbas (2014b). Figures 6.7 and 5.8 show the crack pattern of the specimens at different loading stages up to failure. Table 6.4 lists the compressive strength of the concrete on the date of testing, cracking load, peak load, deflection at peak load, failure mode, service-load crack width, and service mid-span deflection for the tested specimens. In this study, the service load was defined as the load corresponding to a strain of 2000 $\mu\varepsilon$ in the longitudinal bottom bars, as this value yielded reasonable results in the literature (El-Nemr et al. 2018; Mousa et al. 2019c). The

crack width at service load was recorded with a crack-width roller during the test. According to Table 6.4, the service-load crack width was 0.15 mm in 13G#5F and 0.35 mm in the other specimens, which was 70% and 40% narrower than the allowable service-crack width (0.5 mm) in harsh environments according to CAN/CSA S6-19. The average crack spacing at service load was 200, 140, 200, and 185 mm, respectively, in 13G#5, 13G#5F, 7G#5F, and 7G#5FU in the middle third of the specimens. By increasing the load up to 75% of peak load, the crack spacing decreased to 140, 85, 110, and 135 mm, respectively, due to initiation of more cracks.

6.4.2. Load–deflection relationships

The load–deflection behavior of each specimen can be divided into three stages of pre-cracking, post-cracking, and post-peak. Before the first crack initiated, the specimens experienced linear load–deflection behavior with almost the same stiffness (Fig. 6.9). After cracking, the slope of the load–deflection diagram decreased gradually while no noticeable load reduction occurred after crack formation due to presence of fibers in 7G#5F and 7G#5FU. In contrast, a temporary load reduction after crack formation in the GFRP-reinforced flexural elements was reported in some studies in the literature especially for members with relatively low reinforcement ratios (Michaluk et al. 1998; Chang and Seo 2012; Nigro et al. 2012; Goldston et al. 2017). Specimens 7G#5F and 7G#5FU exhibited linear post-cracking behavior at up to 90% of the peak load. Thereafter, the slope of the load deflection decreased approaching the peak load due to gradual concrete crushing as a result of the fibers. Specimen 7G#5FU experienced a gradual load reduction after peak load (post-peak stage) until its final failure. Specimen 7G#5F, however, experienced a rapid decrease in load after concrete crushing, which was then recovered with increasing deflection until a second decrease occurred due to full crushing of the concrete. In contrast, specimens 13G#5 and 13G#5F had a linear post-cracking load–deflection relationship up to shear failure. The same trend was observed in the load–deflection diagram of the specimens at quarter-span (Fig. 6.9). The post-cracking stiffness (the average slope of the load–deflection diagram started from cracking point to peak load) of 13G#5, 13G#5F, 7G#5F, and 7G#5FU was 7.65, 7.74, 4.03, and 4.20 kN/mm, respectively. The service-load deflection was, on average,

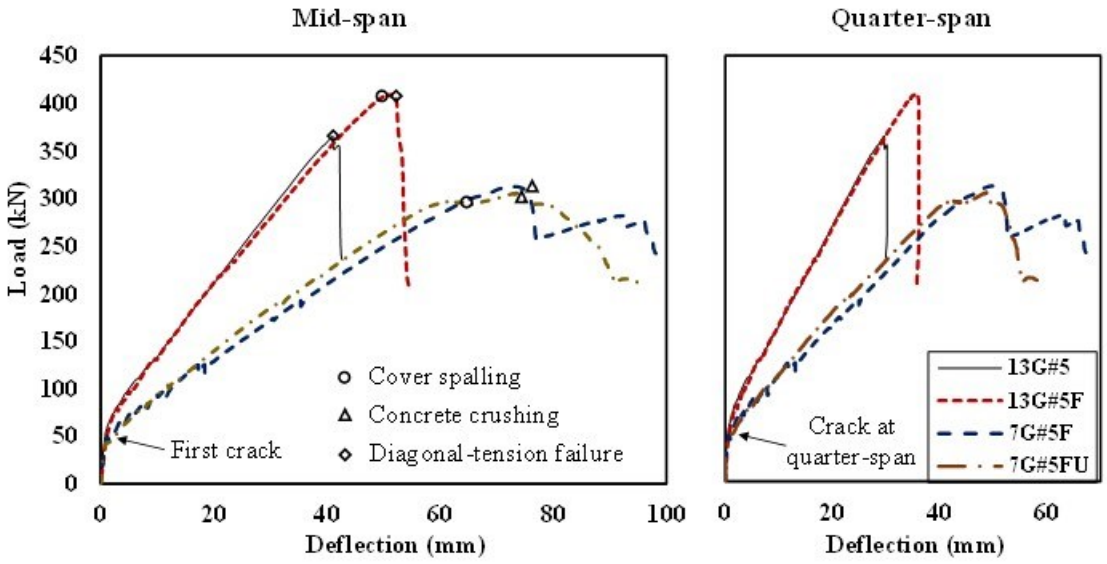

Figure 6.9 Load–deflection diagram of the tested specimens.

3.75±0.01 mm and 2.80±0.3 mm at an average service load of 87±2.0 kN and 54.5±0.1 kN in the specimens reinforced with 13 and 7 longitudinal bars, respectively. Considering all the applied service load as the sustained load, the long-term deflection of the specimens was calculated as 4.50±0.01 mm and 3.36±0.36 mm for the specimens with 13 and 7 longitudinal bars, respectively, considering the time-dependent factor of ξ as in ACI 440.1R-15. These values are 14% and 36% less than L/480 (L is the span length), which is the allowable deflection of flexural elements likely to be damaged by large deformations, as provided for in CAN/CSA S806-12, R2017.

6.4.3. Strain in the reinforcement and concrete

Figure 6.10a presents the relationship between the applied load and the bottom longitudinal bar strain at mid-span. While the strain was minimal before the first crack occurred, a rapid increase in the measured strain was observed in the specimens upon the first crack. After a stabilization period, specimens 13G#5 and 13G#5F exhibited a linear load–strain relationship until the peak load was reached. While a nearly linear load–strain relationship was observed in specimens 7G#5FU and 7G#5F until 95% of the peak load, the slope of the load–strain diagram decreased significantly near the peak load, which can be attributed to gradual crushing of the concrete in these specimens. The maximum recorded mid-span strain

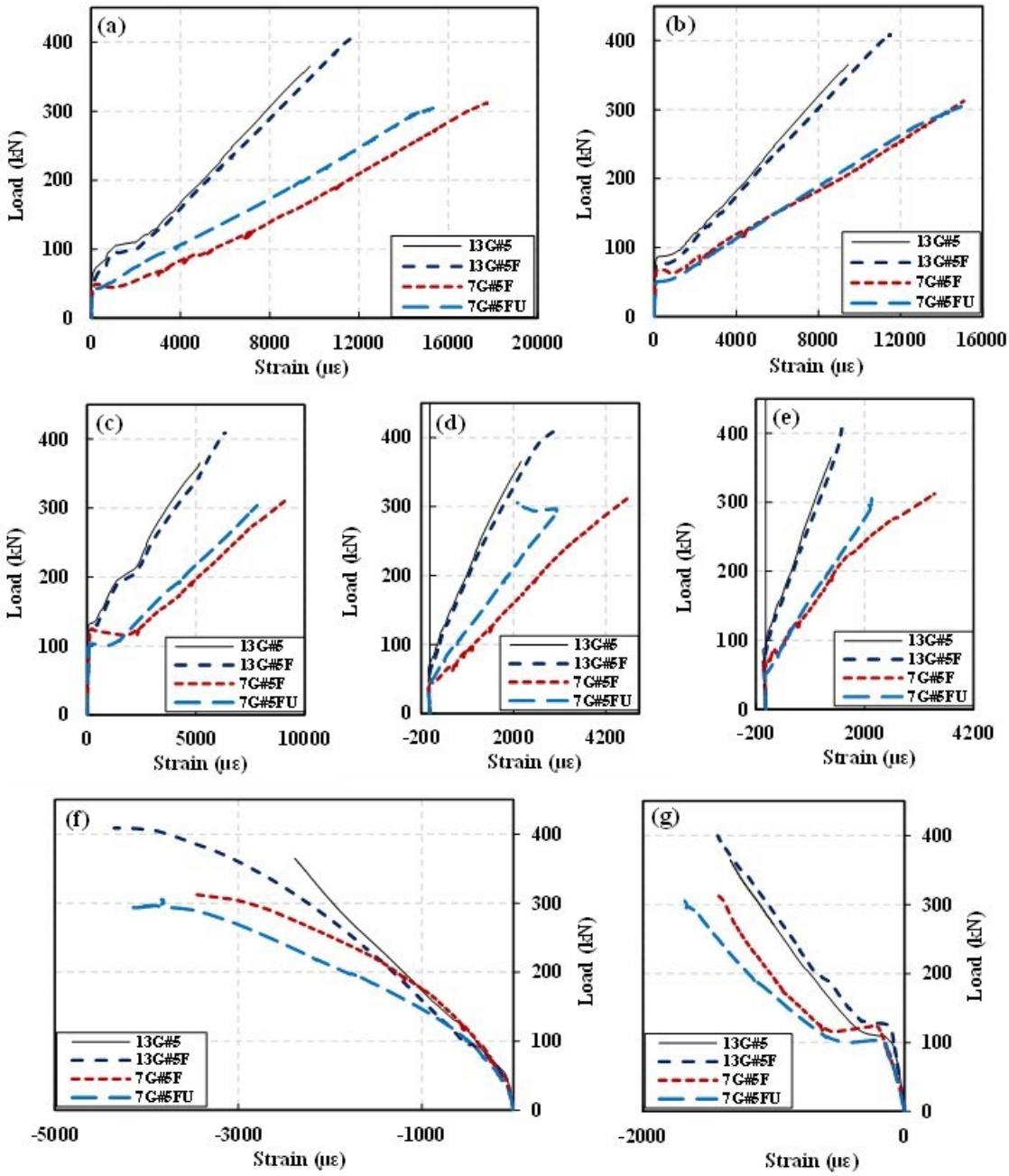

Figure 6.10 Load–strain relationship of the reinforcement and concrete: (a) bottom mesh, mid-span; (b) bottom mesh, 200 mm from the mid-span; (c) bottom mesh, quarter-span; (d) top mesh, mid-span; (e) top mesh, 200 mm from the mid-span; (f) concrete strain, mid-span; and (g) concrete strain, quarter-span.

was 9400, 11800, 17700, and 15400 $\mu\varepsilon$, corresponding to 47%, 59%, 89%, and 77% of the ultimate rupture strain of the longitudinal bars in specimens 13G#5, 13G#5F, 7G#5F, and 7G#5FU, respectively. Figure 6.10b gives the load–strain relationship of the bottom longitudinal bar located 200 mm from the mid-span. Before initiation of the second crack in

the specimens, the recorded strain in the longitudinal bars at the location 200 mm apart from the mid-span was minimal. However, after formation of the second crack in the specimens located within the distance 200 mm from the mid-span, the strain increased rapidly. The load–strain diagram was nearly linear trend after a stabilization period until the peak load was reached. The maximum strain recorded in the bottom bar 200 mm from the mid-span was 10000, 11600, 15100, and 15000 $\mu\varepsilon$, respectively, in 13G#5, 13G#5F, 7G#5F, and 7G#5FU. Figure 6.10c gives the load–strain relationship of the bottom bar at the quarter-span. The recorded strain was minimal before cracking initiated in the zone near the quarter-span. After cracking at the quarter-span, the strain rapidly increased, especially in the specimens reinforced with 7 longitudinal bars. After a linear load–strain behavior, the maximum quarter-span strain at the peak load was 4700, 6400, 9200, and 7900 $\mu\varepsilon$ in 13G#5, 13G#5F, 7G#5F, and 7G#5FU, respectively. Figures 6.10d and 5.10e present the relationship between the load and strain in the longitudinal top bar at mid-span and 200 mm from the mid-span, respectively. There was minimal compressive strain before the flexural cracks crossed the top layer of the reinforcement. Once the cracks had crossed the reinforcement, however, the top bars carried the tensile load since the location of the neutral-axis depth was above the top reinforcement. The load–strain relationship of specimens 13G#5 and 13G#5F was almost linear up to the peak load. In contrast, 7G#5F and 7G#5FU showed some deviations approaching to the peak load, which can be attributed to gradual concrete crushing.

Figures 6.10f and 6.10g represent the recorded concrete compressive strain mid-span and the quarter-span, respectively. The mid-span strain was recorded with three strain gauges; the average values are reported in Fig. 6.10f. After the first crack initiated, the slope of the load-strain curve decreased at mid-span. Specimen 13G#5, however, exhibited nearly linear behavior; when the load increased in the fiber-reinforced specimens, the slope of the load–strain diagram decreased. The maximum recorded concrete compressive strain at mid-span was 2400, 4350 3450, and 3900 $\mu\varepsilon$ in 13G#5, 13G#5F, 7G#5F, and 7G#5FU, respectively. After a rapid increase in concrete compressive strain upon initiation of a flexural crack at

the quarter-span, the load–strain relationship remained almost linear until the peak load was reached.

6.5. Discussion of Test Results

6.5.1. Influence of concrete type

The influence of concrete type can be examined by comparing the results of the specimens 13G#5 and 13G#5F. According to Table 6.4, using FRC did not affect the cracking load. Nevertheless, the initiation width of flexural cracks was 0.05 mm and 0.15 mm in 13G#5F and 13G#5, respectively, denoting a 67% narrower initial crack width with FRC. It can be attributed to the contribution of the fibers in carrying the stresses released upon cracking. Due to the bridging effect of fibers, the service-load crack width was 0.15 mm in 13G#5F, which was 57% narrower than 13G#5. Abbas (2014b) and Caratelli et al. (2011) reported fewer cracks in FRC PCTL segments without reinforcement compared to conventional RC PCTL segments. The hybrid configuration of FRC and GFRP reinforcement in 13G#5F led, however, to flexural cracks with 35% closer spacing than in 13G#5. This could be attributed to improved bond properties of the reinforcement in GFRP-reinforced members made with FRC (Won et al. 2008). Enhancing the bond strength of GFRP bars in concrete reduces crack spacing, leading to a higher number of narrower cracks (Theriault and Benmokrane 1998; El-Nemr et al. 2013). Although 13G#5F had concrete compressive strength 14% lower than 13G#5, it had almost the same post-cracking stiffness. This indicates the efficiency of fibers in improving the post-cracking stiffness of GFRP-reinforced PCTL segments. Using fibers postponed the initiation of shear cracks and controlled their width until the peak load was reached, so that 13G#5F recorded 13% and 24% higher load-carrying capacity and deflection at peak load, respectively, than 13G#5. In addition, using fibers could change the failure mode from diagonal tension failure (shear failure) in 13G#5 to concrete crushing followed by diagonal tension failure (shear-flexural failure) in 13G#5F.

Table 6.4 lists the curvature of the specimens at peak load calculated using the recorded strain in the section. In addition, the deformability of the specimens (J-factor) was calculated

according to CAN/CSA-S6 and is presented in Table 6.4. Using FRC in GFRP-reinforced PCTL-segments improved the curvature at peak load and deformability by 33% and 71%, respectively.

6.5.2. Influence of reinforcement ratio and spacing

A comparison of specimens 7G#5F and 13G#5F could reveal the influence of reinforcement ratio governed by two different spacing values. Increasing the reinforcement ratio by 86% (7G#5F to 13G#5F) enhanced the cracking load by 27%. Enhancing the cracking load by increasing the reinforcement ratio in FRP-reinforced flexural elements is consistent with some studies in the literature (Barris et al. 2017; El-Nemr et al. 2018; Mousa et al. 2019c; Mousa et al. 2019a). The initial crack width was 0.05 mm in 13G#5, which was 50% narrower than in 7G#5F. In addition, the service load crack width (0.15 mm) was 57% narrower in this specimen compared to 7G#5F. In fact, a higher reinforcement ratio can carry greater stress at cracking, thereby tempering crack initiation (Theriault and Benmokrane 1998). Increasing the reinforcement ratio also reduced the crack spacing by 30% and 23% at service load and 75% of the peak load, respectively. The post-cracking stiffness of 13G#5F was 92% than of 7G#5F, which is close to the ratio of reinforcement axial stiffness in these specimens. The peak load enhanced by 32% with increased reinforcement ratio, while the deflection and curvature at peak load decreased by 30% and 24%, respectively. In addition, increasing the reinforcement ratio changed the failure mode from flexural to shear flexural. Increasing the reinforcement ratio enhanced both the flexural and shear capacities of the specimen. Therefore, a greater load should be applied to govern flexural failure. On the other hand, increasing the applied load led to an increase in the specimen's shear force. Shear failure occurred when the increased shear force in the specimen was greater than the increased shear capacity due to a higher reinforcement ratio. Although 13G#5F had a shear flexural failure mode, the deformability index of 13G#5F was 27% higher than that of 7G#5F.

6.5.3. Influence of tie configuration

A comparison of 7G#5F and 7G#5FU reveals the influence of tie configuration. Differences in their concrete properties, however, should also be considered. Table 6.4 indicates that the FRC used in 7G#5FU had higher residual strength than that of 7G#5F. 7G#5FU had slightly higher post-cracking stiffness (4%) and experienced more gradual concrete crushing (Fig. 6.9) than 7G#5F. The slope of the load–strain diagram for the concrete was slightly lower for 7G#5FU than 7G#5F, which can be attributed to its lower peak strength (8.0%). The same justification might be used for 7G#5FU having lower peak load (1.0%) than 7G#5F. Specimens 7G#5F and 7G#5FU had almost the same cracking behavior in terms of initiation width, spacing, and width. In general, it can be concluded that closed ties and U-shaped ties provided similar structural behavior for GFRP-reinforced FRC PCTL segments.

6.6. Analytical Investigation

6.6.1. Flexural strength of GFRP-reinforced FRC PCTL segments

This section introduces two methods to predict the flexural strength of GFRP-reinforced FRC PCTL segments taking into account the contribution of fibers.

6.6.1.1. Simplified method

According to ACI 544.4R-18, the moment capacity of a member with hybrid reinforcement of longitudinal bars and fiber reinforcement (M_{n-HFRC}) can be obtained with this equation:

$$M_{n-HFRC=}M_{n-RC}+M_{n-FRC} \tag{6.2}$$

where M_{n-RC} is the bending-moment capacity of the section with plain concrete, which can be obtained with conventional methods according to ACI 440.1R-15 or CAN/CSA S806-12, R2017. M_{n-FRC} is the bending capacity provided by the fibers, which can be calculated as (ACI 544.4R-18):

$$M_{n-FRC}=f_{150}^{D}\times\frac{bh^2}{6} \tag{6.3}$$

Equation 6.3 was obtained through supposing the neutral axis depth in an FRC section without reinforcement equal to $0.1h$. In addition, a linear stress-strain relationship in compression zone of the section and a constant tensile stress carried out by fibers in the tension zone was assumed. Thereafter, the bending moment presented in Eq. 6.3 was obtained by equalizing the mentioned section to an un-cracked section with the maximum tensile and compressive stress equal to f_{150}^{D} (Vandewalle, L., 2003).

6.6.1.2. Direct method based on the stress–strain behavior of FRC

The flexural strength of GFRP-reinforced FRC segments can be calculated using stress and strain distribution along the cross section. There are several models for the stress–strain relationship of FRC in compression and tension (Soranakom and Mobasher 2007; Bencardino et al. 2008; Chi et al. 2014; ACI 544.7R-16; ACI 544.4R-18; Deng et al. 2021). Figure 6.11 presents the stress–strain model in tension and compression used for the flexural-strength prediction in this study. This model has been adopted from ACI 544.4R-18 based on the model proposed by Soranakom and Mobasher (2007). According to Fig. 6.11a, the tensile response follows a linear behavior with a stiffness of E_c up to the stress and strain at the first crack, σ_{cr} and ε_{cr}, respectively. After cracking, the residual stress value (σ_p) remains constant until the ultimate strain of ε_{tu}. An elastic-plastic behavior was assumed for the compression response with a linear branch with a stiffness of E_c (considering almost the same concrete modulus of elasticity in tension and compression) up to ε_{cy}, followed by the constant stress value of σ_{cy} up to the ultimate concrete compressive strain (ε_{cu}). The parameters used in the stress–strain response of FRC can be obtained with beam and compressive tests. σ_{cr} can be considered equal to f_p obtained with the beam test in ASTM C1609-19. E_c can be simply assumed as $4700\sqrt{f_c'}$ as in ACI 318-19 or obtained directly from the beam test this equation:

$$E_c = \frac{23}{108}\frac{P_{cr}L^3}{\delta_{cr}b_b h_b^3} \tag{6.4}$$

ε_{cr} can be calculated by dividing σ_{cr} by E_c. Since f_{150}^D is calculated based on the uncracked section, it cannot be directly used as σ_p. The literature (ACI 544.7R-16) suggests an adjustment factor ranging from 0.33 to 0.37. According to ACI 544.4R-18, this equation can be used to obtain σ_p from the beam test conducted based on ASTM C1609-19. Eq. 6.5 was derived by the same assumptions explained for obtaining Eq. 6.3.

$$\sigma_p = 0.37 f_{150}^D \tag{6.5}$$

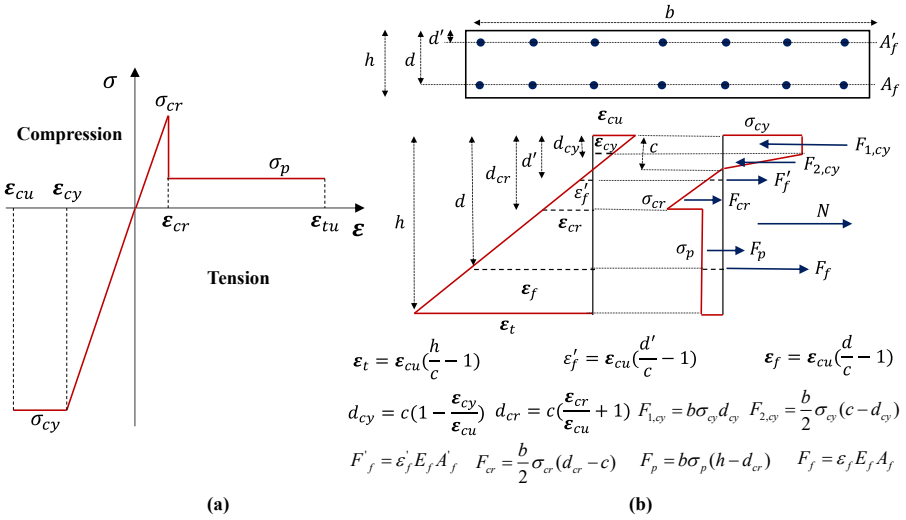

Figure 6.11 (a) Stress–strain model for the FRC; (b) idealized stress and strain distribution.

The parametric-based back-calculation procedure presented by Soranakom and Mobasher (2007) can be used to calculate ε_{tu} according to the beam test results. Since the former approach requires complicated calculations, ε_{tu} can be taken as 2% according to CNR-DT 204/2006 if there are no limitations for the tensile strain limit for FRC in the project. σ_{cy}, ε_{cy}, and ε_{cu} can be estimated based on the compressive stress–strain curve of concrete.

Figure 6.11b shows a typical section of a GFRP-reinforced PCTL segment with a width of b and height of h subjected to combined bending moment and axial load. The figure shows the stress distribution and the resultant forces acting on the segment considering a linear distribution of strain along the section. As concrete crushing is the preferred failure mode for GFRP-reinforced flexural elements according to ACI 440.1R-15 and CAN/CSA S806-12, R2017, the analytical procedure assumes that the concrete reaches its ultimate compressive strain. In addition, the stress distribution presented is valid when ε_t is greater

than ε_{cr} and lower than ε_{tu}. Figure 6.11b presents the relationship between the unknown values and the neutral-axis depth c using strain compatibility. The forces acting on the segments can be calculated by assuming the value of c. The top longitudinal bars are assumed to carry the tensile load, which was observed in the experimental results. When the neutral-axis depth is below the top longitudinal bars, their contribution in carrying compressive stress should be neglected according to ACI 440.1R-15 and CAN/CSA S806-12, R2017. The following equation presents the force equilibrium in the section:

$$F_f + F_f^{'} + F_{cr} + F_p + N - F_{1,cy} - F_{2,cy} = 0 \quad (6.6)$$

By satisfying the equilibrium condition in Eq. 6.6 by adjusting the neutral-axis depth using trial and adjustment, Eq. 6.7 can be used to calculate the nominal moment capacity of the section. The authors used Excel software to minimize the time and effort in conducting the trial and adjustment process.

$$M_{n-HFRC} = F_f d + F_f^{'} d^{'} + F_{cr}\left(\frac{c+2d_{cr}}{3}\right) + F_p\left(\frac{d_{cr}+h}{2}\right) + N\left(\frac{h}{2}\right) - F_{1,cy}\left(\frac{d_{cy}}{2}\right) - F_{2,cy}\left(\frac{2d_{cy}+c}{3}\right) \quad (6.7)$$

6.6.2. Shear strength of segments

During the service stage, a tunnel segment is subjected to a combination of bending moment, axial load, and shear force. To avoid undesirable shear failure, the shear capacity of GFRP-reinforced PCTL segments should be predicted in the design procedure. This section briefly presents the provisions of North American standards (ACI 440.1R-15, CAN/CSA S806-12, R2017, and CAN/CSA S6-19, 2019) that can be employed to predict the shear capacity of GFRP-reinforced NC flexural elements. Thereafter, some methods and models are proposed to consider the contribution of fibers to the shear strength of GFRP-reinforced FRC PCTL segments. As a conservative assumption, the contribution of transverse ties to the shear capacity of the segments is neglected since they cannot provide considerable shear capacity.

6.6.2.1. Shear strength of GFRP-reinforced NC segments

Table 6.5 presents the models recommended in ACI 440.1R-15, CAN/CSA S806-12, R2017, and CAN/CSA S6-19 to predict the shear capacity of GFRP-RC elements. The contribution of the uncracked compression block is the only shear-transferring mechanism considered in

ACI 440.1R-15. CAN/CSA S806-12, R2017, however, considers the contribution of the uncracked concrete and aggregate interlock, while the shear-capacity prediction model in CAN/CSA S6-19 is based on the simplified modified compression field theory model.

6.6.2.2. Shear strength of GFRP-reinforced FRC PCTL segments

ACI 544.4R-18 gives Eq. 6.8 to calculate the shear capacity of a fiber-reinforced concrete sections with steel rebars.

$$V_{FRC} = \left\{ \frac{0.18}{\gamma_c} k_s \left[100\rho(1+7.5\frac{f_{ut-FRC}}{f_t}) f_c^{'} \right]^{\frac{1}{3}} + 0.15\sigma_{cp} \right\} bd \tag{6.8}$$

where $k_s = 1+\sqrt{200/d} \le 2.0$; f_{ut-FRC} can be assumed to be equal to σ_p in Eq. 6.5; f_t is the tensile strength of plain concrete, which can be considered as $0.62\sqrt{f_c^{'}}$; and σ_{cp} is the average normal stress acting on the cross section, which can be taken as N/bh. Equation 6.8 originally proposed by Model Code 2010 (2013) for steel-fiber reinforced concrete sections with conventional strength. To derive Eq. 6.8, the presented equation in EN-1992-1-1 (2004) for plain concrete was modified to consider the effect of FRC toughness in shear strength of the FRC members without shear reinforcement (Di Prisco et al. 2010). Equation 6.8 cannot be directly employed for GFRP-reinforced FRC elements. Since GFRP bars have a lower modulus of elasticity than steel rebars, the compression block depth is smaller and the cracks are wider. Therefore, the shear capacity provided by the uncracked section and aggregate interlock is smaller. In addition, the contribution of the longitudinal bars in terms of dowel action is less with GFRP reinforcement than steel (ACI 440.1R-15). The model presented in Eq. 6.8 is based on semi-empirical models. Therefore, it cannot be modified for GFRP-reinforced FRC elements with an analytical procedure. Some simple methods are, however, presented below to use Eq. 6.8 in designing GFRP-reinforced FRC tunnel segments.

Method I

Equation 6.9 is derived based on the ratio of the concrete shear capacity of GFRP-reinforced flexural elements to their steel counterparts according to the equations in ACI 440.1R-15

and ACI 318-19. This equation can be used to estimate the shear capacity of FRP-reinforced FRC elements.

$$V_{HFRC,I} = \frac{12}{5} k V_{FRC} \tag{6.9}$$

where k is calculated based on Table 6.5.

Table 6.5 Models presented by North American standards for shear-capacity prediction

Standard	Model
ACI 440.1R	$V_c = \frac{2}{5}\sqrt{f_c'} b_w (kd)$ where $k = \sqrt{2\rho n_f + (\rho n_f)^2} - \rho n_f$, $\rho = \frac{A_f}{bd}$, $n_f = \frac{E_f}{E_c}$
CSA S806	$V_c = \left[0.05\lambda k_m k_r (f_c')^{\frac{1}{3}} b_w d_v\right] k_s k_a (1 + \frac{0.3N}{A_g}) \geq 0.1\lambda\sqrt{f_c'} b_w d$, for axial tension $V_c = \left[0.05\lambda k_m k_r (f_c')^{\frac{1}{3}} b_w d_v\right] k_s k_a (1 + \frac{N}{14A_g}) \geq 0.11\sqrt{f_c'} b_w d_v$, for axial compression where $V_c \leq 0.22\sqrt{f_c'} b_w d_v$, $k_a (1 + \frac{N}{14A_g}) \leq 3.0$, $k_m = \sqrt{\frac{V_f d}{M_f}} \leq 1.0$, $k_r = 1 + (E_f \rho_f)^{\frac{1}{3}}$, $1.0 \leq k_a = \frac{2.5}{M_f / (V_f d)} \leq 2.5$, $k_s = \frac{750}{450 + d} \leq 1.0$
CSA S6	$V_c = 2.5\beta f_{cr} b_w d_v$ where $\beta = \left[\frac{0.4}{1 + 1500\varepsilon_x}\right]\left[\frac{1300}{1000 + S_{ze}}\right]$, $\varepsilon_x = \frac{\frac{M_f}{d_v} + V_f - 0.5N}{2E_f A_f} \leq 0.003$ $s_{ze} = \frac{35 s_z}{15 + a_g} \geq 0.85 s_z$

Method II

Equation 6.10 is obtained based on the equations presented in CAN/CSA S6-19 to determine the shear capacity of steel-reinforced and FRP-reinforced sections.

$$V_{HFRC,II} = \frac{1 + 1500(\frac{E_f}{E_s})\varepsilon_x}{1 + 1500\varepsilon_x} V_{FRC} \tag{6.10}$$

where ε_x is obtained according to Table 6.5 and E_s is typical modulus of elasticity of steel reinforcement, which can be taken as equal to 200 GPa.

Method III

According to Eq. 6.8, the ratio of shear capacity of FRC to that of its plain counterpart is $(1+7.5\frac{f_{ut-FRC}}{f_t})^{(1/3)}$. Therefore, the shear capacity of GFRP-reinforced FRC flexural elements can be estimated by multiplying the shear capacity obtained from Table 6.5 according to the different standards by $(1+7.5\frac{f_{ut-FRC}}{f_t})^{(1/3)}$.

6.7. Comparison of Analytical and Experimental Results

Table 6.6 presents the comparison of the experimental bending-moment capacity and theoretical values obtained with the presented analytical procedures. In determining the analytical results, all the reduction factors were considered as equal to 1.0. In the simplified procedure, the bending-moment capacity provided by the fibers (M_{n-FRC}) was added to the values calculated based on ACI 440.1R-15 and CAN/CSA S806-12, R2017 and presented in the table separately for comparison. The required values to obtain the stress–strain behavior of FRC were obtained from the results of the compression and beam testing. Based on the compression test, ε_{cy} was taken as 0.003 for all FRC specimens, while ε_{cu} was taken as 0.0035 for 7G#5F and 7G#5FU and 0.004 for 13G#5F. Specimen 13G#5F experienced concrete spalling and wide shear cracks at the same time. Therefore, it can be inferred that this specimen reached to its flexural and shear capacity almost simultaneously, the experimental results of this specimen can be used to evaluate the analytical models in both shear and flexure. According to Table 6.6, ACI 440.1R-15 estimated the flexural capacity of 7G#5F and 7G#5FU with an error of ±3% while neglecting the contribution of the fibers in this standard underestimated the bending moment capacity of 13G#5F by 8%. CAN/CSA S806-12, R2017 accurately predicted the bending moment capacity of 13G#5F, but overestimated the moment capacity of 7G#5F and 7G#5FU by 15% and 7%, respectively. This can be related to the higher ultimate concrete compressive-strain values at failure in 13G#5F and 7G#5FU compared to 7G#5F. Considering the contribution of the fibers in ACI 440.1R-15 with the simplified method led to an accurate prediction of 13G#5F's flexural

capacity, while it overestimated the flexural capacity of 7G#5F and 7G#5FU by 5%. Applying the simplified method to the values obtained from CAN/CSA S806-12, R2017 overestimated the bending-moment capacity by 13% on average. The direct method based on the stress–strain behavior of the FRC predicted the flexural capacity with an error of less

Table 6.6 Comparison of the analytical and experimental flexural strength values

Specimen ID	$M_{exp.}$ kN.m	Theoretical Values									
		Without considering the contribution of fibers				Considering the contribution of fibers					
		ACI 440.1R		CAN/CSA S806		Simplified method				Direct method	
						ACI 440.1R		CAN/CSA S806			
		M_{Theo} kN.m	$M_{Theo}/M_{exp.}$	$M_{Theo.}$ kN.m	$M_{Theo}/M_{exp.}$	M_{Theo} kN.m	$M_{Theo}/M_{exp.}$	$M_{Theo.}$ kN.m	$M_{Theo.}/M_{exp.}$	$M_{Theo.}$ kN.m	$M_{Theo.}/M_{exp.}$
13G#5F	282	259	0.92	282	1.00	280	0.99	302	1.07	280	0.99
7G#5F	213	217	1.02	244	1.15	223	1.05	250	1.17	221	1.04
7G#5FU	209	203	0.97	223	1.07	219	1.05	239	1.14	206	0.99

Table 6.7 Comparison of the analytical and experimental shear strength values

Specimen ID	$V_{exp.}$ kN	$V_{Theo.}/V_{exp.}$							
		ACI 440.1R	CSA S806	CSA S6	Meth. I	Meth. II	Meth. III		
							ACI 440.1R	CSA S806	CSA S6
13G#5	183	0.63	0.92	0.74	-	-	-	-	-
13G#5F	207	0.51	0.7	0.56	0.63	0.80	0.64	0.88	0.69

than 2% on average. Therefore, the authors recommend the direct method as being the most accurate method presented in this study for estimating the bending-moment capacity of GFRP-reinforced FRC PCTL segments. Furthermore, combining the simplified method and ACI 440.1R-15 is recommended as a simple method with acceptable accuracy.

Table 6.7 compares the experimental shear forces (obtained from the recorded peak load during the test) with the shear capacities estimated by ACI 440.1R-15, CAN/CSA S806-12, R2017, CAN/CSA S6-19, and the three presented methods in this study. With an 8% underestimation, the model presented in CAN/CSA S806-12, R2017 was the least conservative model in predicting the shear capacity of GFRP-reinforced PCTL segments with NC, while the model recommended in ACI 440.1R-15 was the most conservative model with a 37% underestimation. Neglecting the contribution of the fibers underestimated the

shear capacity of 13G#5F by 49%, 30%, and 44% according to ACI 440.1R-15, CAN/CSA S806-12, R2017, CAN/CSA S6-19, respectively. Considering the contribution of the fibers in methods I and II underestimated the shear capacity by 37% and 20%, respectively. Applying method III to the results obtained from the standards improved their prediction accuracy by 25%, so that method III underestimated the shear capacity by 36%, 12%, and 31% when applied to the results obtained from ACI 440.1R-15, CAN/CSA S806-12, R2017, CAN/CSA S6-19, respectively. It should be noted that the shear-capacity ratio of 13G#5F to 13G#5 obtained from V_{FRC} in Eq. 6.8 is 12%, which in agreement with the ratio of the experimental shear capacities of 13G#5F to that of 13G#5. Method III shows accuracy in predicting the contribution of the fibers to the shear capacity of the segments. Applying method III to the results obtained from CAN/CSA S806-12, R2017 yielded the least conservative results among the presented methods with an underestimation of 12%.

6.8. Conclusions

The following conclusions can be drawn:

1. The GFRP-reinforced NC tunnel specimen with a reinforcement ratio 2.6 times the balanced ratio (0.9%) followed a typical cracking and deflection behavior of GFRP-reinforced flexural elements under bending load and finally failed in diagonal tension.
2. Using FRC changed the failure mode to concrete crushing followed by shear failure. The initiation and service-crack widths were 67% and 57% narrower in the FRC specimen, respectively, compared to its NC counterpart. The fiber contribution could enhance the load-carrying capacity, deflection at peak load, maximum concrete compressive strain, and deformability by 12%, 24%, 81%, and 71%, respectively. The service-load crack width and deflection in the GFRP-reinforced FRC tunnel segment with the reinforcement ratio of 0.9% were 70% and 15% lower than the maximum allowable values in CAN/CSA S6-19 and CAN/CSA S806-12, R2017, respectively.
3. The FRC tunnel segment specimen with the reinforcement ratio 1.7 times the balanced ratio (0.48%) failed by gradual concrete crushing. The crack width and

deflection at service load in this specimen were 30% and 36% smaller than the allowable values in CAN/CSA S6-19 and CAN/CSA S806-12, R2017. Increasing the reinforcement ratio by 86% in the GFRP-reinforced FRC PCTL segment enhanced the cracking load, post-cracking stiffness, and peak load by 29%, 92%, and 31%, while reducing the initial crack width, crack spacing, and crack width at service load by 50%, 30%, and 57%, respectively.

4. Comparing the tunnel segment specimens fabricated with closed transverse and U-shaped ties revealed that that these ties provided similar structural behavior in the GFRP-reinforced FRC PCTL segments under bending load.
5. The analytical investigation presented and compared the direct method based on the stress–strain behavior of the FRC and a simplified method based on ACI 440.1R-15. The flexural capacity was predicted with an error of less than 2% and 5% with the direct and simplified methods, respectively.
6. Three methods were presented in this study to predict the shear capacity of GFRP-reinforced FRC PCTL segments. Methods I and II provided highly conservative and conservative results, respectively, while modifying the results obtained from CAN/CSA S806-12 R2017 with method III was less conservative in predicting the shear capacity of GFRP-reinforced FRC PCTL segments. Due to the limited number of specimens in this study, there is a need to investigate a greater number of specimens with different parameters in order to assess the accuracy of the methods presented.

CHAPTER 7 DEVELOPMENT OF STRENGTH INTERACTION DIAGRAMS FOR DESIGNING PRECAST CONCRETE TUNNEL LINING SEGMENTS REINFORCED WITH GFRP BARS

Foreword

Authors and Affiliation:

Seyed Mohammad Hosseini: Ph. D. Candidate, Department of Civil Engineering, University of Sherbrooke, Sherbrooke, Quebec, Canada, J1K 2R1

Salaheldin Mousa: Postdoctoral fellow, Department of Civil Engineering, University of Sherbrooke, Sherbrooke, Quebec, Canada, J1K 2R1

Hamdy M. Mohamed: Research associate and lecturer, Department of Civil Engineering, University of Sherbrooke, Sherbrooke, Quebec, Canada, J1K 2R1.

Brahim Benmokrane: Professor, Department of Civil Engineering, University of Sherbrooke, Sherbrooke, Quebec, Canada, J1K 2R1.

Journal title: Engineering Structures

Paper status: Final version, published online in June 2023.

Contribution in thesis:

In this chapter, novel procedures and equations were developed to obtain design interaction diagrams for GFRP-reinforced PCTL segments. Afterward, a parametric study was performed to evaluate the effect of different parameters on the axial load–bending moment interaction diagrams of GFRP-reinforced PCTL segments. The analytical results were compared to the experimental results from the current study and the literature.

7.1. Abstract

Replacing conventional steel reinforcement with noncorroding glass fiber-reinforced polymer (GFRP) reinforcement can be an effective solution to mitigate the corrosion problem in precast concrete tunnel lining (PCTL) segments. PCTL segments should be effectively designed to withstand the applied load during production, transportation, construction, and service stages. The literature, however, offers limited specific design recommendations or guidelines for designing GFRP-reinforced PCTL segments. In this study, an experimental program was conducted to investigate the effect of reinforcement ratio and tie configuration on the behavior of GFRP-reinforced PCTL segments at the service and ultimate stages. Novel procedures and equations were developed to obtain axial load–bending moment interaction diagrams at the ultimate and service stages. In addition, interaction diagrams were developed to consider the creep-rupture stress limits in GFRP bars. Furthermore, axial load–shear-strength interaction diagrams were developed for GFRP-reinforced PCTL segments, as well as a simplified procedure to control cracking. Afterward, a parametric study was performed to evaluate the effect of concrete compressive strength, reinforcement ratio, and cross-sectional thickness on the axial load–bending moment interaction diagrams of GFRP-reinforced PCTL segments. The analytical results were compared to the experimental results from the current study and the literature. The comparison revealed that the proposed analytical procedure was suitable for designing GFRP-reinforced PCTL segments.

Keywords: Precast concrete tunnel lining (PCTL) segments; glass fiber-reinforced polymer (GFRP) bars; analytical investigation; axial load–bending moment interaction diagram; design procedure.

7.2. Introduction

Using tunnel boring machines (TBMs) to install precast concrete tunnel lining (PCTL) segments is the most popular method for building underground tunnels (Meda et al. 2016). Tunnels are required to have long service lives, but they tend to deteriorate, especially in harsh environments, primarily due to corrosion of conventional steel reinforcement (Li et al. 2020). Glass fiber-reinforced polymer (GFRP) reinforcement is the best alternative to steel reinforcement for dealing with the corrosion issue (Benmokrane et al. 2002; ACI 440.1R-15). In addition, GFRP bars provide unique features that make them a suitable option in PCTL segments (Caratelli et al. 2016). Caratelli et al. (2016) compared the structural performance of a steel-reinforced PCTL segment with a GFRP-reinforced counterpart. The tested GFRP-reinforced tunnel segments experienced tension-controlled failure. They concluded that the overall behavior of the GFRP-reinforced PCTL segment was satisfactory compared to the steel-reinforced counterpart.

It is required in order to design PCTL segments to resist the applied load during the production, transportation, construction, and service stages. The following text summarizes the main loads applied on a tunnel segment and the resultant internal forces during the various stages. During the production stage, segment stripping (demolding) causes a segment to act like two cantilever beams under their own weight. In contrast, the occasional eccentricity of the stack supports produces bending moment and shear force in the segments in the storage stage. During transportation, the occasional eccentricity should be considered, taking into account the dynamic shock factor. Lastly, handling the segments at the construction site causes bending moment and shear force in the segments, depending on the equipment used to lift the segments (ACI 544.7R-16; ACI 533.5R-20). Evaluating the flexural and shear capacities of the segments in the production and transition stages is very great importance. Extensive damage was reported in some practical applications when the design requirements during the production and transition stages were not effectively controlled (Shayanfar et al. 2017; Dastjerdy et al. 2018). During the construction phase, PCTL segments should be effectively designed to withstand the significant thrust force induced during TBM advancement (Ates et al. 2014). After the full ring has been inserted,

grout under high pressure is used to fill the gap between the lining and soil (tail skin back grouting). In this stage, the grouting pressure and the self-weight of the segments cause significant axial loads with small bending moments (Kasper and Meschke 2006; ACI 533.5R-20). Once the tail skin back grouting has been completed, secondary grouting is performed in the construction of some tunnels. As such grouting is localized, it can result in a significant bending moment and shear force combined with a small axial load (ACI 544.7R-16; Jin-long et al. 2018). In some cases, the self-weight of the backup train behind the TBM becomes critical. A combination of axial load (both compression and tension), bending moment, and shear force can be induced as a result of TBM backup load. During the final service stage, PCTL segments are subjected to combined axial load, shear force, and bending moment induced by ground pressure, groundwater, self-weight, surcharge, and ground reaction forces (ACI 544.7R-16; ITA WG2-19; ACI 533.5R-20). Given the different internal forces induced in a tunnel segment during the various loading stages, the segment's axial load–bending moment interaction diagram and shear strength must be determined. In addition, designing a tunnel segment to withstand the load applied during the service stage requires that the design requirements for both ultimate limit state (ULS) and serviceability limit state (SLS) be controlled (Yuan et al. 2012; Liu et al. 2016; ACI 533.5R-20). As serviceability is generally determinative in the design of GFRP-reinforced concrete (GFRP-RC) elements (Barris et al. 2012), controlling the SLS requirements is more important in GFRP-reinforced PCTL segments than steel-reinforced ones. Moreover, while shear capacity is not generally a determinative factor in the design of steel-reinforced PCTL segments (ITA WG2-19), evaluating the shear capacity of GFRP-reinforced PCTL segments has great importance, since the shear strength of GFRP-RC elements is lower than that of their steel-reinforced counterparts (Khavaran 2019). Spagnuolo et al. (2017) compared the axial load–bending moment interaction diagrams of a GFRP-reinforced and a steel-reinforced PCTL segment obtained according to ACI 440.1R-15 and ACI 318-14, respectively. Thereafter, they provided a case study to compare the forces induced in the production and service stages to the axial-flexural capacity of the GFRP-reinforced segment, which failed in the tension-controlled mode.

The literature offers no design procedures or recommendations for designing GFRP-reinforced PCTL segments. In addition, the current FRP-related design guidelines and standards—such as ACI 440.1R-15, CAN/CSA S806-12, R2017, and CAN/CSA S6-19—make no recommendations for using FRP bars in tunnel segments. Furthermore, tunneling-related design standards—such as ACI 533.5R-20 ITA-WG2-19, JSCE (2007), and AFTES-WG7 (1993)—offer no design procedures for GFRP-reinforced tunnel segments. In this study, an experimental program was conducted to investigate the effect of reinforcement ratio and tie configurations on the performance of GFRP-reinforced PCTL segments under service and ultimate conditions. Five full-scale GFRP-reinforced tunnel segments were fabricated and tested under bending load. The experimental program was followed by an analytical study aiming at developing a comprehensive step-by-step design procedure with newly developed closed-form equations and models to derive axial load–bending moment interaction diagrams according to ACI 440.1R and CAN/CSA S806-12, R2017. Both the ultimate and service stages were considered in addition to the creep rupture limit of GFRP bars in the probable scenarios. Furthermore, a novel procedure is presented herein to derive axial load–shear-strength interaction diagrams according to ACI 440.1R-15, CAN/CSA S806-12, R2017, and CAN/CSA S6-19. Lastly, a practical procedure to control crack width in GFRP-reinforced PCTL segments is presented. The developed analytical procedures were compared to the experimental results from this study and the literature. A parametric study was then conducted to evaluate the effect of concrete compressive strength, reinforcement ratio, and cross-sectional thickness on the axial–flexural strength of GFRP-reinforced PCTL segments. The results of this study will be significantly helpful with practical applications of GFRP bars in the tunneling industry and will improve current design guidelines and standards.

7.3. Experimental Data

7.3.1. Material Properties

7.3.1.1. Mechanical properties of GFRP bars

The bars used to assemble the tunnel segment cages were #5 and #6 curvilinear GFRP bars with a radius of 3305 mm. An innovative manufacturing process was developed by Pultrall Inc. (Thetford Mines, QC, Canada) to produce the curvilinear GFRP bars. In such process, the bars were formed into a curvilinear shape before curing using prefabricated molds with the desired curvature radius. The tunnel segment cages were equipped with U-shaped bars as end anchorage for the longitudinal bars. In addition, two types of closed and U-shaped transverse ties were used. Table 7.1 provides the mechanical properties of the GFRP reinforcement obtained according to ASTM D7205-21. Before applying the tensile load, the curvilinear bars were straightened using the test fixture. Then, the tensile load was applied to the specimens until failure. It should be noted that the properties reported in Table 7.1 for the U-shaped bars and transverse ties were obtained by testing straight bars manufactured according to the same process as the curved bars.

Table 7.1 Mechanical properties of the GFRP reinforcement

Reinforcement type	Bar size	Nominal cross-sectional area ($mm^{2)}$	Tensile strength (MPa)	Tensile modulus (GPa)	Tensile strain (%)
Curvilinear longitudinal bars	#5	199	1115 ± 60	55.1 ± 1.25	2.0 ± 0.1
	#6	284	1,068 ± 49	52.9 ± 0.6	2.0 ± 0.1
U-shaped bars	#5	199	1,283 ± 42	53.5 ± 1.1	2.4 ± 0.1
	#6	284	1,131 ± 35	53.2 ± 2.2	2.1 ± 0.0
U-shaped and closed ties	#4	129	1,248 ± 74	55.6 ± 1.6	2.2 ± 0.1

Note: the nominal diameters of #4, #5, and #6 bars are 13, 15, and 20 mm; respectively.

7.3.1.2. Concrete properties

The concrete mix had a target 28-day compressive strength of 40 MPa. The actual compressive strength was obtained by testing three 100 × 200 mm concrete cylinders for each specimen. Table 7.2 gives the average results for each specimen.

7.3.2. Details of the Segments and Test Matrix

The experimental phase included testing five full-scale specimens under three-point bending load. The specimens were rhomboidal in shape with an arc length of 3100 mm, width of

Table 7.2 Test matrix and test results

ID	longitudinal bars	Tie configuration	$f_c^{'}$ (MPa)	Bending moment at peak (kN·m)	Failure mode	Service moment (kN·m)	Crack width at service moment (mm)	Deflection at service moment (mm)	Crack width at the average service moment (mm)	Deflection at the average service moment (mm)
7G#5	7 #5 bars	Closed ties	48	215	C.C	38	0.35	2.47	0.70	7.70
7G#6	7 #6 bars	Closed ties	54	249	C.C	57	0.35	4.04	0.35	4.95
7G#5U	7 # 5 bars	U-shaped ties	44	181	C.C	36	0.40	2.76	0.80	10.54
13G#5	13 #5 bars	Closed ties	51	249	D.T	69	0.35	5.23	0.25	2.97
13G#6	13 #6 bars	Closed ties	47	281	D.T	80	0.25	6.04	0.15	2.66

Note: C.C denotes concrete crushing and D.T denotes diagonal tension failure.

1500 mm, and thickness of 250 mm. The internal radius of the tunnel segment specimens was 3250 mm, while the external radius was 3500 mm. Figure 7.1 provides the geometry and reinforcement details of the specimens. Each specimen had transverse ties and longitudinal bars anchored at the end with U-shaped closing bars. The test parameters included the number (7 and 13) and size (#5 and #6) of longitudinal bars at four different reinforcement ratios and the type of transverse ties (closed and U-shaped ties). Table 7.2 presents the test matrix and reinforcement details of the specimens. In the specimen designation, the first number denotes the number of longitudinal bars, the letter G stands for GFRP reinforcement, the following term indicates the size of longitudinal bars, and the letter U identifies the specimen with U-shaped transverse ties (7G#5U).

7.3.3. Test Setup and Instrumentation

The tunnel segment specimens were loaded monotonically with a three-point load test setup with a clear span of 2400 mm. The load was applied in a displacement-controlled manner at a rate of 0.8 mm/min. Three linear potentiometers distributed over the width of the specimen measured the mid-span deflection corresponding to the applied load (Fig. 7.2). As shown in Fig. 7.1, four strain gauges were installed on the bottom longitudinal bars at mid-span to record the bars' tensile strain. In addition, three concrete strain gauges were installed on the top surface of the concrete around the mid-span to record the concrete compressive strain.

7.4. Test Results

7.4.1. Moment–Deflection Relationship

All the specimens followed a linear moment–deflection relationship from the beginning of the test up to initiation of the first crack (Fig. 7.3). As a result of the transition from the gross section to the effective section, the flexural stiffness reduced considerably after the first crack appeared. A nearly linear behavior was observed in the specimens in the post-cracking stage up to the peak moment as a result of the linear elastic behavior of the GFRP reinforcement. The moment capacity decreased after the peak load was reached. Figure 7.3a presents the effect of increasing the size and number of the longitudinal bars on the moment–deflection behavior. As can be seen, increasing the reinforcement ratio enhanced the post-cracking stiffness and load-carrying capacity of the specimens while decreasing the deflection corresponding to the peak load. Figure 7.3b gives the effect of tie configuration on the moment–deflection relationship of the segments tested. Replacing closed ties with U-shaped ties in the segments reduced the post-cracking stiffness by 5% (the variation in concrete strength was considered).

7.4.2. General Behavior and Failure Mechanism

The segments exhibited the typical cracking pattern of a GFRP-reinforced flexural element under three-point bending load. The number and width of flexural cracks increased with load, and shear–flexural cracks started to appear. Lastly, specimens 7G#5, 7G#6, and 7G#5U failed as a result of concrete spalling on the compression side. Specimens 13G#5 and 13G#6, however, experienced diagonal tension failure (Fig. 7.4). Table 7.2 lists the peak bending moment, deflection corresponding to the peak bending moment, and failure mode of the tested specimens. Table 7.2 shows that increasing the reinforcement ratio enhanced the load-carrying capacity while employing U-shaped transverse ties decreased the peak load.

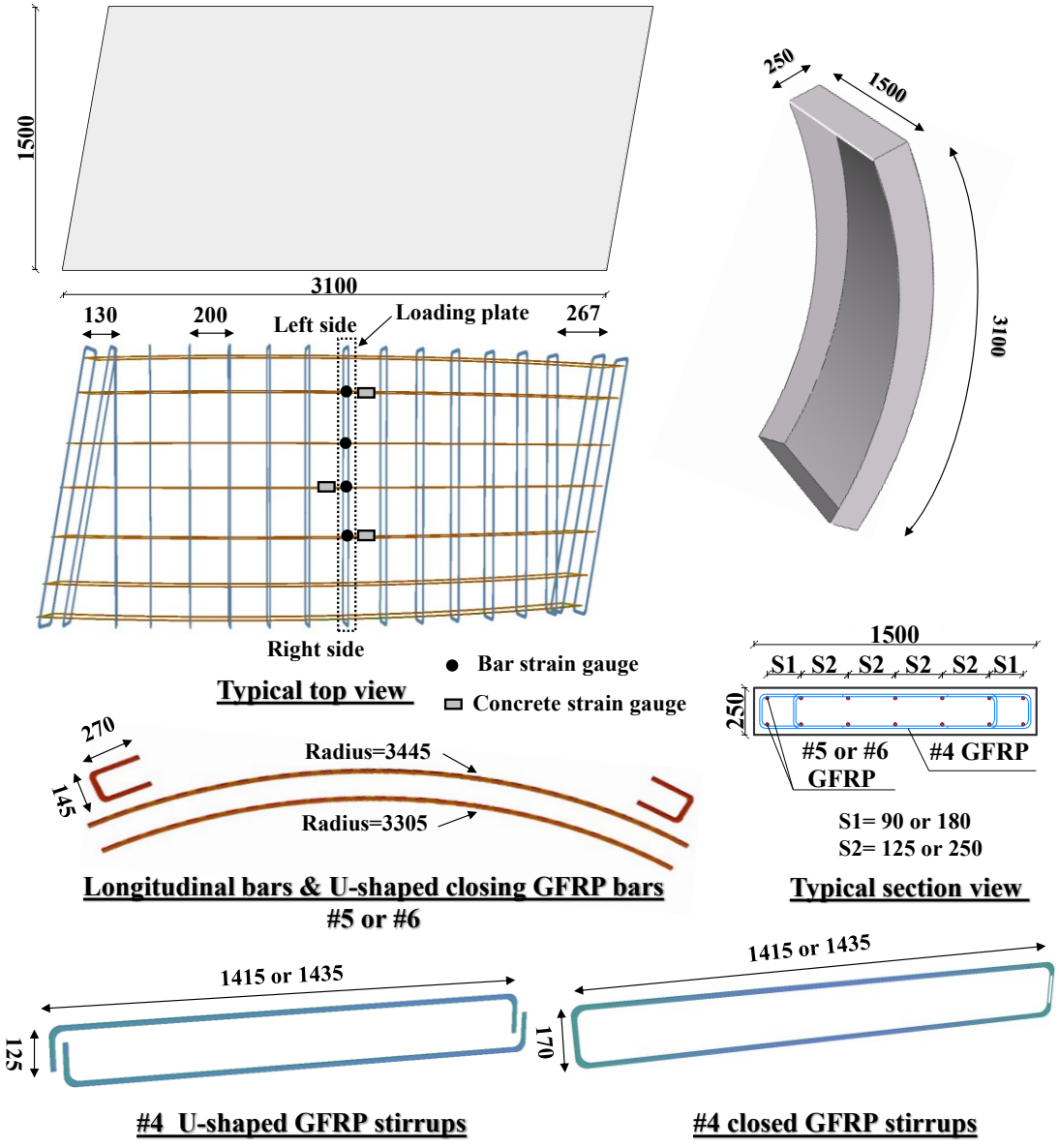

Figure 7.1 Specimen geometry and reinforcement details (dimensions in mm).

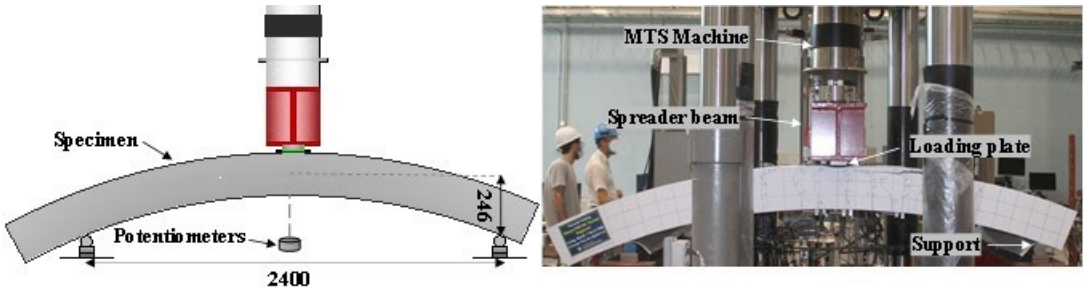

Figure 7.2 Test setup (dimensions in mm).

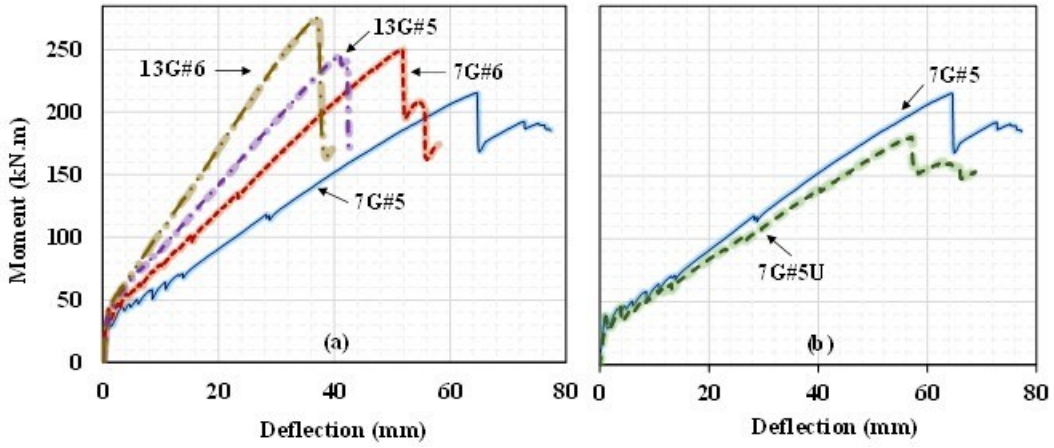

Figure 7.3 Moment–deflection behavior of the tested specimens: (a) the effect of bar size and spacing; (b) the effect of tie configuration.

Figure 7.4 Failure mode of the tested specimens.

7.4.3. Strain in the Reinforcement and Concrete

Figures 7.5a and 7.5b shows the relationship between the bending moment and the recorded strain in the reinforcement and concrete, respectively. Figure 7.5a shows a nearly linear moment–strain relationship in the pre-cracking and post-cracking stages. The maximum recorded strain in the tensile reinforcement was 16300, 12200, and 12800, 9400, and 8300 $\mu\varepsilon$ in 7G#5, 7G#6, 7G#5U, 13G#5, and 13G#6 respectively, corresponding to 82%, 61%, 64%, 47%, and 42% of the maximum tensile strain in the longitudinal bars. The relationship between the moment and concrete strain in 7G#6, 13G#5, and 13G#6 was almost linear up to the failure (Fig. 7.5b). In contrast, the slope of the moment–strain diagram decreased,

approaching the maximum concrete compressive strain at the peak moment in 7G#5 and 7G#5U. The maximum recorded concrete compressive strain in 7G#5, 7G#6, 7G#5U, 13G#5, and 13G#6 was 2950, 2875, 2870, 2730, and 2500 $\mu\varepsilon$, respectively.

7.4.4. Serviceability

The service moment in this study is defined as the recorded bending moment when the strain in the tensile reinforcement reaches 2000 $\mu\varepsilon$ (ISIS 2007). Using this criterion yielded different service moments in the specimens, as reported in Table 7.2. Table 7.2 reports the experimental crack width and deflection corresponding to the reported service moments. For comparison purposes, the crack width and deflection at the bending moment equal to the average service moment of all specimens (56 kN.m) are reported. Increasing the reinforcement ratio by 43%, 86%, and 165% decreased the crack width corresponding to the average service moment by 50%, 64%, and 79%, respectively. The reduction was 36, 61, and 65%, respectively, for the deflection values. Replacing the closed ties with U-shaped ties increased the crack width and deflection at the average service moment by 14% and 36%, respectively.

7.5. Analytical Investigation

During the production and transition stages, PCTL segments are subjected to bending load and shear force. Such elements are subjected to a combination of axial load, bending

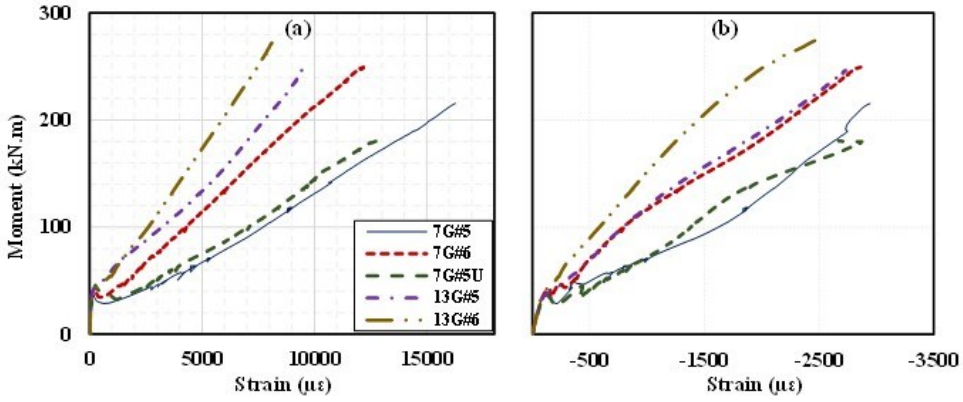

Figure 7.5 Moment–strain relationship of the tested specimens: (a) strain in the tensile reinforcement; (b) strain in concrete.

moment, and shear force during the service stage (ACI 544.7R-16). It is necessary to evaluate their capacity to withstand the applied loads in the design procedure. The design of tunnel segments in practice begins by selecting the appropriate geometry, reinforcement detail, and concrete strength for the segments in a segmental ring. Then, the strength of the segments is compared to the critical cases obtained with different loading conditions and at various critical locations along the tunnel (ACI 533.5R-20). In such cases, deriving interaction diagrams is much preferable for a segment compared to the case-by-case design-check procedure. This section provides analytical procedures to obtain the axial load–bending moment interaction diagrams at the ultimate and service stages, and considering creep rupture and fatigue, as well as the axial load–shear-strength interaction diagram for GFRP-reinforced PCTL segments. The procedures to evaluate the cracking and deflection at the service stage are also presented. The analytical procedure for the axial load–bending moment interaction diagrams was derived from ACI 440.1R-15 and CAN/CSA S806-12, R2017. CAN/CSA S6-19 was also used to derive the procedure to evaluate the shear capacity and cracking. As the goal was to propose closed-form equations in the analytical procedure, it was assumed that identical reinforcement areas and moduli of elasticity were used in the bottom and top meshes of GFRP-reinforced PCTL segments (which is probable in actual applications) to shorten the equations. In general, this section presents a comprehensive design procedure for GFRP-reinforced PCTL segments in the production, transition, and service stages. The last part of this section presents the analytical results obtained for the tested specimens and from the literature compared to the experimental results.

7.5.1. Axial Load–bending Moment Interaction Diagram at the Ultimate Stage

ACI 440.1R-15 and CAN/CSA S806-12, R2017 state that the contribution of FRP bars in compression should be neglected. In contrast, some studies in the literature reported that this underestimates the capacity of FRP-reinforced elements subjected to a combination of axial load and bending moment. Such underestimations can be up to 27% in some cases (Hadhood et al. 2017; Salah-Eldin et al. 2019; Bakouregui et al. 2021). We considered two scenarios for deriving the capacity of GFRP-reinforced PCTL segments. The first considers the

contribution of GFRP bars in compression, while the second neglects it. The analytical procedure presented considers both cases of compression and tension failure modes. There are no provisions in ACI 440.1R-15 and CAN/CSA S806-12, R2017 for the flexural capacity of GFRP-reinforced elements subjected to bending moment and tensile axial load. Furthermore, the ACI 440.1R-15 does not provide provisions related to the combination of bending moment and axial compression. Nevertheless, the main assumptions in ACI 440.1R-15 and CAN/CSA S806-12, R2017 were used to develop the equations related to a combination of bending moment and axial load.

7.5.1.1. Considering the contribution of GFRP bars in compression

Deriving the axial load–bending moment interaction diagram requires that points be determined related to the cases of pure axial compression, combination of axial compression and bending moment, pure bending moment, a combination of axial tension and bending moment, and pure axial tension. Note that pure axial tension is not a practical case, but it is required to complete the diagram. The following procedure can be used to derive the interaction diagram according to the above cases. Figure 7.6 shows the main parameters employed in the analytical investigations.

1. Pure axial compression ($P \neq 0$ and $M_n = 0$). The axial resistance in compression can be obtained by considering the contribution of the reinforcement and concrete in compression. Equation 7.1 can be used to predict the axial compression resistance in the design according to ACI 440.1R-15.

$$P_{rc,ACI} = 0.8\varphi(\alpha_1 f_c^{l}(A_g - 2A_f) + 2A_f E_f \varepsilon_{cu}) \tag{7.1}$$

where ε_{cu} should be considered equal to 0.003 and the reduction factor φ should be considered equal to 0.65 (ACI 318-19). For designing according to CAN/CSA S806-12, R2017, the following equation can be employed.

$$P_{rc,CSA} = 0.8(\alpha_1 \varphi_c f_c^{l}(A_g - 2A_f) + 2\varphi_f A_f E_f \varepsilon_{cu}) \tag{7.2}$$

where ε_{cu} should be considered equal to 0.0.0035.

2. Combination of axial load and bending moment when $c \geq (h/\beta_1)$ ($P \neq 0$ and $M_n \neq 0$). In this condition, c can be obtained by trial and adjustment using the force equilibrium and strain compatibility. In this case, $\beta_1 c$ should not be considered greater than h in the related calculations since assuming the compression block depth greater than the sectional thickness does not make sense. In lieu of the described trial and adjustment procedure, the values in this case can be estimated by following the general trend of the diagram since this condition occurs in a very small portion of the diagram. According to an initial case study performed by the authors, the range in the common sectional geometries of tunnel segments in which the neutral-axis depth exceeds h/β_1 is a few millimeters or even less.

3. Combination of axial load and bending moment when $c_b \leq c \leq (h/\beta_1)$ ($P \neq 0$ and $M_n \neq 0$). The bending moment capacity in this case can be calculated using stress and strain compatibility in the section. Equation 7.3 presents the bending moment capacity for different axial-load levels in the design according to ACI 440.1R-15. The equation is only valid when $c_b \leq c \leq (h/\beta_1)$ where $c_b = d(\varepsilon_{cu}/(\varepsilon_{cu}+\varepsilon_{fu}))$.

$$M_{n,ACI} = \varphi\left[m\left(\frac{h}{2} - \frac{\beta_1 c}{2}\right) + l\left(\frac{d-c}{c}\right)\left(d - \frac{h}{2}\right) + l\left(\frac{d'-c}{c}\right)\left(d' - \frac{h}{2}\right)\right] \qquad c_b \leq c \leq \beta_1 h \tag{7.3}$$

where l and m can be obtained with Eqns. 7.4 and 7.5, respectively. Equations 7.6 and 7.7 present the values of α_1 and β_1 as in ACI 440.1R-15. The value of c can be calculated with the strain compatibility in the section. Closed-form equations, however, were developed and reported in the appendix to find the neutral-axis depth when $c \geq c_b$.

$$l = A_f E_f \varepsilon_{cu} \tag{7.4}$$

$$m = \alpha_1 \beta_1 f_c' b c \tag{7.5}$$

$$\alpha_1 = 0.85 \tag{7.6}$$

$$0.65 \leq \beta_1 = 0.85 - \left[0.05(f_c' - 28)/7\right] \leq 0.85 \tag{7.7}$$

The reduction factor (φ) should be considered equal to 0.65 when $\rho \geq 1.4\rho_{fb}$ and $0.3+0.25(\rho_f / \rho_{fb})$ when $\rho_{fb} \leq \rho < 1.4\rho_{fb}$ as in ACI 440.1R-15 (equations were developed and presented in the appendix to calculate ρ_{fb}). In the design according to ACI 440.1R-15, ε_{fu} is equal to $C_e\varepsilon^*_{fu}$ where C_e is an environmental reduction factor and ε^*_{fu} is the guaranteed rupture tensile strain of the GFRP reinforcement. As PCTL segments are generally exposed to soil and weather, C_e should be considered equal to 0.7.

Equation 7.8 presents the bending moment capacity according to CAN/CSA S806-12, R2017.

$$M_{n,CSA} = \varphi_c m(\frac{h}{2} - \frac{\beta_1 c}{2}) + \varphi_f l(\frac{d-c}{c})(d - \frac{h}{2}) + \varphi_f l(\frac{d^{'}-c}{c})(d^{'} - \frac{h}{2}) \qquad c_b \leq c \leq \beta_1 h \tag{7.8}$$

where α_1 and β_1 can be calculated using the following equations:

$$\alpha_1 = 0.85 - 0.0015 f_c^{'} \geq 0.67 \tag{7.9}$$

$$\beta_1 = 0.97 - 0.0025 f_c^{'} \geq 0.67 \tag{7.10}$$

The reduction factors φ_c and φ_f are 0.7 and 0.75, respectively, as in CAN/CSA S806-12, R2017.

4. Combination of axial load and bending moment when $c \leq c_b$ ($P \neq 0$ and $M_n \neq 0$). As failure is governed by the tensile rupture of the GFRP bars in this case, the concrete compressive strain is lower than the ultimate compressive strain, and the values for the compressive block coefficients (α_1 and β_1) are not valid. Our study used the equations proposed by Collins and Mitchell (1997) for the values of α and β when the concrete compressive strain was lower than its ultimate value, as follows:

$$\alpha = \frac{1}{\beta}\left[(\frac{\varepsilon_c}{\varepsilon_c^{'}}) - \frac{1}{3}(\frac{\varepsilon_c}{\varepsilon_c^{'}})^2 \right] \tag{7.11}$$

$$\beta = \frac{4 - (\varepsilon_c / \varepsilon_c^{'})}{6 - 2(\varepsilon_c / \varepsilon_c^{'})} \tag{7.12}$$

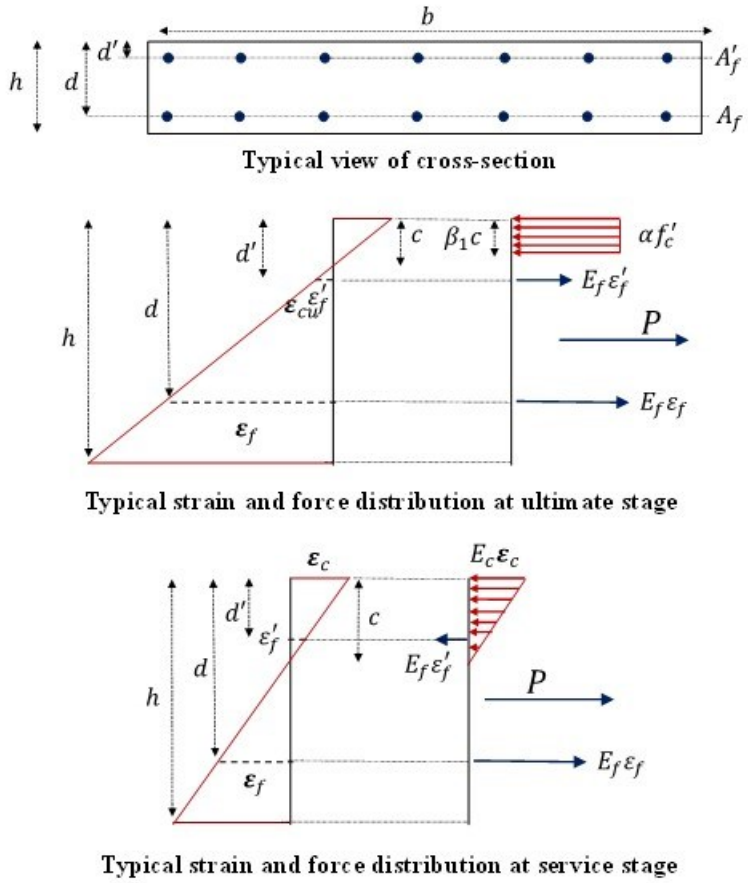

Figure 7.6 Schematic cross-sectional view of the parameters used in analytical investigation.

where Eq. 7.13 can be used to obtain $\varepsilon_c^{'}$, considering the concrete modulus of elasticity (E_c) equal to $4700\sqrt{f_c^{'}}$ as in ACI 318-19.

$$\varepsilon_c^{'} = 1.71\frac{f_c^{'}}{E_c} \tag{7.13}$$

A trial-and-adjustment procedure can be used to find the neutral-axis depth and concrete compression block coefficient. Using the strain compatibility and considering ε_{fu} as the strain in the tensile bars, the bending moment capacity of the section for each case of axial load can then be obtained with an equation similar to Eq. 7.3. Instead of resorting to such time-consuming calculations, a nearly linear trend can be estimated for the tensile axial load–bending moment diagram when $\rho \le \rho_{fb}$ (Nanni et al. 2014). While CAN/CSA S806-12,

R2017 does not allow tension-controlled failure (except in certain conditions), ACI 440.1R-15 poses a more restrictive reduction factor of 0.55 for such failure. For a section to be considered compression-controlled, ACI 440.1R-15 and CAN/CSA S806-12, R2017 mention that the reinforcement ratio should remain 1.4 and 1.0 times greater than ρ_{fb}, respectively, in the case of pure bending moment. In such situation, the reinforcement ratio meets the criteria of design standards as well when the section is subjected to axial compressive load and bending moment. The value of balanced reinforcement ratio, however, increased by increasing the axial tensile load. Therefore, a section designed to undergo compression-controlled failure in the case of pure bending moment might experience tension-controlled failure by increasing the value of tensile load.

5. Pure tensile axial load ($P \neq 0$ and $M_n = 0$). The tensile resistance can be estimated by relying on the tensile load carried out by the reinforcement. Equation 7.14 can be used to estimate the tensile resistance in the design according to ACI 440.1R-15.

$$P_{rt,ACI} = 2\varphi A_f E_f \varepsilon_{fu} \tag{7.14}$$

where the reduction factor φ should be considered equal to 0.55. Equation 7.15 presents the tensile resistance according to CAN/CSA S806-12, R2017.

$$P_{rt,CSA} = 2\varphi_f A_f E_f \varepsilon_{fu} \tag{7.15}$$

7.5.1.2. Neglecting the contribution of GFRP bars in compression

The same procedure as in the preceding section can be used to obtain the axial load–bending moment interaction diagram neglecting the contribution of GFRP bars in compression by modifying some of the equations presented. After the neutral-axis depth is calculated, the top and bottom reinforcement are in tension when $c \leq d'$, and the procedure is the same as in section 4.1.1. When $c \geq d'$, the resisting moment can be calculated with Eq. 7.3 or 7.4 considering the term $l(\frac{d'-c}{c})(d'-\frac{h}{2})$ equal to zero. The equations to calculate the neutral-axis depth and the balanced reinforcement ratio when $c \geq d'$ are presented in the appendix.

When $c \geq d$, both the top and bottom reinforcement are in compression. The neutral-axis depth and the resistant moment in this case can be calculated considering the value of A_f equal to zero in the equations presented. For pure compression, supposing the value of E_f equal to zero in Eq. 7.1 or 7.2 yields the compressive capacity.

7.5.2. Axial Load–Bending Moment Interaction Diagram at the Service Stage

According to ACI 533.5R-20, the concrete compressive stress in PCTL segments should be limited to a restricted value of $0.4f_c^{'}$ according to JSCE (2007) and $0.6f_c^{'}$ according to AFTES-WG7 (1993), and MC2010 (2010) under service-load conditions. When the concrete strain at the extreme compression fiber is lower than ε_{cu}, the equivalent concrete block coefficients of α_1 and β_1 in Eqns. 7.9 to 7.12 are not valid. In such cases, the equivalent concrete block coefficients can be obtained with Eqns. 7.11 and 7.12. The procedure in section 7.5.1 for the axial load–bending moment interaction diagram can be modified to obtain the axial load–bending moment interaction diagram for the service stage considering the limits in ACI 533.5R-20 for the concrete compressive stress. For this purpose, $\gamma\varepsilon_{cu}$ should be replaced with ε_{cu} in all related equations. The value of $\gamma\varepsilon_{cu}$ denotes the concrete strain corresponding to the restricting stress. By considering $\alpha f_c^{'}$ equal to $0.4f_c^{'}$ and $0.6f_c^{'}$ for the design according to JSCE (2007) and AFTES-WG7 (1993), and MC2010 (2010), respectively, the value of γ can be obtained with Eq. 7.11. In addition, α and β obtained with Eq. 7.11 and 7.12, respectively, should be replaced with α_1 and β_1 in the related equations. Furthermore, in Eqns. 7.1 and 7.2, the value of $f_c^{'}$ should be replaced with $\alpha f_c^{'}$. Note that all the reduction factors can be assumed equal to 1.0 at the service stage.

According to ACI 533.5R-20, the stress in the reinforcement should be limited to the restricted values under service-load conditions. While ACI 440.1R-15 does not provide a specific limit for the maximum stress in GFRP bars under service-load conditions,

CAN/CSA S806-12, R2017 limits the stress in GFRP bars to $0.25 f_u$ at the service load. Therefore, the axial load–bending moment interaction diagram can also be developed considering the reinforcement's stress limit. A trial-and-adjustment procedure can be used to find the neutral-axis depth considering the force equilibrium and strain compatibility. As a simplified assumption, however, a linear stress–strain curve can be assumed for concrete during service conditions (ACI 318-99). In this case, the neutral-axis depth can be obtained considering the value of λ as the ratio of allowable stress in the service stage to the ultimate tensile strength of the reinforcement (see the appendix A). As mentioned above, the value of λ should be considered 0.25 for the GFRP bars in the design according to CAN/CSA S806-12, R2017. After the neutral-axis depth for each case of axial load has been calculated, Eq. 7.16 can be used to obtain the bending moment considering the stress limit in the reinforcement during the service stage.

$$M_{ser} = \frac{1}{2} b E_c \lambda \varepsilon_{fu} \left(\frac{c}{d-c}\right)\left(\frac{h}{2} - \frac{c}{3}\right) + A_f \lambda f_u \left(d - \frac{h}{2}\right) + A_f \lambda f_u \left(\frac{d' - c}{d-c}\right)\left(d' - \frac{h}{2}\right) \tag{7.16}$$

In the cases where neglecting the contribution of GFRP bars in compression is preferable, the term $\left(\frac{d' - c}{d-c}\right)\left(d' - \frac{h}{2}\right)$ in Eq. 7.16 should be considered zero when $c > d'$. In addition, an equation for the neutral-axis depth in such cases is presented in the appendix A.

In verifying stress for SLS, limiting concrete compressive stress generally becomes more critical when the axial compression load is increased. In contrast, limiting the maximum stress in the tensile reinforcement becomes more determinative when the axial-load level decreases. Therefore, the axial load–bending moment interaction diagram considering both limitations for stress in concrete and reinforcement can be obtained by considering the minimum bending moment values calculated based on the stress limit in the concrete and reinforcement.

7.5.3. Axial Load–Bending Moment Interaction Diagram Considering Creep Rupture Stress Limit

To avoid creep rupture failure in GFRP reinforcement, ACI 440.1R-15 limits the stress in the reinforcement to $0.2f_u$ under sustained loads, while CAN/CSA S806-12, R2017 limits the maximum strain in the reinforcement to 0.002. To consider the stress limit under sustained load, a similar procedure as section 7.4.2 can be used to consider the value λ equal to 0.2 and $0.002E_f / f_u$ for the design according to ACI 440.1R-15 and CAN/CSA S806-12, R2017, respectively.

7.5.4. Axial load–Shear-Strength Interaction Diagram

During the production and transition stages, PCTL segments are subjected to shear force, while, during the service stage, such elements are under a combination of axial load and shear force (ACI 533.5R-20). The shear strength of a GFRP-RC member depends on the level of axial load. The effect of axial load on the shear strength of GFRP-RC members is considered in CAN/CSA S806-12, R2017 and CAN/CSA S6-19, but ignored in ACI 440.1R-15. Table 7.3 summarizes the shear-strength models presented in these codes and guidelines. Since ACI 440.1R-15 only considers the contribution of the uncracked section as the shear transferring mechanism, the effect of axial load on the shear strength of GFRP-RC members can be estimated by its effect on the depth of uncracked block to some extent. A modified ACI 440.1R-15 model was developed based on this assumption and is reported in Table 7.3. By replacing the different values of axial load in the model presented as a modified ACI approach, the axial load–shear-strength interaction diagram can be obtained. Deriving the axial load–shear-strength interaction diagram according to CAN/CSA S806-12, R2017 requires the ratio of the factored shear (V_f) to the factored moment (M_f). In the cases in which this value can be determined or estimated based on the load and boundary conditions, the axial load–shear-strength interaction diagram can be obtained. When that ratio cannot be estimated, however, the minimum value of $0.1\varphi_c\sqrt{f_c'}b_w d$ and $0.11\sqrt{f_c'}b_w d_v$ can be used for

the term $0.05\lambda k_m k_r (f_c^{'})^{1/3} b_w d_v$ as a conservative assumption for the axial tension and axial compression loads, respectively. Note that the value of k_a is related to the sections near the support, which can be considered equal to 1.0 in the calculations for PCTL segments, as the conventional concept of support might not be applicable in a full ring of tunnel segments. The effect of axial load on shear strength is considered through the value of ε_x in CAN/CSA S6-19. In addition to the axial load, the factored shear force and factored bending moment are required to calculate ε_x. Therefore, obtaining the axial load–shear-strength interaction diagram is not applicable according to this standard. Two approaches are suggested here to achieve a conservative estimation. In the first approach, 0.003 can be used for ε_x and the shear strength can be obtained accordingly, leading to identical shear strengths for all the axial load levels. In the second approach, if the ratio of V_f to M_f can be estimated, ε_x can be obtained using the pairs of φP_n and φM_n calculated according to section 7.4.1. Thereafter, the shear strength corresponding to each case of φP_n and φM_n can be calculated. As M_f is supposed to be smaller than φM_n, this approach is also considered conservative.

7.5.5. Cracking and Deflection

7.5.5.1. Cracking

According to ACI 533.5R-20, the crack width in SLS should be effectively controlled to avoid durability problems as a result of increased permeability, excessive water leaks, and reinforcement corrosion. The various standards have specified a range of 0.2 to 0.3 mm as the maximum allowable crack width in steel-reinforced PCTL segments, depending on the environmental conditions and watertightness requirements (ACI 533.5R-20). Since GFRP reinforcement does not corrode, the maximum crack width in GFRP-RC members is 0.5 mm for members subjected to aggressive environments. This limit does not apply, however, to the cases in which watertightness requirements exist, and some aspects should be considered in such cases (ACI 440.1R-15; CAN/CSA S806-12, R2017; CAN/CSA S6-19). Three

approaches can control cracking: the direct method, z -factor, and the maximum spacing between longitudinal bars recommended in CAN/CSA S6-19, CAN/CSA S806-12, R2017

Table 7.3 Shear-strength prediction models in North American design guidelines and standards

<table>
<tr><th>Guideline</th><th colspan="2">Model</th></tr>
<tr><td>ACI 440.1R</td><td colspan="2">$V_c = 0.4\varphi\sqrt{f_c'}b_w(kd)$ where $k = \sqrt{2\rho n + (\rho n)^2} - \rho n$ and $\varphi = 0.75$</td></tr>
<tr><td>Modified ACI</td><td colspan="2">$V_c = 0.4\varphi\sqrt{f_c'}b_w(k_p d)$ where
$k_p = \dfrac{\sqrt{P^2 - 2P\rho n l_p + {l_p}^2 n\rho(n\rho+2)} - n\rho l_p + P}{l_p} \le \dfrac{1}{d}$, $l_p = E_c\varepsilon_c b_w d$,
$\varepsilon_c \le 0.001$, and $\varphi = 0.75$</td></tr>
<tr><td rowspan="3">CSA S806</td><td>Axial tension</td><td>Axial compression</td></tr>
<tr><td>$0.05\varphi_c k_m k_r (f_c')^{1/3} b_w d_v \ge 0.1\varphi_c \lambda\sqrt{f_c'}b_w d$
$V_c = \left[0.05\varphi_c k_m k_r (f_c')^{\frac{1}{3}} b_w d_v\right] k_s k_a (1 + \dfrac{0.3P}{A_g})$
where $\varphi_c = 0.7$</td><td>$V_c = \left[0.05\varphi_c k_m k_r (f_c')^{1/3} b_w d_v\right] k_s k_a (1 + \dfrac{P}{14A_g})$
where
$0.05\varphi_c k_m k_r (f_c')^{1/3} b_w d_v \ge 0.11\sqrt{f_c'}b_w d_v$
and $k_a(1 + \dfrac{P}{14A_g}) \le 3.0$</td></tr>
<tr><td colspan="2">$k_m = \sqrt{\dfrac{V_f d}{M_f}} \le 1.0$, $k_r = 1 + (E_f\rho)^{\frac{1}{3}}$, $k_s = \dfrac{750}{450 + d} \le 1.0$,
$1.0 \le k_a = \dfrac{2.5}{M_f / V_f d} \le 2.5$, and</td></tr>
<tr><td>CSA S6</td><td colspan="2">$V_c = 2.5\beta_v\varphi_c f_{cr} b_w d_v$
where $\beta_v = \left[\dfrac{0.4}{1 + 1500\varepsilon_x}\right]\left[\dfrac{1300}{1000 + S_{ze}}\right]$, $\varepsilon_x = \dfrac{\dfrac{M_f}{d_v} + V_f - 0.5P}{2E_f A_f} \le 0.003$, and
$s_{ze} = 35s_z / (15 + a_g) \ge 0.85s_z$ and $\varphi_c = 0.75$</td></tr>
</table>

and ACI 440.1R-15, respectively. In addition, according to CAN/CSA S806-12, R2017, there is no need to control the crack width if the maximum strain in the FRP tension reinforcement is less than 0.0015 under the service-load condition. As a simple approach, this study suggests the following procedure to control the crack width in GFRP-reinforced PCTL segments.

1. Derive the axial load–bending moment interaction diagram considering the limit of 0.0015 as the strain in the tension reinforcement (CAN/CSA S806-12, R2017) using the procedure in section 7.4.2.

2. When the combination of applied axial load and bending moment during the service stage exceeds what was obtained in the preceding step, the crack width can be calculated and controlled using the following equation according to CAN/CSA S6-19:

$$w_{cr} = 2\frac{f_{FRP}}{E_f}\frac{h-c}{d-c}k_b\sqrt{d_c^2+(s/2)^2} \tag{7.17}$$

where the neutral-axis depth in Eq. 7.17 should be found using trial and adjustment, while a linear stress–strain relationship can be assumed for the concrete in compression. Thereafter, f_{FRP} can be calculated with Eq. 7.18 for substitution in Eq. 7.17.

$$f_{FRP} = \frac{M_{ser} - P(\frac{h}{2}-\frac{c}{3})}{A_f(d-\frac{c}{3})} \tag{7.18}$$

7.5.5.2. Deflection

Deflection of PCTL segments in the service stage is directly obtained using different analysis models, including elastic equation, beam–spring method, finite element modeling, and the distinct element method in ACI 533.5R-20. The obtained deflection under SLS condition should be limited to the allowable values specified in the various standards, guidelines, and project specifications.

7.5.6. Comparison of Experimental and Analytical Results

This section presents and discusses the derived diagrams according to the procedures presented above. All the diagrams are in a normalized form so that $K_n = P / A_g f_c^{'}$, and $R_n = M_n / A_g f_c^{'} h$. In addition, $V_n / A_g f_c^{'}$ was used for the axial load–shear strength interaction diagrams. Since the purpose was to compare the results to the experimental ones, the environmental reduction factor (C_e) was not considered in the analytical procedure. In addition to the five specimens tested in this study, three specimens from Caratelli et al. (2016), and Caratelli et al. (2017)—labelled GFR, GFRP-RR and GFRP-RR (+B)—were used in this section for comparison with the test results. For the specimens tested in this study, the same material properties as what was reported in Table 7.1 (which came from the tensile test results) were employed in the analytical calculations. The interaction diagrams for the specimens showed almost similar trends. Therefore, interaction diagrams are presented only for specimens 7G#5 and 7G#6 to illustrate the overall trend of the specimens and to stay within the manuscript length limits. Given the limited number of specimens tested in the current study and the number of results reported on in the literature, more experimental results are needed to validate the accuracy of the procedures presented.

7.5.6.1. Axial load–bending moment interaction diagram at the ultimate stage

The procedure in section 7.4.1 was used to develop the axial load–bending moment interaction diagram of the specimens at the ultimate stage as in ACI 440.1R-15 and CAN/CSA S806-12, R2017 (Fig. 7.7). The diagrams are presented according to two scenarios: considering and neglecting the contribution of the GFRP bars in compression. In addition, the charts obtained after considering the reduction factors are also presented for comparison. The balanced condition in each chart is specified. Figure 7.7 shows that a linear trend can be assumed for the tension-controlled part of the diagram. In the diagrams considering the reduction factors, the parts related to the tension-controlled failure were not included since ACI 440.1R-15 and CAN/CSA S806-12, R2017 do not recommend that failure mode. Neglecting the contribution of the GFRP bars in compression did not

noticeably affect the axial-flexural strength when the axial-load level was less than $0.25f_c^{'}A_g$ in the specimens. This is because when the axial load level is below $0.06f_c^{'}A_g$ (on average), tensile load is induced in the top reinforcement. In addition, in the axial load levels ranging from $0.06f_c^{'}A_g$ to $0.25f_c^{'}A_g$, strain in the top reinforcement was negligible. Neglecting the contribution of the compression reinforcement at axial-load levels exceeded $0.25f_c^{'}A_g$ yielded predictions of bending moment capacity that were on average, 3.2% and 3.5% lower (averagely) as per ACI 440.1R-15 and CAN/CSA S806-12, R2017, respectively. The predicted bending moment capacity according to ACI 440.1R-15 was less than with CAN/CSA S806-12, R2017 by 6% on average (10% at zero axial load) at axial-load levels less than $0.2f_c^{'}A_g$. This can be mainly attributed to CAN/CSA S806-12, R2017 recommending higher ultimate concrete compressive strain than ACI 440.1R-15. At axial-load levels greater than $0.2f_c^{'}A_g$, the bending moment capacity predicted according to ACI 440.1R-15 was higher than with CAN/CSA S806-12, R2017 (8% higher at the point of maximum predicted bending moment). Moreover, the difference widened as the axial-load level increased. This difference can be attributed to ACI 440.1R-15 having a higher α_1 and lower β_1 than CAN/CSA S806-12, R2017. Table 7.4 compares the experimental and analytical results of the specimens at the ultimate stage. ACI 440.1R-15 and CAN/CSA S806-12, R2017`overestimated the bending moment capacity of the specimens with a flexural failure mode by 6% and 19%, respectively, on average. The overestimations can be related to the higher suggested ultimate concrete compressive strain compared to the experimental values.

7.5.6.2. Axial load–bending moment interaction diagram at the service stage

The axial load–bending moment interaction diagrams were derived based on the procedure in section 7.4.2, as shown in Fig. 7.9. Both of the recommended limits in ACI 533.5R-20 for the maximum concrete compressive stress at the service stage ($0.4f_c^{'}$ and $0.6f_c^{'}$) were considered. In

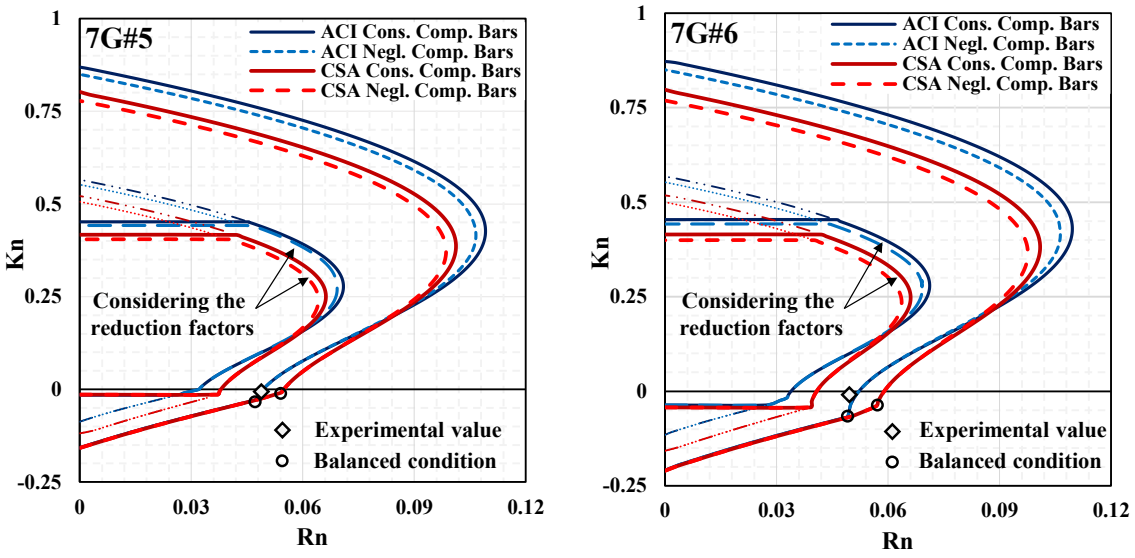

Figure 7.7 Axial load–bending moment interaction diagrams of the selected specimens at the ultimate stage.

addition, the diagrams are presented for both scenarios: that is, considering and neglecting the contribution of the GFRP bars in compression. Figure 7.8 shows that the concrete compressive stress and bar tensile stress reached their maximum values at a certain point indicated in the diagrams for both limitations of $0.4f_c^{'}$ and $0.6f_c^{'}$. When the axial load was greater than that point, the maximum allowable concrete compressive stress controlled the allowable bending moment at each axial-load level. In contrast, the maximum tensile stress in the bars was determinative for the axial-load level lower than the mentioned point. Figure 7.8 indicates that considering or neglecting the contribution of the GFRP bars in compression yielded almost the same results at axial-load levels below $0.2f_c^{'}A_g$. The difference was as low as 1.5% (on average) for axial-load levels higher than $0.2f_c^{'}A_g$. Therefore, it can be concluded that considering or neglecting the contribution of GFRP bars in compression does not noticeably affect the axial–flexural capacity of GFRP-reinforced PCTL segments at the service stage. This can be justified by the small amount of compressive strain induced in the compression reinforcement when the concrete stress was limited to $0.4f_c^{'}$ or $0.6f_c^{'}$. Table 7.4 compares the experimental and analytical results of the specimens for the service stage. Experimental results were obtained based on the measured

Table 7.4 Comparison of the experimental and analytical results at the ultimate, service, and creep-rupture limit stages.

Specimen ID	Experimental values				Experimental to theoretical values				
	$M_{ult.}$ kN.m	$M_{ser.}$ kN.m	$M_{crp.}$ ACI 440.1R kN.m	$M_{crp.}$ CSA S806 kN.m	Ult. ACI 440.1R	Ult. CSA S806	Service	Creep rupture ACI 440.1R	Creep rupture CSA S806
7G#5	213	68	56	38	1.04	1.16	0.99	0.96	0.79
7G#6	243	88	77	39	1.08	1.22	1.05	1.04	1.03
7G#5U	186	65	53	33	1.13	1.24	0.98	1.02	0.88
13G#5	243	106	107	61	1.24	1.40	1.02	0.93	0.87
13G#6	273	116	139	75	1.29	1.45	1.03	0.99	1.00
GFR (Caratelli et al. 2017)	520	n/a*	n/a	n/a	1.04	1.04	n/a	n/a	n/a
GFRP-RR (Caratelli et al. 2017)	313	n/a	n/a	n/a	1.03	1.22	n/a	n/a	n/a
GFRP-RR (+B) (Caratelli et al. 2017)	306	n/a	n/a	n/a	1.06	1.25	n/a	n/a	n/a

* Experimental values were not available.

strain in the longitudinal bars and concrete considering the limits of $0.25\varepsilon_{fu}$ and $0.6f_c^{'}$. Based on Table 7.4, the experimental results are consistent with the analytical results obtained according to the proposed method, with an error of less than 1.0%.

7.5.6.3. Axial load–bending moment interaction diagram considering creep rupture stress limit

Figure 7.9 gives the axial load–bending moment interaction diagram considering the creep rupture limit state according to ACI 440.1R-15 and CAN/CSA S806-12, R2017 for the tested specimens. As shown, at axial loads greater than a certain level (almost $0.1f_c^{'}A_g$ for the design according to CAN/CSA S806-12, R2017 and $0.06f_c^{'}A_g$ according to ACI 440.1R-15, the concrete stress reached $\alpha f_c^{'}$, while the stress in the tensile reinforcement was below the specified limit (α was selected to be 0.6 for producing the diagrams). ACI 440.1R-15,

CAN/CSA S806-12, R2017, and ACI 533.5R-20 do not specify the maximum concrete stress under the sustained load. Since sustained load is generally part of the service load, the concrete stress should be limited under sustained loads as well. Limiting the tensile strain to

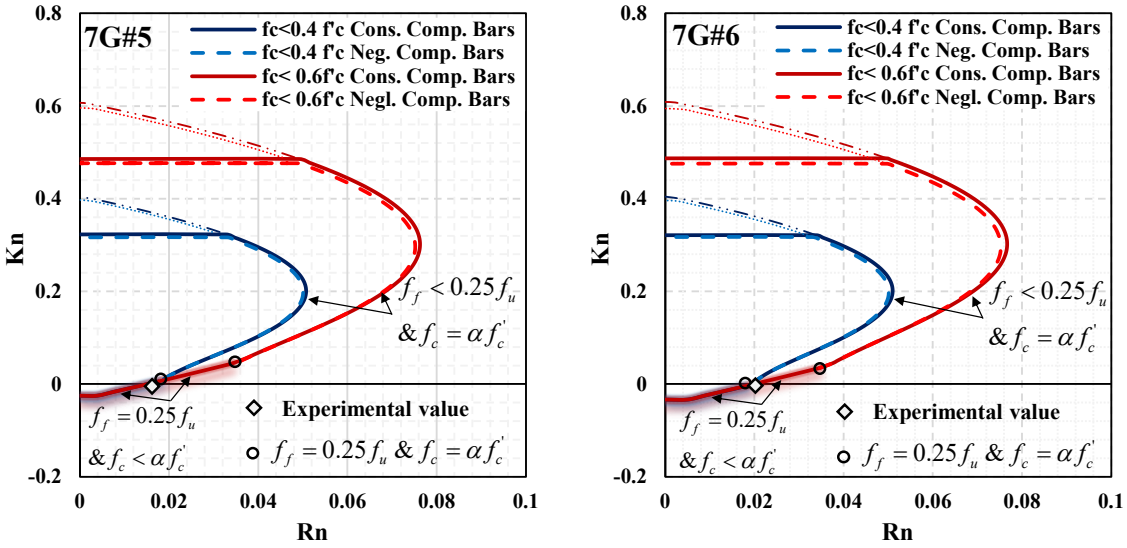

Figure 7.8 Axial load–bending moment interaction diagrams of the selected specimens at the service stage.

0.002 $\mu\varepsilon$ as in CAN/CSA S806-12, R2017 yielded 48% lower bending moment capacity for each axial-load level compared to limiting the tensile stress to $0.2 f_u$ as in ACI 440.1R-15. The experimental values were obtained using the strain measured during the test, as reported in Table 7.4, for both limitations of $\varepsilon_f = 0.002$ and $f_f = 0.2 f_u$. Comparing the analytical and experimental results reveals that the procedure presented in the section 7.3 was 1% and 9% conservative when applied according to CAN/CSA S806-12, R2017 and ACI 440.1R-15, respectively.

7.5.6.4. Axial load–shear strength interaction diagram

Figure 7.10 shows the axial load–shear strength interaction diagrams for the selected tested specimens obtained based on the procedure in section 7.4.4. The diagrams are presented according to CAN/CSA S806-12, R2017, CAN/CSA S6-19, and the modified ACI 440.1R-15 model in both scenarios: considering and neglecting the reduction factors. In deriving the axial load–shear strength interaction diagrams according to CAN/CSA S806-12, R2017 and

CAN/CSA S6-19, the ratio of factored bending moment to the factored shear force was assumed based on the test setup and loading system. The shear capacity predicted according to the modified ACI 440.1R-15 approach started from zero in the pure axial load and increased gradually by increasing the axial-load level. However, when the neutral axis depth reached to the effective depth (d), increasing the axial load level had no effect on the shear capacity anymore. In the prediction based on CAN/CSA S806-12, R2017, the minimum values for $0.05k_m k_r (f_c^{'})^{1/3} b_w d_v$ were determinative. The shear capacity based on CAN/CSA S806-12, R2017 increased gradually by increasing the axial-load level. As the term $k_a(1+(P/14A_g))$ reached its maximum value in 7G#6, the shear capacity remained constant afterward. The term $0.11\sqrt{f_c^{'}} b_w d_v$ was determinative in the parts related to compressive axial load. Therefore, applying the reduction factor in CAN/CSA S806-12, R2017 did not change the shear capacity in the axial compression force, unlike the axial tension force. The predicted shear capacity based on CAN/CSA S6-19 was the same for the axial loads approximately ranging from $-0.1A_g f_c^{'}$ to $0.1A_g f_c^{'}$. This is because the maximum value of $\varepsilon_x = 0.003$ specified by CAN/CSA S6-19 became determinative in the mentioned range. Thereafter, the shear capacity increased rapidly as a result of ε_x decreasing and remained constant when ε_x reached zero. Figure 7.8 shows that, when the axial compression load was greater than $0.25 f_c^{'} A_g$, the modified ACI 440.1R-15, CAN/CSA S6-19, and CAN/CSA S806-12, R2017 equations yielded the highest to the lowest predicted values, respectively. Yet the values predicted according to the standards varied greatly at axial-load levels below $0.25 f_c^{'} A_g$. For example, in the case of zero axial load, CAN/CSA S806-12, R2017, CAN/CSA S6-19, and the modified ACI 440.1R-15 equations yielded the highest to the lowest predicted values. Therefore, a general conclusion about the conservativeness of the standards cannot be made because it depends on the axial-load level. Specimens 13G#5 and 13G#6 aside,

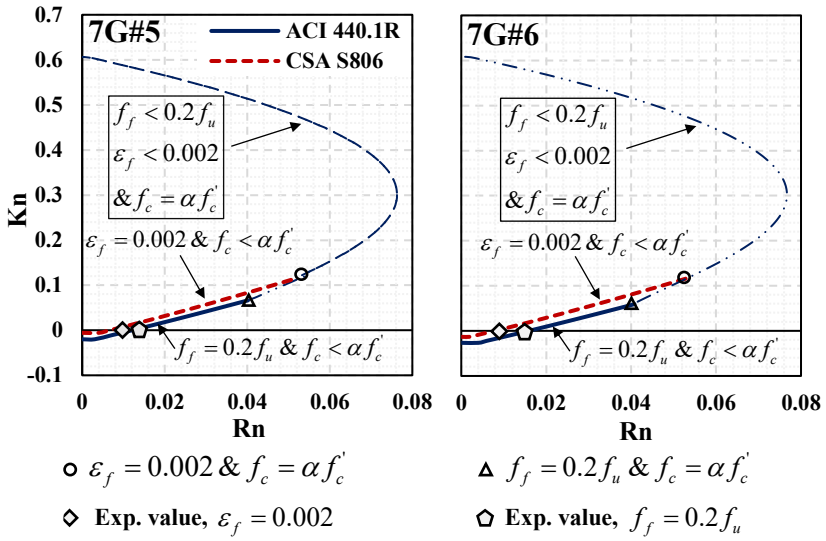

Figure 7.9 Axial load–bending moment interaction diagrams of the selected specimens considering the creep–rupture stress limit.

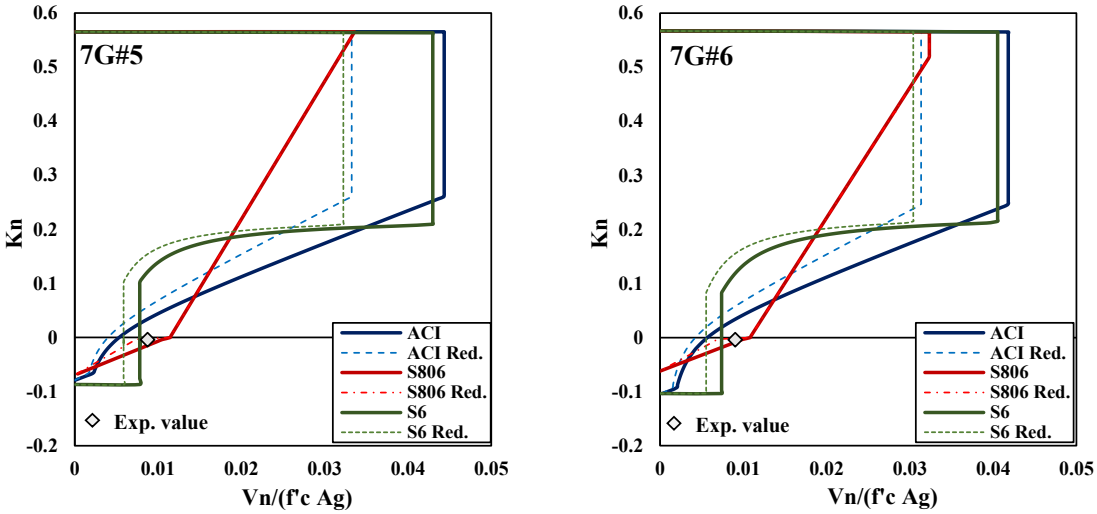

Figure 7.10 Axial load–shear strength interaction diagrams of the selected specimens.

the other tested specimens did not reach their full shear capacity. Table 7.5 presents a comparison of the experimental shear force to the analytical shear capacity. The modified ACI 440.1R-15 and CAN/CSA S6-19 equations were at least 39% and 20% conservative, on average, while the shear capacity predicted according to CAN/CSA S806-12, R2017 was greater than the experimental value by 3%, on average.

Table 7.5 Comparison of the experimental and analytical results for shear capacity and crack width.

Specimen ID	Experimental values				Theoretical to experimental values			
					Shear capacity			Crack width
	V kN	M_{crack} kN.m	$M_{crack,0.5}$ kN.m	Crack width $\varepsilon_f = 0.0015$, mm	ACI 440.1R	CSA S806	CSA S6	
7G#5	158	30	41	0.30	0.66	1.18	0.95	0.77
7G#6	183	36	72	0.20	0.67	1.08	0.86	0.83
7G#5U	133	27	36	0.30	0.76	1.32	1.06	0.81
13G#5	183	52	88	0.15	0.76	1.03	0.84	0.77
13G#6	206	60	170	0.15	0.77	0.91	0.73	0.90
GFR (Caratelli et al. 2017)	320	n/a	n/a	n/a	0.48	1.07	0.70	n/a
GFRP-RR (Caratelli et al. 2017)	313	n/a	n/a	n/a	0.38	0.83	0.61	n/a
GFRP-RR (+B) (Caratelli et al. 2017)	306	n/a	n/a	n/a	0.39	0.85	0.62	n/a

Note: M_{crack} is the bending moment corresponding to a strain of 0.0015 in longitudinal bars and $M_{crack,0.5}$ is the bending moment corresponding to a crack width of 0.5 mm.

7.5.6.5. Control of cracking

Figure 7.11 gives the axial load–bending moment interaction diagram considering the limit of 0.0015 as the tensile strain in the longitudinal bars. Until the axial-load level reached around $0.15 f_c^{'} A_g$, the strain limit of 0.0015 was determinative. Increasing the axial load caused the concrete compressive stress to reach $\alpha f_c^{'}$ (α was considered 0.6 to draw the diagrams) while the tensile strain remained below 0.0015. Table 7.5 compares the experimental and analytical results for the proposed cracking control procedure. In addition, the experimental crack width corresponding to the bending moment recorded at the strain of 0.0015 $\mu\varepsilon$ is reported. Furthermore, the bending moment corresponding to the measured crack width of 0.5 mm (as the maximum allowable crack width during the service stage) is presented. The method presented to obtain the theoretical bending moment at a strain of 0.0015 $\mu\varepsilon$ was 18% conservative. In addition, comparing the experimental crack width corresponding to the strain of 0.0015 $\mu\varepsilon$ revealed that, when the longitudinal bar strain was less than 0.0015, the crack width remained below 0.5 mm. Therefore, the procedure

presented in section 7.4.5 seems to be quite reliable in the procedure for controlling cracking in GFRP-reinforced PCTL segments.

7.6. Parametric Study

This section presents a parametric study assessing the effect of three determinative parameters—concrete compressive strength, reinforcement ratio, and sectional thickness—on the axial load–bending moment interaction diagrams for GFRP-reinforced PCTL segments at the ultimate and service stages. Only one scenario considering the contribution of GFRP bars in compression was selected in the parametric study to derive the charts, while the reduction factors were not

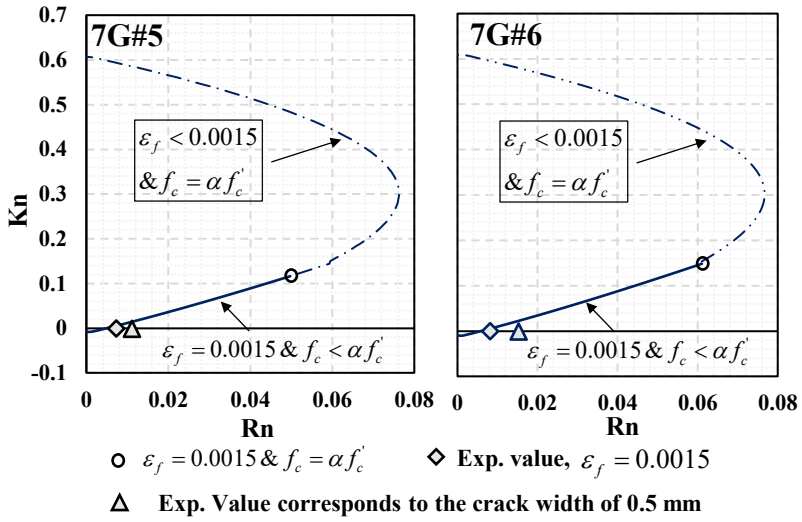

Figure 7.11 Axial load–bending moment interaction diagrams considering crack control strain.

considered. In addition, the procedure recommended in ACI 440.1R-15 was used in the calculations at the ultimate stage. For the service stage, the limits of $0.6f_c'$ and $0.25f_u$ were selected for the maximum stress in the concrete and reinforcement, respectively. The width of the selected segment for the parametric study was 1000 mm; #5 GFRP bars were used as longitudinal bars as mechanical properties reported in Table 7.1. The distance between the centroid of the top and bottom reinforcement to the concrete surface was assumed to be 60 mm. The recommended concrete compressive strength for PCTL segment ranged between 34 MPa and 60 MPa, according to ACI 533.5R-20. Therefore, four concrete compressive

strengths were designated for the parametric study: 35, 45, 55, and 60 MPa. In addition, three sectional thicknesses of 200, 300, and 400 mm were selected based on the practical applications in tunneling projects (ITA WG2-19; ACI 533.5R-20). For the reinforcement ratio, $1.5\rho_b$ (0.00396), $2.5\rho_b$ (0.0066), and $3.5\rho_b$ (0.00924) were designated. The mentioned balanced reinforcement ratio (ρ_b) and the corresponding reinforcement percentages were obtained considering concrete strength and sectional thickness equal to 45 MPa and 300 mm, respectively. In assessing a parameter, the other two were assumed to be constant.

7.6.1. Effect of concrete compressive strength

The effect of concrete compressive strength on the axial load–bending moment interaction diagrams at the ultimate and service stages is shown in Figs. 7.12a and 7.12b, respectively. The selected reinforcement ratio was equal to $2.5\rho_b$ (0.0066), while the thickness of the section was considered to be 300 mm for all the cases. According to Fig. 7.12a, the concrete compressive strength did not have a noticeable effect on the axial–flexural strength in the parts with tension-controlled failure. When the failure was governed by concrete crushing, increasing the concrete strength enhanced the bending moment capacity, becoming more pronounced by increasing the axial load level. For instance, when the concrete strength increased from 35 MPa to 60 MPa, the bending moment capacity increased by 22% in the case of zero axial load. When the axial load reached 80% of the nominal axial capacity in the case of 35 MPa, the increase was 160%. In addition, the axial load level corresponding to the maximum bending moment increased by increasing the concrete strength. Furthermore, increasing the concrete strength increased the axial load and bending moment corresponding to the balanced condition. According to Fig. 7.12b, the effect of concrete strength on the axial–flexural strength at the service stage was minimal when the maximum allowable stress in the tensile bars was determinative. When the concrete compressive stress was determinative, increasing the concrete strength enhanced the bending moment at each axial load level. In addition, increasing the concrete strength increased the axial load level

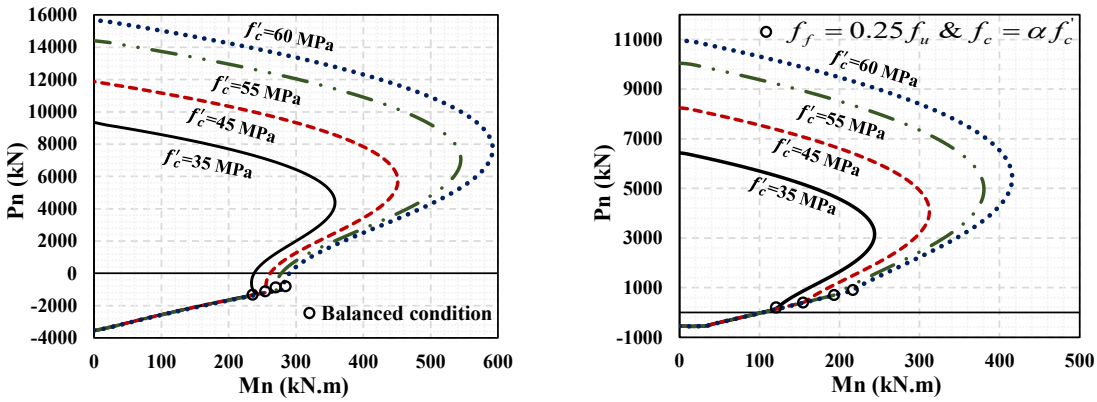

Figure 7.12 Effect of concrete compressive strength on the axial load–bending moment interaction diagram: (a) ultimate stage; (b) service stage.

corresponding to the point at which the allowable concrete compressive stress and the allowable bar tensile stress came together.

7.6.2. Effect of the Reinforcement Ratio

Figures 7.13a and 7.13b show the axial load–bending moment interaction diagrams considering three levels of reinforcement ratios of $1.5\rho_b$ (0.00396), $2.5\rho_b$ (0.0066), and $3.5\rho_b$ (0.00924) for the ultimate and service stages, respectively. To derive the diagrams, the concrete compressive strength and thickness of the section were assumed to be 45 MPa and 300 mm, respectively. In the case of tension-controlled failure, the bending moment capacity increased considerably by increasing the reinforcement ratio. In addition, the tensile load and bending moment corresponding to the balanced condition increased by increasing the reinforcement ratio. When the axial load was zero, increasing the reinforcement ratio from $1.5\rho_b$ to $3.5\rho_b$ enhanced the bending moment capacity by 43%. The effect of reinforcement ratio on the bending moment capacity decreased by increasing the axial load level. Increasing the reinforcement ratio from $1.5\rho_b$ to $3.5\rho_b$ only enhanced the bending moment capacity corresponding to the point of maximum bending moment in the diagram by 4%. Figure 7.13b shows that increasing the reinforcement ratio from $1.5\rho_b$ to $3.5\rho_b$ enhanced the bending moment capacity at service load on average by 125% when the maximum tensile

stress in the bars was determinative. When the axial load in the parts controlled by the maximum concrete stress was increased, the effect of reinforcement ratio on the bending moment capacity was negligible. In addition, increasing the reinforcement ratio decreased the axial load corresponding to the condition at which both limitations for the stress in the reinforcement and concrete were reached.

7.6.3. Effect of sectional thickness

The effect of three sectional thicknesses of 200, 300, and 400 mm on the axial load–bending moment interaction diagram at the ultimate and service stages is shown in Figs. 7.14a and 6.14b, respectively. Identical concrete compressive strength (45 MPa) and reinforcement area (1588 mm^2) equal to $2.5\rho_b$ when the thickness was 300 mm) was supposed to derive the diagrams for the selected thicknesses. Increasing the thickness of the section effectively enhanced the bending moment capacity, especially for the compression-controlled failure cases (Fig. 7.14a). Increasing the thickness from 200 mm to 400 mm improved the bending moment capacity by 310% on average in the case of axial compression load. In addition, increasing the thickness increased the axial load level corresponding to the balanced condition. As shown in Fig. 7.14b, the bending moment capacity was enhanced by increasing the thickness in general, considering the limitations of the service stage. The increase was, however, more pronounced when the allowable concrete stress became determinative. Increasing the thickness from 200 to 400 mm enhanced the bending moment capacity by 142% at the zero axial load level. The enhancement was 302% at the point on the diagram related to the maximum bending moment.

7.6.4. Discussion

According to the parametric study with the selected parameters, increasing the concrete compressive strength effectively enhanced axial–flexural capacity when the axial load level was greater than $0.15f_c^{'}A_g$, especially for the design at the service stage (Fig. 7.12). In contrast,

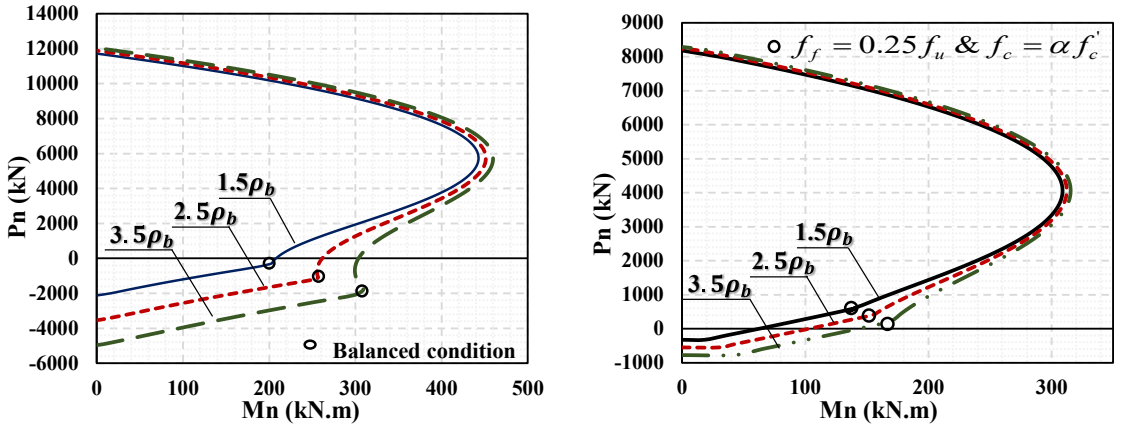

Figure 7.13 Effect of reinforcement ratio on the axial load–bending moment interaction diagram: (a) ultimate stage; (b) service stage.

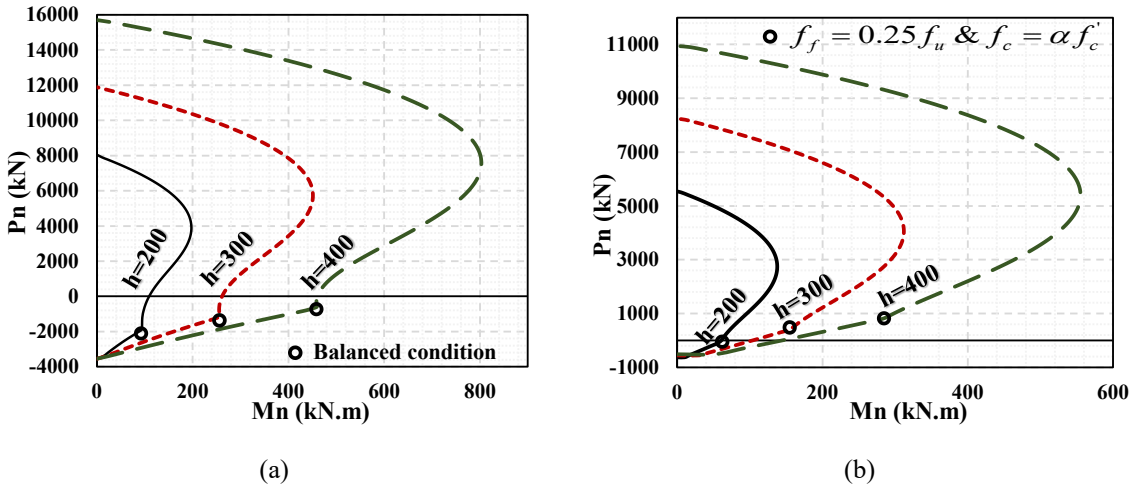

Figure 7.14 Effect of sectional thickness on the axial load–bending moment interaction diagram: a) ultimate stage; b) service stage.

increasing the reinforcement ratio was more effective than increasing the concrete strength (Fig. 7.13) to improve the axial–flexural capacity at axial loads below $0.15 f_c' A_g$. Our results indicate that increasing the sectional thickness greatly increased the axial-flexural capacity at all the axial load levels (Fig. 7.14).

7.7. Conclusions

The following conclusions can be drawn from the results of the experimental and analytical studies:

1. Increasing the reinforcement ratio in the tunnel segment specimens by increasing bar size and decreasing bar spacing enhanced the post-cracking stiffness and the load-carrying capacity of the specimens. In addition, increasing the reinforcement ratio by 43%, 86%, and 165% decreased the crack width corresponding to the service moment by 50%, 64%, and 79%, respectively. The reduction was 36%, 61%, and 65%, respectively, for deflection values. Replacing the closed ties with U-shaped ties increased the crack width and deflection at the average service moment by 14% and 36%, respectively, while decreasing the peak load by 12%.
2. Neglecting the contribution of GFRP bars in compression did not have a noticeable effect on predicting the axial–flexural strength when the axial load level was less than $0.25f_c^{'}A_g$. In contrast, doing so at axial load levels greater than $0.25f_c^{'}A_g$ lowered the prediction of bending moment capacity in the specimens by 3%.
3. In contrast to the axial load levels below $0.2f_c^{'}A_g$, the ACI 440.1R-15 equation predicted higher bending moment capacity than the CAN/CSA S806-12, R2017 equation for the axial loads greater than $0.2f_c^{'}A_g$. The ACI 440.1R-15 and CAN/CSA S806-12, R2017 equations overestimated the bending moment capacity of the tested GFRP-reinforced segments by 6% and 19% (on average), respectively.
4. The experimental results were very consistent with the analytical results obtained based on the proposed method to obtain axial load–bending moment interaction diagram at the service stage.
5. The creep–rupture stress limit was generally determinative in the specimens when the axial load level was less than $0.1f_c^{'}A_g$ and $0.06f_c^{'}A_g$, considering the limitations provide for in CAN/CSA S806-12, R2017 and ACI 440.1R-15, respectively. Employing the creep–rupture control procedure developed based on CAN/CSA S806-12, R2017 and ACI 440.1R-15 yielded 1% and 9% conservative results on average for the tested specimens, respectively.
6. According to the parametric study, increasing the concrete compressive strength to enhance axial–flexural capacity was effective when the axial load level was greater than $0.15f_c^{'}A_g$. In contrast, increasing the reinforcement ratio was more effective in

improving the axial–flexural capacity at the axial loads below $0.15 f_c^{'} A_g$. Increasing the sectional thickness greatly increased the axial-flexural capacity at all axial load levels.

CHAPTER 8 DEFLECTION CONTROL METHODOLOGIES FOR CURVILINEAR CONCRETE MEMBERS REINFORCED WITH GFRP BARS

Foreword

Authors and Affiliation:

Seyed Mohammad Hosseini: Ph. D. Candidate, Department of Civil Engineering, University of Sherbrooke, Sherbrooke, Quebec, Canada, J1K 2R1

Salaheldin Mousa: Postdoctoral fellow, Department of Civil Engineering, University of Sherbrooke, Sherbrooke, Quebec, Canada, J1K 2R1

Hamdy M. Mohamed: Research associate and lecturer, Department of Civil Engineering, University of Sherbrooke, Sherbrooke, Quebec, Canada, J1K 2R1.

Brahim Benmokrane: Professor, Department of Civil Engineering, University of Sherbrooke, Sherbrooke, Quebec, Canada, J1K 2R1.

Journal title: ACI Structural Journal

Paper status: Accepted on May 2023.

Contribution in thesis:

Control of deflection at service stage is among the important criteria in designing GFRP-reinforced members. This chapter presents novel deflection prediction methodologies for curvilinear GFRP-RC elements with a focus on PCTL segments. To the best of the authors' knowledge, the equations and procedures developed in this chapter are novel and cannot be found elsewhere in the literature. The information presented in this chapter will be significantly useful for design engineers and for improving design standards.

8.1. Abstract

This article reports the results of a comprehensive analytical study implemented to develop deflection prediction methodologies for curvilinear reinforced concrete (RC) members with glass fiber-reinforced polymer (GFRP) reinforcement, focusing on precast concrete tunnel lining (PCTL) segments. The first step involved modifying the procedures for estimating elastic deflection, cracking moment, and cracked moment of inertia, which were then introduced for use with curvilinear members. In the next step, three methodologies of effective moment of inertia, integration of curvature, and integration of curvature considering tension–stiffening were developed for curvilinear members. Then, the analytical results were compared to the experimental database, and a novel method was developed for predicting deflection in curvilinear GFRP-RC members. In the third and final step, a procedure was developed to adapt the presented methodologies for use with a tunnel segment under real load and boundary conditions. The results indicate that the proposed method could predict the deflection of curvilinear GFRP-reinforced concrete members with high accuracy.

Keywords: Reinforced concrete (RC); glass fiber-reinforced polymer (GFRP); curvilinear RC members; precast concrete tunnel lining segments; deflection; effective moment of inertia.

8.2. Introduction

Curvilinear reinforced concrete (RC) elements are widely used in many types of structures, such as tunnels, bridges, water tanks, and culverts (Khaloo et al. 2020). Precast concrete tunnel lining (PCTL) segments number among the most frequently used curvilinear RC elements. When a tunnel is bored with a tunnel boring machine (TBM), such segments are placed sequentially as the boring advances (ACI 544.7R-16). Corrosion is one of the major problems associated with RC structures reinforced with conventional steel reinforcement. Such issues are exacerbated in the corrosive environment of tunnels (Caratelli et al. 2016; ACI 533.5R-20). Replacing steel reinforcement with glass fiber-reinforced polymer (GFRP) reinforcement is recognized as a viable solution for dealing with corrosion issues (Robert and Benmokrane 2013). Serviceability often governs the design of flexural members reinforced with GFRP bars either through cracking, deflection, or stress verification (ACI 440.1R-15). In general, curvature, loading distribution, span length, and boundary conditions do not play a considerable role in cracking control and stress verification procedures as they are mainly related to sectional properties. These issues must be considered in predicting deflection. Due to of commercial GFRP bars having lower moduli of elasticity than steel rebars, deflection in GFRP-RC flexural members at service load is generally greater than in steel-RC members (Mota et al. 2006). Therefore, employing effective methodologies to predict the deflection of GFRP-RC members with high accuracy is of great importance.

Two common approaches can be employed to calculate the immediate deflection of flexural RC elements: (1) using the general assumptions of elastic deflection calculation along with the effective moment of inertia (I_e) and (2) integration of curvature along the length of member. I_e considers the effective transition between the gross moment of inertia (I_g) in uncracked regions of a member to the cracked moment of inertia (I_{cr}) in the cracked part considering the effect of tension stiffening. Branson (1963) originally assumed the rigidities of the cracked and uncracked parts of a RC element as springs in parallel. His assumption can be written in the form of Eq. 8.1 as a general model to predict I_e in RC members.

$$I_e = k_1 I_g + k_2 I_{cr} \leq I_g \tag{8.1}$$

where k_1 and k_2 are functions of the ratio of cracking to applied moment (M_{cr} / M_a), which has been empirically proposed. Equation 8.1 based on Branson's recommendations can predict the deflection of simply supported straight rectangular concrete beams reinforced with typical amounts of steel reinforcement with reasonable accuracy. Such models, however, underestimate the deflection of FRP-RC elements, as it was correlated for beams with I_g / I_{cr} smaller than approximately 4.0, while I_g / I_{cr} in FRP-RC members generally ranges between 5 to 25 (Bischoff 2005). Besides, supposing parallel springs for the rigidities of uncracked and cracked sections in Eq. (1) is an incorrect assumption since they are series springs (Bischoff and Scanlon 2007; Bischoff 2020). By neglecting such wrong assumptions, various researchers tried to modify the values of k_1 and k_2 based on the experimental results of FRP-RC beams(Benmokrane et al. 1996; Gao et al. 1998; Theriault and Benmokrane 1998; Alsayed et al. 2000; Toutanji and Saafi 2000; Yost et al. 2003; Mousavi and Esfahani 2012; Adam et al. 2015; Zhang et al. 2015; Arabshahi et al. 2022). Bischoff (2005) developed a new form of equation (Eq. 8.2) for I_e based on the true assumption of series spring for the cracked and uncracked rigidities in a flexural member.

$$I_e = \frac{I_{cr}}{1 - \eta\beta(M_{cr} / M_a)} \leq I_g \tag{8.2}$$

where η is $1 - I_{cr} / I_g$ and β is the tension-stiffening factor varying between 0 and 1 for the case of no tension stiffening and full tension stiffening, respectively, suggested to be taken as (M_{cr} / M_a). Employing Eq. 8.2 yielded reasonably conservative estimations for deflection of simply supported FRP-RC members.

Integration of curvature along the member is another approach to general deflection calculation proposed in the literature by various researchers and in standards (Razaqpur et al. 2000; Rasheed et al. 2004; Bischoff and Gross 2011b; CAN/CSA S806-12, R2017). The general concept of this method is to obtain curvature in each section and integrate it along the length of the member. Curvature in uncracked and cracked parts is calculated using the gross and cracked moment of inertia, respectively, neglecting the effect of tension stiffening.

The effect of tension stiffening can be considered by obtaining the curvature of the cracked part with the effective moment of inertia in each section (Bischoff and Gross 2011b) or by linear interpolation of the section curvature (Rasheed et al. 2004). Bischoff and Gross (2011b) employed an approach integrating curvature, assuming the gross moment of inertia in the uncracked regions and the effective moment of inertia derived from Eq. (8.2) for the cracked regions. They proposed the following equation as the equivalent moment of inertia by simplifying the integrals based on different load and boundary conditions:

$$I_e = \frac{I_{cr}}{1-\gamma\eta(M_{cr}/M_a)^2} \leq I_g \tag{8.3}$$

where γ is a factor considering the effect of load and boundary conditions. Equation (8.3) seems to be the most theoretically correct method in the literature; It has also been adopted by ACI 440.1R-15. In general, neglecting tension stiffening led to deflection being overestimated, while considering it equal to what proposed by Bischoff and Gross (2011b) underestimated deflection. The accuracy, however, depends on the reinforcement's axial stiffness, estimated cracking moment, estimated concrete modulus of elasticity, moment level on which deflecting is calculated, load and boundary conditions, and so on (Bischoff 2005; Bischoff and Gross 2011b; Bischoff and Gross 2011a; Bischoff 2020).

The deflection prediction methodologies in the literature for FRP-RC members generally deal with straight members without axial load. In addition, there are no recommendations for adapting the available methodologies for complex load and boundary conditions in real applications. This paper presents an analytical study performed to propose deflection prediction methodologies to estimate the deflection of curvilinear GFRP-RC members under service-load conditions. The focus of this study was to adapt the methodologies for PCTL segments. The methodologies, however, are general and can be used for any type of curvilinear member.

8.3. Research Significance

ACI 440.1R-15 and CAN/CSA S806-12, R2017 propose deflection prediction methodologies for serviceability control in straight GFRP-RC members. To the best of the authors' knowledge, the literature contains no methodology for predicting the deflection of

curvilinear GFRP-RC elements. This study is pioneering in the development of novel deflection prediction methodologies for curvilinear GFRP-RC elements with a focus on PCTL segments. The methodologies presented were verified with the test data from 11 full-scale GFRP-reinforced PCTL segments. To the best of the authors' knowledge, the equations and procedures developed in this study are novel and cannot be found elsewhere in the literature. The results of this study will be significantly useful for design engineers and for improving design standards.

8.4. Summary of Experimental Program

Eleven full-scale curvilinear GFRP-reinforced PCTL segments were constructed and tested under bending load. An overview of the specimens' details, reinforcement characteristics, test setup, and instrumentation is reported in the following; detailed information can be found in papers previously published by the authors.(Hosseini et al. 2022a; Hosseini et al. 2022b) The specimens had internal and external radii of 3250 and 3500 mm, respectively, and measured 3100 mm in length, 1500 mm in width, and 250 mm in thickness (Fig. 8.1). The test parameters include reinforcement ratio (0.48%, 69%, 0.90%, and 1.28%), concrete type (normal-strength concrete [NSC] and fiber-reinforced concrete [FRC]), concrete strength (NSC and high-strength concrete [HSC]), and tie configuration (closed ties and U-shaped ties). Sand-coated #5 and #6 GFRP bars were used as longitudinal reinforcement and end-anchorage U-shaped bars. The transverse ties were sand-coated #4 GFRP bars, either U-shaped or closed ties. Tables 8.1 and 8.2 report the properties of reinforcement and concrete, respectively. The specimens were tested under three-point bending load until failure (Fig. 8.1). Three linear potentiometers (LPOTs) recorded mid-span deflection; the quarter-span deflection was recorded with two LPOTs installed at the quarter-span. Table 8.2 presents the test matrix and the key experimental results for the tested specimens. In order to investigate the deflection behavior at the service stage and compare the experimental results with the analytical procedure, some reference points must be specified. In the following, two references points for GFRP-reinforced flexural elements in the literature were defined (ISIS Canada Research Network 2007; Bischoff and Gross 2011a): (1) moment corresponding to 30% of the peak moment and (2) moment corresponding to a strain of 2000

Table 8.1 Mechanical properties of the GFRP reinforcement

Reinforcement type	Bar size	Bar diameter (mm)	Nominal cross-sectional area ($mm^{2)}$	Tensile modulus of elasticity (GPa)	Ultimate strength (MPa)	Ultimate strain (%)
Curvilinear longitudinal GFRP bars	#5	15.0	199	55.1 ± 1.25	1,115 ± 60	2.0 ± 0.1
	#6	20.0	284	52.9 ± 0.6	1,068 ± 49	2.0 ± 0.1
U-shaped GFRP bars*	#5	15.0	199	53.5 ± 1.1	1,283 ± 42	2.4 ± 0.1
	#6	20.0	284	53.2 ± 2.9	1,131 ± 35	2.1 ± 0.0
U-shaped and closed GFRP ties*	#4	13.0	129	55.6 ± 1.6	1,248 ± 74	2.2 ± 0.1

*The reported values are based on applying tension to straight bars manufactured with the same process as the bent bars.

Table 8.2 Test matrix and the test results

Specimen ID	Concrete type	Longitudinal reinforcement	Tie configuration	$f_c^{'}$, MPa	f_p, MPa	f_{150}^{D}, MPa	M_{cr}, kN.m	M_n, kN.m	Deflection at service moment (mm)		
									0.3 M_p	2000 με	1.1 M_{cr}
7G#5	NC	7 #5 bars	Closed ties	48	-	-	38	213	11.7	2.5	3.0
7G#6	NC	7 #6 bars	Closed ties	54	-	-	42	243	9.2	3.5	2.6
13G#5	NC	13 #5 bars	Closed ties	51	-	-	42	243	6.2	5.2	1.8
13G#6	NC	13 #6 bars	Closed ties	47	-	-	42	273	6.9	6.0	1.5
7G#5U	NC	7 #5 bars	U-shaped ties	44	-	-	37	177	9.5	2.6	3.3
7G#5H	HSC	7 #5 bars	Closed ties	86	-	-	49	247	10.4	2.7	3.4
13G#5H	HSC	13 #5 bars	Closed ties	90	-	-	44	257	6.5	3.7	1.9
7G#5HU	HSC	7 #5 bars	U-shaped ties	87	-	-	41	227	9.8	2.1	2.9
7G#5F	FRC	7 #5 bars	Closed ties	50	4.5	0.8	33	210	9.8	2.5	2.5
13G#5F	FRC	13 #5 bars	Closed ties	44	4.0	1.3	30	273	8.2	3.8	1.9
7G#5FU	FRC	7 #5 bars	U-shaped ties	46	4.3	1.0	31	230	9.6	3.1	1.9

Notes: 1 mm = 0.0394 in.; 1 kN·m = 0.7376 kip-ft; 1 MPa = 145 psi.

$\mu\varepsilon$ in the tensile reinforcement. The latter sometimes leads to defining a service moment that is lower than the cracking moment. This might lead to unrealistic predictions for deflection at the service load. Therefore, a moment corresponding to 1.1 times the cracking moment was introduced as an alternative to the moment corresponding to a strain of 2000 $\mu\varepsilon$ when the obtained service moment is smaller than the cracking moment. Mota et al. (2006) applied the same approach.

8.5. Analytical Investigations

This section presents the deflection prediction methodologies developed for use with GFRP-reinforced curvilinear members. Initially, two methods were proposed to calculate elastic

deflection in curvilinear structural elements. The cracking moment to be used in calculating deflection is discussed and proposed. After that, the procedures and models developed to obtain the cracked moment of inertia in GFRP-reinforced NSC, HSC and FRC PCTL segments are described. Subsequently, three procedures for calculating deflection are presented and adapted for use in curvilinear RC members. Thereafter, the results obtained from the presented procedures are compared with the experimental results. Subsequently, a

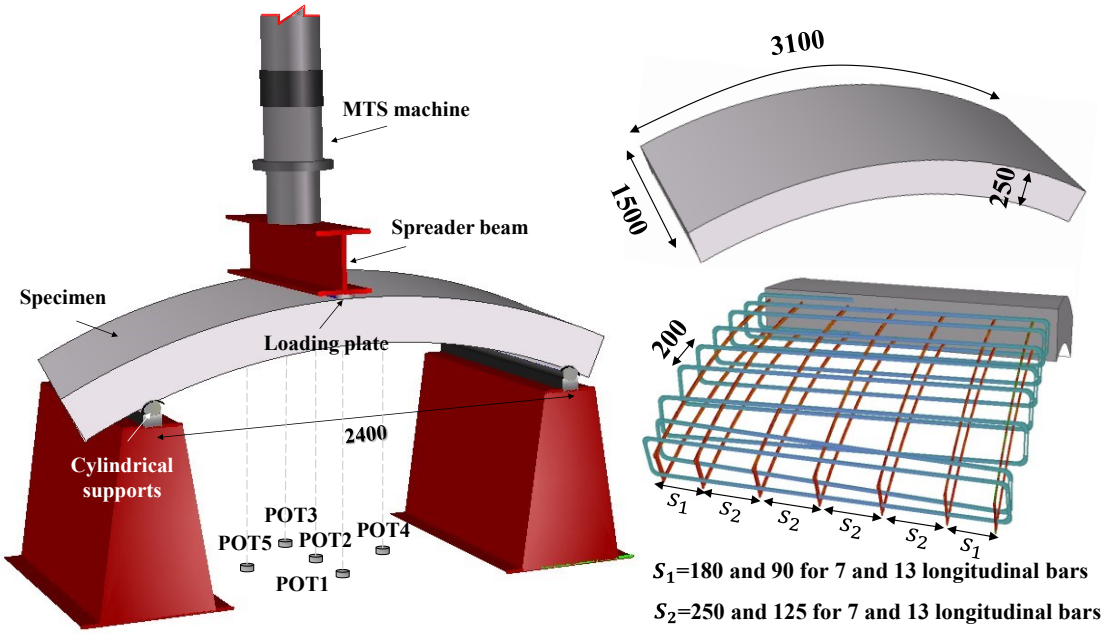

Figure 8.1 Specimens geometry, reinforcement details, test setup, and instrumentations, dimensions in mm (Note: 1 mm = 0.0394 in).

model is proposed capable of predicting deflection in curvilinear GFRP-RC members with high accuracy. Lastly, a procedure was developed to employ the deflection prediction methodologies presented for tunnel segments under actual loading and boundary conditions. While the methodologies presented focus mainly on tunnel segments, they can also be used effectively to estimate the service-load deflection of different types of curvilinear GFRP-RC members.

8.5.1. Calculating elastic deflection in curvilinear members

When the ratio of radius to the sectional height in a curved member is greater than 2, the fundamental concepts related to the relationship between curvature and deflection as well as the strain energy due to the bending can be approximated by that of straight members (Boresi

et al. 1988). Below, the two methods commonly used to calculate elastic deflection in straight members were modified for use with curvilinear members.

Figure 8.2 shows the centerline of a curvilinear member before and after deformation induced by an external force. The radial deflection at each point is r_θ. Consider a small element of CD with the arc length of ds. The exaggerated shape shows that the centerline

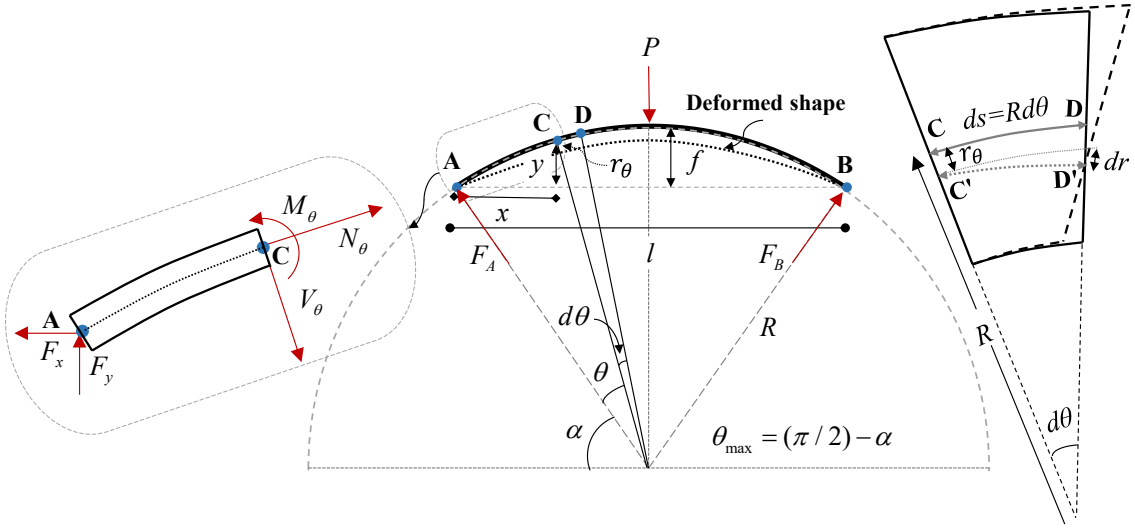

Figure 8.2 Geometrical parameters, deformation parameters, external loads, and internal forces in a curvilinear member with load and boundary conditions similar to the test specimens (deformations and curvatures are exaggerated).

of the segment is specified as CD and C' D' after deformation. Radial deformation at the point C is r_θ, while such deformation is $r_\theta + dr$ at point D. Therefore, the relationship between the radial deflection and curvature in the element is:

$$\frac{d^2r}{ds^2} = -\phi_\theta = \frac{M_\theta}{E_\theta I_\theta} \tag{8.4}$$

Obtaining the above equation assumed small deformations. In addition, the curvilinearity effect of the member on the basic assumptions of internal stresses, curvature, rotation, and deflection was ignored given the high ratio of curvature to thickness in the member. Considering $ds = Rd\theta$, rotation can be obtained with the following equation:

$$\Theta_\theta = \int -\phi_\theta R d\theta + C_1 \tag{8.5}$$

where C_1 can be obtained according to the boundary conditions. Using a similar approach, radial deflection in each section can be obtained as follows:

$$r_\theta = \int (\int -\phi_\theta ds + C_1) R d\theta + C_2 \tag{8.6}$$

To obtain the vertical deflection, dr in each point should be multiplied by $\sin(\theta)$ in the integral. Therefore, the following equation is obtained to calculate the vertical deflection in a polar coordinate system in a curvilinear member:

$$\Delta_\theta = \int (\int -\phi_\theta R d\theta + C_1) R \sin(\theta) d\theta + C_2 \tag{8.7}$$

where C_2 can be obtained using boundary conditions. When it is aimed to calculate the deflection at a certain location, deflection can be obtained using a virtual work method with this equation:

$$\Delta = \sum \int \frac{m_\theta M_\theta}{E_\theta I_\theta} R d\theta \tag{8.8}$$

where m_θ is the moment induced as a result of a unit dummy load applied at the point where deflection is being calculated. It should be noted that the deflections resulting from shear and axial forces are neglected as they are generally insignificant when the span length-to-depth ratio is large.(Boresi et al. 1988) According to the presented methods, an equation for calculating the elastic deflection of the test specimens were developed as reported in Appendix B.

8.5.2. Cracking moment

Cracking moment (M_{cr}) is one of the most influential parameters in estimating the deflection in an RC member. Therefore, predicting the exact cracking moment is of great importance in accurately estimating deflection. Equalizing the maximum tensile stress in the uncracked section to the maximum tensile capacity of concrete ($0.62\sqrt{f_c'}$ according to ACI 318-19 yields the theoretical cracking moment ($M_{cr,theo}$). Shrink restraint in an RC member might lead to pre-existing tensile stresses in the member, which reduce the cracking moment (Scanlon and Bischoff 2008). Bischoff and Gross (2011b) reported a range of 0.48 to 1.44

with median of 0.85 for the ratio of theoretical to experimental cracking moment based on the extensive data from literature for FRP-RC flexural members. ACI 318-19 recommends multiplying the theoretical cracking moment by 0.67 in the deflection-calculation procedure. The ratio of theoretical to experimental cracking moment in the tested specimens was 0.7±0.02, 0.58±0.04, and 0.61±0.02 for NSC, HSC, and FRC specimens, respectively. There is need for an extensive study to determine the value of cracking moment in different concrete types for FRP-RC members. Given the lack of such study, our study recommends taking M_{cr} equal to $0.7M_{cr,theo}$ for NSC GFRP-reinforced tunnel segments and $0.6M_{cr,theo}$ for HSC and FRC GFRP-reinforced tunnel segments according to the experimental results.

8.5.3. Cracked moment of inertia

Calculating the cracked moment of inertia is essential in all the deflection-calculation methods presented. In the following, the procedures to calculate the cracked moment of inertia for GFRP-reinforced NSC, HSC and FRC tunnel segments were presented. The contribution of reinforcing top bars is neglected in the presented procedures as a simplifying and conservative assumption.

8.5.3.1. GFRP-reinforced NSC and HSC curvilinear members

When there is no axial load, the cracked moment of inertia does not depend on the applied bending moment on a section in which a linear stress–strain relationship is considered for concrete in compression. When axial load is present, both the axial load and bending moment in the section affect the cracked moment of inertia. The cracked moment of inertia in such conditions can be calculated with the following equation when the contribution of the top reinforcement is neglected.

$$I_{cr} = \frac{bd^3}{3} k_a{}^3 + n_f A_f d^2 (1-k_a)^2 \tag{8.9}$$

where Eq. 8.10 can be used to calculate k_a.

$$k_a = \frac{\sqrt{N^2 - 2N\omega n\rho_f + \omega^2 n\rho_f (n\rho_f + 2)} - n\rho_f \omega + N}{\omega} \tag{8.10}$$

where $\omega = E_c \varepsilon_c bd$. As can be inferred from Eq. 8.10, the un-cracked depth depends on the level of axial load and the maximum concrete compressive strain. Eq. 8.11 presents the relationship between the bending moment, axial load, k_a and ε_c in a section.

$$M_a = n\rho_f \omega d(1-k_a)(\frac{3-k_a}{9}) + N(\frac{h}{2} - \frac{k_a d}{3}) \tag{8.11}$$

Inserting k_a from Eq. 8.10 into Eq. 8.11 yields an equation with ε_c as its unknown variable. Due to complexity, however, there is no closed form solution for that equation. In such situations, the value of ε_c can be found by trial and adjustment. Subsequently, the values of k_a and I_{cr} can be calculated. The presented equations are based on linear concrete stress–strain assumption in compression, which is valid until around $0.7 f_c^{'}$ (Park and Paulay 1991). According to a preliminary comparison conducted by the authors for the tested specimens, neglecting the effect of axial load led to an error of around 10% in the value of k_a for a given value of M_a when the axial load was below $\pm 0.0045 f_c^{'} A_g$. When the axial load was increased, neglecting such contributions led to considerable errors.

8.5.3.2. Curvilinear GFRP-reinforced FRC members

Finding the cracked moment of inertia in an FRC section considering the contribution of fibers requires assuming a stress–strain model for FRC in compression and tension. Figure 8.3 presents the stress and stress distribution in the section based on the stress–strain model for FRC. This model was adopted and simplified for the service stage based on the provisions in ACI 544.4R-18. The parameters used in the stress–strain response of FRC can be obtained with beam testing as well as stress and strain compatibility. σ_{cr} and σ_p can be taken equal to f_p and $0.37 f_{150}^{D}$, respectively (ACI 544.7R-16; ACI 544.4R-18; ASTM C1609-19). Equations 8.12 and 8.13 form a system of equations with two unknown variables—ε_c and k_a—which can be obtained through trial and adjustment.

$$F_f + F_{cr} + F_p + N - F_c = 0 \tag{8.12}$$

$$M_a = F_f d + F_{cr}(\frac{k_a d + 2d_{cr}}{3}) + F_p(\frac{d_{cr} + h}{2}) + N(\frac{h}{2}) - F_c(\frac{k_a d}{3}) \tag{8.13}$$

After obtaining ε_c and k_a, the cracked moment of inertia considering the contribution of fibers can be calculated with the following equation.

$$I_{cr} = \frac{M_a k_a d}{E_c \varepsilon_c} \tag{8.14}$$

8.5.4. Deflection prediction using effective moment of inertia

The effective moment of inertia proposed by Bischoff (2005) [Eq. 8.2] can be replaced with the value of I_θ in the methods presented to calculate deflection when the relationship between the applied loads and internal forces can be specified. This method is referred herein as I_e. This procedure does not consider the effect of load and boundary conditions or variations in the axial load in the member. It does take into account the effect of tension stiffening by using the tension-stiffening factor of β. This factor theoretically varies between 0 and 1 depending on the level of bending moment. Bischoff (2005) recommended using M_{cr} / M_a as the tension-stiffening factor. As this method supposes a constant effective moment of inertia along the member, it is simple to use but its accuracy depends on the types of loading, boundary conditions, reinforcement ratio, and level of bending moment. The best accuracy is expected for simply supported beams with point load or distributed load (Bischoff and Gross 2011b). In addition, the axial-load level and its variation along the member might greatly affect accuracy. In the case of FRC, the contribution of the fibers can be considered using the effect of fibers on the cracked moment of inertia as well as their effect on the tension-stiffening behavior of the concrete. Bischoff (2007) proposed modifications to Eq. 8.2 to consider the contribution of fibers for both cracking moment of inertia and tension stiffening. This study relies only on the effect of fibers on the cracked moment of inertia to consider the contribution of fibers in calculating the calculation of GFRP-reinforced FRC PCTL segments since considering the effect of FRC on the tension stiffening leads to impractical and complex procedures.

8.5.5. Deflection prediction using integration of curvature

For predicting of deflection using integration of curvature, the cracked parts and uncracked parts of the member should be specified based on the bending-moment diagram. Thereafter, the deflection-calculation equations can be used by substituting I_θ with gross and cracked

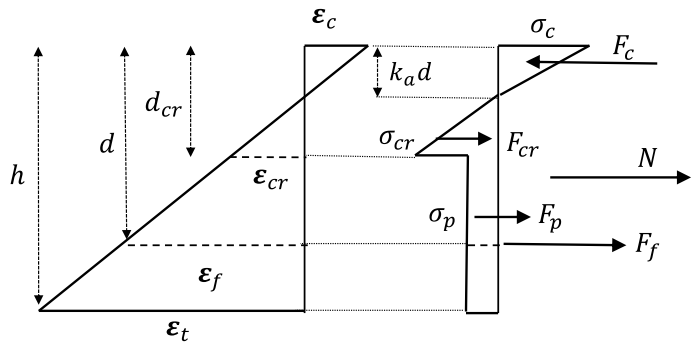

Figure 8.3 Assumed model for distribution of stress and strain in the cross section of FRC specimens.

moment of inertia in the uncracked and cracked sections, respectively. This method is referred to as the Integ. method herein. Equation 8.15 can be used to calculate the deflection through integration of curvature in the virtual work method.

$$\Delta = \sum_{Un-cracked} \int \frac{m_\theta M_\theta}{E_c I_g} R d\theta + \sum_{Cracked} \int \frac{m_\theta M_\theta}{E_c I_{cr,\theta}} R d\theta \tag{8.15}$$

Equation (8.15) could be simplified with this approach:

$$\Delta = \Delta_g + \delta\Delta_{cr} \tag{8.16}$$

where Δ_g and $\delta\Delta_{cr}$ can be calculated with these equations (see appendix C):

$$\Delta_g = \frac{1}{E_c I_g} \int m_\theta M_\theta R d\theta \tag{8.17}$$

$$\delta\Delta_{cr} = \sum_{i=1}^{n} \frac{\eta_i}{E_c} \int \frac{m_\theta M_\theta}{I_{cr,i}} R d\theta \tag{8.18}$$

These equations are valid for all types of loading and boundary conditions, provided that no settlement or movement has occurred in the supports and that the relationship between the applied load and internal forces can be determined. Since variations in the axial-load level changes the value of I_{cr}, using a constant value for I_{cr} might be a source of errors in the

calculation procedure. To account for the effect of axial load on deflection calculation, the cracked sections along the member can be divided into a reasonable number of parts. The values of η_i and $I_{cr,i}$ for each part can be calculated by obtaining $\delta\Delta_{cr}$ and summing $\delta\Delta_{cr,i}$ along the cracked section. When the level of axial load and its variation along the member are not significant, however, the minimum value of I_{cr} along the member expected in a section with the greatest bending moment and the lowest axial load can be used for all the cracked sections as a conservative simplification.

Simplifying the presented equations for load and boundary conditions similar to the tested specimens leads to the following equation to calculate the deflection at mid-span (see appendix C):

$$\Delta = \frac{\lambda}{E_c I_{cr}} \tag{8.19}$$

where λ is calculated using Eq. (8.20).

$$\lambda = 2(1-\eta)[\int_0^{\frac{\pi}{2}-\alpha} C_\theta R d\theta + (\frac{\eta}{1-\eta})\int_{\theta_g}^{\frac{\pi}{2}-\alpha} C_\theta R d\theta] \tag{8.20}$$

where $C_\theta = m_{(\pi/2)-\alpha} M_\theta$. Equation 8.20 is valid for those types of load and boundary conditions where the distribution of bending moment is symmetrical, and the uncracked section starts at the supports an angle θ_g, followed by a cracked section from θ_g to mid-span. In addition, I_{cr} of the critical section (often located at mid-span) was used as the cracked moment of inertia for all the cracked sections in Eq. 8.15, since the level of axial load was not significant. The angle θ_g corresponds to the angle from the support to the point at which $M_\theta = M_{cr}$. For the load and boundary conditions of the tested specimens, θ_g can be obtained with this equation

$$\theta_g = \sin^{-1}(\frac{\cot(\alpha)(2C_b - C_a) - \sqrt{(2PR)^2 + 4C_a C_b - (C_a)^2}}{2PR(\cot^2(\alpha)+1)}) - \alpha \tag{8.21}$$

where $C_a = 2Pf\cot(\alpha) + Pl - 4M_{cr}$ and $C_b = PR\cot(\alpha)$. It should be noted that M_{cr} is dependent to the level of axial load. When the variation in axial load is not significant, however, M_{cr} obtained from the minimum axial load along the member can be used as a

conservative assumption for simplicity. For the tested specimens, the integrals in Eq. 8.20 were obtained and are reported in appendix C.

8.5.6. Deflection prediction using integration of curvature considering tension stiffening

Due to the effect of tension stiffening, the stiffness in the cracked parts of an element is greater than the cracked moment of inertia (Bischoff and Gross 2011b). By supposing $I_\theta = I_{cr,\theta} / \left[1-\eta_\theta \beta_\theta (M_{cr,\theta} / M_\theta)\right]$ in the calculations related to the cracked parts of the section, the effect of tension stiffening can be considered. In such situations, deflection can be obtained with

$$\Delta = \sum_{Un-cracked} \int \frac{m_\theta M_\theta}{E_c I_g} R d\theta + \sum_{Cracked} \int \frac{m_\theta M_\theta (1-\eta_\theta \beta_\theta (M_{cr,\theta} / M_\theta))}{E_c I_{cr,\theta}} R d\theta \tag{8.22}$$

This method is referred as Integ. TS herein when β is considered as M_{cr} / M_θ according to the recommendation of Bischoff and Gross (2011b). To simplify Eq. 8.22, Eq. 8.16 can be used employing the same equation as Eq. 8.17 for Δ_g. In this case, $\delta\Delta_{cr}$ should be calculated as

$$\delta\Delta_{cr} = \sum_{i=1}^{n} \frac{\eta_i}{I_{cr,i} E_c} \int m_\theta M_\theta (1-\eta_i \beta_i (M_{cr,i} / M_\theta)) R d\theta \tag{8.23}$$

Note that Eq. 8.23 requires greater computational effort than Eq. 8.18, especially when the effect of axial load is to be considered. For load and boundary conditions similar to those of the test specimens when the axial load and its variation are not significant, we have:

$$\Delta = \frac{2}{E_c I_{cr}} [(1-\eta) \int_0^{\frac{\pi}{2}-\alpha} m_\theta M_\theta R d\theta + \eta \int_{\theta_g}^{\frac{\pi}{2}-\alpha} m_\theta M_\theta ((1-\beta \left(\frac{M_{cr}}{M_\theta} \right)) R d\theta] \tag{8.24}$$

Equation 8.19 can be used to calculate the mid-span deflection once the value of λ has been determined with this equation (see appendix C):

$$\lambda = 2(1-\eta)[\int_0^{\frac{\pi}{2}-\alpha} C_\theta R d\theta + \eta \int_{\theta_g}^{\frac{\pi}{2}-\alpha} (C_\theta - C_{\theta_g}) R d\theta] \tag{8.25}$$

where $C_{\theta_g} = (M_{cr})^2 / P$.

8.5.7. Evaluation of the presented methods with experimental data

Table 8.3 presents the ratio of the theoretical to the experimental mid-span deflection of the tested specimens. In addition, Figs. 8.4 and 8.5 compare the experimental and analytical moment-deflection curves of the specimens. The moment–deflection curves were drawn up to 50% of the experimental bending-moment capacity of the specimens. Table 8.3 provides a comparison of the mid-span deflection at the loads corresponding to the three references points of 2000 $\mu\varepsilon$, 1.1 M_{cr}, and 0.3 M_n, when applicable. The deflection in FRC specimens was obtained according to two scenarios of considering or neglecting contribution of the fibers. The average and standard deviation are presented separately for each concrete type. In this study, $3320\sqrt{f_c'} + 6900$ was used as the concrete modulus of elasticity according to ACI 363R-10.

According to Table 8.3, applying the I_e, and Integ. methods overestimated the deflection of NSC tunnel segment specimens by 20% and 50%, respectively, on average, for different reference points. In contrast, considering tension stiffening based on the Integ. TS method underestimated deflection by 33%, on average. In the HSC specimens, the overestimation yielded by the I_e, and Integ. methods was 3% and 33%, respectively. In contrast, considering the tension stiffening with the Integ. TS method underestimated the deflection by 54%. Neglecting the contribution of the fibers in FRC tunnel segment specimens resulted in a significant overestimation of the deflection (42% for I_e and 81% for Integ. methods). Considering the contribution of the fibers by taking into account their effect on the cracked moment of inertia reduced the overestimation of the I_e and Integ. methods by 12% and 43%, respectively. The Integ. TS method underestimated the deflection by 30% and 41%, respectively, on average, when neglecting or considering the contribution of the fibers.

Table 8.3 and Figs. 8.4 and 8.5 reveal that the accuracy of these deflection prediction methods depends on the reinforcement ratio and concrete type. For instance, I_e underestimated the deflection of 7G#5 by 5%, while it overestimated the deflection of 7G#6

Table 8.3 Comparison of the experimental and analytical results

ID	Deflection-calculation method											
	I_e			Integ.			Integ. TS			Modified model		
	$\Delta_{theo.}$ / $\Delta_{exp.}$											
	2000 $\mu\varepsilon$	1.1 M_{cr}	0.3 M_n	2000 $\mu\varepsilon$	1.1 M_{cr}	0.3 M_n	2000 $\mu\varepsilon$	1.1 M_{cr}	0.3 M_n	2000 $\mu\varepsilon$	1.1 M_{cr}	0.3 M_n
NSC specimens												
7G#5	n/a	0.93	0.96	n/a	1.05	1.13	n/a	0.29	0.51	n/a	1.14	1.00
7G#6	1.02	0.91	1.13	1.38	1.23	1.37	0.35	0.32	0.66	0.98	0.91	1.07
13G#5	1.44	1.68	1.35	1.74	2.24	1.61	0.85	0.64	0.85	1.14	1.15	1.09
13G#6	1.17	1.53	1.13	1.39	2.00	1.33	0.81	0.63	0.82	0.91	0.80	0.91
7G#5U	n/a	0.84	0.80	n/a	1.15	1.04	n/a	0.27	0.35	n/a	1.10	0.90
Average	1.21	1.18	1.07	1.50	1.53	1.30	0.67	0.43	0.64	1.01	1.02	0.99
STD	0.21	0.39	0.21	0.21	0.55	0.22	0.28	0.19	0.21	0.12	0.16	0.09
HSC specimens												
7G#5H	n/a	0.63	1.10	n/a	0.86	1.40	n/a	0.20	0.53	n/a	1.01	0.98
13G#5H	1.15	1.00	1.23	1.51	1.34	1.50	0.48	0.36	0.73	0.94	1.05	1.01
7G#5HU	n/a	0.92	1.17	n/a	1.28	1.45	-	0.26	0.63	n/a	1.15	1.04
Average	1.15	0.85	1.17	1.51	1.16	1.45	0.48	0.27	0.63	0.94	1.07	1.01
STD	n/a	0.19	0.07	n/a	0.26	0.05	n/a	0.08	0.10	n/a	0.07	0.03
FRC specimens neglecting the contribution of fibers												
7G#5F	1.09	1.09	1.25	1.50	1.50	1.51	0.33	0.33	0.76	1.34*	1.34	1.32
13G#5F	1.83	2.53	1.35	2.23	3.27	1.52	1.07	1.14	1.01	1.68	2.29	1.28
7G#5FU	1.32	1.04	1.32	1.78	1.43	1.55	0.47	0.34	0.89	1.57	1.41	1.40
Average	1.41	1.55	1.31	1.84	2.07	1.53	0.62	0.60	0.89	1.63	1.68	1.33
STD	0.38	0.85	0.05	0.37	1.04	0.02	0.39	0.46	0.13	0.08	0.53	0.06
FRC specimens with considering the contribution of fibers												
7G#5F	0.97	0.97	1.18	1.33	1.33	1.43	0.31	0.31	0.72	0.98	0.98	1.11
13G#5F	1.39	1.83	1.13	1.69	2.33	1.28	0.83	0.90	0.85	1.06	1.22	0.98
7G#5FU	0.90	0.66	1.06	1.27	0.97	1.27	0.37	0.30	0.72	1.00	0.92	1.06
Average	1.09	1.15	1.12	1.43	1.54	1.33	0.50	0.50	0.76	1.01	1.04	1.05
STD	0.27	0.61	0.06	0.23	0.70	0.09	0.28	0.34	0.08	0.04	0.16	0.07

Note: Integ. refers to the integration-of-curvature method and Integ. TS refers to the integration-of curvature method considering tension stiffening.

* The values were obtained with the same modification parameters as NSC.

and 13G#5 by 2% and 49%, respectively. Generally, Integ. TS significantly underestimated the mid-span deflection, which was more pronounced at the lower reinforcement ratio. The approach to calculating deflection yielded relatively more reasonable results for FRC specimens (Fig. 8.5). In general, according to the average for all the specimens and references points, the ratio of theoretical to experimental deflection was 1.11, 1.41, and 0.55 for the I_e, Integ., and Integ. TS methods, respectively. Therefore, although using effective

moment of inertia is simpler than the other methods, it yielded the most accurate results with acceptable conservativeness. As mentioned above, however, the method's accuracy depends on the load and boundary conditions (Bischoff and Gross 2011b).

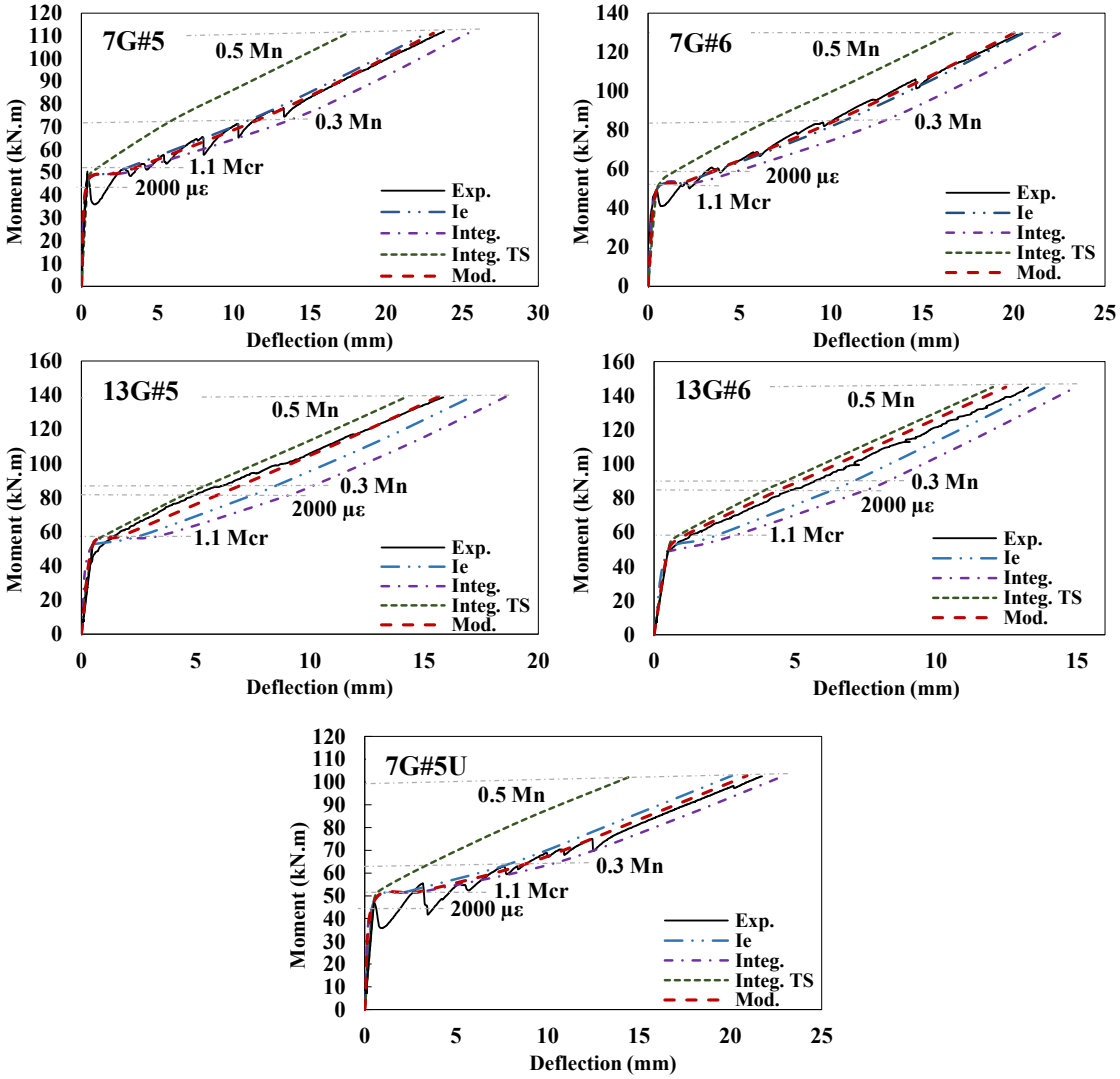

Figure 8.4 Comparison of the experimental and analytical moment–deflection diagrams of the NSC specimens. (Note: 1 mm = 0.0394 in; 1 kN·m = 0.7376 kip-ft)

8.5.8. Proposed model

The method based on integration of curvature considering the tension-stiffening factor equal to M_{cr} / M_{θ} seems to be theoretically correct. As reported in the preceding section, it considerably underestimated the mid-span deflection. Underestimation with such methods is consistent with some studies in the literature (Bischoff and Gross 2011b; Mousa et al.

2019b). The underestimation was greater at the reference points of 2000 $\mu\varepsilon$ and 1.1 M_{cr}, especially in the NSC specimens with lower reinforcement ratios. To help demonstrate the reason for such underestimation, Fig. 8.6 presents the theoretical mid-span moment–curvature diagrams of 7G#5 and 13G#6 specimens obtained based on the I_e, Integ., and Integ. TS methods. In addition, the experimental moment–curvature diagram was drawn for comparison using the strain values recorded during the test. The I_e, and Integ. TS methods yielded similar curvatures in a section since they use the same equation for the moment of inertia in a section. Figure 8.6 shows that the curvature of specimen 7G#5 increased rapidly after initiation of the first crack and thereafter approached the curvature obtained from the cracked moment of inertia by increasing the applied bending moment.

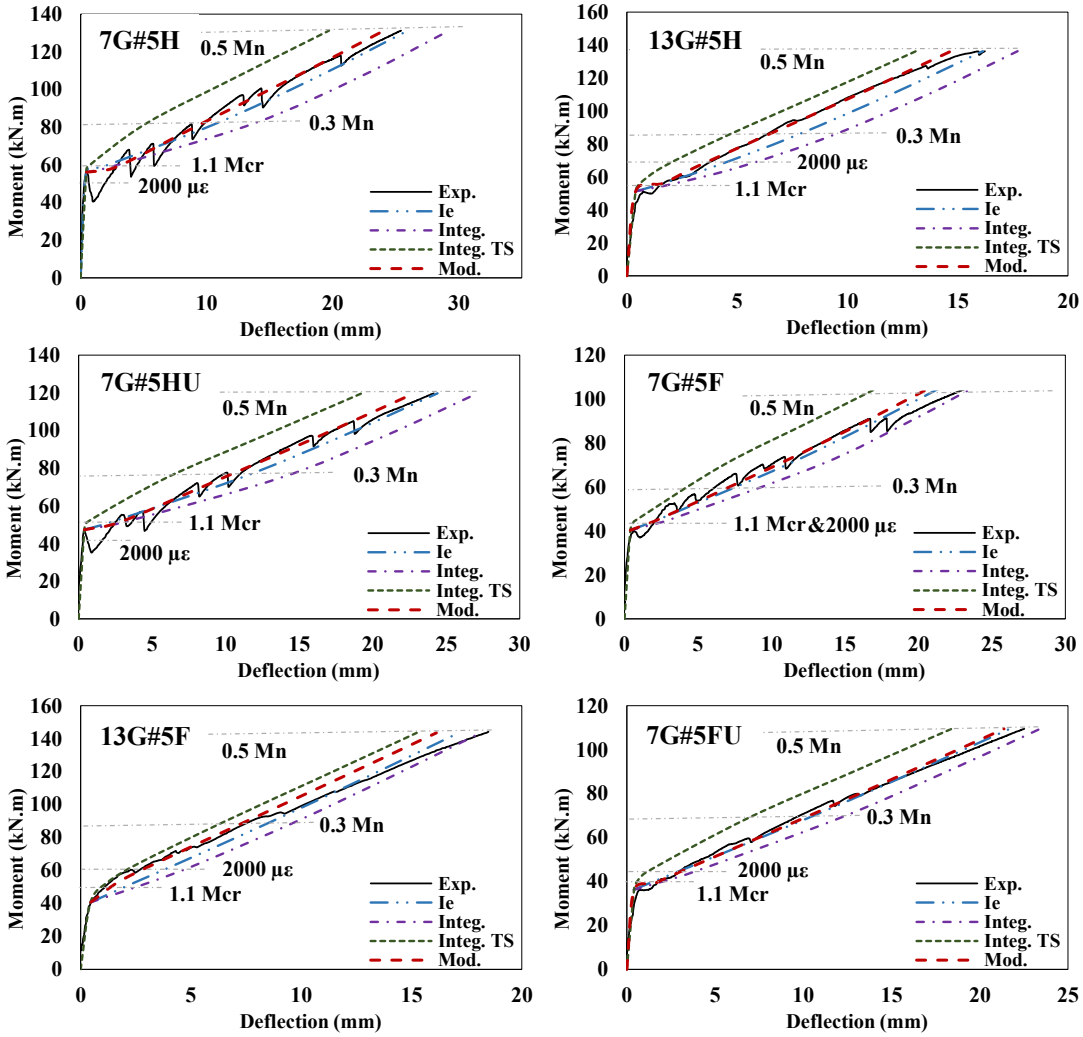

Figure 8.5 Comparison of the experimental and analytical moment–deflection diagrams of the HSC and FRC specimens. (Note: 1 mm = 0.0394 in; 1 kN·m = 0.7376 kip-ft)

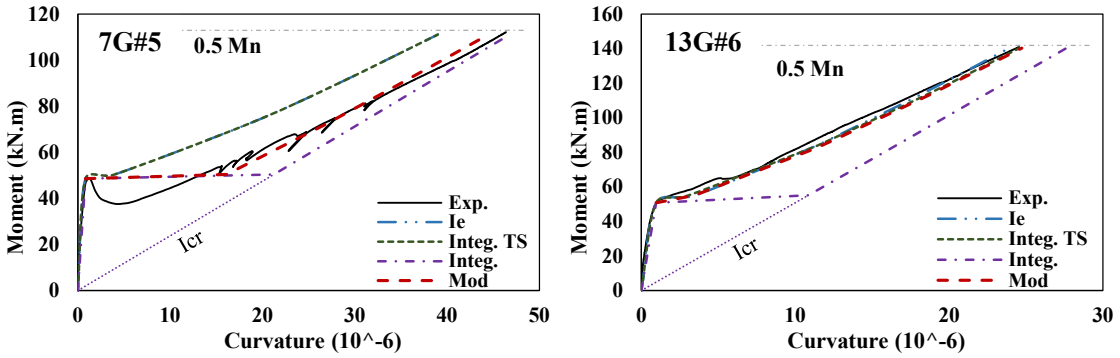

Figure 8.6 Comparison of the experimental and analytical moment–curvature diagrams for specimens 7G#5 and 13G#6. (Note: 1 mm = 0.0394 in; 1 kN·m = 0.7376 kip-ft)

In contrast, considering tension stiffening by setting the tension-stiffening factor equal to M_{cr} / M_{θ} did not follow the experimental trend. In that case, the initial increase of curvature upon cracking was not considered and the tension-stiffening factor was overestimated. Increasing the reinforcement ratio in 13G#6 eliminated the initial curvature increase, and the tension-stiffening factor was predicted with good accuracy. Comparing the moment–curvature diagrams of all tested specimens revealed that the rapid increase in the curvature at cracking and the accuracy of M_{cr} / M_{θ} as the tension-stiffening factor depended primarily on the reinforcement ratio, concrete strength, and concrete type. This study developed the following equations to modify the values of η and β for use in the presented method based on Integ. TS.

$$\beta_m = m\left(\frac{f_c^{'}\rho_f}{f_{c,n}^{'}\rho_{fb}}\right)^p \left(\frac{M_{cr}}{M_{\theta}}\right) \quad \text{where} \quad m\left(\frac{f_c^{'}\rho_f}{f_{c,n}^{'}\rho_{fb}}\right)^p \le 1.0 \tag{8.26}$$

$$\eta_n = 1 - n\left(\frac{f_{c,n}^{'}\rho_{fb}}{f_c^{'}\rho_f}\right)^q \frac{I_{cr}}{I_g} \quad \text{where} \quad n\left(\frac{f_{c,n}^{'}\rho_{fb}}{f_c^{'}\rho_f}\right)^q \ge 1.0 \tag{8.27}$$

where $f_{c,n}^{'}$ is 80 MPa (11.6 ksi) for HSC and 40 MPa (5.8 ksi) for NSC and FRC. The modification constants m, n, p, and q were obtained using regression analysis according to the results for different types of concrete and are reported in Table 8.4. The effect of the reinforcement ratio on the tension-stiffening characteristic was considered using the ratio of ρ_f to ρ_{fb}. Yost et al. (2003) and Mousavi and Esfahani (2012) used a similar approach to consider the effect of the reinforcement ratio on the deflection of GFRP-RC beams. In addition, the

Table 8.4 Proposed coefficients to be used in the proposed model

Concrete type	*M*	*n*	*p*	*q*
NSC	0.14	4.0	1.12	1.0
HSC	0.65	5.0	0.26	0.8
FRC	0.30	7.7	0.70	2.3

ratio of $f'_{c,n} / f'_c$ was added to the proposed model to consider the effect of variations in concrete strength in the specimens. The modified deflection values can be obtained by replacing the values of η and β in the equations presented to calculate the deflection considering tension-stiffening factor. Equation 8.28 presents the modified value of curvature in each section in the proposed modified model.

$$\phi_\theta = \frac{M_\theta}{E_c I_{cr}}(1-\eta_n \beta_m \frac{M_{cr}}{M_\theta}) \tag{8.28}$$

Appendix D describes the procedure used to obtain the modified equations. Figure 8.7a shows the main concepts of the assumed moment–curvature response in the modified (referred to as Mod. herein) and Integ. TS methods (the graphs are for specimen 7G#5). Tension stiffening at a certain bending moment refers to change in curvature ($\Delta\Phi$) relative to the curvature of the cracked member obtained using I_{cr} . $\Delta\Phi_{\max}$ is the maximum possible tension stiffening at cracking. This is the tension-stiffening value considered in Integ. TS right after the formation of the first crack. This can be the main reason for the significant underestimation of the integration-of-curvature method considering tension stiffening in calculating deflection for the bending moments near the cracking load. An indirect method was used to consider the curvature increase when the first crack appeared by modifying the value of η by η_n (see appendix D). By using η_n, the maximum change in curvature will be limited to $\Delta\Phi_{\mathrm{m}}$. Increasing the bending moment decreases the tension-stiffening effect. The ratio of change in curvature at a certain bending moment ($\Delta\Phi$) to the maximum change in curvature at cracking is known as the tension-stiffening factor. Since using M_{cr} / M_θ overestimated the tension-stiffening effect, the modified tension-stiffening factor of β_m is proposed, which reduces the value of M_{cr} / M_θ according to the reinforcement ratio, concrete strength, and the modification factors. Figure 8.7b presents the curvature value along the tunnel segment specimen obtained using the I_e, Integ., Integ. TS, and modified

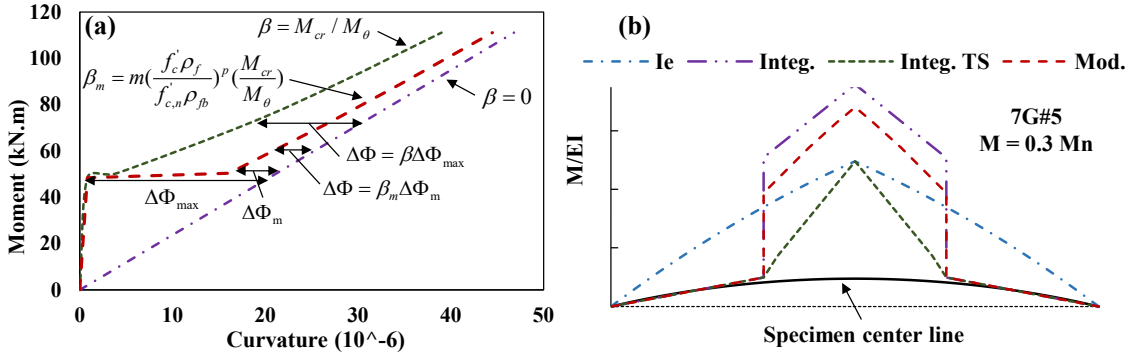

Figure 8.7 Comparison of the curvature response of different deflection-calculation methods: (a) moment–curvature response; (b) curvature along the specimen. (Note: 1 mm = 0.0394 in; 1 kN·m = 0.7376 kip-ft)

methods (note that the specimens' centerline was selected as the x-axis for a better view). As can be seen, the methods based on the integration of curvature yielded minimal curvature in the uncracked sections. In the cracked sections, using I_{cr} in the Integ. method eventually increased the curvature right after passing θ_g; the curvature increased linearly up to the mid-span. In contrast, using the effective moment of inertia according to Eq. 8.2 led to gradual increase in curvature. In the modified method, an increase in curvature after passing from the uncracked region is considered and the curvature modeled to gradually increase up to mid-span.

Figure 8.6 presents a comparison of the moment–curvature obtained using the proposed equations and the experimental results for 7G#5 and 13G#6. As can be seen, the modified model fitted well with the experimental moment–curvature of the sections. The moment–deflection relationships obtained with the modified model for different specimens appear in Figs. 8.4 and 8.5. As shown, the modified model was quite consistent with the experimental results for all the specimens. In addition, Table 8.3 gives the ratio of theoretical to experimental mid-span deflection for the modified model. Considering an average for different reference points, the developed modified model predicted the mid-span deflection with conservativeness of 1%, 2%, and 3% in the NSC, HSC, and FRC tunnel segment specimens, respectively. Therefore, the modified model accurately predicted the mid-span deflection for the tested specimen with acceptable conservativeness of 2% on average.

8.5.9. Discussion

As mentioned, the coefficients presented for the modified model were obtained based on the experimental data. As the number of specimens was limited, the accuracy of the coefficients needs to be further verified with an extensive database. In particular, the coefficients for the FRC specimens are valid when the properties of the FRC are similar or superior to that in the current study. Should the mechanical properties of the FRC be lower than the FRC in this study, the coefficients for NSC herein should be used. The validity of the coefficients in the presence of axial load also needs to be validated. In fact, the diagrams in Fig. 8.6 are valid when then the axial load is not significant. It is expected, however, that compressive axial load would improve the tension-stiffening behavior (Ng et al. 2019).

In general, the Integ. TS method should not be used to calculate deflection in curvilinear GFRP-RC members with low reinforcement ratios as it significantly underestimates deflection. A designer may, however, opt for the I_e, Integ., or Mod. method based on design considerations. In fact, each of these methods has advantages and disadvantages. Using I_e simplifies the deflection-calculation procedure but does not guarantee that the effect of loading and boundary conditions is considered. The Mod. method could provide more accurate results than the other methods, but it requires more computational effort. Lastly, the Integ. method could be a suitable conservative option when the designer is unsure about the member's tension-stiffening characteristics. In addition, this method requires less computational effort than the Mod. method. The following section provides the procedure developed for adopting the I_e, Integ., or Mod. methods for GFRP-reinforced PCTL segments under real loading and boundary conditions. The procedure is general and can be used for other types of curvilinear members.

8.5.10. Development of the methods for use under real loading and boundary conditions

The integration-based methods presented above include several assumptions that might not be met in tunnel segments or other curvilinear members under real load and boundary conditions. The equations presented require the relationship between the applied loads and

the internal forces in the member. This is because the complexity of the load and boundary conditions in tunnel segments and some curvilinear members make it generally impossible to determine such relationships. In addition, the axial load on the member relates the cracked moment of inertia in each section to the combination of axial load and bending moment. Therefore, some main parameters in the equations vary from section to section. The following procedure adapts the deflection-calculation procedures presented for designing GFRP-reinforced PCTLs under real loading and boundary conditions.

8.5.10.1. Step I: Finding the forces and initial deflection at the joints using first-order analysis

Generally, there is interaction between the applied loads and deflection in tunnel segments and other RC structures. In such situations, the internal forces and estimated approximate deformation must be found with a first-order analysis, which requires an estimate of the moment of inertia to be used in the analysis procedure. This must be accomplished despite the moment of inertia varying section by section in RC structures. The common design practice in such cases is to use an initial estimation of the moment of inertia in the members. Zadeh and Nanni (2017) proposed the following equations for the first-order estimation of the moment of inertia of GFRP-RC slab members and columns.

$$I_{slab} = \left[0.10 + 0.15(E_f / E_s)\right] I_g \le 0.25 I_g \tag{8.29}$$

$$I_{column} = \left[0.40 + 0.15(E_f / E_s)\right] I_g \le 0.55 I_g \tag{8.30}$$

When a designer expects the axial load of a member to be greater than $0.1 f_c^{'} A_g$, it can be assumed to be a column. Otherwise, the initial moment of inertia proposed for slabs can be used in the analysis. The reduced flexural rigidity (I_r) for use in the related calculations can be obtained with the following equation (where relevant) (ACI 533.5R-20):

$$I_r = I_j + (4 / n_s)^2 \times I \tag{8.31}$$

where I_j is the moment of inertia at the joint, which is taken as zero in the design; n_s is the number of segments in a ring, excluding the key segment, which should be considered greater than four; and I denotes the lining moment of inertia, which can be calculated with

Eq. 8.29 or 8.30 according to the axial-load level. The internal forces and joint deformations can be estimated with the first-order analysis using one of the analysis methods such as elastic equation method, beam-spring method, finite element modeling (FEM), and discrete element method (DEM) (ACI 533.5R-20).

8.5.10.2. Step II: Calculating rotation and deflection in the selected segments

The critical segments for the deflection control can be determined based on the results from step I. Figure 8.8 provides a schematic view of a segment considered for the deflection control procedure. The effect of the other segments and the joints on the boundary conditions of the segment is modeled by vertical, horizontal, and rotational springs. A schematic arbitrary external load is shown, which varies according to the loading conditions. Note that the displayed springs and external load do not play a role in the calculation procedure, which will be described below and presented solely to show a semi-real condition of a segment. The analysis in step 1 is supposed to yield the forces and moments as well as the deformations and rotation of the joints. The following procedure is proposed to obtain the rotation and deflection diagrams of GFRP-reinforced PCTL segments. In addition, Fig. 8.9 shows a hypothetical schematic view of the proposed procedure.

1. Divide the tunnel segment into certain number of elements (even number) referred to as n_{seg}. In such situation, $\Delta\theta = 2\theta_{\max} / n_{seg}$.
2. Designate each element as n_i, $i = 1, 2, 3, ..., n_{seg}$. The angle between starting point of the element n_i and the starting point of the segment is $i\Delta\theta$.
3. Specify the axial load (N_i) and bending moment (M_i) at the points corresponding to $\alpha + i\Delta\theta$, where $i = 1, 2, 3, ...n_{seg}$ based on the results in the step I (refer to Fig. 8.5 for the definitions of α and $\theta_{\max}$).
4. Calculate the cracking moment of inertia ($M_{cr,i}$) for each point according to the axial-load level.
5. For the points where $M \geq M_{cr,i}$, calculate the cracked moment of inertia ($I_{cr,i}$).

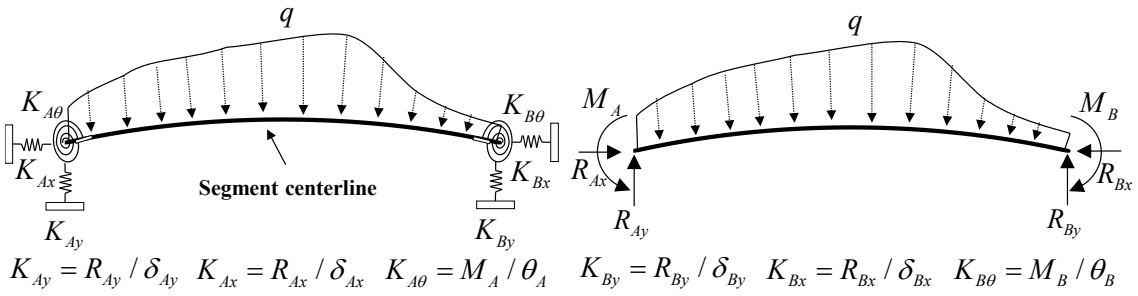

Figure 8.8 A schematic view of a tunnel segment considered for deflection calculation.

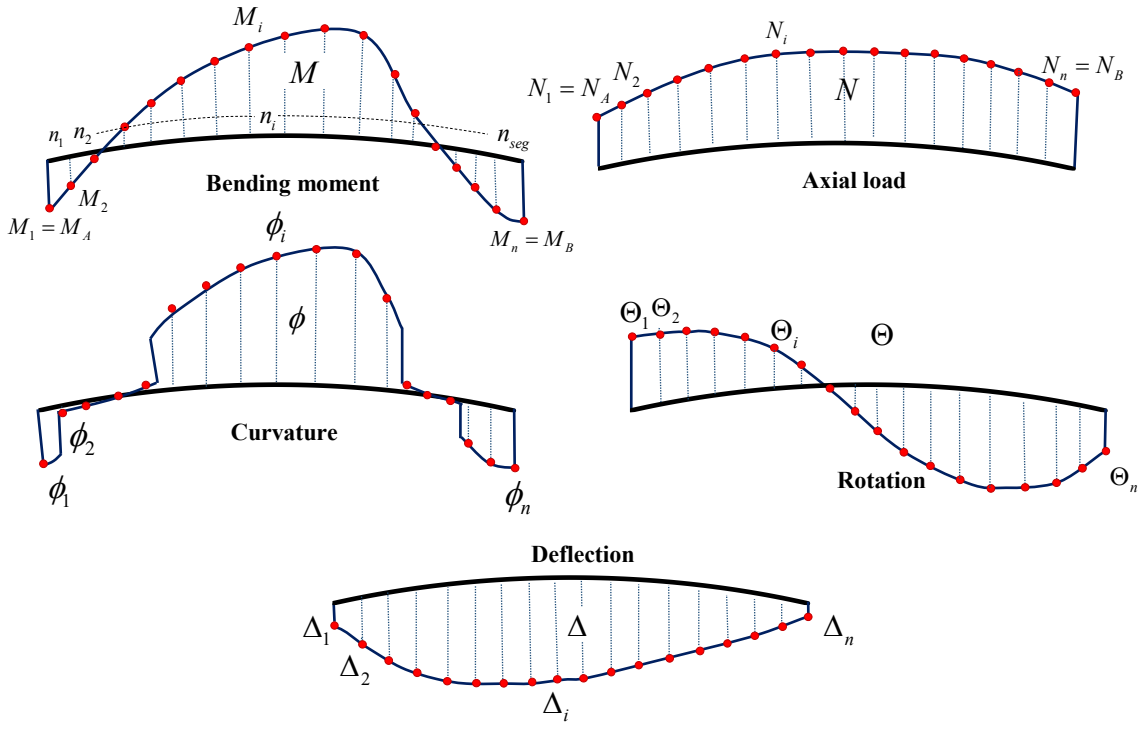

Figure 8.9 A schematic view of the proposed deflection-calculation procedure for GFRP-reinforced PCTL segments under real load and boundary conditions.

6. For deflection calculation based on the effective moment of inertia, consider the moment of inertia for each point (I_i) according to Eq. 8.32. For the other methods, where $M \geq M_{cr,i}$, calculate the moment of inertia based on the deflection-calculation method to be used. Equations 8.33, and 8.34 represent the moment of inertia based on the Integ., and Mod. methods, respectively. When $M \leq M_{cr,i}$, consider I_i equal to I_g.

$$I_i = \frac{I_{cr,i}}{1-\eta_i\beta_i\left(\frac{M_{cr,i}}{M_{\theta,i}}\right)} \tag{8.32}$$

$$I_i = I_{cr} \tag{8.33}$$

$$I_i = \frac{I_{cr,i}}{1-\eta_{n,i}\beta_{m,i}\left(\frac{M_{cr,i}}{M_{\theta,i}}\right)} \tag{8.34}$$

7. Calculate the curvature value at each point using the following equation:

$$\phi_i = \frac{M_i}{E_c I_i} \tag{8.35}$$

8. Use Eq. 8.5 to find the rotation at each point (Θ_i) using numerical methods to calculate integral. C_1 is equal to the rotation at the starting point of the segment (Θ_A) determined in step I. The trapezoidal rule or Simpson's rule might be used to find the rotation based on the curvature at each point (see appendix E for the detailed equations).
9. Use Eq. 8.38 to find the deflection (Δ) at each point using numerical methods (Δ_A is determined in step I). Again, the trapezoidal rule or Simpson's rule might be used to find deflection (see appendix E).

$$\Delta_\theta = \int \Theta_\theta R\sin(\theta)d\theta + \Delta_A \tag{8.38}$$

Appendix E presents a design example according to the presented procedure for one of the specimens tested. In the example, the procedure overestimated the deflection by 8% when following the Mod. method. The procedure entails two main sources of error: (1) using a numerical model to solve the integral and (2) using an initial moment of inertia to obtain the initial internal forces, rotations, and deformations at the supports in step I. The former can be minimized by increasing the number of elements in the analysis. In addition, the latter might be improved by performing further rounds of analysis with the data obtained from the preceding rounds. In addition to these sources of error, estimating the exact cracking moment is of great importance in minimizing errors in calculating deflection.

8.6. Conclusions

The following conclusions can be drawn from the results of this study.

1. Applying the effective moment of inertia developed for curvilinear members based on Bischoff's model (Bischoff 2005) overestimated deflection by 20%, 3%, and 12% in the NSC, HSC, and FRC specimens, respectively, on average, for different reference points.
2. Neglecting tension stiffening in the integration-of-curvature method overestimated deflection by 50%, 33%, and 43% in the NSC, HSC, and FRC curvilinear specimens, respectively. Considering the contribution of tension stiffening in curvilinear GFRP-RC members, however, underestimated deflection by 33%, 54%, and 41% in the NSC, HSC, and FRC specimens.
3. A comparison of the experimental and analytical results revealed that the accuracy of the methodologies presented depends on the reinforcement ratio, concrete strength, and concrete type. A new model was proposed and validated based on the experimental data to consider the effect of these parameters on a deflection prediction method. The proposed model could predict deflection at the service load with 2% conservativeness.
4. Employing the effective moment of inertia is a simple method with acceptable conservativeness (11% on average in the tested specimens). Its accuracy, however, depends on the load and boundary conditions. The proposed method is capable of providing more accurate results than the other methods although it requires more computational effort. Lastly, the integration of curvature while neglecting tension stiffening is a conservative option (41% on average) when a designer is not sure about the tension-stiffening characteristics of the member.

CHAPTER 9 CURVILINEARITY EFFECT ON THE FLEXURAL AND SHEAR STRENGTH OF CURVED GFRP-REINFORCED CONCRETE MEMBERS

Foreword

Authors and Affiliation:

Seyed Mohammad Hosseini: Ph. D. Candidate, Department of Civil Engineering, University of Sherbrooke, Sherbrooke, Quebec, Canada, J1K 2R1

Salaheldin Mousa: Postdoctoral fellow, Department of Civil Engineering, University of Sherbrooke, Sherbrooke, Quebec, Canada, J1K 2R1

Hamdy M. Mohamed: Research associate and lecturer, Department of Civil Engineering, University of Sherbrooke, Sherbrooke, Quebec, Canada, J1K 2R1.

Brahim Benmokrane: Professor, Department of Civil Engineering, University of Sherbrooke, Sherbrooke, Quebec, Canada, J1K 2R1.

Journal title: ACI Structural Journal

Paper status: Submitted on May 2023.

Contribution in thesis:

Existing design recommendations do not specifically account for the curvilinear shape of GFRP-RC curvilinear members. To fill this gap, in-depth models were developed to predict flexural and shear strength, considering the effect of curvilinearity. The models incorporated the additional stresses caused by force deviation and accounted for the flexural and shear strength. Experimental validation was conducted, followed by a parametric study to explore the influence of various parameters on the strength of curvilinear GFRP-RC members.

9.1. Abstract

Curvilinear shape of reinforced concrete (RC) curved members induces some additional stresses in the member which affects the flexural and shear strength. This issue has not been investigated in curvilinear RC members reinforced with GFRP bars in the literature. In addition, there is no specific design recommendations to consider the effect of curvilinearity on the flexural and shear strength of GFRP-RC curved members. This study pioneers in the development of models to predict flexural and shear strength of curvilinear GFRP-RC members with a focus on precast concrete tunnel lining segments. 11 full-scale GFRP-reinforced curvilinear tunnel segment specimens were tested under bending load to investigate their flexural and shear behavior. Then, a model was developed for flexural strength prediction of curvilinear GFRP-RC members. It was followed by the development of two shear strength prediction models based on modified compression field theory (MCFT) and critical shear crack theory (CSCT). After comparing the experimental and analytical results, a parametric study was performed aiming at evaluating the effect of different parameters on the flexural and shear strength of GFRP-reinforced curvilinear members. The results indicated that neglecting the curvilinearity effect led to a 17% overestimation of the flexural capacity while the proposed models could predict the flexural capacity of the specimens accurately. The proposed models based on MCFT named semi-simplified modified compression field theory (SSMFT) and improved simplified modified compression field theory (ISMCFT) predicted the shear capacity of the specimens with 28% conservativity. In addition, the modified critical shear crack theory (MCSCT) model was 10% conservative in predicting the shear capacity of GFRP-RC curvilinear members.

Keywords: Curvilinear; glass fiber-reinforced polymer (GFRP); flexural strength; shear strength; modified compression field theory (MCFT); critical shear crack theory (CSCT)

9.2. Introduction

Corrosion of steel reinforcement is among the major risks that endanger the service life of conventional reinforced concrete (RC) members. The application of glass fiber-reinforced polymer (GFRP) reinforcement in RC structures can prevent the corrosion problem (Gudonis et al. 2013). Several studies investigated the flexural and shear performance of GFRP-RC straight members under bending load few of them are cited here (Benmokrane et al. 1996; Theriault and Benmokrane 1998; Toutanji and Saafi 2000; Vijay and GangaRao 2001; El-Sayed et al. 2005; Razaqpur and Isgor 2006; Kassem et al. 2011; El-Nemr et al. 2013; Razaqpur and Spadea 2015; El-Nemr et al. 2018; Khavaran 2019; Mousa et al. 2019c; Mousa et al. 2020; Alguhi and Tomlinson 2021; Ali et al. 2021; Protchenko et al. 2021). Design equations and guidelines were codified and presented in different design standards such as ACI 440.1R-15, CAN/CSA S806-12 (R2017), and CAN/CSA S6-19, etc. The general concept of flexural strength prediction in GFRP-reinforced flexural elements is similar to that of steel-reinforced ones. However, some modifications were recommended by ACI 440.1R-15, CAN/CSA S806-12 (R2017), and CAN/CSA S6-19 on the proposed models for steel-RC members to be used for RC members reinforced with GFRP bars. The proposed models for flexural and shear strength of GFRP-RC members were widely validated and improved by different studies (Kassem et al. 2011; Adam et al. 2015; Razaqpur and Spadea 2015; El-Nemr et al. 2018; Khavaran 2019; Mousa et al. 2020; Alguhi and Tomlinson 2021; Ali et al. 2021; Protchenko et al. 2021). Among the shear strength prediction models, modified compression field theory (MCFT) is popular and reliable (Bentz et al. 2006; Sadeghian and Vecchio 2018). The simplified form of MCFT (SMCFT) is adopted by CAN/CSA S6-19 for both steel-RC and GFRP-RC members. Some studies validated SMCFT for GFRP-RC members and founded it as a reliable and conservative model (Hoult et al. 2008; Khavaran 2019; Alguhi and Tomlinson 2021). As another shear predicting model, critical shear crack theory (CSCT) originally proposed by Muttoni and Fernández Ruiz (2008) and developed in recent years (Cavagnis et al. 2015; Ruiz et al. 2015; Cavagnis et al. 2018; Cavagnis et al. 2020). CSCT has a high accuracy in predicting shear capacity of steel-RC slabs without transverse reinforcement (Cavagnis et al. 2020).

However, its accuracy in predicting shear capacity of GFRP-RC members has not yet been validated.

Curvilinear RC members are commonly used in many types of structures including tunnels, culverts, bridges, etc. In particular, the application of GFRP reinforcement in precast concrete tunnel lining segments becomes popular due to their unique advantages (Caratelli et al. 2016; Caratelli et al. 2017; Spagnuolo et al. 2017). The curvilinear shape of RC members leads to inducing some additional stresses in the section. Such stresses affect the shear capacity of an RC curvilinear member (Campana et al. 2014). In addition, deviation of the forces carried out by the tensile reinforcement may increase the splitting stresses and cause the concrete cover spalling under tensile reinforcement (Fernández Ruiz et al. 2010). Although it is necessary to consider the effect of curvilinear shape on the flexural and shear strength of GFRP-RC curvilinear members, to the best of the author's knowledge, there are no specific design recommendations for designing curvilinear GFRP-RC members. This study pioneers in development of in-depth models to predict flexural and shear strength of GFRP-reinforced curvilinear members with focus on precast concrete tunnel lining segments. 11 full-scale GFRP-RC curvilinear tunnel segments were tested under bending load as the experimental database. Thereafter, the effect of curvilinear shape on the additional stresses due to deviation of the forces was discussed. In the next step, a model was developed to consider the effect of curvilinearity on the flexural strength of GFRP-reinforced curvilinear members. Following that, two shear strength prediction models were developed based on MCFT and CSCT for estimating shear capacity of curvilinear GFRP-RC members. The experimental results were then employed to validate the proposed models. Finally, a parametric study was conducted to investigate the effect of different parameters on the flexural and shear strength of curvilinear GFRP-RC members.

9.3. Research Significance

The use of GFRP reinforcement in curvilinear RC members becomes popular especially in precast concrete tunnel lining segments. However, to the best of authors' knowledge, there is no design recommendations or models available in the literature and design standards to consider the effect of curvilinearity. Due to lack of such specific design recommendations,

curvilinearity effect is generally ignored by design engineers which might lead to considerable overestimations in the flexural and shear capacity of curvilinear members. In this study, novel models and procedures were developed to predict flexural and shear strength of GFRP-reinforced curvilinear members. The results of this paper are greatly helpful for design engineers and design standards.

9.4. Summary of Experimental Program

9.4.1. Specimen details and test matrix

The effect of curvilinearity was experimentally investigated by testing 11 full-scale GFRP-reinforced curvilinear tunnel segment specimens under a bending load. The specimens measured 3100 mm in arc length, 1500 mm in width, and 250 mm in thickness with a centerline radius of 3375 mm (Fig. 9.1). Four different reinforcement ratios of 0.48, 69, 0.90, and 1.28%, two concrete types of NC and FRC, two concrete 28-days compressive strengths of 40 and 80 MPa, and two different tie configurations of closed and U-shaped were designated as the investigated parameters. Table 9.1 presents the specimens' detail and test matrix. In the specimens' designation, the first term indicates the number of longitudinal bars; the size of longitudinal bars was identified by the term after the letter "G"; the specimens with HSC and FRC were specified with the terms "H" and "F", respectively; the term "U" indicates the specimens with U-shaped ties.

Figure 9.1 Specimens geometry and details (dimensions are in mm).

Table 9.1 Test matrix and experimental results

Specimen ID	longitudinal reinforcement	Longitudinal reinforcement ratio (%)	Transverse reinforcement	Tie configuration	Concrete type	f_c', MPa	f_p, MPa	f_{150}^D, MPa	M_u, kN.m
7G#5	7 bars #5	0.48	#4 @ 200 mm	Closed ties	NC	48	-	-	213
7G#5U	7 bars #5	0.48	#4 @ 200 mm	U-shaped ties	NC	44	-	-	177
7G#5H	7 bars #5	0.48	#4 @ 200 mm	Closed ties	HSC	86	-	-	247
7G#5HU	7 bars #5	0.48	#4 @ 200 mm	U-shaped ties	HSC	87	-	-	227
7G#5F	7 bars #5	0.48	#4 @ 200 mm	Closed ties	FRC	50	4.5	0.8	210
7G#5FU	7 bars #5	0.48	#4 @ 200 mm	U-shaped ties	FRC	46	4.3	1.0	230
7G#6	7 bars #6	0.69	#4 @ 200 mm	Closed ties	NC	54	-	-	243
13G#5	13 bars #5	0.90	#4 @ 200 mm	Closed ties	NC	51	-	-	241
13G#5H	13 bars #5	0.90	#4 @ 200 mm	Closed ties	HSC	90	-	-	257
13G#5F	13 bars #5	0.90	#4 @ 200 mm	Closed ties	FRC	44	4.0	1.3	273
13G#6	13 bars #6	1.28	#4 @ 200 mm	Closed ties	NC	47	-	-	273

9.4.2. Materials, test setup, and instrumentations

In each specimen, curvilinear sand-coated #5 and #6 GFRP bars were used as longitudinal reinforcement. U-shaped bars of the same size were employed to provide end-anchorage for the longitudinal bars. Two different types of transverse ties in the form of sand-coated #4 GFRP closed and U-shaped were used for transverse reinforcement. The mechanical properties of the reinforcement obtained based on ASTMD7205-21 (2021) were reported in Table 9.2.

This study used three types of concrete: NC, HSC, and FRC. Three concrete cylinders were tested for each specimen based on ASTMC39/C39M-21 to obtain the compressive strength of the specimens at the test date. To obtain the peak strength and residual strength of FRC, three beam samples 100×100×500 mm in size were tested for each FRC specimen according to ASTM C1609-19.

Three-point load test setup was employed to test the curvilinear segments under bending load (Fig. 9.2). Mid-span deflection was recorded using three linear potentiometers (LPOTs)

Table 9.2 Mechanical properties of reinforcement

Type of reinforcement	Reinforcement size	Nominal cross-sectional area ($mm^{2)}$	Tensile modulus of elasticity (GPa)	Ultimate strength (Mpa)	Ultimate strain (%)
Curvilinear bars	#5	199	55.1 ± 1.25	1,115 ± 60	2.0 ± 0.1
	#6	284	52.9 ± 0.6	1,068 ± 49	2.0 ± 0.1
U-shaped end-anchorage bars	#5	199	53.5 ± 1.1	1,283 ± 42	2.4 ± 0.1
	#6	284	53.2 ± 2.9	1,131 ± 35	2.1 ± 0.0
U-shaped and closed ties	#4	129	55.6 ± 1.6	1,248 ± 74	2.2 ± 0.1

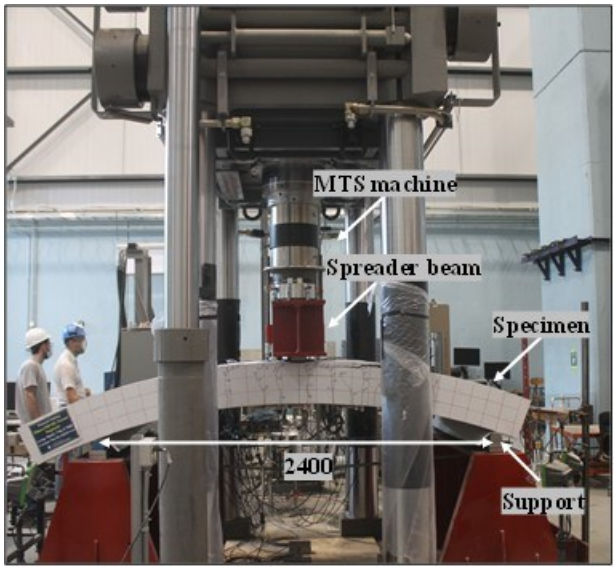

Figure 9.2 Test setup (dimensions are in mm).

distributed along the mid-span. Mid-span strain of tensile reinforcement and top fiber of concrete was recorded through four and three strain gauges, respectively, distributed along the width of the member.

9.4.3. Summary of test results

The specimens followed a similar cracking behavior of simply-supported RC members under bending load. However, the cracks formed perpendicular to the bottom longitudinal

bars. Concrete crushing occurred in the specimens with the reinforcement ratios of 0.48% and 0.69% (Fig. 9.3). However, a critical shear crack formed in the specimens with higher reinforcement ratio which led to diagonal tension failure in those specimens (Fig. 9.3). Table 9.1 reports the actual compressive strength of the specimens, peak stress of FRC, residual stress of FRC, and recorded peak moment.

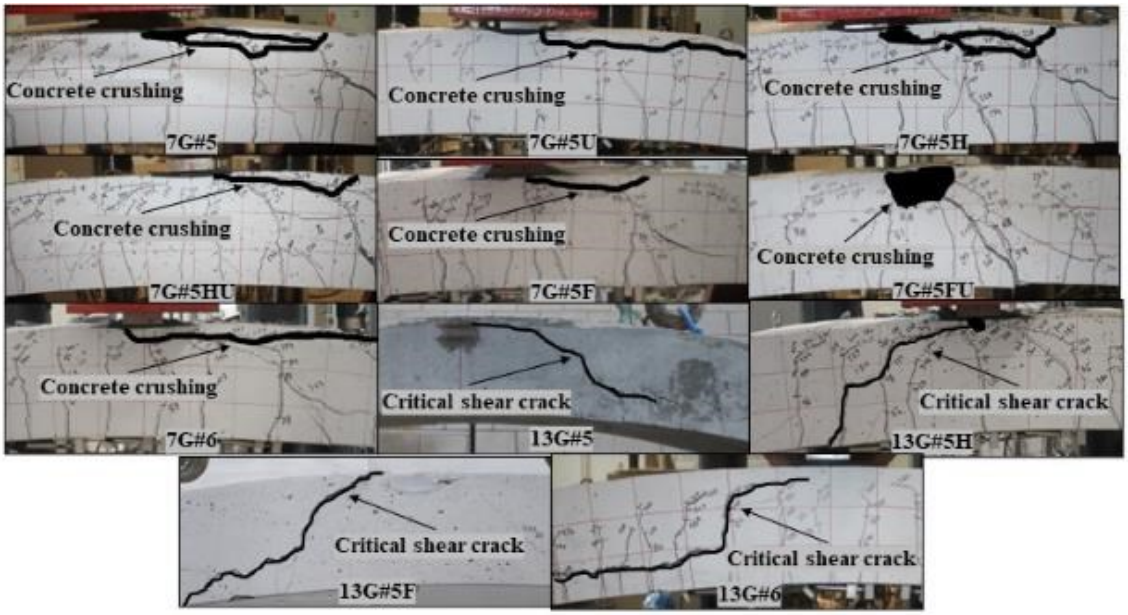

Figure 9.3 Failure mode of the specimens.

9.5. Analytical Investigations

In this section, the effect of curvilinear shape of the member on the additional stresses induced in the section is discussed. Then, a model is developed to predict flexural capacity of GFRP-reinforced curvilinear members. Following that, two shear capacity prediction models were developed based on MCFT and CSCT. In the next step, the experimental and analytical results were compared. Finally, a parametric study was performed to investigate the effect of different parameters on the flexural and shear capacity of GFRP-reinforced curvilinear members.

9.5.1. Additional stresses due to curvilinear shape of the member

In a typical one-way flat slab or beam under bending load, the elements are subjected to unidirectional compression or tension stress as well as shear stresses (if any). However, in the curvilinear members, deviation of compression and tension forces induces tensile stresses in the direction perpendicular to the principal stresses. In order to better illustrate this point, Fig. 9.4a represents the forces apply on an element of a curvilinear RC member under bending load. Consider an element with the and arc angle of d_θ and arc radius of R. The enlarged element with exaggerated curvature is shown in Fig. 9.4a. Axial load, shear force and bending moment are applying on the element. As a result of the applying load, normal and shear stresses are induced in the section. The normal stresses are shown in Fig. 9.4b while the shear stresses are not shown in the Figure for more clarity. At ultimate load, the compressive stresses (σ_c) in the section follow a typical stress-strain curve of concrete. In addition, it was supposed that the top and bottom meshes carry the tensile loads of T' and T, respectively. Section A-A represents the element in a distance between the neutral axis and top mesh reinforcement. Due to deviation of compressive stresses with a degree of $d_\theta / 2$, tensile vertical normal stresses (σ_t) induce in the element. By equating the sum of the forces in the vertical direction to zero, σ_t can be calculated using Eq. 9.1 provided that $r >> h$, where h is the height of the section.

$$\sigma_t = \frac{C}{bR} \tag{9.1}$$

where C is resultant of the stresses applying on the section from the top of the section to the point where σ_t is calculated. In the following sections, analytical procedures were developed to incorporate the effect of σ_t on the flexural and shear strength of GFRP-reinforced curvilinear members. It should be noted that in the case of negative curvature, deviation of the forces causes compressive vertical stresses in the segment which generally increases the flexural and shear strength. This paper developed the procedures with focus on the members with positive curvature as considering the tensile vertical stresses is more critical for design purposes.

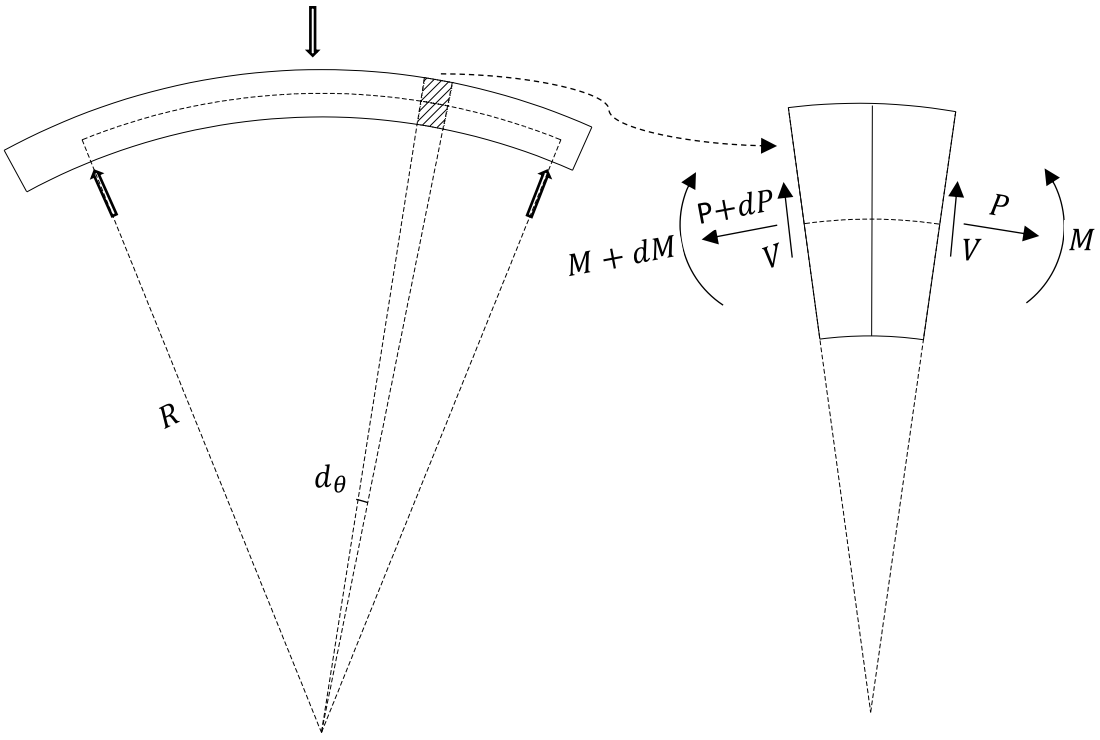

(a) The forces acting on an element of a tunnel segment under bending load

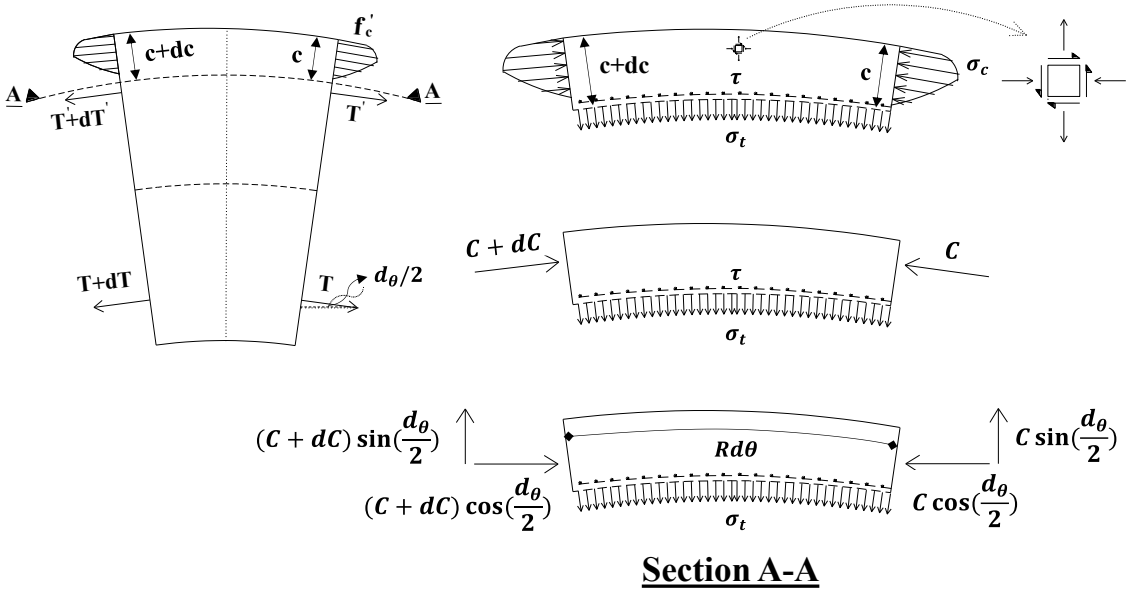

(b) The stresses acting on an element of tunnel segment

Figure 9.4 Deviation forces and stresses in a tunnel segment under bending load.

9.5.2. Flexural strength prediction

9.5.2.1. Development of general flexural strength model

As discussed, the elements in a curvilinear RC member are subjected to two-dimensional normal compression-tension stresses. Such concrete elements can tolerate lower compressive stress and strain compared to the elements under unidirectional compressive stresses so that the higher the tensile stresses, the lower the compressive capacity of the element. In Fig. 9.5, the ratio of ultimate compressive stress to the uniaxial compressive strength ($\sigma_c / f_c^{'}$) is given as a function of tensile stress ratio ($\sigma_t / f_c^{'}$) according to some related studies in the literature for NSC (Kupfer et al. 1969; Nelissen 1972; Tasuji et al. 1978; Hussein and Marzouk 2000). The ultimate compressive strain of concrete (ε_{cu}) subjected to two-dimensional compression-tension normal stresses is also presented as a function of tensile stress ratio in Fig. 9.5 based on the results of Kupfer et al. (1969); Nelissen (1972); Tasuji and Nilson (1978). As can be seen in Fig. 9.5, assuming a linear relationship for σ_c-σ_t and ε_{cu}-σ_t is a good approximation for design purposes. This is what recommended by Nelissen (1972); Tasuji and Nilson (1978) as the best probable fitting for two-dimensional compression-tension stresses. Direct tension test is the best representative of tensile strength of concrete. However, due to difficulty of tension test, splitting tensile strength, f_{ct}, can be used in the calculations. In general, tensile strength obtained from the tensile test is around 40% smaller than f_{ct} (Darwin et al. 2016). This study suggests employing $0.6f_{ct}$ as the ultimate tensile stress of concrete. Eqns. 9.2 and 9.3 are proposed to calculate the ultimate compressive strength ($f_{ctu}^{'}$) and strain (ε_{ctu}) of concrete subjected to two-dimensional compression-tension stresses, respectively.

$$f_{ctu}^{'} = f_c^{'}(1-\frac{\sigma_t}{0.6f_{ct}}) \tag{9.2}$$

$$\varepsilon_{ctu} = \varepsilon_{cu}(1-\frac{\sigma_t}{0.6f_{ct}}) \tag{9.3}$$

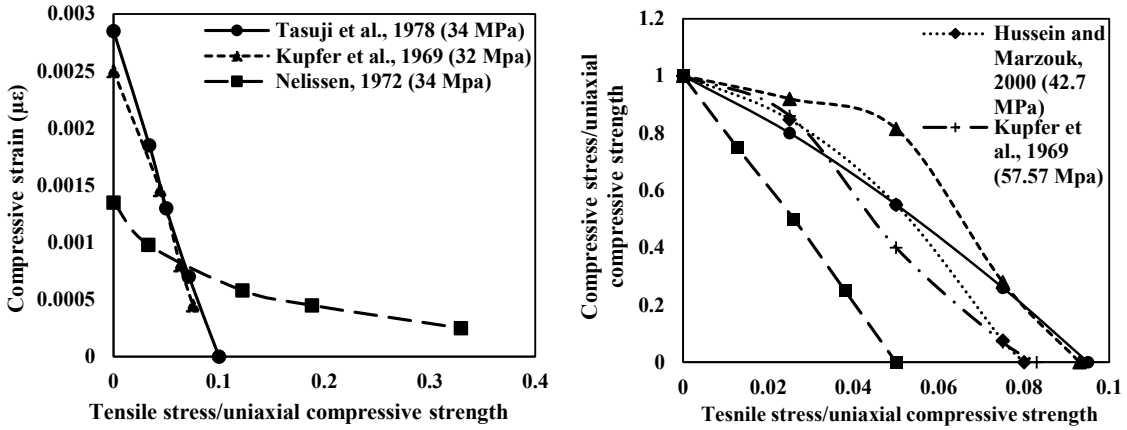

Figure 9.5 Compressive stress and strain capacity of concrete subjected to two-dimensional compression-tension stresses.

where ε_{cu} is the ultimate compressive strain of concrete. ACI 440.1R-15 and CAN/CSA S806-12, R2017 recommend 0.003 and 0.0035 as the value of ε_{cu}, respectively. However, Chang and Seo (2012) suggested the value of 0.004 for ultimate concrete compressive strain in GFRP-reinforced one-way slabs. The authors suggest taking 0.0035 as the value of ε_{cu}. f_{ct} can be obtained directly from splitting tensile test of concrete. ACI 318-14 and Zheng et al. (2001) propose $0.56\sqrt{f_c'}$ and $0.46\sqrt{f_c'}$ for the value of f_{ct}, respectively. The authors recommend $0.56\sqrt{f_c'}$ for f_{ct} based on ACI 318-14 as a rational assumption for design purposes. As the value of σ_t is not constant across the cross-section, f_{ctu}' and ε_{ctu} vary from the neutral axis to the top of the section. An approach can be considering the average value in the calculations. However, a conservative approach for design purposes is to calculate σ_t at the neutral axis level and obtain the ultimate stress and strain accordingly.

In order to consider the effect of curvilinear shape of the member for calculating the flexural strength, a flowchart is represented in Fig. 9.6. The procedure was presented assuming compression-controlled failure in GFRP-reinforced flexural element. This failure mode is what proposed by ACI 440.1R-15 and CAN/CSA S806-12 (R2017), and CAN/CSA S6-19. The available equations to obtain the compression block depth coefficients in different standards are valid when the concrete strain is equal to ε_{cu}. The following

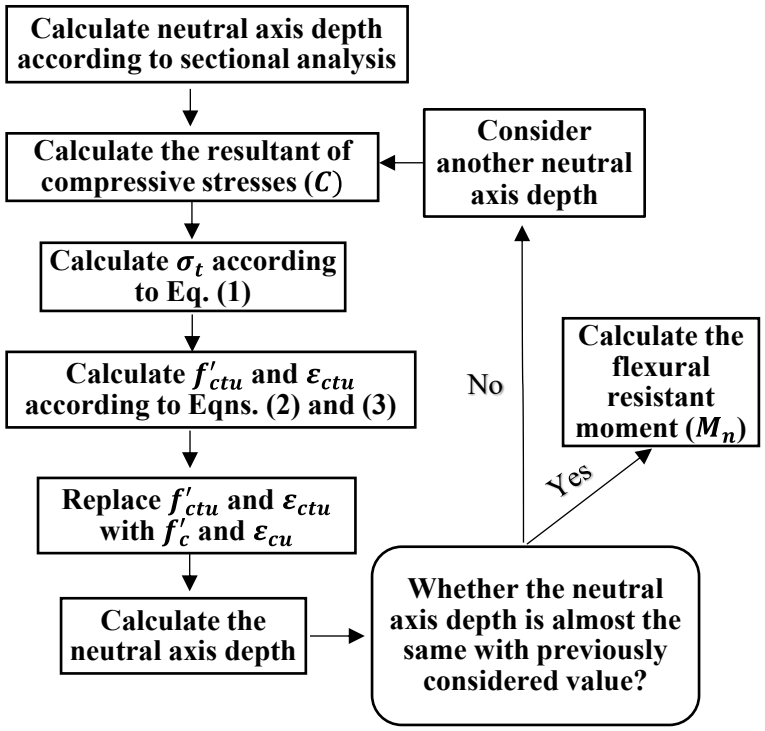

Figure 9.6 Flowchart for calculating flexural strength of curvilinear members with compression-controlled failure mode.

equations derived based on Todeschini's model (Todeschini et al. 1964) can be used to calculate α and β in any range of concrete strain (Tehrani et al. 2019):

$$\alpha = \frac{Ln\left[1+(\varepsilon_c/\varepsilon_0)^2\right]}{(\varepsilon_c/\varepsilon_0)} \tag{9.4}$$

$$\beta = 2+\frac{4}{\alpha(\varepsilon_c/\varepsilon_0)^2}[\tan^{-1}(\varepsilon_c/\varepsilon_0)-(\varepsilon_c/\varepsilon_0)] \tag{9.5}$$

where ε_0 is $1.71\frac{f_c'}{E_c}$.

9.5.2.2. Considerations for HSC members

According to the results of Hussein and Marzouk (2000), a linear relationship for σ_c-σ_t and ε_{cu}-σ_t can be assumed for HSC under biaxial compression-tension stresses. Therefore,

Eqns. 9.2 and 9.3 is valid for HSC curvilinear members as well. ACI 363R-10 suggests the following model for splitting tensile strength of HSC:

$$f_{ct} = 0.32 f_c^{'0.63} \tag{9.6}$$

Ozbakkaloglu and Saatcioglu (2004) proposed the following equation to obtain the ultimate compressive strain of HSC:

$$\varepsilon_{cu} = 0.0036 - (f_c^{'} - 30) \times 10^{-5} \geq 0.0027 \tag{9.7}$$

Todeschini's model (Todeschini et al. 1964) is originally proposed for NSC. However, the same concrete stress block coefficients as presented in Eqns. 9.4 and 9.5 are suggested in this study for HSC. In addition, assuming a linear stress-strain behavior for HSC when $\varepsilon_c \leq \varepsilon_0$ is a rational assumption (Collins and Mitchell 1997). According to the presented information, the same procedure as for NSC can be employed for HSC to find the flexural strength by replacing f_{sp} and ε_{cu} obtained from Eqns. 9.6 and 9.7 in the related equations presented for NSC.

9.5.2.3. Considerations for FRC members

Assuming a linear behavior for FRC under compression-tension stress is valid according to Karimipour et al. (2021) showing that Eqns. 9.2 and 9.3 can be employed for FRC curvilinear members as well. It should be noted that the role of fibers on the mechanical behavior of FRC become more pronounced after cracking. This is while tensile stresses induced due to deviation of the forces in curvilinear members are generally much less than the ultimate tensile strength of concrete. However, estimating the ultimate tensile strength of FRC is necessary for employing Eqns. 9.2 and 9.3. In general, splitting tensile strength of concrete is around 35% smaller than the modulus of rupture obtained from the beam test (Darwin et al. 2016). Therefore, this study suggests f_{ct} to be approximated by $0.65 f_p$ obtained by the beam test performed according to ASTM C1609-19. Ultimate compressive strain in FRC is generally greater than that of NSC. It is recommended to employ the ultimate strain obtained from compression test on FRC samples. In the absence of such results for FRC, ε_{cu} can be assumed as 0.0035 (ACI 544.4R-18). In lieu of more accurate flexural strength prediction

using stress-strain response of FRC in compression and tension, the following equation can be used:

$$M_{n=}M_{n-RC}+M_{n-FRC} \tag{9.8}$$

where M_{n-RC} is the bending moment capacity without considering the contribution of fibers but with ε_{cu} related to FRC. Similar procedure as presented for NSC can be employed to find M_{n-RC}. Eq. 9.9 is presented by ACI 544.4R-18 to simply estimate M_{n-FRC}, the bending capacity provided by the fibers:

$$M_{n-FRC}=f_{150}^{D}\times\frac{bh^2}{6} \tag{9.9}$$

9.5.3. Shear Strength Prediction

9.5.3.1. Shear strength prediction based on modified compression field theory

MCFT is a general model originally proposed by Vecchio and Collins (1986) for members with or without transverse reinforcement. In the general model, both vertical and horizontal stresses were considered. Fig. 9.7 shows the general concept of MCFT, and the equations simplified for the case of members without transverse reinforcement. Shear capacity of curvilinear members can be estimated using MCFT by simultaneous solving of the equations presented in Fig. 9.7 (generally with computer aid programs). f_z refers to the vertical stresses which can be obtained based on Eq. 9.1. To provide practical procedures for design purposes, Bentz et al. (2006) developed simplified modified compression field theory (SMCFT) which was later adopted by CAN/CSA S6-19 as the shear design method for both steel-RC and FRP-RC elements. As one of the simplifying assumptions, SMCFT neglect presence of vertical stresses (f_z). The following procedure was employed to simplify MCFT considering the vertical stress of f_z to consider the curvilinear shape of member. It was aimed to use somewhat similar approach as Bentz et al. (2006) to simplify MCFT to provide familiar equations for design engineers. The contribution of top mesh longitudinal reinforcement was neglected for simplicity. In addition, a constant f_z was assumed across the effective shear depth. Eqns. 9.11 and 9.14 can be re-arranged to yield:

$$v = v_{ci} - f_z \cot(\theta) \tag{9.23}$$

$$v = f_1 \cot(\theta) - f_z \cot(\theta) \tag{9.24}$$

Eqns. 9.23 and 9.24 can be written as:

$$v = \beta\sqrt{f_c'} - f_z \cot(\theta) \tag{9.25}$$

As SMCFT considers f_z equal to zero, v becomes equal to $\beta\sqrt{f_c'}$. It can be inferred from Eq. 9.25 that presence of vertical stresses reduces capacity of the member to carry shear stresses. From Eq. 9.21, β is given by:

$$\beta = \frac{0.33\cot(\theta)}{1+\sqrt{500\varepsilon_1}} \tag{9.26}$$

In addition, from Eqns. 9.18, 9.19, and 9.22, β should meets the following condition:

$$\beta \le \frac{0.18}{0.31+\frac{0.686 s_{ze}\varepsilon_1}{\sin(\theta)}} \tag{9.27}$$

Where

$$s_{ze} = \frac{35 s_z}{a_g + 16} \tag{9.28}$$

The maximum shear strength is obtained when Eqns. 9.26 and 9.27 results in a same value of β leading to the following equation:

$$\tan(\theta) = \frac{0.568 + 1.258\frac{s_{ze}\varepsilon_1}{\sin(\theta)})}{1+\sqrt{500\varepsilon_1}} \tag{9.29}$$

The value of ε_1 can be related to ε_x and ε_2 by rearranging Eqns. 9.15 and 9.16 as follows:

$$\varepsilon_1 = \varepsilon_x(1+\cot^2(\theta)) + \varepsilon_2 \cot^2(\theta) \tag{9.30}$$

As compressive stress of f_2 is relatively small, $\varepsilon_2 \approx f_2 / E_c$. On the other hand, from Eqns. 9.11 and 9.12 we have

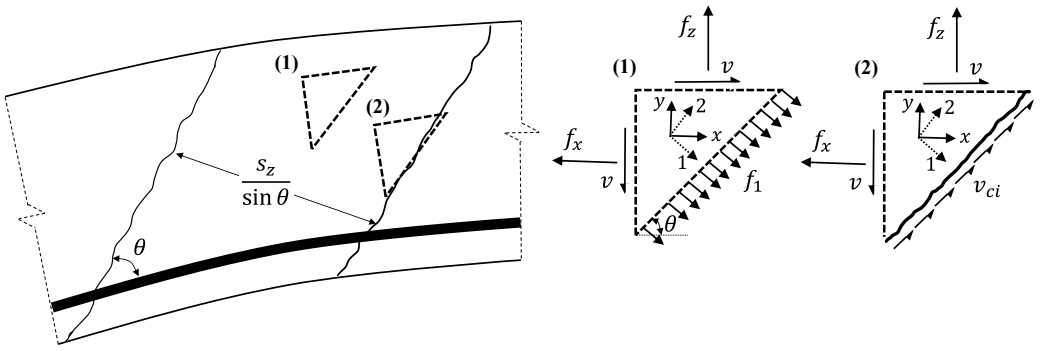

Average stresses:

$$f_x = f_1 - v\cot(\theta) \quad (10)$$

$$f_z = f_1 - v\tan(\theta) \quad (11)$$

$$v = \frac{f_1 + f_2}{\tan(\theta) + \cot(\theta)} \quad (12)$$

Stresses at cracks:

$$f_x + v\cot(\theta) + v_{ci}\cot(\theta) = 0 \quad (13)$$

$$f_z + v\tan(\theta) - v_{ci}\tan(\theta) = 0 \quad (14)$$

Average strains:

$$\tan^2(\theta) = \frac{\varepsilon_x + \varepsilon_2}{\varepsilon_z + \varepsilon_2} \quad (15)$$

$$\varepsilon_1 = \varepsilon_x + \varepsilon_z + \varepsilon_2 \quad (16)$$

$$\gamma_{xz} = 2(\varepsilon_x + \varepsilon_2)\cot(\theta) \quad (17)$$

Crack widths:

$$w = s_\theta \varepsilon_1 \quad (18)$$

$$s_\theta = \frac{s_z}{\sin(\theta)} \quad (19)$$

Concrete stress-strain relationships:

$$f_2 = \frac{f_c'}{0.8 + 170\varepsilon_1}\left[2\frac{\varepsilon_2}{\varepsilon_c'} - (\frac{\varepsilon_2}{\varepsilon_c'})^2\right] \quad (20)$$

$$f_1 = 0.33\sqrt{f_c'} / (1 + \sqrt{500\varepsilon_1}) \quad (21)$$

Shear stress on crack:

$$v_{ci} \le \frac{0.18\sqrt{f_c'}}{0.31 + \frac{24w}{a_g + 16}} \quad (22)$$

Figure 9.7 General concept of MCFT, and the equations simplified for the case of members without transverse reinforcement.

$$f_2 = f_1\cot^2(\theta) - f_z(1 + \cot^2(\theta)) \quad (9.31)$$

Therefore, by considering $E_c = 4950\sqrt{f_c'}$ (to round the numbers), Eq. 9.30 can be written as:

$$\varepsilon_1 = \varepsilon_x(1 + \cot^2(\theta)) + \frac{\cot^4(\theta)}{15000(1 + \sqrt{500\varepsilon_1})} - \frac{f_z\cot^2(\theta)(1 + \cot^2(\theta))}{4950\sqrt{f_c'}} \quad (9.32)$$

The values of ε_1 and θ can be found by simultaneous solving of Eqns. 9.29 and 9.32 which is difficult. In general, the values of the second and third terms in Eq. 9.32 are relatively small compared to the first term. In addition, neglecting contribution of f_z (in the case of tensile vertical stresses) in Eq. 9.32 is a conservative assumption since neglecting f_z increases the value of ε_1 leading to smaller value of β. According to the mentioned assumptions, Eq. 9.32 can be simplified as follows:

$$\varepsilon_1 \approx \varepsilon_x(1+\cot^2(\theta)) \tag{9.33}$$

Rearranging Eqns. 9.33 and 9.29 yields the following equation to be solved for predicting the value of θ:

$$\tan(\theta) \approx \frac{0.568+1.258\frac{s_{ze}\varepsilon_x(1+\cot^2(\theta))}{\sin(\theta)})}{1+\sqrt{500\varepsilon_x(1+\cot^2(\theta))}} \tag{9.34}$$

Where ε_x is the strain at the mid-height of the section which will be discussed later. After finding the values of ε_1 and θ using Eqns. 9.33 and 9.34, β can be calculated using either Eq. 9.26 or Eq. 9.27. It should be noted that the calculated values in the mentioned equations might have marginal difference due to approximations employed to obtain Eq. 9.33. To avoid difficult calculation procedures, simplified equations were proposed in the literature to estimate β. Bentz et al. (2006) suggested the following which was later adopted by CAN/CSA S6-19.

$$\beta = \frac{0.4}{1+1500\varepsilon_x}.\frac{1300}{1000+s_{ze}} \tag{9.35}$$

Eq. 9.35 was derived supposing the vertical stresses of f_z equal to zero; however, as the value of third term in Eq. 9.35 is relatively small, Eq. 9.35 can be used in the presence of vertical stresses as well. The value of ε_x can be obtained based on accurate sectional analysis. However, CAN/CSA S6-19 suggests the following equation in lieu of more accurate calculations:

$$\varepsilon_x = \frac{\frac{M_f}{d_{long}}+V_f+0.5N_f}{2E_fA_f} \tag{9.36}$$

According to CAN/CSA S6-19, ε_x should be limited to 0.003 in the related calculations. In addition, the critical section for shear near the supports should be located d_v from face of support. Furthermore, for negative values ε_x, it should be considered equal to zero. Eq. 9.35 was originally suggested for steel-RC members in which ε_x does not significantly exceed

0.001. This is while GFRP-RC members generally exceed such limit leading to underestimation of β using the linear approach of Eq. 9.35 (Khavaran 2019). Hoult et al. (2008) suggested the following model to provide a more accurate estimation for β in FRP-RC members.

$$\beta = \frac{0.3}{0.5 + (0.15 + 1000\varepsilon_x)^{0.7}} \cdot \frac{1300}{1000 + s_{ze}} \tag{9.37}$$

Simplified equations were also proposed in the literature to find the value of θ. Bentz et al. (2006) suggested Eq. 9.38 for predicting θ which was later adopted by CAN/CSA S6-19.

$$\theta = (29^\circ + 7000\varepsilon_x)(0.88 + \frac{s_{ze}}{2500}) \tag{9.38}$$

Similar to Eq. 9.35, Eq. 9.38 was originally proposed for steel-RC members leading to overestimation of θ. Eqns. 9.39 and 9.40 was proposed by Johnson (2014) for FRP-RC members with ε_x below and over 0.009, respectively.

$$\theta = (29^\circ + 7000\varepsilon_x - 400000\varepsilon_x^2)(0.88 + \frac{s_{ze}}{2500}) \le 75^\circ \tag{9.39}$$

$$\theta = 60(0.88 + \frac{s_{ze}}{2500}) \le 75^\circ \tag{9.40}$$

After finding θ, and β, shear capacity of an FRP-reinforced curvilinear member can be obtained through the following equation:

$$V = (\beta\sqrt{f_c'} - f_z \cot(\theta))b_w d_{long} = (\beta\sqrt{f_c'} - \frac{C}{b_w R}\cot(\theta))b_w d_{long} \tag{9.41}$$

In lieu of more accurate calculations to predict compression force in the section, Eq. 9.42 can be used to find the shear capacity supposing that $\varepsilon_f = 2\varepsilon_x$.

$$V = (\beta\sqrt{f_c'} - \frac{2\rho_f E_f \varepsilon_x d}{R}\cot(\theta))b_w d_{long} \tag{9.42}$$

In this paper, employing Eqns. 9.26, 9.33, and 9.34 to find the values of θ, and β referred to semi-simplified modified compression field theory (SSMCFT) while using Eqns. 9.37, 9.39, and 9.40 refers to improved simplified modified compression field theory (ISMCFT).

9.5.3.2. Shear strength prediction based on critical shear crack theory

The main concepts and formulations of CSCT to be used for predicting shear capacity of one-way slabs without transverse reinforcement were developed by (Muttoni and Fernández Ruiz 2008). The key assumption of CSCT is that shear strength of a RC member without transverse reinforcement is governed by formation of a critical shear crack preventing concrete to resist against shear force. Therefore, characteristics of the critical shear crack is the main determinative factor is CSCT. This theory considers contribution of aggregate interlock, residual tensile strength, inclination of compression chord, and dowel action in shear transferring mechanism (Muttoni and Fernández Ruiz 2008; Cavagnis et al. 2020). Cavagnis et al. (2020) evaluated validity of CSCT and presented it as a practical design expression. This method is originally developed for steel-RC members without transverse reinforcement. However, as it considers the strain effect, it has possibility to be adopted for FRP-RC members as well. Eq. 9.43 is presented for the shear strength of a member without transverse reinforcement using CSCT.

$$V_{CSC} = 0.015 k_c k_\beta \left(\frac{d_{dg}}{\varepsilon_f d}\right)^{0.5} \sqrt{f_c'} b d \tag{9.43}$$

where $d_{dg} = 16 + d_g$, d_g is the maximum aggregate size; ε_f is strain in longitudinal reinforcement; k_c and k_β are the parameters considering shape and location of the critical shear crack which can be obtained through Eqns. 9.44 and 9.45, respectively;.

$$k_c = \frac{1}{1 - 0.5 h_f / r_f} \tag{9.44}$$

$$k_\beta = \left(\frac{\beta_{AB}}{\beta_0}\right)^2 \tag{9.45}$$

Where r_f the distance between the tip of the CSC and the load acting on the compression face which can be assumed equal to d; h_f is the distance from the top compressive fiber and the tip of CSC considered equal to $d - d_f$ where d_f can be taken as $(d - c) + (d/6)\sin(22.5^\circ)$; β_0 is 60 degrees and β_{AB} can be calculated according to Eq. 9.46:

$$\beta_{AB} = 45^{\circ} + 15^{\circ}\alpha_A^{1/3} \leq 90^{\circ} \tag{9.46}$$

where $\alpha_A = M_f / (V_f d)$. The tip of critical shear crack can be assumed as the critical section to find ε_f, M_f, V_f. Fig. 9.8 shows the main concepts and parameters used in CSCT for a curvilinear member. It should be noted that for the cases where $\varepsilon_f \leq 0$, Eq. 9.43 is not valid. In addition, this Equation might yield unreasonable results for the cases with very small value of ε_f. However, no limitations were reported by Cavagnis et al. (2020) on the minimum applicable amount of strain in longitudinal bars for CSCT.

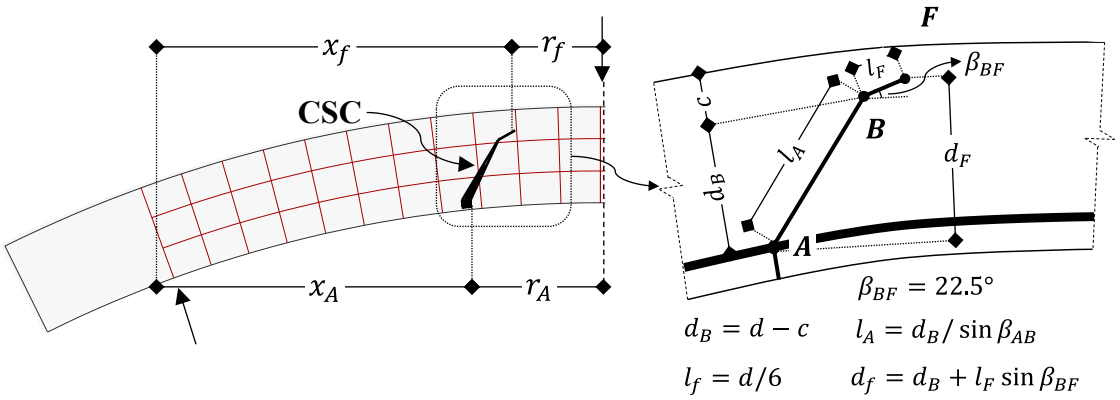

Figure 9.8 General assumptions of critical shear crack theory model.

To account for curvilinear shape of the member, consider Fig. 9.9. According to this Figure, deviation of the tensile force in the section caused an additional shear force (ΔV) to be transmitted through CSC. Therefore, the total shear force to be transmitted through the CSC is:

$$V_{CSC} = V_f + \Delta V \tag{9.47}$$

Campana et al. (2014) proposed the following equation to account for the additional shear force caused by curvilinear shape of the member

$$\Delta V = \frac{2\lambda da}{2zR - (\lambda d)^2} V_f \tag{9.48}$$

Where z is the distance from resultant of compression stresses in the section to the bottom longitudinal reinforcement; a is the horizontal distance between the tip of CSC to the support; λ is the coefficient considering the angle α (the slope of the resultant of the forces

carried by reinforcement) which can be taken as 0.5 until availability of further research. Eq. 9.49 presents the required shear capacity of FRP-RC curvilinear members without transverse reinforcement considering the curvilinearity effect according to CSCT.

$$V_c = \frac{V_{CSC}}{(1+\frac{2\lambda da}{2zR-(\lambda d)^2})} \tag{9.49}$$

In the straight member where $R \to \infty$, $V_c = V_{CSC}$. Increasing the curvature of the member, however, reduces the shear capacity according to Eq. 9.49. In this study, "Modified Critical Shear Crack Theory (MCSCT) refers to the proposed method to consider the curvilinearity effect in CSCT.

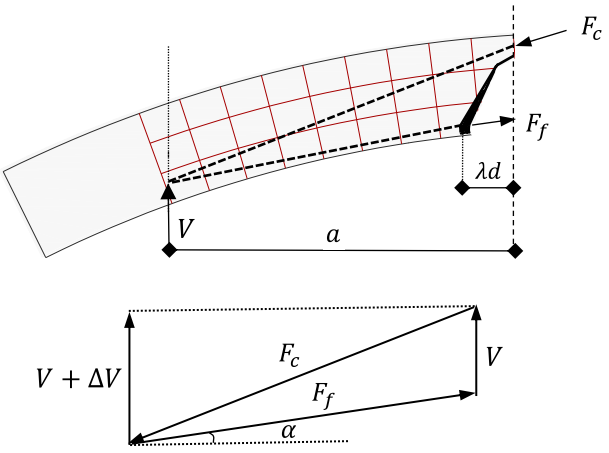

Figure 9.9 Considering curvilinear shape of the member in critical shear crack theory model.

9.5.3.3. Considerations for HSC

Similar strengths for aggregates and concrete are expected in HSC, leading cracks to break through the aggregates. This negatively affect the capacity of aggregate interlocking in transferring shear stresses (El-Sayed et al. 2006; ACI 363R-10). Bentz et al. (2006) recommends taking a_g equal to zero when concrete compressive strength is greater than 70 MPa. The same approach can be employed for d_g in CSCT. To account the negative effect of employing HSC on aggregate interlock mechanism, CAN/CSA S6-19 indirectly limits concrete compressive strengths to 64 MPa in calculating the shear capacity of concrete.

9.5.3.4. Considerations for FRC

The MCFT and CSCT do not take into account contribution of fibers in carrying shear force. Modifying the mentioned theories for FRC needs a comprehensive in-depth analysis with extensive experimental validations and modeling which is not the scope of this study. In the following, a simple rational approach is introduced to find shear strength of FRP-reinforced FRC curvilinear members. According to the model presented in ACI 544.4R-18 for shear capacity of steel-reinforced FRC elements, the ratio of shear capacity of FRC elements to those from plain concrete is $[1+7.5(f_{ut-FRC}/f_t)]^{(1/3)}$. Where $f_{ut-FRC}=0.37f_{150}^{D}$, and f_t is the tensile strength of plain concrete under flexure, which can be considered as $0.62\sqrt{f_c'}$ according to ACI 318-19. To consider contribution of fibers in FRP-reinforced curvilinear members, the shear capacity obtained based on MCFT and CSCT without considering the contribution of fibers can be multiplied by $(1+7.5\frac{f_{ut-FRC}}{f_t})^{(1/3)}$.

9.5.4. Comparison Between Experimental and Analytical Results

The experimental bending moment capacity of the specimens were compared with the theoretical values as listed in Table 9.3. Theoretical values were obtained supposing two scenarios of considering and neglecting the curvilinearity effect. While all the tested specimens were included in the Table, the discussion in this section is mainly oriented to the specimens with flexural failure mode. The experimental and theoretical ultimate tensile strains were also included in Table 9.3 for comparison. According to Table 9.3, neglecting the curvilinear shape of the GFRP-reinforced curvilinear specimens led to 17% overestimation of the predicted bending moment capacity on average. However, employing the presented method in this study to consider the curvilinearity effect could predict the flexural strength of GFRP-reinforced tunnel segments accurately (with an error of 1%) on average for all the specimens with flexural failure mode. Modified ultimate compressive strain based on the proposed method was also in good agreement with the experimental results for NSC and HSC specimens. For FRC specimens, ε_{ctu} was lower than the

experimental results. This is reasonable as ε_{ctu} is employed to calculate M_{n-RC}. Adding M_{n-FRC} to M_{n-RC} for finding the flexural strength of FRC specimens indirectly refers to considering a greater value of ultimate compressive strain compared to ε_{ctu}.

Table 9.3 compares the experimental results with analytical results obtained from the developed models for shear capacity. Two scenarios of considering and neglecting curvilinearity effect was employed for comparison. The results for all the specimens were presented. However, the following discussion is mainly focused on the specimens which experienced shear failure. The ratio of theoretical to the experimental shear strength neglecting the curvilinear shape of the specimens was on average 0.96 when SSMCFT was employed. This is while SMCFT generally provides a high level of conservativity since it only considers aggregate interlock as the shear transferring mechanism. For the members with similar loading and boundary conditions with the test specimens, the contribution of aggregate interlock on the shear strength ranges generally from 50% to 80% (Cavagnis et al. 2020). This is in good agreement with the ratio of 0.6 reported by Alguhi and Tomlinson (2021) as the ratio of predicted shear capacity to the experimental shear strength of GFRP-reinforced flexural elements according to SMCFT. Therefore, it shows that when SMCFT is compared by itself, neglecting the curvilinearity effect leads to overestimation of shear strength. Considering the curvilinearity effect employing SSMCFT and ISMCFT predicted the shear capacity with averagely 28% conservativity. Therefore, the proposed methods provide a rational level of conservativity aligning with the conservativity level of SMCFT for straight GFRP-reinforced members. In addition, SSMCFT and ISMCFT yielded close results for NSC and FRC specimens while the predicted shear capacity by ISMCFT was slightly greater than SSMCFT for HSC specimens. Neglecting curvilinearity effect in CSCT led to 5% of overestimation in predicting shear capacity of GFRP-reinforced flexural elements. Employing MCSCT, however, predicted shear capacity with 10% conservativity. In general, MCSCT is suggested as the most accurate method to predict shear capacity of GFRP-reinforced curvilinear members with a slight level of conservativity. In addition, ISMCFT and SSMCFT are suggested as simple, reliable, and conservative methods to

Table 9.3 Comparison between the experimental and analytical results

ID	Experimental values			Theoretical values								
				Proposed method				$V_{Theo.}/V_{\exp.}$				
				Case 1		Case 2		SSMCFT		ISMCFT	MCSCT	
	$M_{\exp.}$ kN.m	$V_{\exp.}$ kN.m	$\varepsilon_{cu,\exp.}$	ε_{cu}	$M_{Theo.}/M_{\exp.}$	ε_{ctu}	$M_{Theo.}/M_{\exp.}$	Case 1	Case 2	Case 2	Case 1	Case 2
Specimens with flexural failure mode												
7G#5	213	158	0.0030	0.0035	1.12	0.0031	0.99	0.80	0.58	0.58	0.92	0.75
7G#5U	186	133	0.0029	0.0035	1.22	0.003	1.06	0.98	0.75	0.74	1.10	0.93
7G#5H	247	185	0.0029	0.0030	1.08	0.0028	0.99	0.88	0.65	0.65	0.97	0.81
7G#5HU	227	168	0.0027	0.0031	1.15	0.0028	1.02	1.00	0.81	0.85	1.04	0.88
7G#5F	213	156	0.0035	0.0035	1.18	0.0030	1.00	1.08	0.88	0.92	1.13	0.95
7G#5FU	210	153	0.0039	0.0040	1.24	0.0033	1.02	0.90	0.70	0.69	1.04	0.88
7G#6	243	183	0.0029	0.0035	1.18	0.0029	1.01	0.97	0.76	0.76	1.13	0.99
Specimens with shear failure mode												
13G#5	243	183	0.0027	0.0035	1.31	0.0029	1.05	0.99	0.74	0.73	1.09	0.92
13G#6	273	206	0.0025	0.0035	1.29	0.0028	1.09	0.91	0.64	0.64	1.00	0.83
13G#5H	257	193	0.0029	0.0031	1.37	0.0027	1.14	0.96	0.77	0.81	1.01	0.87
13G#5F	273	205	0.0044	0.0045	1.26	0.0036	1.00	0.97	0.74	0.73	1.10	0.97

* Note: Case 1 does not consider the curvilinearity effect and Case 2 considers the effect of curvilinearity.

predict shear capacity of GFRP-reinforced curvilinear members. However, more research data is needed for further validation of the mentioned models.

9.5.5. Parametric Study

This section presents the results of a parametric study performed to investigate the effect of five key parameters of curvature radius, axial load level, concrete strength, reinforcement ratio, and sectional thickness on the flexural and shear strength of curvilinear GFRP-reinforced members under bending load. The proposed flexural strength prediction method,

SSMCFT, and MCSCT were employed for the parametric study. The selected member for the parametric study was from NSC and had width of 1000 mm with the same length and boundary conditions as the tested specimens. Reinforcement configurations and properties were supposed the same as the tested specimens while #5 GFRP bars was supposed for longitudinal reinforcement. The reference member in the parametric study had concrete compressive strength of 45 MPa, thickness of 300 mm, reinforcement ratio of $2.5\rho_b$ equal to 0.0096, curvature radius of 3305 mm, with no axial load. Three different concrete compressive strengths of 35, 45, and 55 MPa were designated for the parametric study which was within the range of recommended compressive strength for tunnel segments according to ACI 533.5R-20. Three curvature radiuses of 1805, 3305, and 4805 mm were selected corresponded to conventional radiuses for wastewater tunnels, metro tunnels, and highway tunnels, respectively. Four axial load levels of 0, $0.15f_c^{'}A_g$, $0.3f_c^{'}A_g$, and $0.45f_c^{'}A_g$ were considered based on probable axial load levels for tunnel segments in the field applications (Arnau and Molins 2012; ACI 544.7R-16; ACI 533.5R-20). Three sectional thicknesses of 200, 300, and 400 mm were selected based on the typical thicknesses of tunnel segments in real tunneling projects (Arnau and Molins 2012; ACI 533.5R-20). Finally, three reinforcement ratios of 0.0058, 0.0096, and 0.0134 were designated corresponded to $1.5\rho_b$, $2.5\rho_b$, and $3.5\rho_b$, respectively, where ρ_b is the balanced reinforcement ratio of the reference specimen obtained based on ACI 440.1R-15. In the following, the effect of each parameter on the flexural and shear strength of GFRP-reinforced curvilinear members is presented. To investigate the net effect of each parameter, the other parameters kept constant and equal to what designated for the reference member. It should be noted that all the presented diagrams are in a normalized form so that $K_n = V_n / A_g f_c^{'}$, and $R_n = M_n / A_g f_c^{'} h$ where $f_c^{'}$, A_g, and h were equal to those selected for the reference segments.

9.5.5.1. Effect of curvature

The effect of curvature radius on the flexural and shear strength is shown in Fig. 9.10a. In addition, flexural and shear strength in the case of zero curvature (straight member) are shown for comparison. A general trend is decreasing the flexural and shear strength of

curvilinear GFRP-reinforced members by increasing the curvature of the member. Compared to the straight member, flexural strength reduces by 14, 19, and 29% in the curvilinear member with curvature radius of 4805, 3305, and 1805 mm, respectively. It shows a nearly linear flexural strength decrement trend by increasing the curvature of the member.

Considering the curvilinearity effect employing SSMCFT yielded 90, 35, and 21% lower shear strength compared to the straight member for curvature radius of 1805, 3305, and 4805 mm, respectively. The mentioned values were 32, 17, and 12% in MCSCT. It shows that employing SSMCFT to consider the curvilinearity effect has more decremental effect on shear capacity of a curvilinear member compared to MCSCT. It can be justified by the fact that SSMCFT considers aggregate interlock as the only shear transferring mechanisms while MCSCT consider all other shear transferring mechanisms. This is while the induced tensile stresses due to curvilinear shape of the member has more detrimental effect on the aggregate interlock mechanism compared to the other mechanisms. To help demonstrate this concept, consider Eq. 9.23. According to this Equation, increasing the tensile vertical stresses can even result in losing the capability of the member to transfer shear stress through the cracked surface. In such situation, SSMCFT yielded the shear strength of the member equal to zero. More research is still needed to verify the ability of GFRP-reinforced curvilinear members with high curvature in transferring shear forces.

9.5.5.2. Effect of axial load

Many curvilinear structural members such as PCTL segments may be subjected to combination of axial load and bending moment because of applied loads. The effect of axial load level on the flexural and shear strength of GFRP-reinforced curvilinear members is shown in Fig. 9.10b for four axial load levels of 0, $0.15f_c^{'}A_g$, $0.3f_c^{'}A_g$, and $0.45f_c^{'}A_g$. In general, by increasing the axial load level, the compression force in the section increases leading to increasing the vertical tensile stresses. In addition, increasing the axial load level increases the neutral axis depth. In such situation, the conservative assumption of employing σ_t calculated at the neutral axis depth in the related calculations might lead to too

conservative results. Therefore, the other presented approach suggesting taking an average value of σ_t in the compression block depth was employed in this section. According to Fig. 9.10b increasing the axial load from zero to $0.3f_c^{'}A_g$ enhanced the flexural strength of GFRP-reinforced straight members while further increase in the axial load slightly reduced the flexural strength. In the case of curvilinear members, flexural strength improved by increasing the axial load up to $0.15f_c^{'}A_g$. However, further increase in the axial load level led to reduction of flexural capacity which became more pronounced by increasing the axial load level from $0.3f_c^{'}A_g$ to $0.45f_c^{'}A_g$. Compared to the straight member, the flexural strength of curvilinear member was 10, 15, 28, and 88% lower in the axial load levels of 0, $0.15f_c^{'}A_g$, $0.3f_c^{'}A_g$, and $0.45f_c^{'}A_g$. It can be justified by the fact that increasing the axial load level increases the value of σ_t leading to more decrease in the ultimate concrete stress and strain.

According to Fig. 9.10b, increasing the axial load level from 0 to $0.3f_c^{'}A_g$ enhanced shear capacity according to SSMCFT and MCSCT. As bottom longitudinal bars underwent compressive strain in the case of $0.45f_c^{'}A_g$, MCSCT was not valid to predict shear capacity in that case. In addition, as ε_x was negative in the axial load levels of $0.3f_c^{'}A_g$ and $0.45f_c^{'}A_g$, it was taken equal to zero in SSMCFT for those cases. This is why SSMCFT yielded the same result for straight member in the axial load levels of $0.3f_c^{'}A_g$ and $0.45f_c^{'}A_g$. However, since the vertical stresses increased in the axial load level of $0.45f_c^{'}A_g$ compared to $0.3f_c^{'}A_g$, SSMCFT yielded slightly lower shear capacity in the former for curvilinear member. Considering curvilinearity effect through SSMCFT led to 26, 40, 30, and 32% lower shear capacity compared to the straight member in the axial load levels of 0, $0.15f_c^{'}A_g$, $0.3f_c^{'}A_g$, and $0.45f_c^{'}A_g$. Employing MCSCT resulted in 17, 17, and 10% lower shear capacity prediction in curvilinear member compared to the corresponded straight member in the axial load levels of 0, $0.15f_c^{'}A_g$, $0.3f_c^{'}A_g$.

9.5.5.3. Effect of concrete strength

The effect of concrete compressive strength on the flexural and shear capacity of GFRP-reinforced curvilinear members were investigated through three different concrete strengths of 35, 45, and 55 MPa (Fig. 9.10c). According to Fig. 9.10c, flexural strength enhances almost linearly by increasing compressive strength. The curvilinear member with concrete compressive strengths of 35, 45, and 55 MPa had 17, 19, and 20% lower flexural capacity compared to its straight counterpart. It shows a slight increase in the load reduction due to curvilinearity effect by enhancing the concrete strength in GFRP-reinforced curvilinear members. It can be justified by increasing the compression forces in the section as a result of enhancing concrete compressive strength which leads to increase in the value of σ_t. Shear strength of both straight and curvilinear members followed a nearly linear trend by increasing the concrete compressive strength. The shear capacity calculated based on SSMCFT and MCSCT was almost 26% and 21% smaller in curvilinear member than those for straight member for different concrete compressive strengths. Therefore, it can be concluded that concrete compressive strength has no considerable effect on the reduction of shear capacity due to curvilinearity effect.

9.5.5.4. Effect of reinforcement ratio

Fig. 9.10d shows the effect of reinforcement ratio on the flexural and shear capacity of GFRP-reinforced curvilinear members employing three different reinforcement ratios of $1.5\rho_b$ (0.0058), $2.5\rho_b$ (0.0096), and $3.5\rho_b$ (0.0134) calculated based on ACI 440.1R-20. Increasing reinforcement ratio increased the flexural strength with a nearly linear trend. Flexural strength of GFRP-reinforced curvilinear member decreased by 16, 19, and 21% compared to the straight member, respectively, for $1.5\rho_b$, $2.5\rho_b$, and $3.5\rho_b$. Increasing reinforcement ratio in curvilinear members leads to increase in the value of σ_t and decrease of flexural strength consequently. Increasing the reinforcement ratio enhanced the shear capacity of GFRP-reinforced curvilinear members with a linear trend. The obtained shear capacity of curvilinear member was 23, 26, and 28% lower than the straight member for the reinforcement ratios of $1.5\rho_b$, $2.5\rho_b$, and $3.5\rho_b$, respectively, according to SSMCFT.

However, the predicted shear capacity was almost 21% lower in curvilinear member compared to the straight member based on MCSCT for different reinforcement ratios.

9.5.5.5. Effect of sectional thickness

Fig. 9.10e presents the effect of increasing the sectional height from 200 mm to 400 mm on the flexural and shear strength of curvilinear members. Increasing the sectional thickness increased the flexural and shear capacities of a GFRP-reinforced curvilinear member with a nearly linear trend. Increasing the sectional thickness intensified the reducing effect of curvilinearity on the flexural strength of curvilinear members. It can be inferred by 15, 19, and 21% lower flexural capacity of GFRP-reinforced curvilinear member with the thicknesses of 200, 300, and 400 mm, respectively, compared to the straight member. Shear capacity calculated based on SSMCFT was 30, 26, and 23% lower in curvilinear member compared to the straight member with the thicknesses of 200, 300, and 400 mm, respectively. The mentioned values were 13, 17, and 18% for MCSCT.

9.6. Conclusions

In this paper, the summary of an experimental program performed on 11 full-scale curvilinear GFRP-reinforced tunnel segment specimens was reported. Then, an analytical study was presented aiming at proposing some models to predict flexural and shear capacities of curvilinear GFRP-RC members with focus on precast concrete tunnel lining segments. In the analytical study, the effect of curvilinear shape of the member on the stresses induced in the section was discussed. Afterwards, a model was developed to consider the effect of curvilinearity on flexural strength of GFRP-reinforced curvilinear members. Following that, two models were proposed to predict shear capacity of GFRP-reinforced curvilinear members based on MCFT and CSCT. After comparing the experimental and analytical results, a parametric study performed to investigate the effect of

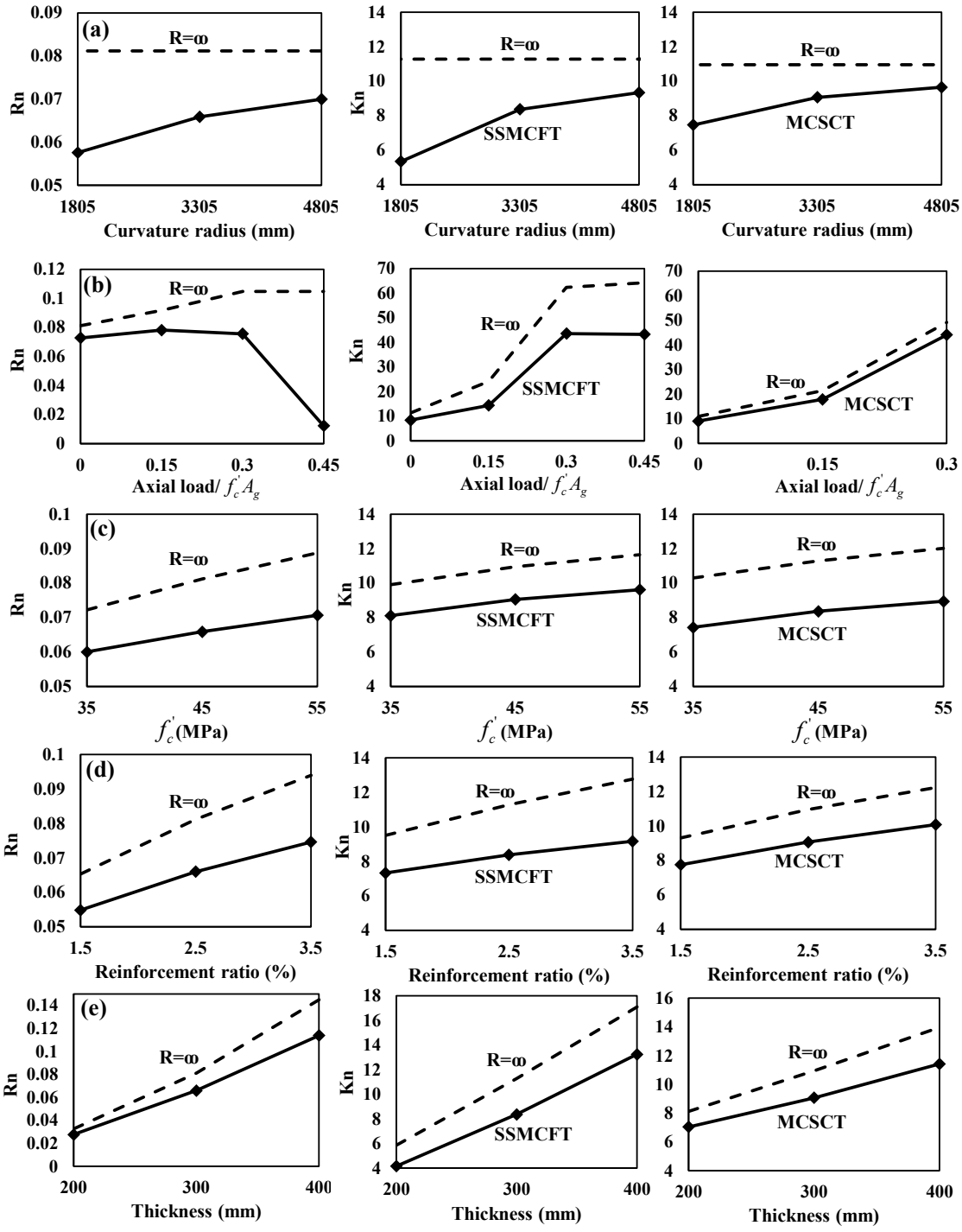

Figure 9.10 The results of the parametric study: (a) effect of curvature radius; (b) effect of axial load level; (c) effect of concrete strength; (d) effect of reinforcement ratio; (e) effect of sectional thickness.

different parameters on the flexural and shear capacities of GFRP-reinforced curvilinear members. The following conclusions can be drawn:

1. Deviation of compression and tension forces in a curvilinear RC member induces tensile stresses in the direction perpendicular to the principal stresses. Such stresses mainly depend on the curvature radius and the amount of compression stresses induced in the section.
2. Neglecting the curvilinear shape of the GFRP-reinforced curvilinear members led to 17% overestimation of the predicted bending moment capacity. However, employing the presented model in this study to consider the curvilinearity effect could predict the flexural strength of GFRP-reinforced tunnel segments accurately.
3. The two shear capacity prediction models proposed based on MCFT (SSMCFT and ISMCFT) predicted the shear capacity with 28% conservativity. Therefore, the proposed models provided a rational level of conservativity aligning with the conservativity level of MCFT for straight GFRP-reinforced members. Using CSCT led to 5% of overestimation in predicting shear capacity of GFRP-RC curvilinear members. However, the proposed model based on modifications on CSCT (MCSCT) predicted shear capacity of GFRP-RC curvilinear members with 10% conservativity.
4. As the most accurate method to predict shear capacity of GFRP-reinforced curvilinear members with a slight level of conservativity, MCSCT is recommended. In addition, ISMCFT and SSMCFT are reliable methods to predict shear capacity of GFRP-reinforced curvilinear members. However, the mentioned models need to be further validated with more research data.
5. Flexural strength of curvilinear GFRP-reinforced members decreased with a nearly linear trend by increasing the curvature of the member. Increasing the curvature reduces the shear capacity of GFRP-reinforced curvilinear members. The reduction trend is more pronounced in SSMCFT compared to MCSCT.
6. Increasing the axial load level led to a relatively lower flexural strength in a curvilinear GFRP-reinforced member compared to its straight counterpart. A same trend was observed by increasing the concrete strength, sectional thickness, and reinforcement ratio. However, concrete compressive strength has no noticeable effect on the reduction

of shear capacity due to curvilinearity effect. In addition, increasing axial load level, sectional thickness, and reinforcement ratio did not follow a general trend in the shear strength reduction because of curvilinearity effect.

CHAPTER 10 GENERAL CONCLUSIONS AND RECOMMENDATIONS

10.1. Summary

The focus of this project was to elaborate on the structural performance of precast concrete tunnel lining segments reinforced with GFRP bars under monotonic bending load. The experimental program includes fabrication and testing of 12 full-scale PCTL segments under three-point bending load. The test parameters were the type of reinforcement (steel and GFRP), reinforcement ratio (0.48, 0.69, 0.90, and 1.28%), concrete strength (NSC and HSC), concrete type (NC and FRC), and tie configurations (closed ties and U-shaped ties). The test results were evaluated in terms of cracking behavior, failure mechanism, deflection behavior, serviceability, strain behavior, ductility, and deformability. The experimental program was followed by and analytical investigation to evaluate the existing design provisions and to develop new design procedures for GFRP-reinforced PCTL segments. The provisions of North American design standards of ACI 440.1R-15, CAN/CSA S806-12 (R2017), CAN/CSA S6-19, and AASHTO-18 to predict flexural strength, shear strength, cracking behavior, and deflection behavior were evaluated. Then, new procedures were developed to obtain design interaction diagrams for GFRP-reinforced PCTL segments. In addition, novel deflection prediction methodologies were proposed for calculating deflection of GFRP-reinforced PCTL segments at service load. Finally, new procedures were developed to consider the effect of curvilinear shape of GFRP-reinforced PCTL segments on their flexural and shear strength.

10.2. Conclusions

The following conclusions can be drawn based on the experimental and analytical investigations conducted in this research program:

- Concrete-crushing failure mode was observed in the GFRP-reinforced specimen with the reinforcement ratio 40% and 100% higher than the balanced ratio. Further increase in the reinforcement ratio of the GFRP-reinforced specimens changed the failure mode to diagonal-tension failure. Nevertheless, flexural-dominant behavior was observed in all the GFRP-reinforced specimens up to peak load. The steel-reinforced specimen experienced concrete crushing after yielding of the steel reinforcement.
- Increasing the reinforcement ratio by 44, 85 and 165% in the GFRP-reinforced specimen enhanced the load-carrying capacity by 16, 16 and 30%, respectively, and improved the post-cracking stiffness by 45, 90 and 140%, respectively.
- All GFRP-reinforced specimens satisfied the crack-width requirement in CAN/CSA S6-19 at service load. In addition, the deflection and crack width in GFRP-reinforced tunnel segments could be close to that of steel-reinforced ones by providing around 50% of the axial stiffness of the steel reinforcement.
- Employing HSC changed the failure mode from shear to shear-flexure in GFRP-reinforced PCTL segments with high reinforcement ratio. In addition, using HSC enhanced the post-cracking stiffness and load-carrying capacity by 7% and 17%, respectively. Furthermore, employing HSC enhanced the cracking load by 18% while did not have noticeable effect on the crack width and spacing.
- Increasing the reinforcement ratio in GFRP-reinforced HSC PCTL segments changed the failure mode from flexure to shear-flexure. Increasing the reinforcement ratio by 86% improved the post-cracking stiffness and load carrying capacity by 68% and 17%, respectively. In addition, crack width at service load effectively decreased by 50% through increasing the reinforcement ratio.
- The procedure presented to modify the ACI 440.1R-15 model in terms of the compression-block coefficients and ultimate compressive strain predicted the flexural strength of both NSC and HSC specimens fabricated with closed ties with an error of less than 1.0% while overestimating that of the HSC specimen fabricated with U-shaped ties by 10%.
- Among the North American standards evaluated, CAN/CSA S806-12, R2017 yielded the most accurate results in predicting the shear capacity of GFRP-reinforced HSC PCTL

segments with an underestimation of 7%. ACI 440.1R-15 gave the most conservative results. Modifying the ACI 440.1R-15 model based on the method presented in this study improved the prediction accuracy by 5%.

- Using FRC in the GFRP-reinforced specimen with high reinforcement ratio changed the failure mode from shear failure to concrete crushing followed by shear failure. The initiation and service-crack widths were 67% and 57% narrower in the FRC specimen, respectively, compared to its NC counterpart. The fiber contribution could enhance the load-carrying capacity, deflection at peak load, maximum concrete compressive strain, and deformability by 12%, 24%, 81%, and 71%, respectively.
- Increasing the reinforcement ratio by 86% in the GFRP-reinforced FRC PCTL segment enhanced the cracking load, post-cracking stiffness, and peak load by 29%, 92%, and 31%, while reducing the initial crack width, crack spacing, and crack width at service load by 50%, 30%, and 57%, respectively.
- Two methods were presented to predict flexural capacity of GFRP-reinforced FRC PCTL segments: direct method based on the stress–strain behavior of the FRC and a simplified method based on ACI 440.1R-15. The flexural capacity was predicted with an error of less than 2% and 5% with the direct and simplified methods, respectively.
- Three methods were presented in this study to predict the shear capacity of GFRP-reinforced FRC PCTL segments. Methods I and II provided highly conservative and conservative results, respectively, while modifying the results obtained from CAN/CSA S806-12, R2017 with method III was less conservative in predicting the shear capacity of GFRP-reinforced FRC PCTL segments.
- Replacing the closed ties with U-shaped ties in NC specimens increased the crack width and deflection at the average service moment by 14% and 36%, respectively, while decreasing the peak load by 12%. Tie configuration did not have noticeable effect on the cracking and deflection behavior of GFRP-reinforced HSC PCTL segments. However, the HSC specimen with U-shaped ties had 9% lower load-carrying capacity compared to the specimen with closed ties. This is while GFRP-reinforced FRC PCTL segments with U-shaped and closed ties provided similar structural behavior.

- The ACI 440.1R-15 equation predicted higher bending moment capacity than the CAN/CSA S806-12, R2017 equation for the axial loads greater than $0.2 f_c^{'} A_g$. The ACI 440.1R-15 and CAN/CSA S806-12, R2017 equations overestimated the bending moment capacity of the tested GFRP-reinforced segments by 6% and 19% (on average), respectively.
- The experimental results were very consistent with the analytical results obtained based on the proposed method to obtain axial load–bending moment interaction diagram at the service stage. In addition, employing the creep–rupture control procedure developed based on CAN/CSA S806-12, R2017 and ACI 440.1R-15 yielded 1% and 9% conservative results on average for the tested specimens, respectively.
- Increasing the concrete compressive strength to enhance axial–flexural capacity was effective when the axial load level was greater than $0.15 f_c^{'} A_g$. In contrast, increasing the reinforcement ratio was more effective in improving the axial–flexural capacity at the axial loads below $0.15 f_c^{'} A_g$. Increasing the sectional thickness greatly increased the axial-flexural capacity at all axial load levels.
- Applying the effective moment of inertia developed for curvilinear members based on Bischoff's model overestimated deflection by 20%, 3%, and 12% in the NSC, HSC, and FRC GFRP-reinforced PCTL segments, respectively.
- Accuracy of the presented deflection prediction methodologies depends on the reinforcement ratio, concrete strength, and concrete type. A new model was proposed and validated based on the experimental data to consider the effect of these parameters on a deflection prediction method. The proposed model could predict deflection at the service load with 2% conservativeness.
- Employing the effective moment of inertia to calculate deflection is a simple method with acceptable conservativeness (11% on average in the tested specimens). Its accuracy, however, depends on the load and boundary conditions. The proposed method is capable of providing more accurate results than the other methods although it requires more computational effort. Lastly, the integration of curvature while neglecting tension stiffening is a conservative option (41% on average) when a designer is not sure about the tension-stiffening characteristics of the member.

- Deviation of compression and tension forces in a curvilinear RC member induces tensile stresses in the direction perpendicular to the principal stresses. Such stresses mainly depend on the curvature radius and the amount of compression stresses induced in the section.
- Neglecting the curvilinear shape of the GFRP-reinforced curvilinear members led to 17% overestimation of the predicted bending moment capacity. However, employing the presented model in this study to consider the curvilinearity effect could predict the flexural strength of GFRP-reinforced tunnel segments accurately.
- The two shear capacity prediction models proposed based on MCFT (SSMCFT and ISMCFT) predicted the shear capacity with 28% conservativity. Using CSCT led to 5% of overestimation in predicting shear capacity of GFRP-RC curvilinear members. However, the proposed model based on modifications on CSCT (MCSCT) predicted shear capacity of GFRP-RC curvilinear members with 10% conservativity.
- Flexural strength of curvilinear GFRP-reinforced members decreased with a nearly linear trend by increasing the curvature of the member. Increasing the curvature reduces the shear capacity of GFRP-reinforced curvilinear members. The reduction trend is more pronounced in SSMCFT compared to MCSCT.
- Increasing the axial load level led to a relatively lower flexural strength in a curvilinear GFRP-reinforced member compared to its straight counterpart. A same trend was observed by increasing the concrete strength, sectional thickness, and reinforcement ratio. However, concrete compressive strength has no noticeable effect on the reduction of shear capacity due to curvilinearity effect. In addition, increasing axial load level, sectional thickness, and reinforcement ratio did not follow a general trend in the shear strength reduction because of curvilinearity effect.
- The structural performance of the GFRP-reinforced PCTL segments was satisfactory in terms of crack width and propagation, deflection, and load-carrying capacity. Replacement steel reinforcement with GFRP reinforcement in PCTL segments can effectively eliminate the risk of corrosion while satisfying the structural requirements.
- The experimental evidence and outcomes of this investigation demonstrate the effectiveness of the curvilinear GFRP bars as reinforcement for PCTL segments. The

promising results presented herein open the way for the use of PCTL segments reinforced with the developed curvilinear GFRP bars in major tunneling applications.

10.3. Recommendations for Future Work

Despite the contribution made by this research study, further investigations should be carried out to elaborate the following remarks:

1. A finite element model should be developed using the obtained experimental results to evaluate the influence of various parameters. In addition, the effect of real loading and boundary conditions on the performance of GFRP-reinforced PCTL segments should be investigated using a finite element model.
2. It is advantageous to test the GFRP-reinforced PCTL segments under a test setup with a more similar load and boundary conditions compared to the real applications. In particular, it is interesting to investigate the effect of different axial load levels on the performance of GFRP-reinforced PCTL segments and evaluate the validity of the presented methods to derive interaction diagrams.
3. It is interesting to investigate the effect of curvature radius of GFRP-reinforced PCTL segments by testing the tunnel segment specimens with different curvature radiuses. Then, the validity of the proposed methods to predict flexural and shear capacity of curvilinear GFRP-RC members should be evaluated.
4. In this research program, only one type of FRC was employed in GFRP-reinforced PCTL segments. It is advantageous to investigate the performance of GFRP-reinforced FRC PCTL segments with different types of FRC with different fiber dosages.
5. It is interesting to perform life-cycle cost analysis on GFRP-reinforced PCTL segments and compared it with steel-reinforced counterparts.
6. To improve serviceability issues, it is interesting to investigate feasibility and performance of prestressed GFRP-reinforced PCTL segments.
7. The performance of joints and sections near the joint area in GFRP-reinforced PCTL segments should be investigated experimentally and numerically.

10.4. Conclusions

Les conclusions suivantes peuvent être tirées sur la base des études expérimentales et analytiques menées dans le cadre de ce programme de recherche :

- Le mode de rupture par écrasement du béton a été observé dans l'échantillon renforcé de PRFV avec un rapport de renforcement de 40 % et 100 % supérieur au rapport d'équilibre. Une augmentation supplémentaire du rapport de renforcement des spécimens renforcés de PRFV a changé le mode de rupture en rupture de tension diagonale. Néanmoins, un comportement dominant en flexion a été observé dans tous les spécimens renforcés de PRFV jusqu'à la charge maximale. L'échantillon renforcé d'acier a subi un écrasement du béton après la plastification de l'armature d'acier.
- L'augmentation du taux de renforcement de 44, 85 et 165 % dans l'éprouvette renforcée en PRFV a amélioré la capacité de charge de 16, 16 et 30 %, respectivement, et amélioré la rigidité post-fissuration de 45, 90 et 140 %, respectivement. Tous les spécimens renforcés de PRFV ont satisfait à l'exigence de largeur de fissure de la norme CAN/CSA S6-19 à la charge de service. De plus, la déflexion et la largeur des fissures dans les segments de tunnel renforcés de PRFV pourraient être proches de celles des segments de tunnel renforcés d'acier en fournissant environ 50 % de la rigidité axiale de l'armature en acier.
- L'utilisation de BHR a changé le mode de rupture du cisaillement au cisaillement-flexion dans les segments RTBP renforcés de PRFV avec un rapport de renforcement élevé. De plus, l'utilisation de BHR a amélioré la rigidité post-fissuration et la capacité de charge de 7% et 17%, respectivement. De plus, l'utilisation de BHR a amélioré la charge de fissuration de 18 % sans avoir d'effet notable sur la largeur et l'espacement des fissures.
- L'augmentation du taux de renforcement dans les segments BHR renforcés de PRFV a fait passer le mode de rupture de flexion à cisaillement-flexion. L'augmentation du taux de renforcement de 86 % a amélioré la rigidité post-fissuration et la capacité de charge de 68 % et 17 %, respectivement. De plus, la largeur des fissures à la charge de service a effectivement diminué de 50 % grâce à l'augmentation du taux de renforcement.

- La procédure présentée pour modifier le modèle ACI 440.1R-15 en termes de coefficients de bloc de compression et de contrainte de compression ultime a prédit la résistance à la flexion des spécimens BNR et BHR fabriqués avec des liens fermés avec une erreur inférieure à 1,0 % tout en surestimant que de l'échantillon BHR fabriqué avec des attaches en forme de U de 10 %.
- Parmi les normes nord-américaines évaluées, la CAN/CSA S806-12, R2017 a donné les résultats les plus précis pour prédire la capacité de cisaillement des segments de RTBP en BHR renforcés de PRFV avec une sous-estimation de 7 %. ACI 440.1R-15 a donné les résultats les plus conservateurs. La modification du modèle ACI 440.1R-15 basée sur la méthode présentée dans cette étude a amélioré la précision de la prédiction de 5 %.
- L'utilisation de BF dans l'échantillon renforcé de PRFV avec un rapport de renforcement élevé a changé le mode de rupture de la rupture par cisaillement à l'écrasement du béton suivi d'une rupture par cisaillement. Les largeurs des fissures d'initiation et de service étaient respectivement de 67 % et 57 % plus étroites dans l'échantillon BF, par rapport à son homologue BN. La contribution des fibres pourrait améliorer la capacité de charge, la déflexion à la charge maximale, la déformation maximale en compression du béton et la déformabilité de 12 %, 24 %, 81 % et 71 %, respectivement.
- L'augmentation du taux de renforcement de 86 % dans le segment RTBP en BF renforcé de PRFV a amélioré la charge de fissuration, la rigidité post-fissuration et la charge de pointe de 29 %, 92 % et 31 %, tout en réduisant la largeur initiale des fissures, l'espacement des fissures, et la largeur des fissures à la charge de service de 50 %, 30 % et 57 %, respectivement.
- Deux méthodes ont été présentées pour prédire la capacité de flexion des segments RTBP en BF renforcé de PRFV: une méthode directe basée sur le comportement contrainte-déformation du BF et une méthode simplifiée basée sur ACI 440.1R-15. La capacité de flexion a été prédite avec une erreur inférieure à 2 % et 5 % avec les méthodes directe et simplifiée, respectivement.
- Trois méthodes ont été présentées dans cette étude pour prédire la capacité de cisaillement des segments RTBP en BF renforcé de PRFV. Les méthodes I et II ont fourni des résultats très conservateurs et conservateurs, respectivement, tandis que la

modification des résultats obtenus à partir de la norme CAN/CSA S806-12, R2017 avec la méthode III était moins conservatrice pour prédire la capacité de cisaillement des segments RTBP en BF renforcé de PRFV.

- Le remplacement des tirants fermés par des tirants en U dans les éprouvettes BN a augmenté la largeur de fissure et la déflexion au moment de service moyen de 14 % et 36 %, respectivement, tout en diminuant la charge de pointe de 12 %. La configuration des liens n'a pas eu d'effet notable sur le comportement de fissuration et de déflexion des segments RTBP en BHR renforcé de PRFV. Cependant, le spécimen BHR avec des liens en forme de U avait une capacité de charge inférieure de 9% par rapport au spécimen avec des liens fermés. C'est alors que les segments RTBP en BHR renforcé de PRFV avec des liens en forme de U et fermés ont fourni un comportement structurel similaire.
- L'équation ACI 440.1R-15 prévoyait une capacité de moment de flexion plus élevée que l'équation CAN/CSA S806-12, R2017 pour les charges axiales supérieures à . Les équations ACI 440.1R-15 et CAN/CSA S806-12, R2017 ont surestimé la capacité de moment de flexion des segments renforcés de PRFV testés de 6 % et 19 % (en moyenne), respectivement.
- Les résultats expérimentaux étaient très cohérents avec les résultats analytiques obtenus sur la base de la méthode proposée pour obtenir le diagramme d'interaction charge axiale-moment de flexion à l'étape de service. De plus, l'utilisation de la procédure de contrôle de la rupture par fluage développée sur la base des normes CAN/CSA S806-12, R2017 et ACI 440.1R-15 a donné des résultats prudents de 1 % et 9 % en moyenne pour les éprouvettes testées, respectivement.
- L'augmentation de la résistance à la compression du béton pour améliorer la capacité de flexion axiale était efficace lorsque le niveau de charge axiale était supérieur à $0.15 f_c^{'} A_g$. En revanche, l'augmentation du rapport de renforcement était plus efficace pour améliorer la capacité de flexion axiale aux charges axiales inférieures à $0.15 f_c^{'} A_g$. L'augmentation de l'épaisseur de la section a considérablement augmenté la capacité de flexion axiale à tous les niveaux de charge axiale.

- L'application du moment d'inertie effectif développé pour les éléments curvilignes sur la base du modèle de Bischoff a surestimé la flèche de 20 %, 3 % et 12 % dans les segments RTBP en BN, BHR, and BF renforcé de PRFV, respectivement.
- La précision des méthodologies de prévision de déviation présentées dépend du rapport de ferraillage, de la résistance du béton et du type de béton. Un nouveau modèle a été proposé et validé sur la base des données expérimentales pour considérer l'effet de ces paramètres sur une méthode de prédiction de déviation. Le modèle proposé pourrait prédire la déviation à la charge de service avec une prudence de 2 %.
- L'utilisation du moment d'inertie effectif pour calculer la flèche est une méthode simple avec une prudence acceptable (11 % en moyenne sur les éprouvettes testées). Sa précision dépend cependant de la charge et des conditions aux limites. La méthode proposée est capable de fournir des résultats plus précis que les autres méthodes bien qu'elle nécessite plus d'efforts de calcul. Enfin, l'intégration de la courbure en négligeant le raidissement en traction est une option prudente (41 % en moyenne) lorsqu'un concepteur n'est pas sûr des caractéristiques de raidissement en traction de l'élément.
- La déviation des forces de compression et de traction dans un élément BA curviligne induit des contraintes de traction dans la direction perpendiculaire aux contraintes principales. Ces contraintes dépendent principalement du rayon de courbure et de la quantité de contraintes de compression induites dans la section.
- Négliger la forme curviligne des éléments curvilignes renforcés de PRFV a conduit à une surestimation de 17 % de la capacité de moment de flexion prévue. Cependant, l'utilisation du modèle présenté dans cette étude pour prendre en compte l'effet de curvilinéarité pourrait prédire avec précision la résistance à la flexion des segments de tunnel renforcés de PRFV.
- Les deux modèles de prédiction de la capacité de cisaillement proposés basés sur MCFT (SSMCFT et ISMCFT) ont prédit la capacité de cisaillement avec une conservativité de 28 %. L'utilisation de CSCT a conduit à une surestimation de 5 % dans la prédiction de la capacité de cisaillement des éléments curvilignes en BA renforcés de PRFV. Cependant, le modèle proposé basé sur les modifications du CSCT (MCSCT) a prédit la

capacité de cisaillement des éléments curvilignes en BA renforcés de PRFV avec une conservativité de 10 %.

- La résistance à la flexion des éléments curvilignes renforcés de PRFV a diminué avec une tendance presque linéaire en augmentant la courbure de l'élément. L'augmentation de la courbure réduit la capacité de cisaillement des éléments curvilignes renforcés de PRFV. La tendance à la réduction est plus prononcée dans SSMCFT que dans MCSCT.
- L'augmentation du niveau de charge axiale a entraîné une résistance à la flexion relativement plus faible dans un élément curviligne renforcé en PRFV par rapport à son homologue droit. Une même tendance a été observée en augmentant la résistance du béton, l'épaisseur de la section et le taux de renforcement. Cependant, la résistance à la compression du béton n'a pas d'effet notable sur la réduction de la capacité de cisaillement due à l'effet de curvilinéarité. De plus, l'augmentation du niveau de charge axiale, de l'épaisseur de la section et du rapport de renforcement n'a pas suivi une tendance générale dans la réduction de la résistance au cisaillement en raison de l'effet de curvilinéarité.
- Les performances structurelles des segments en RTBP renforcés de PRFV ont été satisfaisantes en termes de largeur de fissure et de propagation, de déflexion et de capacité de charge. Le renforcement en acier de remplacement avec un renforcement en PRFV dans les segments RTBP peut éliminer efficacement le risque de corrosion tout en satisfaisant aux exigences structurelles.
- Les preuves expérimentales et les résultats de cette enquête démontrent l'efficacité des barres PRFV curvilignes comme renfort pour les segments RTBP. Les résultats prometteurs présentés ici ouvrent la voie à l'utilisation de segments RTBP renforcés avec les barres PRFV curvilignes développées dans les principales applications de tunnelage.

10.5. Recommandations pour des travaux futurs

Malgré l'apport apporté par cette étude de recherche, des investigations complémentaires doivent être menées pour élaborer les remarques suivantes :

1. Un modèle d'éléments finis doit être développé en utilisant les résultats expérimentaux obtenus pour évaluer l'influence de divers paramètres. De plus, l'effet du chargement réel et des conditions aux limites sur les performances des segments de RTBP renforcés de PRFV devrait être étudié à l'aide d'un modèle d'éléments finis.

2. Il est avantageux de tester les segments RTBP renforcés de PRFV dans une configuration de test avec une charge et des conditions aux limites plus similaires par rapport aux applications réelles. En particulier, il est intéressant d'étudier l'effet de différents niveaux de charge axiale sur les performances des segments RTBP renforcés de PRFV et d'évaluer la validité des méthodes présentées pour dériver des diagrammes d'interaction.

3. Il est intéressant d'étudier l'effet du rayon de courbure des segments de RTBP renforcés de PRFV en testant les spécimens de segment de tunnel avec différents rayons de courbure. Ensuite, la validité des méthodes proposées pour prédire la capacité de flexion et de cisaillement des éléments curvilignes en BA renforcés de PRFV doit être évaluée.

4. Dans ce programme de recherche, un seul type de BF a été utilisé dans les segments RTBP renforcés de PRFV. Il est avantageux d'étudier les performances des RTBP en BF renforcé de PRFV avec différents types de BF avec différents dosages de fibres.

5. Il est intéressant d'effectuer une analyse du coût du cycle de vie sur les segments RTBP renforcés de PRFV et de le comparer avec des homologues renforcés d'acier.

6. Pour améliorer les problèmes de service, il est intéressant d'étudier la faisabilité et les performances des segments RTBP précontraints et renforcés de PRFV.

7. La performance des joints et des sections près de la zone de joint dans les segments de RTBP renforcés de PRFV doit être étudiée expérimentalement et numériquement.

REFERENCES

AASHTO (American Association of State Highway and Transportation Officials). 2018. AASHTO LRFD bridge design guide specifications for GFRP–reinforced concrete. 2nd ed. Washington, DC: AASHTO LRFD.

Abbas, S.;Soliman, A. M., and Nehdi, M. L., 2014a. "Experimental Study on Settlement and Punching Behavior of Full-Scale Rc and Sfrc Precast Tunnel Lining Segments." *Engineering structures*, 72, 1-10.

Abbas, S.;Soliman, A. M., and Nehdi, M. L., 2014b. "Mechanical Performance of Reinforced Concrete and Steel Fiber-Reinforced Concrete Precast Tunnel Lining Segments: A Case Study." *ACI Materials Journal*, 111(5), 501.

Abdelkarim, O. I.;Ahmed, E. A.;Mohamed, H. M., and Benmokrane, B., 2019. "Flexural Strength and Serviceability Evaluation of Concrete Beams Reinforced with Deformed GFRP Bars." *Engineering Structures*, 186, 282-296.

Abdul-Salam, B.;Farghaly, A. S., and Benmokrane, B., 2016. "Mechanisms of Shear Resistance of One-Way Concrete Slabs Reinforced with FRP Bars." *Construction and Building materials*, 127, 959-970.

Abed, F.;Al-Mimar, M., and Ahmed, S., 2021. "Performance of BFRP RC Beams Using High Strength Concrete." *Composites Part C: Open Access*, 4, 100107.

ACI Committee 318, 1999, "Building Code Requirements for Structural Concrete (ACI 318-99)," American Concrete Institute, Farmington Hills, MI, 392 pp.

ACI Committee 363, 2010, "Report on High-Strength Concrete (ACI 363R-10)," American Concrete Institute, Farmington Hills, MI, 65 pp.

ACI Committee 440, 2015, "Guide for the Design and Construction of Structural Concrete Reinforced with Fiber-Reinforced Polymer Bars (ACI 440.1R-15)," American Concrete Institute, Farmington Hills, MI, 88 pp.

ACI Committee 440, 2022, "Building Code Requirements for Structural Concrete Reinforced with Glass Fiber-Reinforced Polymer (GFRP) Bars—Code and Commentary (ACI 440.11-22)," American Concrete Institute, Farmington Hills, MI, 260 pp.

ACI Committee 544, 2016, “Report on Design and Construction of Fiber-Reinforced Precast Concrete Tunnel Segments (ACI 544.7R-16),” American Concrete Institute, Farmington Hills, MI, 41 pp.

ACI Committee 544, 2016, “Report on Indirect Method to Obtain Stress-Strain Response of Fiber-Reinforced Concrete (FRC) (ACI 544.8R-16),” American Concrete Institute, Farmington Hills, MI, 22 pp.

ACI Committee 544, 2018, “Guide to Design with Fiber-Reinforced Concrete (ACI 544.4R-18),” American Concrete Institute, Farmington Hills, MI, 44 pp.

ACI Committee 318, 2019, “Building Code Requirements for Structural Concrete (ACI 318-19) and Commentary (ACI 318R-19) ,” American Concrete Institute, Farmington Hills, MI, 624 pp.

ACI Committee 533, 2020, “Guide for Precast Concrete Tunnel Segments (ACI 533.5R-20),” American Concrete Institute, Farmington Hills, MI, 85 pp.

Adam, M. A.;Said, M.;Mahmoud, A. A., and Shanour, A. S., 2015. ″Analytical and Experimental Flexural Behavior of Concrete Beams Reinforced with Glass Fiber Reinforced Polymers Bars,″ *Construction and Building Materials*, 84, 354-366.

French Tunneling and Underground Space Association (AFTES), 1993, “Considerations on the Usual Methods of Tunnel Lining Design (AFTES-WG7),″.

Al-Rubaye, M.;Manalo, A.;Alajarmeh, O.;Ferdous, W.;Lokuge, W.;Benmokrane, B., and Edoo, A., 2020. ″Flexural Behaviour of Concrete Slabs Reinforced with GFRP Bars and Hollow Composite Reinforcing Systems.″ *Composite structures*, 236, 111836.

Alca, N.;Alexander, S. D., and MacGregor, J. G., 1997. ″Effect of Size on Flexural Behavior of High-Strength Concrete Beams.″ *ACI Structural Journal*, 94(1), 59-67.

Alguhi, H., and Tomlinson, D., 2021. ″One-Way Shear Strength of FRP–Reinforced Concrete Members without Stirrups: Design Provision Review.″ *Journal of Composites for Construction*, 25(3), 04021016.

Ali, A. H.;Mohamed, H. M.;Chalioris, C. E., and Deifalla, A., 2021. ″Evaluating the Shear Design Equations of FRP-Reinforced Concrete Beams without Shear Reinforcement.″ *Engineering Structures*, 235, 112017.

Alsayed, S.;Al-Salloum, Y., and Almusallam, T., 2000. "Performance of Glass Fiber Reinforced Plastic Bars as a Reinforcing Material for Concrete Structures." *Composites Part B: Engineering*, 31(6-7), 555-567.

Angelakos, D.;Bentz, E. C., and Collins, M. P., 2001. "Effect of Concrete Strength and Minimum Stirrups on Shear Strength of Large Members." *Structural Journal*, 98(3), 291-300.

Arabshahi, A.;Tavakol, M.;Sabzi, J., and Gharaei-Moghaddam, N., 2022, "Prediction of the Effective Moment of Inertia for Concrete Beams Reinforced with FRP Bars Using an Evolutionary Algorithm." *Proc., Structures*, Elsevier, 684-705.

Arnau Delgado, O., 2012. "Structural Response of Precast Concrete Segmental Tunnel Linings."

Arnau, O., and Molins, C., 2011. "Experimental and Analytical Study of the Structural Response of Segmental Tunnel Linings Based on an in Situ Loading Test. Part 2: Numerical Simulation." *Tunnelling and Underground Space Technology*, 26(6), 778-788.

Arnau, O., and Molins, C., 2012. "Three Dimensional Structural Response of Segmental Tunnel Linings." *Engineering Structures*, 44, 210-221.

Arnau, O., and Molins, C., 2015. "Theoretical and Numerical Analysis of the Three-Dimensional Response of Segmental Tunnel Linings Subjected to Localized Loads." *Tunnelling and Underground Space Technology*, 49, 384-399.

Ashour, S. A., 2000. "Effect of Compressive Strength and Tensile Reinforcement Ratio on Flexural Behavior of High-Strength Concrete Beams." *Engineering Structures*, 22(5), 413-423.

ASTM C39/C39M-21, 2021, "Standard Test Method for Compressive Strength of Cylindrical Concrete Specimens." ASTM International, West Conshohocken, PA, 8 pp.

ASTM C1609-19, 2019, "Standard Test Method for Flexural Performance of Fiber-Reinforced Concrete (Using Beam with Third-Point Loading)." ASTM International, West Conshohocken, PA, 9 pp.

ASTM D7205-21, 2021, "Standard Test Method for Tensile Properties of Fiber Reinforced Polymer Matrix Composite Bars." ASTM International, West Conshohocken, PA, 13 pp.

ASTM 8505-23, 2023, "Standard Specification for Basalt and Glass Fiber Reinforced Polymer (FRP) Bars for Concrete Reinforcement." ASTM International, West Conshohocken, PA, 8 pp.

Ates, U.;Bilgin, N., and Copur, H., 2014. "Estimating Torque, Thrust and Other Design Parameters of Different Type Tbms with Some Criticism to Tbms Used in Turkish Tunneling Projects." *Tunnelling and underground space technology*, 40, 46-63.

Attia, K.;Alnahhal, W.;Elrefai, A., and Rihan, Y., 2019. "Flexural Behavior of Basalt Fiber-Reinforced Concrete Slab Strips Reinforced with BFRP and GFRP Bars." *Composite structures*, 211, 1-12.

Austrian Society for Concrete and Construction Technology, 2011, "Guideline for Concrete Segmental Lining Systems (OVBB 2011).

Avanaki, M. J.;Hoseini, A.;Vahdani, S.;de Santos, C., and de la Fuente, A., 2018. "Seismic Fragility Curves for Vulnerability Assessment of Steel Fiber Reinforced Concrete Segmental Tunnel Linings." *Tunnelling and Underground Space Technology*, 78, 259-274.

Bakouregui, A. S.;Mohamed, H. M.;Yahia, A., and Benmokrane, B., 2021. "Axial Load–Moment Interaction Diagram of Full-Scale Circular Lwscc Columns Reinforced with BFRP and GFRP Bars and Spirals: Experimental and Theoretical Investigations." *Engineering Structures*, 242, 112538.

Barris, C.;Torres, L.;Miàs, C., and Vilanova, I., 2012. "Design of FRP Reinforced Concrete Beams for Serviceability Requirements." *Journal of Civil Engineering and Management*, 18(6), 843-857.

Barris, C.;Torres, L.;Vilanova, I.;Mias, C., and Llorens, M., 2017. "Experimental Study on Crack Width and Crack Spacing for Glass-FRP Reinforced Concrete Beams." *Engineering Structures*, 131, 231-242.

Basaran, B., and Kalkan, I., 2020. "Investigation on Variables Affecting Bond Strength between FRP Reinforcing Bar and Concrete by Modified Hinged Beam Tests." *Composite structures*, 242, 112185.

Bencardino, F.;Rizzuti, L.;Spadea, G., and Swamy, R. N., 2008. "Stress-Strain Behavior of Steel Fiber-Reinforced Concrete in Compression." *Journal of Materials in Civil Engineering*, 20(3), 255-263.

Benmokrane, B.;Chaallal, O., and Masmoudi, R., 1996. "Flexural Response of Concrete Beams Reinforced with FRP Reinforcing Bars." *ACI Structural Journal*, 93(1), 46-55.

Benmokrane, B.;Wang, P.;Ton-That, T. M.;Rahman, H., and Robert, J.-F., 2002. "Durability of Glass Fiber-Reinforced Polymer Reinforcing Bars in Concrete Environment." *Journal of Composites for Construction*, 6(3), 143-153.

Bentz, E. C.;Vecchio, F. J., and Collins, M. P., 2006. "Simplified Modified Compression Field Theory for Calculating Shear Strength of Reinforced Concrete Elements." *ACI Structural Journal*, 103(4), 614.

Bilotta, E., 2017, "Behaviour of Segmental Tunnel Lining under Static and Dynamic Loads." Univ. of Naples Federico II.

Bischoff, P., 2007. "Deflection Calculation Using an Effective Moment Inertia for Frc." *Special Publication*, 248, 17-30.

Bischoff, P.;Gross, S., and Ospina, C., 2009. "The Story Behind Proposed Changes to Aci 440 Deflection Requirements for Frp-Reinforced Concrete." *Serviceability of Concrete Members Reinforced with Internal/External FRP Reinforcement, SP-264, C. Ospina, P. Bischoff, and T. Alkhardaji, eds. American Concrete Institute, Farmington Hills, MI*, 53-76.

Bischoff, P. H., 2005. "Reevaluation of Deflection Prediction for Concrete Beams Reinforced with Steel and Fiber Reinforced Polymer Bars." *Journal of Structural Engineering*, 131(5), 752-767.

Bischoff, P. H., 2020. "Comparison of Existing Approaches for Computing Deflection of Reinforced Concrete." *ACI Structural Journal*, 117(1).

Bischoff, P. H., and Gross, S. P., 2011a. "Design Approach for Calculating Deflection of Frp-Reinforced Concrete." *Journal of Composites for Construction*, 15(4), 490-499.

Bischoff, P. H., and Gross, S. P., 2011b. "Equivalent Moment of Inertia Based on Integration of Curvature." *Journal of Composites for Construction*, 15(3), 263-273.

Bischoff, P. H., and Scanlon, A., 2007. "Effective Moment of Inertia for Calculating Deflections of Concrete Members Containing Steel Reinforcement and Fiber-Reinforced Polymer Reinforcement." *ACI Structural Journal*, 104(1), 68.

Blom, C. B. M., 2004. "Design Philosophy of Concrete Linings for Tunnels in Soft Soils."

Boresi, A. P.;Sidebottom, O. M., and Saunders, H., 1988. "Advanced Mechanics of Materials (4th Ed.)." *J. Vib. Acoust*, 110(2), 256-257.

Branson, D. E.,1963, "Instantaneous and Time-Dependent Deflections of Simple and Continuous Reinforced Concrete Beams." Alabama. State Highway Department.

Campana, S.;Fernández Ruiz, M., and Muttoni, A., 2014. "Shear Strength of Arch-Shaped Members without Transverse Reinforcement." *ACI Structural Journal*, 111(3).

Canadian Standards Association (CSA), 2019, "Canadian Highway Bridge Design Code (CSA S6-19)," CSA Group, Mississauga, ON, Canada, 1185 pp.

Canadian Standards Association (CSA), 2017 (Reapproved), "Design and Construction of Building Components with Fiber Reinforced Polymers (CAN/CSA S806-12, R2017)," CSA Group, Mississauga, ON, Canada, 187 pp.

Canadian Standards Association (CSA), 2019, "Design of Concrete Structures (CAN/CSA-A23.3-19)," CSA Group, Mississauga, ON, Canada,

Caratelli, A.;Meda, A., and Rinaldi, Z., 2012. "Design According to Mc2010 of a Fibre-Reinforced Concrete Tunnel in Monte Lirio, Panama." *Structural Concrete*, 13(3), 166-173.

Caratelli, A.;Meda, A.;Rinaldi, Z., and Romualdi, P., 2011. "Structural Behaviour of Precast Tunnel Segments in Fiber Reinforced Concrete." *Tunnelling and Underground Space Technology*, 26(2), 284-291.

Caratelli, A.;Meda, A.;Rinaldi, Z., and Spagnuolo, S., 2016. "Precast Tunnel Segments with GFRP Reinforcement." *Tunnelling and underground space technology*, 60, 10-20.

Caratelli, A.;Meda, A.;Rinaldi, Z.;Spagnuolo, S., and Maddaluno, G., 2017. "Optimization of GFRP Reinforcement in Precast Segments for Metro Tunnel Lining." *Composite structures*, 181, 336-346.

Cavagnis, F.;Ruiz, M. F., and Muttoni, A., 2015. "Shear Failures in Reinforced Concrete Members without Transverse Reinforcement: An Analysis of the Critical Shear Crack Development on the Basis of Test Results." *Engineering Structures*, 103, 157-173.

Cavagnis, F.;Ruiz, M. F., and Muttoni, A., 2018. "A Mechanical Model for Failures in Shear of Members without Transverse Reinforcement Based on Development of a Critical Shear Crack." *Engineering Structures*, 157, 300-315.

Cavagnis, F.;Simões, J. T.;Ruiz, M. F., and Muttoni, A., 2020. "Shear Strength of Members without Transverse Reinforcement Based on Development of Critical Shear Crack." *ACI Structural Journal*, 117(1).

Chang, K., and Seo, D., 2012. "Behavior of One-Way Concrete Slabs Reinforced with GFRP Bars." *Journal of Asian Architecture and Building Engineering*, 11(2), 351-358.

Chi, Y.;Xu, L., and Zhang, Y., 2014. "Experimental Study on Hybrid Fiber–Reinforced Concrete Subjected to Uniaxial Compression." *Journal of Materials in Civil Engineering*, 26(2), 211-218.

Cignitti, F.;Sorge, R.;Meda, A.;Nerilli, F., and Rinaldi, Z., 2012, "Numerical Analysis of Precast Tunnel Segmental Lining Supported by Full-Scale Experimental Tests." *Proc., Geotechnical Aspects of Underground Construction in Soft Ground-Proceedings of the 7th International Symposium on Geotechnical Aspects of Underground Construction in Soft Ground*, 481-487.

Italian National Research Council (CNR), 2006. Guidelines for the Design, Construction and Production Control of Fibre Reinforced Concrete Structures (CNR DT 204/2006) ".

International Federation for Structural Concrete (fib), 2010, Model Code for Concrete Strcutures (MC 2010) ".

Collins, M. P., and Mitchell, D.,1997, *Prestressed Concrete Structures*, Response Publications.

Conforti, A.;Tiberti, G.;Plizzari, G. A.;Caratelli, A., and Meda, A., 2017. "Precast Tunnel Segments Reinforced by Macro-Synthetic Fibers." *Tunnelling and Underground Space Technology*, 63, 1-11.

Conforti, A.;Trabucchi, I.;Tiberti, G.;Plizzari, G. A.;Caratelli, A., and Meda, A., 2019. "Precast Tunnel Segments for Metro Tunnel Lining: A Hybrid Reinforcement Solution Using Macro-Synthetic Fibers." *Engineering structures*, 199, 109628.

Darwin, D.;Dolan, C. W., and Nilson, A. H.,2016, *Design of Concrete Structures*, McGraw-Hill Education New York, NY, USA:.

Dastjerdy, B.;Hasanpour, R., and Chakeri, H., 2018. "Cracking Problems in the Segments of Tabriz Metro Tunnel: A 3d Computational Study." *Geotechnical and Geological Engineering*, 36(4), 1959-1974.

de Almeida, I. R., 1991. "Resistance of High Strength Concrete to Sulfate Attack: Soaking and Drying Test." *Special Publication*, 126, 1073-1092.

De la Fuente, A.;Pujadas, P.;Blanco, A., and Aguado, A., 2012. "Experiences in Barcelona with the Use of Fibres in Segmental Linings." *Tunnelling and Underground Space Technology*, 27(1), 60-71.

Deng, Z.;Liu, X.;Yang, X.;Liang, N.;Yan, R.;Chen, P.;Miao, Q., and Xu, Y., 2021. "A Study of Tensile and Compressive Properties of Hybrid Basalt-Polypropylene Fiber-Reinforced Concrete under Uniaxial Loads." *Structural Concrete*, 22(1), 396-409.

Dev, A.;Chellapandian, M., and Prakash, S. S., 2020. "Effect of Macrosynthetic and Hybrid Fibers on Shear Behavior of Concrete Beams Reinforced with GFRP Bars." *Journal of Bridge Engineering*, 25(7), 04020031.

Di Carlo, F.;Meda, A., and Rinaldi, Z., 2016. "Design Procedure for Precast Fibre-Reinforced Concrete Segments in Tunnel Lining Construction." *Structural Concrete*, 17(5), 747-759.

Di Prisco, M.;Colombo, M., and Dozio, D., 2013. "Fibre-Reinforced Concrete in Fib Model Code 2010: Principles, Models and Test Validation." *Structural Concrete*, 14(4), 342-361.

Di Prisco, M.;Plizzari, G., and Vandewalle, L., 2010. "MC2010: Overview on the Shear Provisions for FRC." *fib Bulletin*, 57, 61-75.

Ding, Y.;Liu, H.;Pacheco-Torgal, F., and Jalali, S., 2011. "Experimental Investigation on the Mechanical Behaviour of the Fiber Reinforced High-Performance Concrete Tunnel Segment." *Composite Structures*, 93(4), 1284-1289.

Ding, Y.;Ning, X.;Zhang, Y.;Pacheco-Torgal, F., and Aguiar, J., 2014. "Fibres for Enhancing of the Bond Capacity between GFRP Rebar and Concrete." *Construction and Building Materials*, 51, 303-312.

El-Nemr, A.;Ahmed, E. A., and Benmokrane, B., 2013. "Flexural Behavior and Serviceability of Normal-and High-Strength Concrete Beams Reinforced with Glass Fiber-Reinforced Polymer Bars." *ACI Structural Journal*, 110(6).

El-Nemr, A.;Ahmed, E. A.;El-Safty, A., and Benmokrane, B., 2018. "Evaluation of the Flexural Strength and Serviceability of Concrete Beams Reinforced with Different Types of GFRP Bars." *Engineering Structures*, 173, 606-619.

El-Sayed, A.;El-Salakawy, E., and Benmokrane, B., 2005. "Shear Strength of One-Way Concrete Slabs Reinforced with Fiber-Reinforced Polymer Composite Bars." *Journal of Composites for Construction*, 9(2), 147-157.

El-Sayed, A. K.;El-Salakawy, E. F., and Benmokrane, B., 2006. "Shear Capacity of High-Strength Concrete Beams Reinforced with Frp Bars." *ACI Materials Journal*, 103(3), 383.

Esfahani, M. R.;Rakhshanimehr, M., and Mousavi, S. R., 2013. "Bond Strength of Lap-Spliced GFRP Bars in Concrete Beams." *Journal of Composites for Construction*, 17(3), 314-323.

Fabozzi, S., 2017, "Behaviour of Segmental Tunnel Lining under Static and Dynamic Loads." PhD Thesis, University of Naples Federico II, Naples, Italy.

Fernández Ruiz, M.;Plumey, S., and Muttoni, A., 2010. "Interaction between Bond and Deviation Forces in Spalling Failures of Arch-Shaped Members without Transverse Reinforcement." *ACI Structural Journal*, 107, 346-354.

Gao, D.;Benmokrane, B., and Masmoudi, R., 1998. "A Calculating Method of Flexural Properties of Frp-Reinforced Concrete Beam: Part 1: Crack Width and Deflection." *Technical Rep*.

Ghafari, N., 2013. "Corrosion Control in Underground Concrete Structures Using Double Waterproofing Shield System (Dws)." *International Journal of Mining Science and Technology*, 23(4), 603-611.

Goldston, M.;Remennikov, A.;Saleh, Z., and Sheikh, M. N., 2019, "Experimental Investigations on the Behavior of GFRP Bar Reinforced Hsc and Uhsc Beams under Static and Impact Loading." *Proc., Structures*, Elsevier, 109-123.

Goldston, M.;Remennikov, A., and Sheikh, M. N., 2017. "Flexural Behaviour of GFRP Reinforced High Strength and Ultra High Strength Concrete Beams." *Construction and Building materials*, 131, 606-617.

Gong, C.;Ding, W.;Mosalam, K. M.;Günay, S., and Soga, K., 2017. "Comparison of the Structural Behavior of Reinforced Concrete and Steel Fiber Reinforced Concrete Tunnel Segmental Joints." *Tunnelling and Underground Space Technology*, 68, 38-57.

Gross, S. P.;Yost, J. R.;Dinehart, D. W.;Svensen, E., and Liu, N. (2003). "Shear Strength of Normal and High Strength Concrete Beams Reinforced with GFRP Bars." *High Performance Materials in Bridges*, 426-437.

Gudonis, E.;Timinskas, E.;Gribniak, V.;Kaklauskas, G.;Arnautov, A. K., and Tamulėnas, V., 2013. "FRP Reinforcement for Concrete Structures: State-of-the-Art Review of Application and Design." *Engineering Structures and Technologies*, 5(4), 147-158.

Habeeb, M., and Ashour, A. F., 2008. "Flexural Behavior of Continuous GFRP Reinforced Concrete Beams." *Journal of Composites for Construction*, 12(2), 115-124.

Hadhood, A.;Mohamed, H. M., and Benmokrane, B., 2017. "Failure Envelope of Circular Concrete Columns Reinforced with Glass Fiber-Reinforced Polymer Bars and Spirals." *ACI Structural Journal*, 114(6), 1417-1428.

Hadhood, A.;Mohamed, H. M., and Benmokrane, B., 2018. "Assessing Stress-Block Parameters in Designing Circular High-Strength Concrete Members Reinforced with FRP Bars." *Journal of Structural Engineering*, 144(10), 04018182.

Hassoun, M. N., and Al-Manaseer, A., 2020, *Structural Concrete: Theory and Design*, John wiley & sons.

Hatami, F., and Dehghani, A., 2021. "Flexural Behavior of One-Way Concrete Slabs by Hybrid Glass Fiber-Reinforced Polymer-Steel Reinforcements." *ACI Structural Journal*, 118(1).

Heilegger, R., and Beil, A., 2020. "Full Automated Tunnel Segment Production System. A Case Study." *Tunnel Boring Machines*, CRC Press, 215-222.

Hosseini, S.-A.;Nematzadeh, M., and Chastre, C., 2021. "Prediction of Shear Behavior of Steel Fiber-Reinforced Rubberized Concrete Beams Reinforced with Glass Fiber-Reinforced Polymer (GFRP) Bars." *Composite structures*, 256, 113010.

Hosseini, S. M.;Mousa, S.;Mohamed, H. M., and Benmokrane, B., 2022a. "Structural Behavior of Precast Reinforced Concrete Tunnel Segments with Glass Fiber-Reinforced Polymer Bars and Ties under Bending Load." *ACI Structural Journal*, 119(1), 307-319.

Hosseini, S. M.;Mousa, S.;Mohamed, H. M.;Eslami, A., and Benmokrane, B., 2022b. "Experimental and Analytical Study on Precast High-Strength Concrete Tunnel Lining Segments Reinforced with Gfrp Bars." *Journal of Composites for Construction*, 26(5), 04022062.

Hoult, N.;Sherwood, E.;Bentz, E. C., and Collins, M. P., 2008. "Does the Use of FRP Reinforcement Change the One-Way Shear Behavior of Reinforced Concrete Slabs?" *Journal of Composites for Construction*, 12(2), 125.

Hussein, A., and Marzouk, H., 2000. "Behavior of High-Strength Concrete under Biaxial Stresses." *ACI Materials Journal*, 97(1), 27-36.

ISIS Canada Research Network, 2007, "Reinforced Concrete Structures with Fibre Reinforced Polymers *ISIS Manual No. 3*, University of Manitoba, Winnipeg, MB, Canada,

Issa, M. S.;Metwally, I. M., and Elzeiny, S. M., 2011. "Influence of Fibers on Flexural Behavior and Ductility of Concrete Beams Reinforced with GFRP Rebars." *Engineering Structures*, 33(5), 1754-1763.

Jin-long, L.;Hamza, O.;Davies-Vollum, K. S., and Jie-qun, L., 2018. "Repairing a Shield Tunnel Damaged by Secondary Grouting." *Tunnelling and underground space technology*, 80, 313-321.

Johnson, D. T., 2014, "Investigation of Glass Fibre Reinforced Polymer (GFRP) Bars as Internal Reinforcement for Concrete Structures." Ph.D. Thesis, University of Toronto.

Japan Society of Civil Engineers (JSCE), 2007, "Standard Specifications for Tunneling: Shield Tunnels".

Karimipour, A.;Edalati, M., and de Brito, J., 2021. "Biaxial Mechanical Behaviour of Polypropylene Fibres Reinforced Self-Compacting Concrete." *Construction and Building Materials*, 278, 122416.

Kasper, T.;Edvardsen, C.;Wittneben, G., and Neumann, D., 2008. "Lining Design for the District Heating Tunnel in Copenhagen with Steel Fibre Reinforced Concrete Segments." *Tunnelling and Underground Space Technology*, 23(5), 574-587.

Kasper, T., and Meschke, G., 2006. "On the Influence of Face Pressure, Grouting Pressure and Tbm Design in Soft Ground Tunnelling." *Tunnelling and underground space technology*, 21(2), 160-171.

Kassem, C.;Farghaly, A. S., and Benmokrane, B., 2011. "Evaluation of Flexural Behavior and Serviceability Performance of Concrete Beams Reinforced with FRP Bars." *Journal of Composites for Construction*, 15(5), 682-695.

Khaloo, A.;Moradi, H.;Kazemian, A., and Shekarchi, M., 2020. "Experimental Investigation on the Behavior of RC Arches Strengthened by GFRP Composites." *Construction and Building materials*, 235, 117519.

Khavaran, A., 2019, "Investigation of Shear-Critical One-Way Concrete Slabs Internally Reinforced with GFRP Bars." PhD dissertation, University of Toronto, Canada.

Kim, B.;Doh, J.-H.;Yi, C.-K., and Lee, J.-Y., 2013. "Effects of Structural Fibers on Bonding Mechanism Changes in Interface between GFRP Bar and Concrete." *Composites Part B: Engineering*, 45(1), 768-779.

Kim, B., and Lee, J.-Y., 2019. "Resistance of Interfacial Debonding Failure of GFRP Bars Embedded in Concrete Reinforced with Structural Fibers under Cycling Loads." *Composites Part B: Engineering*, 156, 201-211.

Kupfer, H.;Hilsdorf, H. K., and Rusch, H., 1969, "Behavior of Concrete under Biaxial Stresses." *Proc., Journal Proceedings*, 656-666.

Lau, D., and Pam, H. J., 2010. "Experimental Study of Hybrid FRP Reinforced Concrete Beams." *Engineering Structures*, 32(12), 3857-3865.

Lee, J.-H., 2017. "Influence of Concrete Strength Combined with Fiber Content in the Residual Flexural Strengths of Fiber Reinforced Concrete." *Composite structures*, 168, 216-225.

Lee, J.-H.;Cho, B., and Choi, E., 2017. "Flexural Capacity of Fiber Reinforced Concrete with a Consideration of Concrete Strength and Fiber Content." *Construction and Building materials*, 138, 222-231.

Lee, J.-H.;Cho, B.;Choi, E., and Kim, Y.-H., 2016. "Experimental Study of the Reinforcement Effect of Macro-Type High Strength Polypropylene on the Flexural Capacity of Concrete." *Construction and Building materials*, 126, 967-975.

Li, C.;Chen, Q.;Wang, R.;Wu, M., and Jiang, Z., 2020. "Corrosion Assessment of Reinforced Concrete Structures Exposed to Chloride Environments in Underground Tunnels: Theoretical Insights and Practical Data Interpretations." *Cement and Concrete Composites*, 112, 103652.

Liao, L.;de la Fuente, A.;Cavalaro, S., and Aguado, A., 2015. "Design of Frc Tunnel Segments Considering the Ductility Requirements of the Model Code 2010." *Tunnelling and Underground Space Technology*, 47, 200-210.

Liao, L.;de la Fuente, A.;Cavalaro, S., and Aguado, A., 2016. "Design Procedure and Experimental Study on Fibre Reinforced Concrete Segmental Rings for Vertical Shafts." *Materials & Design*, 92, 590-601.

Liu, X.;Bai, Y.;Yuan, Y., and Mang, H. A., 2016. "Experimental Investigation of the Ultimate Bearing Capacity of Continuously Jointed Segmental Tunnel Linings." *Structure and Infrastructure Engineering*, 12(10), 1364-1379.

Löfgren, I.,2005, *Fibre-Reinforced Concrete for Industrial Construction-a Fracture Mechanics Approach to Material Testing and Structural Analysis*, Chalmers University of Technology.

Lu, C., Cai, Q., Xu, K., Sha, X. and Yan, Y., 2022, September. Comparison of flexural behaviors between plain and steel-fiber-reinforced concrete beams with hybrid GFRP and steel bars. *Structures* 43, 1-11.

Maidl, B., Herrenknecht, M., Maidl, U. and Wehrmeyer, G., 2011. *Mechanised shield tunnelling*. John Wiley & Sons.

Mansur, M.;Chin, M., and Wee, T., 1997. "Flexural Behavior of High-Strength Concrete Beams." *Structural Journal*, 94(6), 663-674.

Masmoudi, R.;Theriault, M., and Benmokrane, B., 1998. "Flexural Behavior of Concrete Beams Reinforced with Deformed Fiber Reinforced Plastic Reinforcing Rods." *Structural Journal*, 95(6), 665-676.

Meda, A.;Rinaldi, Z.;Caratelli, A., and Cignitti, F., 2016. "Experimental Investigation on Precast Tunnel Segments under Tbm Thrust Action." *Engineering Structures*, 119, 174-185.

Meda, A.;Rinaldi, Z.;Spagnuolo, S.;De Rivaz, B., and Giamundo, N., 2019. "Hybrid Precast Tunnel Segments in Fiber Reinforced Concrete with Glass Fiber Reinforced Bars." *Tunnelling and underground space technology*, 86, 100-112.

Meng, G.;Gao, B.;Zhou, J.;Cao, G., and Zhang, Q., 2016. "Experimental Investigation of the Mechanical Behavior of the Steel Fiber Reinforced Concrete Tunnel Segment." *Construction and Building Materials*, 126, 98-107.

Michaluk, C. R.;Rizkalla, S. H.;Tadros, G., and Benmokrane, B., 1998. "Flexural Behavior of One-Way Concrete Slabs Reinforced by Fiber Reinforced Plastic Reinforcements." *Structural Journal*, 95(3), 353-365.

Molins, C., and Arnau, O., 2011. "Experimental and Analytical Study of the Structural Response of Segmental Tunnel Linings Based on an in Situ Loading Test.: Part 1: Test Configuration and Execution." *Tunnelling and Underground Space Technology*, 26(6), 764-777.

Morgan, H., 1961. "A Contribution to the Analysis of Stress in a Circular Tunnel." *Geotechnique*, 11(1), 37-46.

Mostofinejad, D.;Hosseini, S. M.;Tehrani, B. N., and Hosseinian, S. M., 2021. "Empirical Models for Prediction of Frost Resistance of Normal-and High-Strength Concretes." *Iranian Journal of Science and Technology, Transactions of Civil Engineering*, 1-25.

Mota, C.;Alminar, S., and Svecova, D., 2006. "Critical Review of Deflection Formulas for FRP-RC Members." *Journal of Composites for Construction*, 10(3), 183-194.

Mousa, S.;Mohamed, H. M., and Benmokrane, B., 2019a. "Cracking and Crack Control in Circular Concrete Bridge Members Reinforced with Fiber-Reinforced Polymer Bars." *Journal of Bridge Engineering*, 24(1), 04018108.

Mousa, S.;Mohamed, H. M., and Benmokrane, B., 2019b. "Deflection Prediction Methodology for Circular Concrete Members Reinforced with Fiber-Reinforced Polymer Bars." *ACI Structural Journal*, 116(2), 279-293.

Mousa, S.;Mohamed, H. M., and Benmokrane, B., 2019c. "Strength and Deformability Aspects of Circular Concrete Members Reinforced with Hybrid Carbon-Frp and Glass-FRP under Flexure." *Journal of Composites for Construction*, 23(2), 04019005.

Mousa, S.;Mohamed, H. M.;Benmokrane, B., and Nanni, A., 2020. "Flexural Behavior of Long-Span Square Reinforced Concrete Members with Uniformly Distributed Fiber-Reinforced Polymer Bars." *ACI Structural Journal*.

Mousavi, S. R., and Esfahani, M. R., 2012. "Effective Moment of Inertia Prediction of FRP-Reinforced Concrete Beams Based on Experimental Results." *Journal of Composites for Construction*, 16(5), 490-498.

Muttoni, A., and Fernández Ruiz, M., 2008. "Shear Strength of Members without Transverse Reinforcement as Function of Critical Shear Crack Width." *ACI Structural Journal*, 105, 163-172.

Naaman, A., and Jeong, M., 1995, "45 Structural Ductility of Concrete Beams Prestressed with FRP Tendons." *Proc., Non-Metallic (FRP) Reinforcement for Concrete Structures: Proceedings of the Second International RILEM Symposium*, CRC Press, 379.

Nanni, A., De Luca, A. and Zadeh, H., 2014. *Reinforced concrete with FRP bars Mechanics and design*, pp. 978.

Nehdi, M. L.;Abbas, S., and Soliman, A. M., 2015. "Exploratory Study of Ultra-High Performance Fiber Reinforced Concrete Tunnel Lining Segments with Varying Steel Fiber Lengths and Dosages." *Engineering structures*, 101, 733-742.

Nelissen, L., 1972. "Biaxial Testing of Normal Concrete." *HERON, 18 (1), 1972*.

Ng, P. L.;Gribniak, V.;Jakubovskis, R., and Rimkus, A., 2019. "Tension Stiffening Approach for Deformation Assessment of Flexural Reinforced Concrete Members under Compressive Axial Load." *Structural Concrete*, 20(6), 2056-2068.

Nigro, E.;Bilotta, A.;Cefarelli, G.;Manfredi, G., and Cosenza, E., 2012, "Flexural Tests on GFRP RC Slabs: Experimental Results and Numerical Simulations." *Proc., 6th International Conference on Bridge Maintenance, Safety and Management*, CRC Press/Balkema, Taylor & Francis group Stresa, Lake Maggiore, Italy.

Ospina, C. E., and Bakis, C. E., 2007. "Indirect Flexural Crack Control of Concrete Beams and One-Way Slabs Reinforced with FRP Bars." *Proceedings of FRPRCS*, 8.

Ozbakkaloglu, T., and Saatcioglu, M., 2004. "Rectangular Stress Block for High-Strength Concrete." *ACI Structural Journal*, 101(4), 475-483.

Park, R., and Paulay, T.,1991, *Reinforced Concrete Structures*, John Wiley & Sons.

Patil, G. M.;Chellapandian, M., and Prakash, S. S., 2020. "Effectiveness of Hybrid Fibers on Flexural Behavior of Concrete Beams Reinforced with Glass Fiber-Reinforced Polymer Bars." *ACI Structural Journal*, 117(5).

Plizzari, G., and Tiberti, G., 2006. "Steel Fibers as Reinforcement for Precast Tunnel Segments." *Tunnelling and Underground Space Technology*, 21(3), 438-439.

Plizzari, G., and Tiberti, G., 2007, "Structural Behavior of SFRC Tunnel Segments." *Proc., Proceedings of the 6th international conference on fracture mechanics of concrete and concrete structures*, 17-22.

Poh, J.;Tan, K.;Peterson, G., and Wen, D., 2005, "Structural Testing of Steel Fibre Reinforced Concrete (SFRC) Tunnel Lining Segments in Singapore." Report.

Protchenko, K.;Leśniak, P.;Szmigiera, E., and Urbański, M., 2021. "New Model for Analytical Predictions on the Bending Capacity of Concrete Elements Reinforced with FRP Bars." *Materials*, 14(3), 693.

Rasheed, H. A.;Nayal, R., and Melhem, H., 2004. "Response Prediction of Concrete Beams Reinforced with FRP Bars." *Composite structures*, 65(2), 193-204.

Razaqpur, A.;Svecova, D., and Cheung, M. S., 2000. "Rational Method for Calculating Deflection of Fiber-Reinforced Polymer Reinforced Beams." *Structural Journal*, 97(1), 175-184.

Razaqpur, A. G., and Isgor, O. B., 2006. "Proposed Shear Design Method for FRP-Reinforced Concrete Members without Stirrups." *ACI Structural Journal*, 103(1), 93.

Razaqpur, A. G., and Spadea, S., 2015. "Shear Strength of FRP Reinforced Concrete Members with Stirrups." *Journal of Composites for Construction*, 19(1), 04014025.

Robert, M., and Benmokrane, B., 2013. "Combined Effects of Saline Solution and Moist Concrete on Long-Term Durability of GFRP Reinforcing Bars." *Construction and Building materials*, 38, 274-284.

Ruiz, M. F.;Muttoni, A., and Sagaseta, J., 2015. "Shear Strength of Concrete Members without Transverse Reinforcement: A Mechanical Approach to Consistently Account for Size and Strain Effects." *Engineering Structures*, 99, 360-372.

Sadeghian, V., and Vecchio, F., 2018. "The Modified Compression Field Theory: Then and Now." *ACI Struct J, Special Publication (SP-328: Shear in Structural Concrete)*, 3.1-3.20.

Salah-Eldin, A.;Mohamed, H. M., and Benmokrane, B., 2019. "Axial–Flexural Performance of High-Strength-Concrete Bridge Compression Members Reinforced with Basalt-FRP Bars and Ties: Experimental and Theoretical Investigation." *Journal of Bridge Engineering*, 24(7), 04019069.

Scanlon, A., and Bischoff, P. H., 2008. "Shrinkage Restraint and Loading History Effects on Deflections of Flexural Members." *ACI Structural Journal*, 105(4), 498.

Schnütgen, B., 2003. "Design of Precast Steel Fibre Reinforced Tunnel Elements." *Proceedings of the RILEM TC*, 145-152.

Shayanfar, M. A.;Mahyar, P.;Jafari, A., and Mohtadinia, M., 2017. "Classification of Precast Concrete Segments Damages During Production and Transportation in Mechanized Shield Tunnels of Iran." *Civil Engineering Journal*, 3(6), 412-426.

Shi, F.;Pham, T. M.;Hao, H., and Hao, Y., 2020. "Post-Cracking Behaviour of Basalt and Macro Polypropylene Hybrid Fibre Reinforced Concrete with Different Compressive Strengths." *Construction and Building materials*, 262, 120108.

Sika Group, 2019, "Product Data Sheet: Sika® Fibermesh®-150 F, Monofilament Polypropylene Fibres for Explosive Spalling Protection." Sika Group, Zurich, Switzerland.

Sivagamasundari, R., and Kumaran, G., 2008. "A Comparative Study on the Flexural Behaviour of One-Way Concrete Slabs Reinforced with GFRP Reinforcements and Conventional Reinforcements When Subjected to Monotonic and Repeated Loading." *The Open Civil Engineering Journal*, 2(1).

Soranakom, C., and Mobasher, B., 2007. "Closed-Form Solutions for Flexural Response of Fiber-Reinforced Concrete Beams." *Journal of engineering mechanics*, 133(8), 933-941.

Spagnuolo, S.;Meda, A.;Rinaldi, Z., and Nanni, A., 2017. "Precast Concrete Tunnel Segments with GFRP Reinforcement." *Journal of Composites for Construction*, 21(5), 04017020.

Spagnuolo, S.;Meda, A.;Rinaldi, Z., and Nanni, A., 2018. "Curvilinear GFRP Bars for Tunnel Segments Applications." *Composites Part B: Engineering*, 141, 137-147.

Sun, Q., Jin, Q., Gao, Y., Li, H. and Cao, Y., 2021. Flexural behavior of PVA-FRC GFRP reinforced concrete beams. *Polymer Composites*, 42(7), pp.3331-3348.

Tasuji, M. E., and Nilson, A. H., 1978, "Stress-Strain Response and Fracture of Concrete in Biaxial Loading." *Proc., Journal Proceedings*, 306-312.

Tasuji, M. E.;Slate, F. O., and Nilson, A. H., 1978, "Stress-Strain Response and Fracture of Concrete in Biaxial Loading." *Proc., Journal Proceedings*, 306-312.

Tehrani, B. N.;Mostofinejad, D., and Hosseini, S. M., 2019. "Experimental and Analytical Study on Flexural Strengthening of RC Beams Via Prestressed EBROG CFRP Plates." *Engineering Structures*, 197, 109395.

Tengilimoglu, O., 2019, "An Experimental Study to Investigate the Possibility of Using Macro-Synthetic Fibers in Precast Tunnel Segments " M.Sc. Thesis, Middle East Technical University, Ankara, Turkey.

Tengilimoglu, O., and Akyuz, U., 2020. "Experimental Study on Hybrid Precast Tunnel Segments Reinforced by Macro-Synthetic Fibres and Glass Fibre Reinforced Polymer Bars." *Tunnelling and underground space technology*, 106, 103612.

Theriault, M., and Benmokrane, B., 1998. "Effects of FRP Reinforcement Ratio and Concrete Strength on Flexural Behavior of Concrete Beams." *Journal of Composites for Construction*, 2(1), 7-16.

Todeschini, C. E.;Bianchini, A. C., and Kesler, C. E., 1964, "Behavior of Concrete Columns Reinforced with High Strength Steels." *Proc., Journal Proceedings*, 701-716.

Toutanji, H. A., and Saafi, M., 2000. "Flexural Behavior of Concrete Beams Reinforced with Glass Fiber-Reinforced Polymer (GFRP) Bars." *Structural Journal*, 97(5), 712-719.

Vandewalle, L., 2000. "Cracking Behaviour of Concrete Beams Reinforced with a Combination of Ordinary Reinforcement and Steel Fibers." *Materials and structures*, 33(3), 164-170.

Vecchio, F. J., and Collins, M. P., 1986. "The Modified Compression-Field Theory for Reinforced Concrete Elements Subjected to Shear." *ACI J.*, 83(2), 219-231.

Vijay, P., and GangaRao, H. V., 2001. "Bending Behavior and Deformability of Glass Fiber-Reinforced Polymer Reinforced Concrete Members." *Structural Journal*, 98(6), 834-842.

Waal, R. d., 1999. "Steel Fibre Reinforced Tunnel Segments for the Application in Shield Driven Tunnel Linings." *PhD Thesis, Delft University of Technology, The Netherlands*.

Wang, H., and Belarbi, A., 2013. "Flexural Durability of FRP Bars Embedded in Fiber-Reinforced-Concrete." *Construction and Building materials*, 44, 541-550.

Won, J.-P.;Park, C.-G.;Kim, H.-H.;Lee, S.-W., and Jang, C.-I., 2008. "Effect of Fibers on the Bonds between FRP Reinforcing Bars and High-Strength Concrete." *Composites Part B: Engineering*, 39(5), 747-755.

Yan, F., and Lin, Z., 2017. "Bond Durability Assessment and Long-Term Degradation Prediction for GFRP Bars to Fiber-Reinforced Concrete under Saline Solutions." *Composite structures*, 161, 393-406.

Yan, Z.-g.;Shen, Y.;Zhu, H.-h.;Li, X.-j., and Lu, Y., 2015. "Experimental Investigation of Reinforced Concrete and Hybrid Fibre Reinforced Concrete Shield Tunnel Segments Subjected to Elevated Temperature." *Fire Safety Journal*, 71, 86-99.

Yan, Z.-g.;Zhu, H.-h., and Ju, J. W., 2013. "Behavior of Reinforced Concrete and Steel Fiber Reinforced Concrete Shield Tbm Tunnel Linings Exposed to High Temperatures." *Construction and Building Materials*, 38, 610-618.

Yan, Z.;Shen, Y.;Zhu, H., and Lu, Y., 2016. "Experimental Study of Tunnel Segmental Joints Subjected to Elevated Temperature." *Tunnelling and Underground Space Technology*, 53, 46-60.

Yang, J.-M.;Min, K.-H.;Shin, H.-O., and Yoon, Y.-S., 2012. "Effect of Steel and Synthetic Fibers on Flexural Behavior of High-Strength Concrete Beams Reinforced with FRP Bars." *Composites Part B: Engineering*, 43(3), 1077-1086.

Yao, Y.;Bakhshi, M.;Nasri, V., and Mobasher, B., 2018. "Interaction Diagrams for Design of Hybrid Fiber-Reinforced Tunnel Segments." *Materials and structures*, 51(1), 35.

Yoo, D.-Y.;Banthia, N., and Yoon, Y.-S., 2016. "Flexural Behavior of Ultra-High-Performance Fiber-Reinforced Concrete Beams Reinforced with GFRP and Steel Rebars." *Engineering Structures*, 111, 246-262.

Yoo, D.-Y.;Kwon, K.-Y.;Park, J.-J., and Yoon, Y.-S., 2015a. "Local Bond-Slip Response of GFRP Rebar in Ultra-High-Performance Fiber-Reinforced Concrete." *Composite Structures*, 120, 53-64.

Yoo, D.-Y.;Yoon, Y.-S., and Banthia, N., 2015b. "Flexural Response of Steel-Fiber-Reinforced Concrete Beams: Effects of Strength, Fiber Content, and Strain-Rate." *Cement and Concrete Composites*, 64, 84-92.

Yost, J. R.;Gross, S. P., and Dinehart, D. W., 2003. "Effective Moment of Inertia for Glass Fiber-Reinforced Polymer-Reinforced Concrete Beams." *ACI Structural Journal*, 100(6), 732-739.

Yuan, Y.;Bai, Y., and Liu, J., 2012. "Assessment Service State of Tunnel Structure." *Tunnelling and underground space technology*, 27(1), 72-85.

Zadeh, H. J., and Nanni, A., 2017. "Flexural Stiffness and Second-Order Effects in Fiber-Reinforced Polymer-Reinforced Concrete Frames." *ACI Structural Journal*, 114(2), 533.

Zhang, B.;Masmoudi, R., and Benmokrane, B., 2004. "Behaviour of One-Way Concrete Slabs Reinforced with CFRP Grid Reinforcements." *Construction and Building materials*, 18(8), 625-635.

Zhang, L.;Sun, Y., and Xiong, W., 2015. "Experimental Study on the Flexural Deflections of Concrete Beam Reinforced with Basalt FRP Bars." *Materials and Structures*, 48(10), 3279-3293.

Zheng, W.;Kwan, A., and Lee, P., 2001. "Direct Tension Test of Concrete." *Materials Journal*, 98(1), 63-71.

Zhiqiang, Z., and Mansoor, Y. A., 2013. "Evaluating the Strength of Corroded Tunnel Lining under Limiting Corrosion Conditions." *Tunnelling and underground space technology*, 38, 464-475.

APPENDIX A

In the presence of axial load, the neutral-axis depth can be calculated using Eqns. A.1 and A.2 in the design according to ACI 440.1R-15 and CAN/CSA S806-12, respectively.

$$c = \frac{\sqrt{4lm(d+d') + (-P+2l)^2} - 2l + P}{2m}, \text{ where } c \geq c_b \quad \text{(A.1)}$$

$$c = \frac{\sqrt{4\varphi_c\varphi_f lm(d+d') + (-P+2\varphi_f l)^2} - 2\varphi_f l + P}{2\varphi_c m}, \text{where } c \geq c_b \quad \text{(A.2)}$$

When neglecting the contribution of the bars in compression, the following equations can be used to calculate the neutral-axis depth when $c \geq d'$.

$$c = \frac{\sqrt{4lmd + (l-P)^2} - l + P}{2m}, \text{ where } c \geq c_b \quad \text{(A.3)}$$

$$c = \frac{\sqrt{4\varphi_c\varphi_f lmd + (\varphi_f l - P)^2} - \varphi_f l + P}{2\varphi_c m}, \text{ where } c \geq c_b \quad \text{(A.4)}$$

During the service stage, considering linear stress–strain relationship for the concrete in compression, the following equations can be used for the neutral-axis depth.

$$c = \frac{\sqrt{(P+2j)^2 + 2bE_c\lambda\varepsilon_{fu}\left[j(d+d') + Pd\right]} - 2j - P}{bE_c\lambda\varepsilon_{fu}}, \text{where } \varepsilon_c \leq \gamma\varepsilon_{cu} \quad \text{(A.5)}$$

where j is calculated according to Eq. A.6 and $\varepsilon_c = \frac{c}{d-c}\lambda\varepsilon_{fu}$.

$$j = A_f E_f \lambda \varepsilon_{fu} \tag{A.6}$$

When neglecting the contribution of the bars in compression, Eq. A.5 is modified to Eq. A.7 when $c \geq d^{'}$.

$$c = \frac{\sqrt{(P+j)^2 + 2bE_c\lambda\varepsilon_{fu}\left[jd + Pd\right]} - j - P}{bE_c\lambda\varepsilon_{fu}}, \text{where } \varepsilon_c \leq \gamma\varepsilon_{cu} \tag{A.7}$$

Equations A.8 and A.9 were developed to find the balanced reinforcement ratio in the presence of axial load. To derive the mentioned equations, both top and bottom meshes were considered. It should be noted that, when the neutral-axis depth level is higher than the top reinforcement, neglecting the contribution of the top reinforcement results in a smaller ρ_{fb} value, which is unconservative.

$$\rho_{fb} = \frac{md\varepsilon_{cu} - P(\varepsilon_{cu} + \varepsilon_{fu})}{bE_f(\varepsilon_{cu} + \varepsilon_{fu})\left[\varepsilon_{fu}(d + d^{'}) - \varepsilon_{cu}(d - d^{'})\right]} \geq 0 \tag{A.8}$$

$$\rho_{fb} = \frac{\varphi_c md\varepsilon_{cu} - P(\varepsilon_{cu} + \varepsilon_{fu})}{b\varphi_f E_f(\varepsilon_{cu} + \varepsilon_{fu})\left[\varepsilon_{fu}(d + d^{'}) - \varepsilon_{cu}(d - d^{'})\right]} \geq 0 \tag{A.9}$$

Equations A.10 and A.11 present the balanced reinforcement ratio when the contribution of the bars in compression is neglected.

$$\rho_{fb} = \frac{md\varepsilon_{cu} - P(\varepsilon_{cu} + \varepsilon_{fu})}{bdE_f\varepsilon_{fu}(\varepsilon_{cu} + \varepsilon_{fu})} \geq 0 \tag{A.10}$$

$$\rho_{fb} = \frac{\varphi_c md\varepsilon_{cu} - P(\varepsilon_{cu} + \varepsilon_{fu})}{b\varphi_f E_f\varepsilon_{fu}(\varepsilon_{cu} + \varepsilon_{fu})} \geq 0 \tag{A.11}$$

APPENDIX B

Geometrical parameters

The geometrical parameters shown in Fig. 8.2 can be calculated with the following equations.

$$f = R - \sqrt{R^2 - (\frac{l}{2})^2} \tag{B1}$$

$$y_x = f + R(\frac{\sqrt{R^2 - (\frac{l}{2} - x)^2}}{R} - 1) \tag{B2}$$

$$y_\theta = f + R[\sin(\alpha + \theta) - 1] \tag{B3}$$

For the tested specimens, the geometrical parameters are $\alpha = 1.193 rad$, $\theta_{\max} = 0.378 rad$, l = 2492 mm (98 in), f =238 mm (9.4 in), and R =3375 mm (133 in).

Internal forces

The maximum bending moment and its relation to the applied load can be calculated as follows.

$$M_a = M_{\max} = \frac{P}{2}\left[\frac{l}{2} + f\cot(\alpha)\right] \tag{B4}$$

$$P = \frac{2M_a}{\left[\frac{l}{2} + f\cot(\alpha)\right]} \tag{B5}$$

Calculating elastic deflection of the specimens

The relationship between the applied load and the internal forces for the half length of the tested specimens is presented below:

$$M_\theta = \frac{P}{2}\left[\frac{l}{2} - R\,|\cos(\alpha + \theta)| + (R(\sin(\alpha + \theta) - 1) + f)\cot(\alpha)\right] \tag{B6}$$

$$N_\theta = \frac{P}{2}(\cot(\alpha)\sin(\alpha + \theta) - |\cos(\alpha + \theta)|) \tag{B7}$$

$$V_\theta = \frac{P}{2}(\cot(\alpha)\cos(\alpha + \theta) + \sin(\alpha + \theta)) \tag{B8}$$

Elastic deflection of the tested specimen can be obtained with Eq. 7.8 considering a constant modulus of elasticity along the member:

$$m_\theta = \frac{\partial M_\theta}{\partial P} = \frac{1}{2}\left[\frac{l}{2} - R\cos(\alpha+\theta) + (R(\sin(\alpha+\theta)-1)+f)\cot(\alpha)\right] \quad \text{(B9)}$$

$$\Delta_P = \frac{2}{EI}\int_0^{\frac{\pi}{2}-\alpha} \frac{P}{4}\left[\frac{l}{2} - R\cos(\alpha+\theta) + (R(\sin(\alpha+\theta)-1)+f)\cot(\alpha)\right]^2 Rd\theta$$

(B10)

By finding the integral and simplifying it we have:

$$\Delta_P = \frac{P\overline{R}}{E_c I} \quad \text{(B11)}$$

where $\overline{R}$ can be obtained with the following equation;

$$\overline{R} = \frac{-R}{16s^2}\left[2R^2(\kappa c_1 + s - 2(4c(s-1)-\kappa)) + 4R(2fc+ls)(c_1 - 2c^2 - c\kappa + 2s - 1) + \kappa(2fc+ls)^2\right] \quad \text{(B12)}$$

where $s = \sin(\alpha)$, $c = \cos(\alpha)$, $s_1 = \sin(2\alpha)$, $c_1 = \cos(2\alpha)$, and $\kappa = 2\alpha - \pi$.

Equation B12 is valid when the member has a constant moment of inertia over its length, which happens when the member is uncracked. Note that using Eq. 7.7 results in an equation similar to Eq. B12.

APPENDIX C

Deflection-calculation formula for specimens using the integration of curvature

The following procedure was used to derive the equations presented for deflection prediction using integration-of-curvature method. Bischoff and Gross (2011b) used a similar approach to find the deflection of straight beams.

$$\Delta = \Delta_g + \delta\Delta_{cr} \tag{C1}$$

$$\delta\varphi_\theta = \frac{M_\theta}{E_c I_{cr}} - \frac{M_\theta}{E_c I_g} = \frac{M_\theta}{E_c}\left(\frac{1}{I_{cr}} - \frac{1}{I_g}\right) \tag{C2}$$

$$\delta\Delta_{cr} = 2\int_{\theta_g}^{\frac{\pi}{2}-\alpha} m_\theta \delta\phi_\theta R d\theta \tag{C3}$$

$$\delta\Delta_{cr} = 2\frac{1}{E_c}\left(\frac{1}{I_{cr}} - \frac{1}{I_g}\right)\int_{\theta_g}^{\frac{\pi}{2}-\alpha} m_\theta M_\theta R d\theta \tag{C4}$$

Replacing M_θ and m_θ with those related to the test specimens yields:

$$\Delta_g = \frac{2P}{E_c I_g}\int_0^{\frac{\pi}{2}-\alpha} \frac{1}{4}\left[\frac{l}{2} - R\cos(\alpha+\theta) + (R(\sin(\alpha+\theta)-1)+f)\cot(\alpha)\right]^2 R d\theta \tag{C5}$$

$$\Delta_g = \frac{2P(1-\eta)}{E_c I_{cr}}\int_0^{\frac{\pi}{2}-\alpha} \frac{1}{4}\left[\frac{l}{2} - R\cos(\alpha+\theta) + (R(\sin(\alpha+\theta)-1)+f)\cot(\alpha)\right]^2 R d\theta \tag{C6}$$

$$\delta\Delta_{cr} = \frac{2P}{E_c}\left(\frac{1}{I_{cr}} - \frac{1}{I_g}\right)\int_{\theta_g}^{\frac{\pi}{2}-\alpha} \frac{1}{4}\left[\frac{l}{2} - R\cos(\alpha+\theta) + (R(\sin(\alpha+\theta)-1)+f)\cot(\alpha)\right]^2 R d\theta \tag{C7}$$

$$\delta\Delta_{cr} = \frac{2P\eta}{E_c I_{cr}}\int_{\theta_g}^{\frac{\pi}{2}-\alpha} \frac{1}{4}\left[\frac{l}{2} - R\cos(\alpha+\theta) + (R(\sin(\alpha+\theta)-1)+f)\cot(\alpha)\right]^2 R d\theta \tag{C8}$$

$$\begin{aligned}\Delta = \frac{2P(1-\eta)}{E_c I_{cr}}\Bigg[&\int_0^{\frac{\pi}{2}-\alpha} \frac{1}{4}\left[\frac{l}{2} - R\cos(\alpha+\theta) + (R(\sin(\alpha+\theta)-1)+f)\cot(\alpha)\right]^2 R d\theta + \\ &\left(\frac{\eta}{1-\eta}\right)\int_{\theta_g}^{\frac{\pi}{2}-\alpha} \frac{1}{4}\left[\frac{l}{2} - R\cos(\alpha+\theta) + (R(\sin(\alpha+\theta)-1)+f)\cot(\alpha)\right]^2 R d\theta\Bigg]\end{aligned} \tag{C9}$$

$$C_\theta = \frac{mM_\theta}{P} = \frac{1}{4}\left[\frac{l}{2} - R\cos(\alpha+\theta) + (R(\sin(\alpha+\theta)-1)+f)\cot(\alpha)\right]^2 \quad \text{(C10)}$$

$$\Delta = \frac{2P(1-\eta)}{E_c I_{cr}}[\int_0^{\frac{\pi}{2}-\alpha} C_\theta R d\theta + (\frac{\eta}{1-\eta})\int_{\theta_g}^{\frac{\pi}{2}-\alpha} C_\theta R d\theta] \quad \text{(C11)}$$

Simplifying the equations and finding the integral yields:

$$\Delta = \frac{P\lambda}{E_c I_{cr}} \quad \text{(C12)}$$

$$\lambda = 2(1-\eta)[\int_0^{\frac{\pi}{2}-\alpha} C_\theta R d\theta + (\frac{\eta}{1-\eta})\int_{\theta_g}^{\frac{\pi}{2}-\alpha} C_\theta R d\theta] \quad \text{(C13)}$$

where $\cos(\alpha) = c$, $\sin(\alpha) = s$, $\cos(2\alpha) = c_1$, $\cos(\alpha+\theta_g) = c_2$, $\cos(2\alpha+\theta_g) = c_4$,

$\sin(2\alpha) = s_1$, $\sin(2\theta_g) = s_2$, $\cos(\theta_g) = c_5$, $\alpha_1 = 2\alpha + 2\eta\theta_g - \pi$, $2fc + ls = c_6$.

$$\lambda = \frac{R\left[\begin{array}{l} 2R^2(4\eta cc_3 - 4\eta c_2(c_1+1) - \alpha_1 c_1 - s_1 + 4c(2s - \eta(c_5-2) - 2) - 4\alpha + \eta(s_2 - 4\theta_g) + 2\pi) \\ -4Rc_6(\eta c_3 - 2\eta cc_2 + c_1(1-\eta) + 2(\eta-1)c^2 - \alpha_1 c + 2s - \eta(c-1) - 1) - \alpha_1 {c_6}^2 \end{array}\right]}{16s^2} \quad \text{(C14)}$$

Deflection-calculation formula for the specimens using integration of curvature considering tension stiffening

In the following, the equations presented for deflection prediction using integration of curvature considering tension stiffening were derived and the deflection of the tested specimens was calculated accordingly:

$$\delta\varphi_\theta = \frac{M_\theta}{E_c I_\theta} - \frac{M_\theta}{E_c I_g} = \frac{\eta M_\theta}{E_c I_{cr}}\left(1 - \left(\frac{M_{cr}}{M_\theta}\right)^2\right) \quad \text{(C15)}$$

$$\delta\Delta_{cr} = \frac{2\eta}{E_c I_{cr}}\int_{\theta_g}^{\frac{\pi}{2}-\alpha} mM_\theta\left(\left(1 - \left(\frac{M_{cr}}{M_\theta}\right)^2\right)Rd\theta\right) \quad \text{(C16)}$$

$$\Delta_g = \frac{2(1-\eta)}{E_c I_{cr}}\int_0^{\frac{\pi}{2}-\alpha} mM_\theta R d\theta \quad \text{(C17)}$$

$$\Delta = \frac{2}{E_c I_{cr}}[(1-\eta)\int_0^{\frac{\pi}{2}-\alpha} mM_\theta R d\theta + \eta\int_{\theta_g}^{\frac{\pi}{2}-\alpha} mM_\theta((1-\left(\frac{M_{cr}}{M_\theta}\right)^2)Rd\theta] \quad \text{(C18)}$$

$$\delta\Delta_{cr} = \frac{2P\eta}{E_c I_{cr}}\int_{\theta_g}^{\frac{\pi}{2}-\alpha}\frac{1}{4}(\left[\frac{l}{2} - R\cos(\alpha+\theta) + (R(\sin(\alpha+\theta)-1)+f)\cot(\alpha)\right]^2 - \left(\frac{2M_{cr}}{P}\right)^2)Rd\theta \quad \text{(C19)}$$

$$\Delta_g = \frac{2P(1-\eta)}{E_c I_{cr}}\int_0^{\frac{\pi}{2}-\alpha}\frac{1}{4}\left[\frac{l}{2} - R\cos(\alpha+\theta) + (R(\sin(\alpha+\theta)-1)+f)\cot(\alpha)\right]^2 Rd\theta \quad \text{(C20)}$$

$$\Delta = \frac{2PR}{E_c I_{cr}}[(1-\eta)\int_0^{\frac{\pi}{2}-\alpha}\frac{1}{4}\left[\frac{l}{2} - R\cos(\alpha+\theta) + (R(\sin(\alpha+\theta)-1)+f)\cot(\alpha)\right]^2 d\theta +$$

$$\eta\int_{\theta_g}^{\frac{\pi}{2}-\alpha}\frac{1}{4}(\left[\frac{l}{2} - R\cos(\alpha+\theta) + (R(\sin(\alpha+\theta)-1)+f)\cot(\alpha)\right]^2 - \left(\frac{2M_{cr}}{P}\right)^2)d\theta] \quad \text{(C21)}$$

$$C_\theta = \frac{mM_\theta}{P} = \frac{1}{4}\left[\frac{l}{2} - R\cos(\alpha+\theta) + (R(\sin(\alpha+\theta)-1)+f)\cot(\alpha)\right]^2 \quad \text{(C22)}$$

$$\Delta = \frac{2P}{E_c I_{cr}}[(1-\eta)\int_0^{\frac{\pi}{2}-\alpha} C_\theta R d\theta + \eta\int_{\theta_g}^{\frac{\pi}{2}-\alpha}(C_\theta - (\frac{M_{cr}}{P})^2)Rd\theta] \quad \text{(C23)}$$

$$\Delta = \frac{P\lambda}{E_c I_{cr}} \quad \text{(C24)}$$

$$\lambda = 2[(1-\eta)\int_0^{\frac{\pi}{2}-\alpha} C_\theta R d\theta + \eta\int_{\theta_g}^{\frac{\pi}{2}-\alpha}(C_\theta - (\frac{M_{cr}}{P})^2)Rd\theta] \quad \text{(C25)}$$

$$C_{\theta_g} = (\frac{M_{cr}}{P})^2 = \frac{1}{4}\left[\frac{l}{2} - R\cos(\alpha+\theta_g) + (R(\sin(\alpha+\theta_g)-1)+f)\cot(\alpha)\right]^2 \quad \text{(C26)}$$

$$\lambda = 2[(1-\eta)\int_0^{\frac{\pi}{2}-\alpha} C_\theta R d\theta + \eta\int_{\theta_g}^{\frac{\pi}{2}-\alpha}(C_\theta - C_{\theta_g})Rd\theta] \quad \text{(C27)}$$

The parametric integral can be obtained. Since the expression is lengthy, it is not presented herein.

APPENDIX D

According to Fig. 8.7, $\Delta\Phi_{\max}$ can be obtained with the following equation.

$$\Delta\Phi_{\max} = \frac{M_{cr}}{E_c I_{cr}} - \frac{M_{cr}}{E_c I_g} \tag{D1}$$

The modified method aims at modeling a rapid increase after cracking occurs. Therefore, the second term in Eq. D1 was multiplied by $n(f'_{c,n}\rho_{fb} / f'_c\rho_f)^q$ as follows.

$$\Delta\Phi_{\mathrm{m}} = \frac{M_{cr}}{E_c I_{cr}} - n(\frac{f'_{c,n}\rho_{fb}}{f'_c\rho_f})^q \frac{M_{cr}}{E_c I_g} \tag{D2}$$

$$\Delta\Phi_{\mathrm{m}} = \frac{M_{cr}}{E_c I_{cr}} (1 - n(\frac{f'_{c,n}\rho_{fb}}{f'_c\rho_f})^q \frac{I_{cr}}{I_g}) \tag{D3}$$

It can be inferred that increasing the reinforcement ratio decreased the multiplication factor since the increase after cracking becomes less pronounced. The tension-stiffening factor of β is defined as $\Delta\Phi / \Delta\Phi_{\max}$. The following equation is proposed to reduce the tension-stiffening factor of β to β_m:

$$\beta_m = m(\frac{f'_c\rho_f}{f'_{c,n}\rho_{fb}})^p \frac{\Delta\Phi}{\Delta\Phi_{\max}} \tag{D4}$$

where $\beta_m = \Delta\Phi / \Delta\Phi_m$. The change in curvature in the modified method due to the tension stiffening is:

$$\phi_\theta = \Phi_{\beta=0} - \Delta\Phi \tag{D5}$$

Therefore:

$$\phi_\theta = \frac{M_\theta}{E_c I_{cr}} - \beta_m \Delta\Phi_{\mathrm{m}} \tag{D6}$$

By considering $\beta = M_{cr} / M_\theta$ and inserting the values of $\Delta\Phi_{\mathrm{m}}$ and β_m from Eqns. D3 and D4, respectively, into Eq. D6 yields:

$$\phi_\theta = \frac{M_\theta}{E_c I_{cr}}(1 - m(\frac{f_c^{'}\rho_f}{f_{c,n}^{'}\rho_{fb}})^p (\frac{M_{cr}}{M_\theta})^2 (1 - n(\frac{f_{c,n}^{'}\rho_{fb}}{f_c^{'}\rho_f})^q \frac{I_{cr}}{I_g})) \quad \text{(D7)}$$

Therefore, the curvature in the modified method can be obtained with the following equation:

$$\phi_\theta = \frac{M_\theta}{E_c I_{cr}}(1 - \eta_n \beta_m \frac{M_{cr}}{M_\theta}) \quad \text{(D8)}$$

where η_n can be obtained from the following equation:

$$\eta_n = (1 - n(\frac{f_{c,n}^{'}\rho_{fb}}{f_c^{'}\rho_f})^q \frac{I_{cr}}{I_g}) \quad \text{(D9)}$$

APPENDIX E

In the following, the deflection of one of the tested specimens (7G#5) was calculated based on the presented procedure to consider the effect of real loading and boundary conditions. The deflection was calculated at the service moment corresponding to 0.3 of the bending-moment capacity.

Step I: Finding the internal forces and initial deflection at joints using first order analysis

The reaction forces, distribution of bending moment, distribution of axial load, and rotation at supports were obtained using elastic deflection-calculation procedure and shown in Fig. E1. It should be noted that, as the system was determined, there was no need to consider an initial moment of inertia to obtain the internal forces. Equation 7.29, however, was used to find the initial moment of inertia in determining the rotation at the supports. The rotation at the supports obtained from the first-order analysis was 0.0116 rad.

Step II: Calculating rotation and deflection

This procedure was followed to determine the rotation and deflection diagram of specimen 7G#5 (see Table E1 and Fig. E1).

1. The segment was divided into 24 elements with $\Delta\theta$ equal to 0.0315 rad.
2. The axial load and bending moment for each element was specified, as listed in Table E1.
3. The experimental cracking moment was compared to the bending moment at each point.

4. For the point where the bending moment was greater than the cracking moment, the moment of inertia was calculated according to Eq. 7.34. In contrast, I_g was used when the section was not cracked.
5. The curvature was obtained by dividing the bending moment by E_c I.
6. The value of rotation at each point was founded. The following equations provide the rotation based on trapezoidal rule and Simpson's rule:

$$\Theta_i = -R\left[\frac{\Delta\theta}{2}(\phi_1 + 2\phi_2 + 2\phi_3 + ... + 2\phi_{i-1} + \phi_i)\right] + \Theta_A \quad \text{(E1)}$$

$$\Theta_i = -R\left[\frac{\Delta\theta}{3}(\phi_1 + 4\phi_2 + 2\phi_3 + 4\phi_4 + 2\phi_5 .. + 2\phi_{i-2} + 4\phi_{i-1} + \phi_i)\right] + \Theta_A \quad \text{(E2)}$$

7. The value of $R\theta_\theta \sin(\alpha + \theta)$ was calculated for each point.
8. The following equations were used to find the value of deflection at each point based on trapezoidal rule and Simpson's rule.

$$\Delta_i = -R\left[\frac{\Delta\theta}{2}(\Theta_1 \sin\gamma_1 + 2\Theta_2 \sin\gamma_2 + 2\Theta_3 \sin\gamma_3 + ... + 2\Theta_{i-1} \sin\gamma_{i-1} + \Theta_i \sin\gamma_i)\right] + \Theta_A \quad \text{(E3)}$$

$$\Delta_i = -R\left[\begin{array}{l}\frac{\Delta\theta}{3}(\Theta_1 \sin\gamma_1 + 4\Theta_2 \sin\gamma_2 + 2\Theta_3 \sin\gamma_3 + 4\Theta_4 \sin\gamma_4 + 2\Theta_5 \sin\gamma_5 .. + \\ 2\Theta_{i-2} \sin\gamma_{i-2} + 4\Theta_{i-1} \sin\gamma_{i-1} + \Theta_i \sin\gamma_i)\end{array}\right] + \Theta_A \quad \text{(E4)}$$

where $\gamma_i = \alpha + i\Delta\theta$

According to Table E1, the mid-span deflection obtained was 12.08 mm, which is 8% greater than the experimental deflection. Therefore, the presented procedure yielded accurate result with an acceptable level of conservativeness. As can be inferred from Table E1 and Fig. E1, the rotation and deflection were not symmetrical despite symmetrical loading and boundary conditions. This is due to the initial rotation value at the supports in step I, which was the main source of error in the calculations.

Table E1 Deflection-calculation procedure for 7G#5 using the proposed method.

θ	M_θ kN.m	N_θ kN	$M \geq M_{cr}$	I_{cr} mm^4	I_θ mm^4	I mm^4	ϕ_θ 1/mm	θ_θ rad	$R\theta_\theta$ $\sin(\alpha+\theta)$	Δ_θ mm
0	0	0	No	-	-	1.95E+09	0	0.0116	36.389	0.00
0.0315	6	-2	No	-	-	1.95E+09	1.064E-07	0.011594	36.808	1.15
0.063	12	-4	No	-	-	1.95E+09	2.12E-07	0.011577	37.154	2.32
0.0945	18	-5	No	-	-	1.95E+09	3.17E-07	0.011549	37.425	3.49
0.126	25	-7	No	-	-	1.95E+09	4.22E-07	0.01151	37.622	4.67
0.1575	31	-9	No	-	-	1.95E+09	5.26E-07	0.01146	37.742	5.86
0.189	37	-11	No	-	-	1.95E+09	6.30E-07	0.011398	37.786	7.05
0.2205	43	-13	No	-	-	1.95E+09	7.33E-07	0.011326	37.753	8.24
0.252	49	-14	Yes	7.9E+07	1.07E+08	1.07E+08	1.53E-05	0.010475	35.074	9.39
0.2835	55	-16	Yes	7.9E+07	9.97E+07	9.97E+07	1.84E-05	0.008687	29.189	10.40
0.315	61	-18	Yes	7.9E+07	9.52E+07	9.52E+07	2.13E-05	0.00658	22.164	11.21
0.3465	66	-20	Yes	7.9E+07	9.21E+07	9.21E+07	2.41E-05	0.004167	14.057	11.78
0.378	72	-21	Yes	7.9E+07	9.00E+07	9.00E+07	2.68E-05	0.001461	4.932	12.08
0.4095	66	-20	Yes	7.9E+07	9.21E+07	9.21E+07	2.41E-05	-0.00124	-4.193	12.09
0.441	61	-18	Yes	7.9E+07	9.52E+07	9.52E+07	2.13E-05	-0.00365	-12.304	11.83
0.4725	55	-16	Yes	7.9E+07	9.97E+07	9.97E+07	1.83E-05	-0.00576	-19.344	11.33
0.504	49	-14	Yes	7.9E+07	1.07E+08	1.07E+08	1.52E-05	-0.00754	-25.254	10.63
0.5355	43	-13	No	-	-	1.95E+09	7.32E-07	-0.00839	-27.972	9.79
0.567	37	-11	No	-	-	1.95E+09	6.28E-07	-0.00846	-28.058	8.91
0.5985	31	-9	No	-	-	1.95E+09	5.25E-07	-0.00853	-28.076	8.02
0.63	25	-7	No	-	-	1.95E+09	4.20E-07	-0.00858	-28.028	7.14
0.6615	18	-5	No	-	-	1.95E+09	3.15E-07	-0.00862	-27.913	6.26
0.693	12	-4	No	-	-	1.95E+09	2.10E-07	-0.00864	-27.733	5.38
0.7245	6	-2	No	-	-	1.95E+09	1.05E-07	-0.00866	-27.488	4.51
0.756	0	0	No	-	-	1.95E+09	0	-0.00867	-27.179	3.65

Notes: 1 mm = 0.0394 in.; 1 mm^4 = 2.4×10^{-6} in^4; 1 kN = 0.225 kip; 1 kN·m = 0.7376 kip-ft.

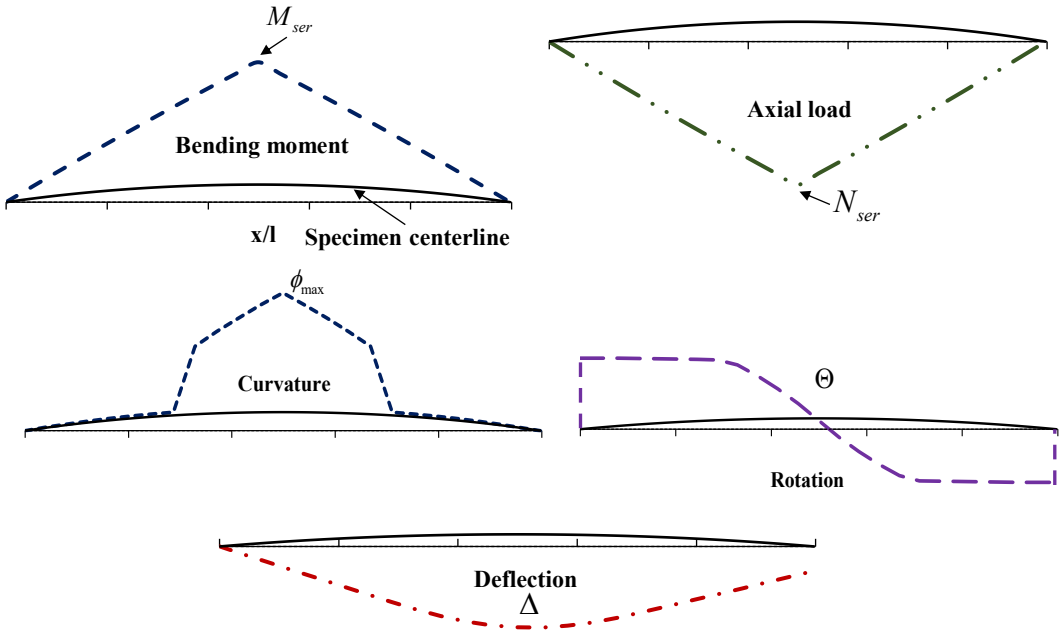

Figure E1 Deflection-calculation procedure for specimen 7G#5 using the proposed procedure.